

PAUL SCHERRER INSTITUT



PSI Scientific Report 2005

Volume 1

Condensed matter,
photons, neutrons and
charged particles

Cover photo:

**Producing nanostructures with
photo-lithography at the
X-ray interference-lithography
beamline (XIL), at the SLS.**

(Photo: H.R. Bramaz)



PSI Scientific Report 2005

Volume 1

Condensed matter,
photons, neutrons and
charged particles

Imprint

PSI Scientific Report 2005 Volume 1

Volume 1 Condensed matter, photons,
neutrons and charged particles

Volume 2 Life sciences and medicine

Volume 3 Energy and environment

Published by

Paul Scherrer Institute

Concept and editorial work by

Juanita Schläpfer-Miller, Beat Gerber

Proof-reading

Terry Groves

Design and layout

Monika Blétry

Available from

Paul Scherrer Institute
Communications Services
5232 Villigen PSI, Switzerland
Phone +41 (0)56 310 42 61
www.psi.ch

PSI public relations

pubrel@psi.ch

Communications officer

Beat Gerber, Phone +41 (0)56 310 29 16

ISSN 1661-7002

Copying is welcomed, provided
the source is acknowledged and an
archive copy sent to PSI.

Paul Scherrer Institute, May 2006

Table of contents 3

Volume 1
Condensed matter, photons,
neutrons and charged particles

4 Foreword from the director

7 Research focus and highlights

- 8 Synchrotron light
- 28 Neutrons and muons
- 48 Particle physics, astrophysics and nuclear chemistry
- 68 Micro- and nanotechnology
- 74 Accelerators

83 User facilities

- 84 Swiss Light Source SLS
- 88 Spallation Neutron Source SINQ
- 92 Swiss Muon Source μ S
- 94 Proton accelerator
- 100 Tandem accelerator

103 Technology transfer

Patents and licenses

111 Facts and figures

Research and user labs
Commission and committees

121 Publications

Lists and links to web

CD with publication lists and links to web



From ivory towers to alpine huts

Do scientists really occupy ivory towers? Do they live a comfortable, even luxurious life without contact to the real world? Researchers prefer to see themselves rather as hearty members of the Swiss Alpine Club, where, until recently, one needed special training and equipment to overnight in high mountain huts. Only those who were prepared for a difficult hike the next day could stay at the top of the mountain.

Earlier, a scientific experiment, like a mountain climb was done in the company of a few colleagues, without mobile phone contact, cut off from the rest of the world. This has changed dramatically in the last few decades. Even inexperienced hikers can stay overnight in alpine huts, transported to their destinations by cable-cars. Responding to the increasing interest of the lay public in research, science has also become more accessible and public-friendly.

Spectacular moments are rare

Mountain climbers were accompanied by live TV cameras for their ascent of the north face of the Eiger. In a similar search for the dramatic, TV crews install themselves in labs in the hope of broadcasting scientific first ascents. Yet spectacular discoveries are rare and often only years later achieve popular recognition and acclaim.

An excellent example of this is the ground-breaking work of Albert Einstein from 1905. One-hundred-years later his works were exulted at PSI and around the world. During the International Year of Physics, Einstein theme tours for the public

were organised at PSI providing basic explanations of the three papers published in his 'annus mirabilis'. Last year the number of visitors at the PSI open day was nearly 10,000 – illustrating that the world of science has learnt to present itself competently and attractively.

Research needs freedom

The question often emerges as to whether taxpayers' money is being used efficiently for research. Perhaps the question should be more directly formulated as: can Switzerland compete globally for the best talent? The usual answers are thus; we need to join forces through better co-ordination, eliminate duplication of efforts and found centres of competence. However, often the most important factor is overlooked: excellence in research requires tolerance and space for unconventional ideas to flourish.

Competence requires time

The Swiss Nobel prize-winner Heinrich Rohrer used to say that; 'One cannot establish a competence centre, at the most it is something that one can become.' In this sense the year 2005 was the start of a vision. Under the leadership of PSI, and supported by the accumulated intelligence of the ETH Domain, large energy research projects will be started which will lead to secure and sustainable energy solutions for Switzerland.

Creative heads will engage with projects to do with mobility, electricity and low temperature heat. We are very grateful for the financial support of the Swiss government and the Canton of Aargau.

to this is PSI's positive reputation within the international scientific community, in Swiss national politics and in our local community. For this trust and recognition, our warmest thanks.

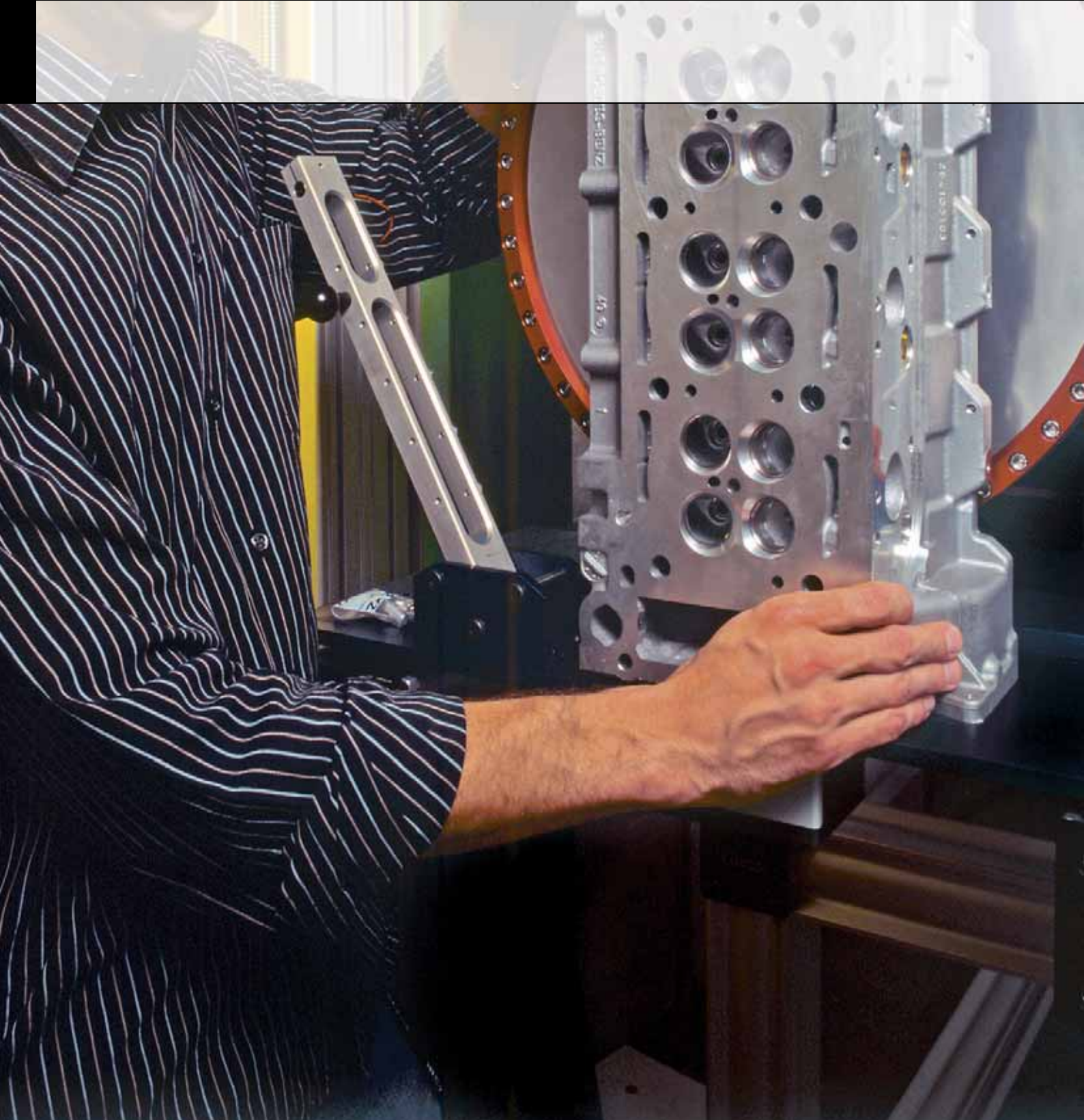
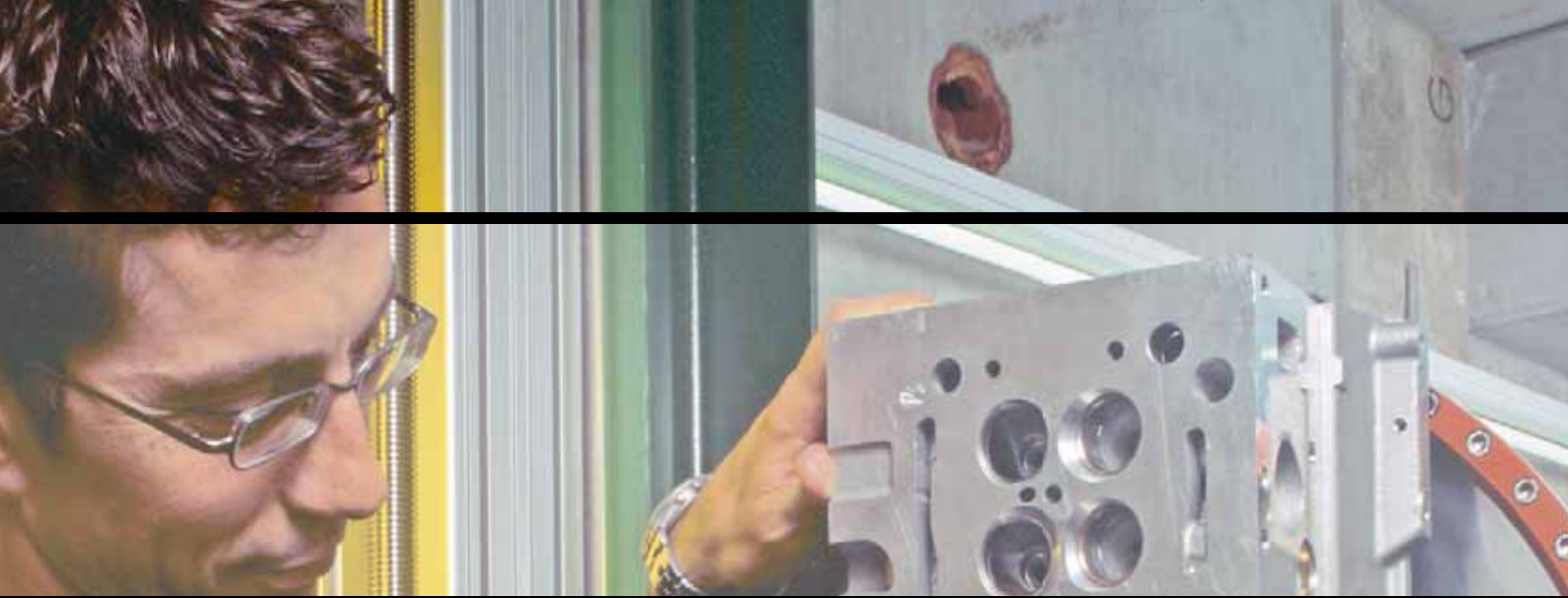
Ralph Eichler, Director PSI

Scientific success in 2005

This volume of the Scientific Report 2005, Volume 1, highlights condensed matter research with photons, neutrons and charged particles. One scientific success was the rediscovery of uses for phase-contrast microscopy (page 8). Thanks to innovative ideas and technical skills, diffraction grating with an absorber of a few nanometers thick can be created for X-rays or neutrons which then produce razor sharp images after a few minutes exposure time. The potential applications for use with X-rays come from biology and medicine and for neutrons from the material sciences. Both techniques show promising applications for external clients of PSI, patents have been applied for.

The international scientific community makes intensive use of the research facilities at PSI, and reports here from the user laboratories bring to light the breadth both of research tools available and the themes studied.

Scientific excellence is always the first priority of PSI and precisely because of this, science must be more accountable to society. Visitor tours and science communication to the public have become part of daily business. The myth that researchers work in an ivory tower is obsolete. As testimony



Research focus and highlights 7

- 8 Synchrotron light
- 28 Neutrons and muons
- 48 Particle physics, astrophysics and nuclear chemistry
- 68 Micro- and nanotechnology
- 74 Accelerators

Condensed matter research at PSI often involves cross discipline and inter-department work. The research departments involved are Synchrotron Radiation and Nanotechnology (SYN); Condensed Matter Research with Neutrons and Muons (NUM); Particles and Matter (TEM). The research departments are supported with the technical expertise of the Department of Large Research Facilities (GFA), which reports along with the user labs, in the next chapter.

The use of muons and neutrons as probes has provided results in the study of water flow in soil, and the characterisation of nanomagnetic structures. Also reported here is the usefulness of the femto-second laser at the SLS, which allows time-resolved experiments with hard X-rays. First results with the Si-microstrip detector are available and high test rates were achieved with the CMS detector prototypes being built for the Large Hadron Collider.

This report only highlights a selection of the work undertaken at PSI in the past year; information about many other engaging projects can be accessed through our website (www.psi.ch).

At the ICON facility neutrons reveal the inside of a motor, in a non-destructive testing method.

(Photo: H.R. Bramaz)

Better X-ray pictures with phase contrast imaging

Franz Pfeiffer, Oliver Bunk, Christian Grünzweig, Xavier Donath, Ian Johnson, Claude Pradervand, Marco Stampanoni, Amela Grosio, Christian Kottler, Jens Bruder, Christian David, *Research Department Synchrotron Radiation and Nanotechnology, PSI*; Gabriel Frei, Guido Kühne, Eberhard Lehmann, Henrik Rønnow, *Research Department Condensed Matter Research with Neutrons and Muons, PSI*

We report on a grating based interferometer for X-ray and neutron phase contrast imaging. As opposed to existing techniques, the method requires only little coherence and can thus be used with low-brilliance radiation sources. In the case of X-rays, the method can significantly improve the contrast of radiographs and has a great potential to reduce the applied dose in medical imaging. For neutrons, the first experimental results obtained at the new ICON facility show that this technique opens up a way to image the influence of the object on the quantum-mechanical phase of the neutron de Broglie wave.

Today a majority of X-ray or neutron radiographic applications are based on the attenuation of the radiation inside the object. However, the imaging of the phase shift of the object can provide new and complementary information. In the case of X-rays, phase sensitive imaging yields an increased contrast for biological samples and thus is of interest for medical applications [1]. Neutron phase measurements, on the other hand, have a long and distinguished history in the exploration of the fundamental properties of quantum mechanics [2]. Phase-contrast imaging relies on refraction, or changes in the angular trajectory of X-rays or neutrons. Just as light rays bend when they enter water from air, X-rays or neutrons deflect as they travel through objects of varying densities. We measure this deflection with an interferometer, which consists of two gratings (Fig. 1). In a simplified picture, it can be thought of as a multi-collimator that translates the angular deflections behind the object into changes of the locally transmitted intensity, which can be detected with a standard imaging detector.

The crucial part of the interferometer is a pair of well-defined gratings – each is a thin slab of material with narrow, closely spaced parallel lines etched into it. The fabrication process for these structures has been developed at the Laboratory for Micro- and Nanotechnology and involves photolithography, deep etching into silicon and electroplating of gold or evaporation of gadolinium.

Synchrotron experiments carried out at the Swiss Light Source yielded high quality phase contrast images and allowed for further improvements in the setup and the data processing algorithms [3, 4, 5].

A new phase in medical imaging

A prerequisite for methods aiming for clinical applications is that they should work with standard and commercially available X-ray generators, and not only with highly brilliant and partially coherent X-rays from a synchrotron [6]. In this particular aspect the grating interferometer is superior to already existing phase-sensitive techniques, because it can be used at low-brilliance sources.

This is demonstrated in Figure 2, where the results of applying our method to a biological object, a small fish, as shown. The conventional X-ray transmission image is shown in Figure 2a, while Figure 2b contains an image of the corresponding phase contrast signal.

As expected, the skeleton of the fish and other highly absorbing structures, such as the calcified ear stones (otoliths) are clearly visible in the conventional radiograph (Fig. 2a and e).

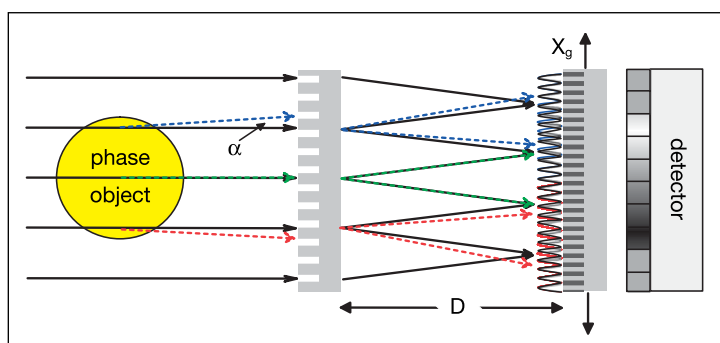


Figure 1: X-ray and neutron grating interferometer.

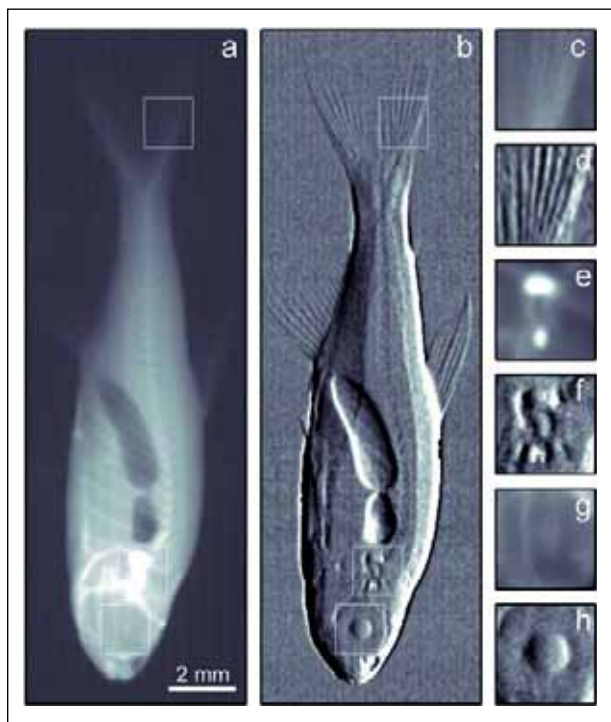


Figure 2: **A small fish (*Paracheirodon axelrodi*) imaged at a standard X-ray tube source. (a) conventional amplitude contrast, (b) differential phase contrast.**

However, small differences in the density of the soft tissue, e.g., the fine structure of the tail fin, eye, and the region around the otoliths is hardly visible in the absorption image (Fig. 2c, e, g). The corresponding phase contrast image, however, reveals these details (Fig. 2d, f, h).

Imaging the neutron nuclear phase shift

Even though neutrons are usually considered to be particles, they nevertheless undergo a similar phase shift as X-rays when passing through matter. To detect this effect, we constructed a grating based neutron interferometer. Figure 3 shows corresponding results for a test sample made of copper (Cu) and titanium (Ti) metal rods. Neutrons delivered at the new cold neutron imaging facility (ICON) at the *Swiss Spallation Neutron Source* were used.

Since the phase contrast signal is a direct measure of the object's local phase gradient $d\Phi(x,y)/dx$, the total phase shift of the object can be retrieved by a simple one-dimensional integration along x .

Due to the similar neutron capture cross-sections and the incoherent scattering lengths, there is not a large difference in the attenuation of the neutron beam in the rods (Fig. 3a). In Figure 3b, however, where the projected neutron nuclear phase shift is shown, a clear difference between Cu and Ti can

be observed. It is interesting to note that Ti has a brighter colour compared to the background, whereas Cu appears darker. This is due to the negative neutron scattering length density of Ti. Consequently, a negative phase shift is measured in the material.

Based on these results we conclude that the method represents a major step forward in phase contrast radiography with incoherent radiation sources. We believe that this method can be implemented without major changes to currently existing medical imaging or non-destructive X-ray testing systems. Our first experimental results with neutrons show that this technique opens up a way for imaging the influence of the object on the quantum-mechanical phase of the neutron de Broglie wave.

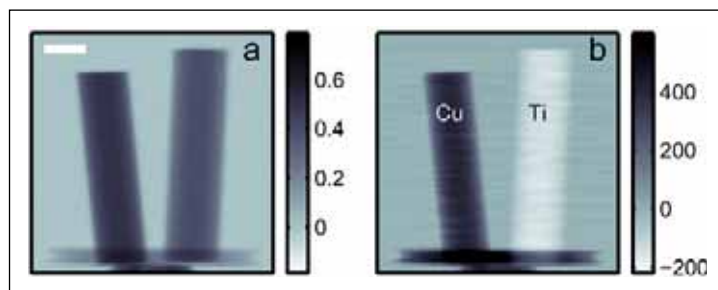


Figure 3: **Conventional neutron attenuation image (a) and retrieved phase image (b) of two metal rods. The scale bar corresponds to 5 mm.**

References

- [1] R. Fitzgerald et al., *Physics Today*, 53 7, 23 (2000)
- [2] H. Rauch, *Neutron Interferometry*, (Oxford University Press, Oxford, 2000)
- [3] C. David et al., *Appl. Phys. Lett.*, 81, 3287 (2002)
- [4] T. Weitkamp et al., *Proc. SPIE*, 5535, 137 (2004)
- [5] T. Weitkamp et al., *Optics Express*, 13, 6296 (2005)
- [6] F. Pfeiffer et al., *Nature Physics*, 2, 258 (2006)

Swiss light shed on the nature of fossilised embryos from the dawn of animal evolution

Philip Donoghue, Neil Gostling, *Dept. of Earth Sciences, University of Bristol, UK*; Stefan Bengtson, Therese Huldtgren, *Dept. of Paleozoology, Swedish Museum of Natural History, Sweden*; Xiping Dong, Fan Peng, *School Of Earth & Space Sciences, Peking University, Beijing, P. R. China*; Marco Stampanoni, *Research Department Synchrotron Radiation and Nanotechnology, PSI*

Although only recently discovered, the fossil record of embryonic development has already begun to challenge cherished hypotheses on the origin of major animal groups. Synchrotron-based X-ray Tomographic Microscopy has provided unparalleled insight into the anatomy and preservation of these fossil remains and this has allowed us to test competing hypotheses on their nature. With knowledge of both adults and embryos from the time of diversification of the major animals groups, it is now possible to test models of developmental evolution based on modern model organisms using information from their long-extinct ancestors.

Fossils represent the only direct record of evolutionary history, but that record has long been denigrated for its failure to provide any insight into embryology. Changes to embryology represent the most potent mechanism of evolutionary change, but until recently fossilisation processes had not been known to preserve structures as delicate as embryos. Remarkably, however, fossilised embryos have now been discovered in rocks deposited at the dawn of animal evolution [1-2]. These remains offer great opportunities for palaeontology to understand developmental evolution, but also great challenges to develop suitable methods of analysis of these microscopic remains. The scanning electron microscope is the routine tool of choice in palaeontology, but it only provides insight into surface morphology [1-2], while embryology mainly concerns events within. Methods such as sectioning have been employed [3] but interpretations of these data have proven highly equivocal [4], and desktop computed tomography provides insufficient resolution and contrast.

SLS provides fundamental insights

To overcome these limitations we have employed synchrotron-based X-ray Tomographic Microscopy (SRXTM) which provides an unparalleled high-resolution, non-destructive approach. It has provided fundamental new insights into the anatomy, development, and fossilisation of early animal embryos, generating data to challenge cherished hypotheses on the role of embryological evolution during the emergence of major animal groups.

Our research has so far focused on attempting to resolve the manner in which embryos are fossilised to determine the veracity of controversial claims of fossilised embryos and larvae from before the Precambrian–Cambrian transition 542 million years ago [3,5]. Embryos underwent a two-stage process of fossilisation: the first in which biogenic structure was replicated by mineral-precipitating bacteria, and a second later stage in which the preserved structure was encrusted by minerals. The distinction between the two phases is picked out by differing levels of X-ray attenuation. This advance has allowed us to reject many claims of embryos and larvae in which the alleged biogenic structures can be shown to be features of post-mortem mineralization.

The second focus of our research has been to unravel the internal structure and anatomy of bona fide fossil embryos recovered from rocks of Cambrian age. In particular, we have elucidated the anatomy of *Markuelia*, the oldest embryo of a complex animal known from the geological record. *Markuelia* has been controversial because of its worm-like form and apparent direct mode of embryonic development; annelids undergo indirect development, passing through metamorphosis from larva to the adult.

SRXTM analysis has allowed us to resolve the anatomy of *Markuelia*, demonstrating that its similarity to annelid worms is superficial and its possession of a terminal mouth, armed with circumferential rows of retractable teeth, together with a host of other features, demonstrate its close evolutionary relationship to the arthropods and a delightfully obscure ensemble of animals including the round worms, hair worms and priapulid worms.

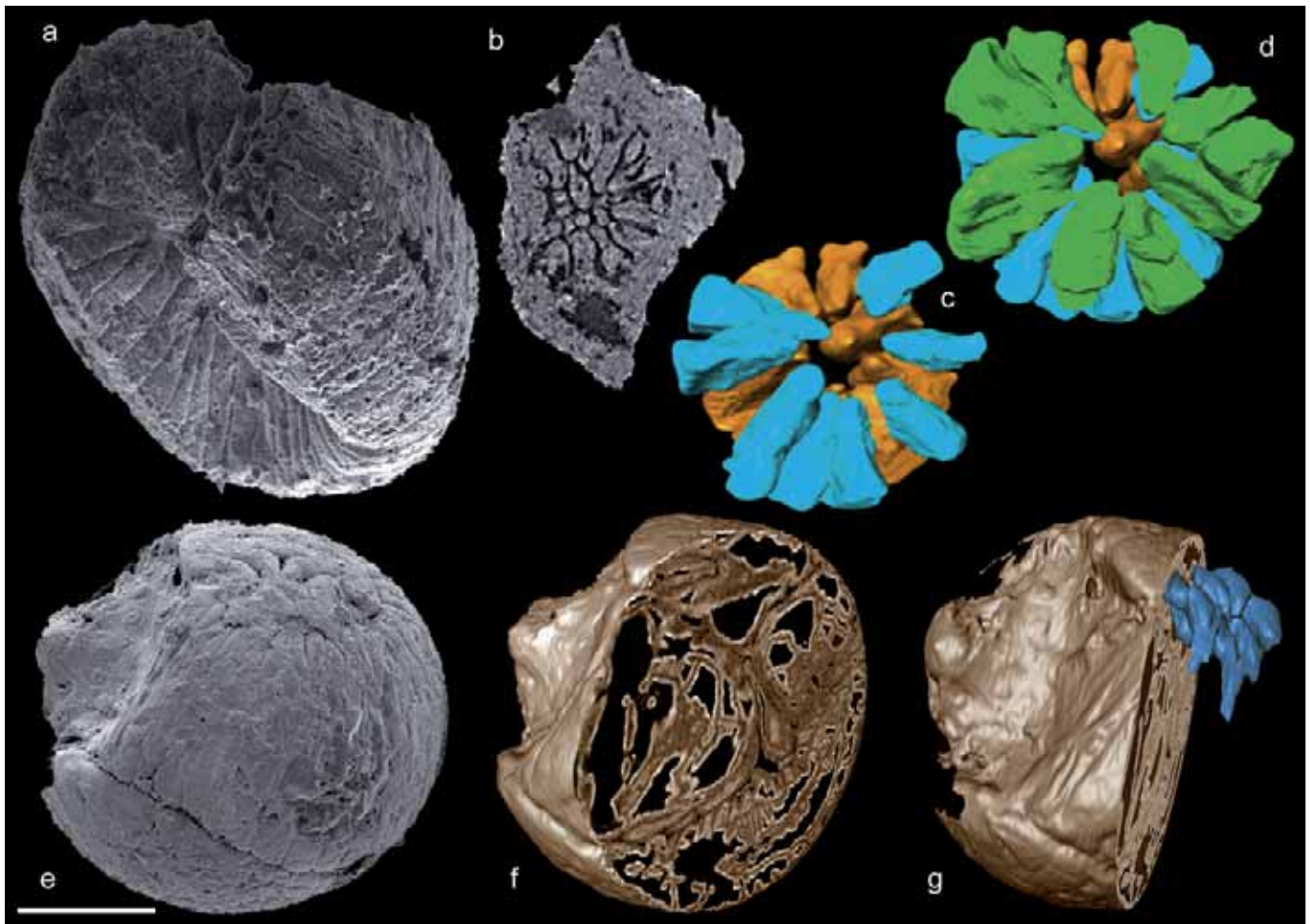


Figure 1: The more than half a billion year old embryos of *Markuelia hunanensis* (a–d) and *Markuelia secunda* (e–g). (a) SEM image of the head region, (b) an XTM image showing the internal structure of the mouth, (c–d) renderings of the teeth in the mouth. (e) SEM image of enrolled embryo (head end at upper left; tail end at top), (f) rendered and virtually sectioned to show internal structure, (g) segmented to show the structure of the tail. Relative scale bar: (a–b) 110 μm , (c–d) 45 μm and (e–f) 150 μm .

Clearly the direct mode of development exhibited by *Markuelia* conflicts with the long held view that metamorphosis is a primitive feature among marine animals [6], and this contradiction is increasingly supported by further discoveries of fossilised embryos [7].

The real significance of *Markuelia* arises from its genealogical proximity to the ancestor of the two main model animals in molecular developmental genetics, *Caenorhabditis elegans* (nematode) and *Drosophila melanogaster* (fruit fly). *Markuelia* provides insight into the characteristics of this ancestor, including issues such as whether or not it was segmented. It thus provides constraint on models of developmental evolution within a major branch of the animal kingdom.

None of these insights would have been possible without SRXTM, a technology that explores the limits of fossil preservation. SRXTM is set to provide a revolution in the palaeontological study on par with the introduction of the electron microscope.

References

- [1] Bengtson, S. & Yue, Z. , Science 277, 1645-1648 (1997)
- [2] Dong, X., Donoghue, P.C.J., Cheng, H. & Liu, J., Nature, 427, 237 (2004)
- [3] Chen, J. et al., Proceedings of the National Academy of Sciences, USA 97, 4457 (2000)
- [4] Xiao, S., Yuan, X. & Knoll, A. H. , Proceedings of the National Academy of Sciences, USA 97, 13684 (2000)
- [5] Chen, J.-Y. et al., Science, 305, 218 (2004)
- [6] Haeckel, E., Quarterly Journal of Microscopical Science, 14, 142-165, 223 (1974)
- [7] Donoghue, P. C. J. & Dong, X. in Evolving form and function: fossils and development (ed. Briggs, D. E. G.) 83 (Yale Peabody Museum, New Haven, 2005)

Ultrafast X-ray absorption spectroscopy at the SLS

Wojciech Gawelda, Steven L. Johnson, Daniel Grolimund, Rafael Abela, Maik Kaiser, *Research Department Synchrotron Radiation and Nanotechnology, PSI*; Wojciech Gawelda, Van T. Pham, Yuri Zaushitsyn, Beatrijs Verbrugge, Majed Chergui, Christian Bressler, *Lab. of Ultrafast Spectroscopy, Ecole Polytechnique Fédérale de Lausanne*; Michele Cascella, Ivano Tavernelli, *Lab. of Comp. Chem. and Biochem., Ecole Polytechnique Fédérale de Lausanne*; Andreas Hauser, *Dept. Of Physical Chemistry, Université de Genève*

Changes in the electronic structure of atoms and molecules determine the nature of bond making and bond breaking in chemical and biochemical reactions. The SLS micro-XAS beamline is equipped with a synchronised femtosecond laser system to allow time-resolved experiments with hard X-rays. With this setup we have recorded the excited state structures of transient chemical species and short-lived radicals in the liquid phase.

Observing molecular pathways during a reaction is vital for the understanding of the elementary steps of chemical and biologic reactivity. Among the different experimental approaches, time-resolved X-ray absorption fine structure spectroscopy (XAFS) has proven to be a very flexible method, allowing visualisation of atomic movements of a selected species (molecule), even in disordered bulk media. In addition, electronic structure changes of photo-excited materials can be measured by X-ray absorption near edge structure (XANES). All this is realised in a pump-probe scheme, where a femtosecond pump laser initiates the reaction and a subsequent X-ray probe pulse measures the local geometric structure as a function of pump-probe time delay.

We have exploited the micro-XAS beamline of the SLS for these experiments with pulse-limited temporal resolution (ca. 100 ps). The results shown below underline the capability of performing these experiments to capture transient electronic and geometric structures in a wide range of systems.

Excited state geometric structures

Aqueous $[\text{Fe}^{\text{II}}(\text{bpy})_3]^{2+}$ undergoes a low-spin to high-spin transition (LS→HS) following pulsed laser excitation. Its HS geometric structure is significantly different from the LS compound, and recent theoretical calculations indicate that the ligand system moves outwards by ca. 0.2 Å. To date, no experimental measurement of the local HS structure has been measured. We have used aqueous solutions at room temperature to capture its excited state for the first time. Figure 1 displays the transient X-ray absorption spectrum 50 ps after excitation

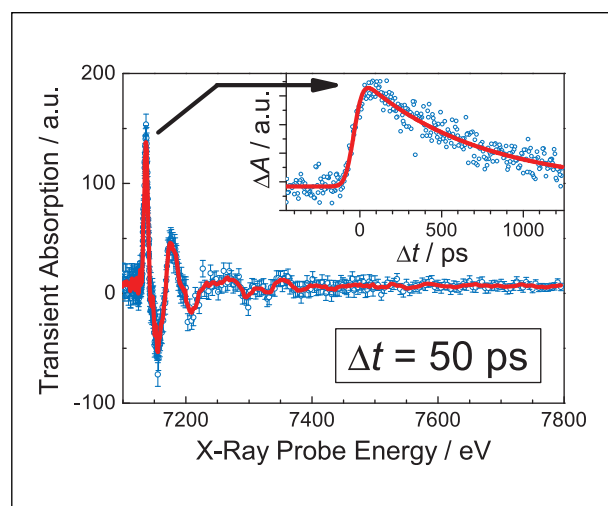


Figure 1: **Transient XAFS spectrum after 50 ps of photo-excited aqueous $\text{Fe}^{\text{II}}(\text{bpy})_3$ at room temperature. The inset displays the temporal behaviour of the lowest energy transient absorption maximum.**

of $[\text{Fe}^{\text{II}}(\text{bpy})_3]^{2+}$ with a 400 nm femtosecond laser pulse. The inset displays a scan of the time delay of these changes (measured at the indicated X-ray energy), which includes the cross correlation time of 100 ps, and the 700 ps decay of the HS compound at room temperature. We simulated the transient EXAFS using the calculated HS structure and overlaid it with the measurement (Fig. 2). Both spectra already agree very well, indicating the general validity of the theoretical estimate for the Fe-N distance change ($\Delta r \approx 0.2$ Å). Our excellent data quality will now permit us to refine our EXAFS fit and obtain accurate values for the Fe-N distance of the HS complex.

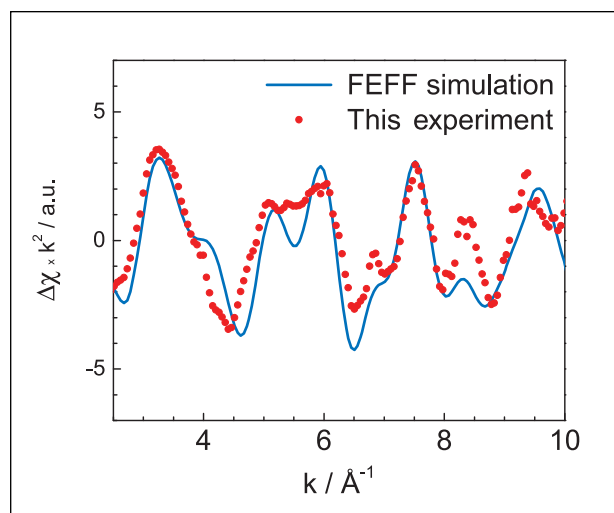


Figure 2: **Transient EXAFS measured after 50 ps time delay together with a simulation of the difference EXAFS assuming the calculated excited state structure.**

Solvation dynamics

Changes in the electronic structure of atoms and molecules determine the nature of bond making and bond breaking in chemical and biochemical reactions. The role of the environment (be it a solvent or a protein) is crucial, involving a structural reorganisation in response to the reaction. The time scale and structure of this reorganisation (the so-called *solvation dynamics*), has so far been investigated only by ultrafast optical spectroscopy on large dye molecules. However, the actual geometric structure around an electronically excited solute cannot be retrieved from such experiments. Using atomic ions (e.g. I) in water, we have probed the solvent shell and the electronic structure of the solute, after ejecting an electron from the ion with a femtosecond laser pulse.

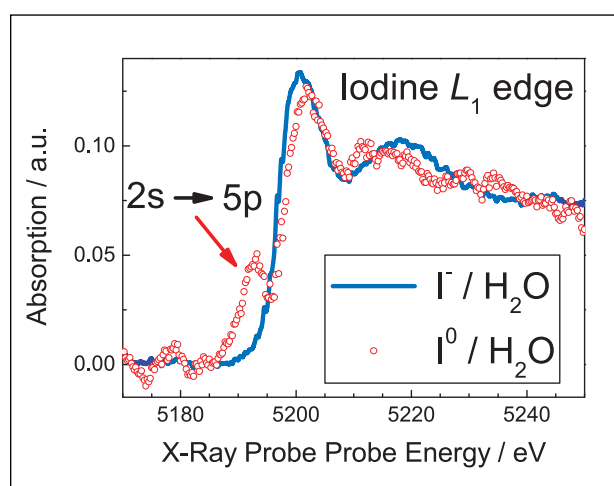


Figure 3: **L1-edge absorption spectra of aqueous iodide before and after laser excitation $\Delta t = 50$ ps).**

Figure 3 shows the absorption spectra before and after laser excitation around the L_1 edge. The excited spectrum shows the appearance of a pre-edge feature due to the allowed $2s \rightarrow 5p$ transition, which becomes possible after removal of the electron (I $^-$ has a closed shell structure and is isoelectronic to Xe) and creation of a hole in the $5p$ shell. The intensity of this feature bears information about the occupancy of the $5p$ orbitals. Above the edge, the difference between I $^-$ and I 0 points to a severe solvent reorganisation around the I 0 solute, as witnessed by the dramatic modifications to the EXAFS modulations.

These results are rationalised by DFT quantum simulations of the electronic structure and the solvent shell structure of I $^-$ and I 0 in water. Figure 4 shows the solvent shell structure and the electron density of I 0 surrounded by water molecules. It can be seen that a triatomic species I(H $_2$ O) $_2$ forms, whereas in the case of I $^-$, the local environment (not shown) is more tetrahedrally oriented. Furthermore, the calculations indicate a partial back electron transfer from the two water molecules of the complex to the I 0 species, in full agreement with the relatively low intensity of the pre-edge feature in the L_1 -edge spectrum (Fig. 3).

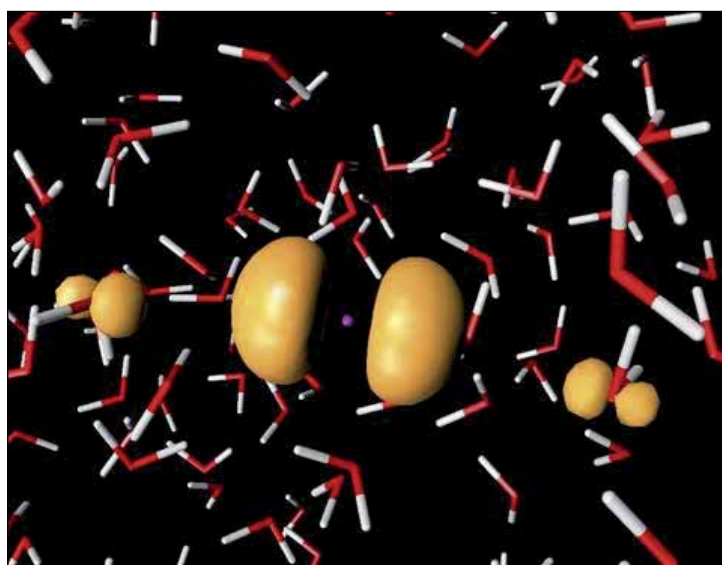


Figure 4: **Structure of the water molecules around I 0 determined by a full quantum mechanical calculation. Two water molecules come close to the solute and transfer part of their electron density to it.**

These results are the first on the solvent shell structure and the involvement of solvent species in determining the electronic structure of simple solutes. They demonstrate the power of ultrafast X-ray absorption spectroscopy as an ideal tool for the study of solvation dynamics, as the retrieved information could not have been obtained by optical techniques.

The antiferromagnetic spin axis of individual domains in LaFeO₃

Slawomir Czekaj, Frithjof Nolting, Laura J. Heyderman, Philip R. Willmott, Michael Horisberger, *Research Department Synchrotron Radiation and Nanotechnology, PSI*; Gerrit van der Laan, *CCLRC, Daresbury Laboratory*

Photoemission electron microscopy has been used to determine the orientation of individual antiferromagnetic domains in LaFeO₃ thin films. We found the antiferromagnetic axes are tilted by 20° out of the surface plane and have a different sign of the X-ray magnetic linear dichroism compared to previous reports on LaFeO₃. Using multiplet calculations, we show that this sign depends on the orientation of the magnetisation with respect to the crystalline axes. This has important bearings on the correct analysis of the coupling between ferromagnetic and antiferromagnetic films in exchange bias systems.

Magnetic microstructures have been of high interest in the last decades due to both their technological and scientific importance. New discoveries expand the possibilities for fundamental research and industrial development. An important class of magnetic multilayers contains antiferromagnetic (AFM; material with anti-parallel spin arrangement on neighbouring atoms) thin films used for pinning the magnetisation direction of a ferromagnetic (FM; material with parallel spin arrangement on neighbouring atoms) layer. This effect is known as exchange bias, discovered five decades ago [1]. An important missing piece of information is the magnetic structure of the AFM at the interface between AFM and FM layer. Recent developments of synchrotron radiation-based techniques have enabled the study of this interface region [2].

Determining spin orientation

We have developed a powerful approach to determine the spin orientation of individual domains [3], based on combining spatially resolved X-ray magnetic linear dichroism (XMLD) images with rotating the orientation of the linear polarization. This enables us to determine the magnetic orientation without the need to know the absolute size and sign of the XMLD. Measurements were performed with an Elmitec PEEM [4] at the SIM beamline [5] at the SLS. The absorption coefficient was measured in electron-yield mode with a typical spatial resolution of about 50 nm. The manipulator allowed a sample rotation about the surface normal (the z-axis) as is shown in Figure 1(a). The linearly polarized X-rays were incident on the sample at a grazing angle of 16° and the polarization axis could

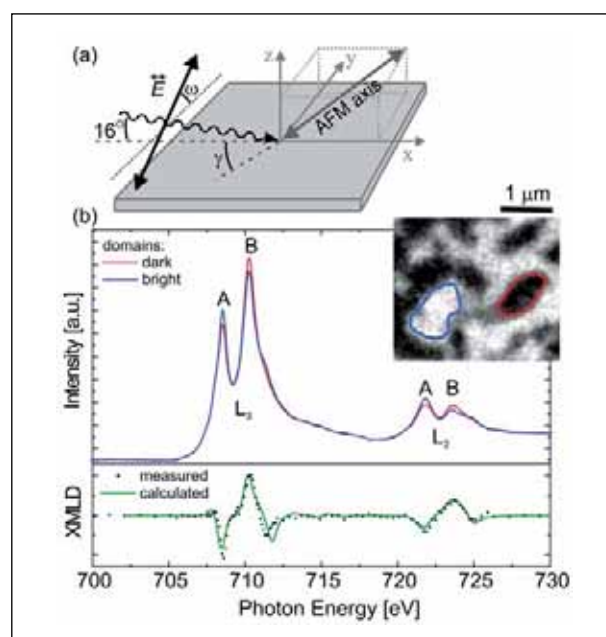


Figure 1: **(a) Experimental geometry.** **(b) Spatially resolved X-ray absorption spectra recorded from a bright and a dark area, together with corresponding difference signal (black dots) and calculated spectrum (solid line) [9]. The inset shows an XMLD image of LaFeO₃ film taken with the E-vector oriented in the plane of the sample ($\gamma = 0$ and $\omega = 0$).**

be rotated continuously from $\omega = 0^\circ$ to 90° , i.e., between in-plane and out-of-plane. The AFM domains in LaFeO₃ were imaged using the XMLD effect associated with the multiplet structure at the Fe L₃ and L₂ absorption edges [2]. The XMLD image was obtained by recording absorption images at photon energies corresponding to the A and B peaks of either the Fe L₃ or L₂ absorption edge (see Fig. 1(b)) and mapping the intensity ratio A/B (see inset of Fig. 1(b)).

Thin films of LaFeO_3 with a thickness of 25 nm were grown on SrTiO_3 (STO) (001) substrates using pulsed laser deposition (PLD) [6]. The samples were deposited at temperatures of around 1000 K with a partial oxygen pressure of 10^{-4} mbar and nitrous oxide was pulsed synchronously with the laser pulse. For all films, X-ray diffraction (XRD) and reflection high-energy electron diffraction (RHEED) indicated epitaxial growth. In order to reduce charging problems associated with PEEM measurements, the low conductivity LaFeO_3 films were capped with 1 nm Pt using magnetron sputtering.

Determination of the orientation of the AFM axis was performed in two steps: first, the in-plane component was measured and second, the out-of-plane component. The intensity at the Fe $L_{3,2}$ absorption edge is given by;

$$I = I_0 + I_2 \cos^2 \alpha$$

where the I_0 is a constant and I_2 is the XMLD signal, whose contribution depends on the angle α between the linear polarization vector (i.e., the E -vector) of incident X-rays and the AFM axis. We probe the XMLD signal by first changing the sample angle γ about the z -axis, and then changing the angle ω of the E -vector (see Fig. 1(a)). We found fourfold symmetry of the in-plane components, seen as a maximal contrast reversal between the XMLD images shown in Figures 2(a) and 2(c). It follows that for the sample angles γ of 0° and 90° the in-plane components of the AFM axes are either parallel or perpendicular to the incident X-rays. Furthermore, we found

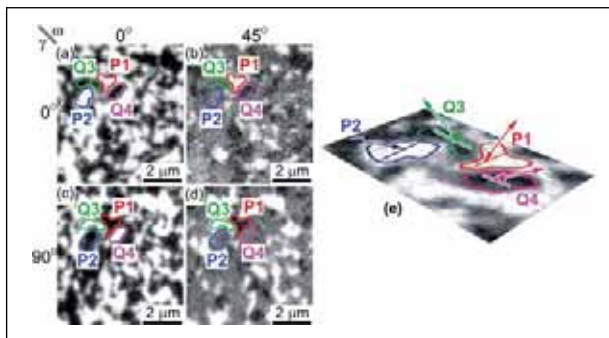


Figure 2: XMLD images for the two in-plane sample angles $\gamma = 0$ and 90° (top and bottom row, respectively) and E -vector angle $\omega = 0$ and 45° (left and right column respectively). (e) Illustration how spin axes are oriented in different domains for thin LaFeO_3 films.

four types of antiferromagnetic domains in thin LaFeO_3 films (see Fig. 2(a)-(d)). This can be explained by considering the crystallographic structure of the films. Our RHEED measurements showed that the epitaxial films are crystallographically twinned, resulting in fourfold symmetry. This is in agreement with the studies of Scholl et al. [3] and Lüning et al. [7] of LaFeO_3 grown by molecular beam epitaxy (MBE) on $\text{STO}(001)$. Interestingly, the observed XMLD has the opposite sign to that expected. It has been shown for $\alpha\text{-Fe}_2\text{O}_3$ that the peak B of the

L_3 and L_2 edges is maximal when the E -vector is parallel to the magnetic axis ($E \parallel M$) [8]. The same is true for LaFeO_3 grown by MBE onto $\text{STO}(001)$ [2,7]. This intensity behaviour is in contrast to Figure 1(b), where the spectra of a bright and dark domain are compared. We have shown that the dark domain is perpendicular to the E -vector, yet the B peak is maximal. Our multiplet calculations in the presence of a cubic crystal field revealed indeed a reversal of the XMLD (see Fig. 1(b)). For LaFeO_3 the dichroism depends on the magnetic orientation; it changes sign when the antiferromagnetic axis rotates from the $\langle 100 \rangle$ to either the $\langle 111 \rangle$ or the $\langle 110 \rangle$ directions.

Conclusion

In conclusion, we have shown that PEEM combined with the XMLD effect can be used to determine the orientation of individual antiferromagnetic domains. Comparing our results with the literature and using multiplet calculations, we show that XMLD is sensitive to the magnetocrystalline anisotropy and can even change its sign. This is the first report of measurements that establish this effect for antiferromagnets. This information is particularly important for the analysis of the coupling between ferromagnetic and antiferromagnetic films in exchange bias systems.

Acknowledgements

We gratefully acknowledge the support from H. Grimmer with the XRD.

References:

- [1] W.H. Meiklejohn and C.P. Bean, Phys. Rev., 102, 1413 (1956).
- [2] A. Scholl, J. Stöhr, J. Lüning et al., Science, 287, 1014 (2000).
- [3] S. Czekaj, F. Nolting, L.J. Heyderman et al., Phys. Rev. B, 73, 020401(R) (2006).
- [4] E. Bauer, J. Phys.: Condens. Matter, 13, 11391 (2001).
- [5] C. Quitmann, U. Flechsig, L. Patthey et al., Surf. Sci., 480, 173 (2001).
- [6] P.R. Willmott and J.R. Huber, Rev. Mod. Phys., 72, 315 (2000).
- [7] J. Lüning, F. Nolting, A. Scholl et al., Phys. Rev. B, 67, 214433 (2003).
- [8] P. Kuiper, B.G. Searle, P. Rudolf et al., Phys. Rev. Lett., 70, 1549 (1993).
- [9] G. van der Laan and B.T. Thole, Phys. Rev. B, 43, 13401 (1991)

X-ray diffraction of electrical multipole moments

Annemieke M. Mulders, Urs Staub, Valerio Scagnoli, *Research Department Synchrotron Radiation and Nanotechnology, PSI*; Stephen W. Lovesey, *ISIS, Rutherford Appleton Laboratories*; Ewald Balcar, *Vienna University of Technology*; Tetsuya Nakamura, *SPring-8/ASRI*; Akiko Kikkawa, *RIKEN SPring-8 Center Harima Insitute*; Gerrit van der Laan, *CCLRC, Daresbury Laboratory*; Jean-Marc Tonnerre, *CNRS Grenoble*

Resonant soft X-ray Bragg diffraction has been exploited to study Dy multipole motifs in DyB₂C₂. It is shown that we can determine the higher multipole charge densities (quadrupole, hexadecapole and hexacontatetrapole) of the Dy ions, which are found to be significantly large and order independently of the magnetic dipole moments. An extended theoretical description is used including the interaction between the 4*f* quadrupole and the quadrupole of the 3*p* core state in the resonant process.

Introduction

Resonant X-ray Bragg scattering has recently become a powerful tool in modern solid-state physics to study magnetic, charge and orbital ordering phenomena. These phenomena are particularly important for 3*d* transition metal oxides, where they are related to the occurrence of colossal magneto-resistance and metal insulator transitions. In Lanthanides, orbital and magnetic ordering occurs too, yet more independently from the electronic properties of the material. The orbital ordering is usually labelled anti-ferroquadrupolar

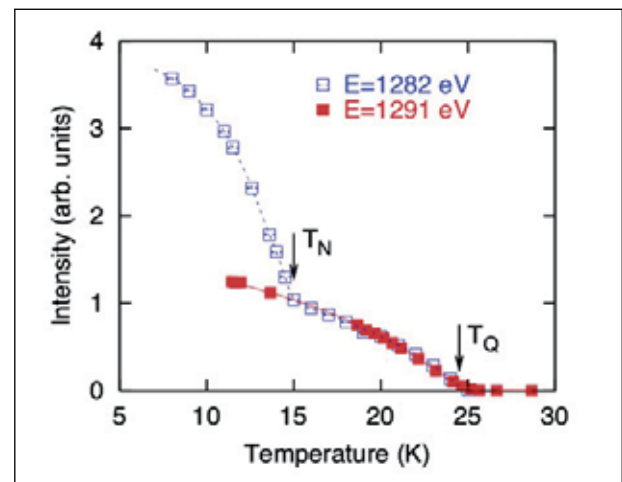


Figure 2: **Temperature dependence of the (0 0 1/2) reflection at two distinct energies of the Dy M₅ edge showing both the sensitivity to orbital and magnetic ordering.**

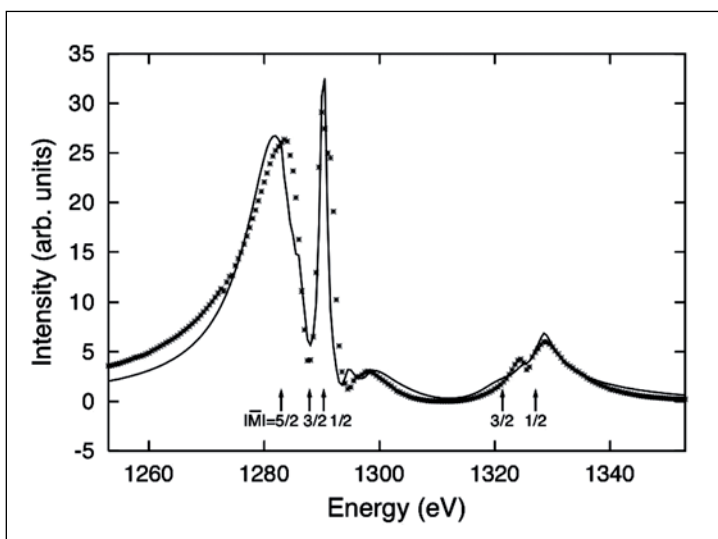


Figure 1: **Observed energy profile (crosses) compared to fit (solid line) of the theory including absorption correction. The corresponding electron density of the Dy ion is shown in Fig. 3.**

(AFQ) of ferroquadrupolar (FQ). Because of the large orbital momentum of the lanthanides, higher multipoles can contribute to the order too. However, very little is known, as it is very difficult to observe that experimentally. To date, quadrupoles (rank 2) are frequently determined with resonant X-ray scattering. Hexadecapoles (rank 4) have been observed with resonant X-ray scattering in DyB₂C₂ [1] and with non-resonant X-ray scattering in CeB₆ [2], but hexacontatetrapoles (rank 6) have not been observed in the solid state. Higher order multipoles can significantly contribute to AFQ transitions and their relevance is rather controversial in NpO₂ [3] URu₂Si₂ [4] or V₂O₃. [5]

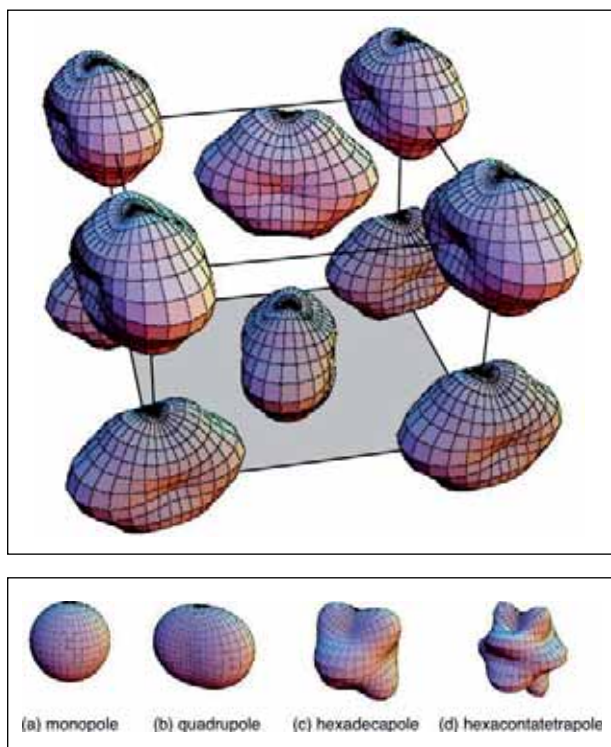


Figure 3: **Upper graphic: Dy charge density and multipole motif in the AFQ phase of DyB_2C_2 . The basal plane is indicated in grey. Note the 90° zig-zag alignment of the Dy orbitals along c and the canted zig-zag alignment along the $[110]$ direction. A spherical charge density has been subtracted to highlight the asphericity. Lower graphic: Calculated charge density of Dy $4f$ electrons with monopole moment (a) and an additional quadrupole moment (rank 2) (b), hexadecapole moment (rank 4) (c) or hexacontatetrapole moment (rank 6) (d).**

Soft X-rays at low temperature

We have developed resonant soft X-ray scattering for low temperatures $T < 20$ K and applied it to the Dy $M_{4,5}$ edges. Figure 1 shows the energy scan of the $(0\ 0\ \frac{1}{2})$ reflection, which is a crystallographic forbidden reflection. This reflection is sensitive to the ordering of the quadrupoles, reflecting the asphericity of the $4f$ electron density of the Dy ions, as proven by hard X-ray resonant scattering. [1] The temperature dependence of the reflection is connected with the ordering of the quadrupoles at 25 K and some of the spectra features are also influenced by the magnetic phase transition occurring at 15 K. The individual features in the spectra are caused by the interference of three, and two harmonic oscillators for the M_5 and M_4 edges, respectively. This interference is caused by the splitting of the core state in the resonant process due to the quadrupole interaction between the $4f$ shell and the core hole.

This interaction makes the energy shape of the scattering sensitive to the higher multipole components of rank 4 and

6. A fit to the theoretical model including this interaction and the absorption correction is shown in Figure 1. Based on this novel interaction, we are able for the first time to extract the higher multipole contribution to an orbital ordering of the charge density as exemplified in Figure 3. The higher multipole contributions of rank 4 and 6 are significant and of the order of 20-30 % compared to the quadrupole.

Conclusions

These results show that the structural, magnetic and multipolar interaction cooperate along the c -direction, while they compete within the a,b plane. These findings demonstrate a new extension of the resonant Bragg diffraction method for the observation of high-order multipole motifs.

References

- [1] Y. Tanaka, T. Inami, S. W. Lovesey, K. S. Knight, F. Yakhou, D. Mannix, J. Kokubun, M. Kanazawa, K. Ishida, S. Nanao, T. Nakamura, H. Yamauchi, H. Onodera, K. Ohoyama, Y. Yamaguchi, *Phys. Rev. B*, **69**, 24427 (2004)
- [2] Y. Tanaka, U. Staub, K. Katsumata, S. W. Lovesey, J. E. Lorenzo, Y. Narumi, V. Scagnoli, S. Shimomura, Y. Tabata, and Y. Onuki, Y. Kuramoto, A. Kikkawa, T. Ishikawa, H. Kitamura, *Europhys. Lett.*, **68**, 671 (2004)
- [3] S. W. Lovesey, E. Balcar, C. Detlefs, G. van der Laan, D. S. Sivia, and U. Staub, *J. Phys.: Condens. Mat.*, **15**, 4511 (2003)
- [4] A. Kiss and P. Fazekas, *Phys. Rev. B*, **71**, 54415 (2005).
- [5] S. W. Lovesey, K. S. Knight, and D. S. Sivia, *Phys. Rev. B*, **65**, 224402 (2002)

Scattered photons reveal the magnetic interaction between atoms

Gheorghe Sorin Chiuzbaian, Peter Amann, Luc Patthey, *Research Department Synchrotron Radiation and Nanotechnology, PSI*; Giacomo Ghiringhelli, Claudia Dallera, Lucio Braicovich, *Politecnico di Milano, Italy*; Xiaoqiang Wang, Marco Grioni, *Ecole Polytechnique Fédérale, Lausanne*

Measuring – or feeling – magnetic interactions seems simple at first glance: bringing two magnets together gives one an immediate idea. But what happens when the “magnets of interest” are so tiny that they amount to nothing more than atoms? X-rays generated at the Swiss Light Source allow us to “zoom in” on magnetic interactions relevant at inter-atomic scale. We present the first evidence of local spin flips of atomic moments in a “photon-in, photon-out” scattering experiment.

Driven by the desire to create smaller, better and cheaper electronic devices, scientists are continually searching for novel materials. Digital cameras which fit into a pocket or light-weight portable computers are some of the daily visible examples made possible by these efforts.

In a similar way to architects combining building materials with known properties into new buildings, material scientists need to understand the way atoms interact when set together in a crystal. Therefore, the precise experimental characterization of inter-atomic interactions plays a key role. It serves to validate the theories describing materials at the inter-atomic scale and sets reference points for future models. This study exemplifies how scattering of X-rays can help us to gain such information about a prototypical material, nickel oxide [1]. The method is, however, applicable to a wide range of materials.

Magnetic moments

How can we “zoom in” on the magnetic interactions between atoms? Put simply, in insulating materials the atomic magnetic moments are like tiny magnetic needles pinned on the carrying atoms, at their crystal sites. As with any other magnets their interaction depends on their orientation, so that changing their relative direction requires some extra energy. For example, in anti-ferromagnetic materials the local magnetic moments are oriented alternatively parallel and anti-parallel to the magnetisation axis: the net magnetisation is zero despite a strong magnetic interaction between neighbouring atoms. This is the case of nickel oxide at room temperature, as depicted in Figure 1. How can we tell how strong the mag-

netic interaction is between the nickel atoms? Quantum mechanics helps with a simple way to measure it: flipping one of the local magnetic moments (atomic spin) relative to the neighbouring moments, increases the energy of the system by a certain quantified amount. In principle, measuring the energy difference between the ground state and the various spin-flipped states delivers a straightforward solution for the determination of the magnetic exchange interaction. The idea of using X-ray scattering for this purpose was theoretically put forward in 1998 by de Groot et al. [2] but its practical implementation was delayed by the relative weakness of the magnetic interaction: the experiment requires excellent resolving power.

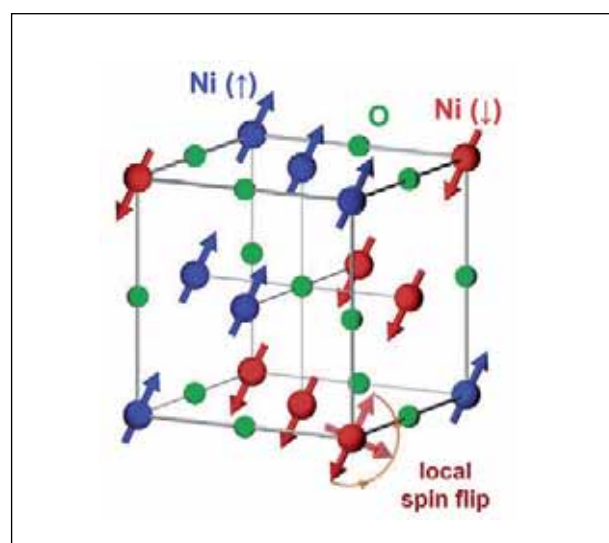


Figure 1: **Schematic representation of local spin flip excitations in nickel oxide: one arbitrary nickel magnetic spin changes its relative orientation to the surrounding local moments.**

The experiment

At the Surface Interface: Spectroscopy (SIS) beamline we were able to find the evidence of such local spin flip excitations in a “photon-in photon-out” experiment (see also Reference [3] for more details on technique). Incoming photons with well defined energy are directed onto a sample of interest (in our case the nickel oxide) and the energy of scattered (outgoing) photons is recorded with high resolution (see Fig. 2). The difference between the energy of the incoming and outgoing photons gives the amount of energy transferred to the sample. The transferred energy results in local excitations, like the local spin flips.

The SIS beamline provides a high flux X-ray beam and convenient photon energies for these types of experiments. The detection is performed by employing a diffraction grating which separates the photons in space according to their energy.

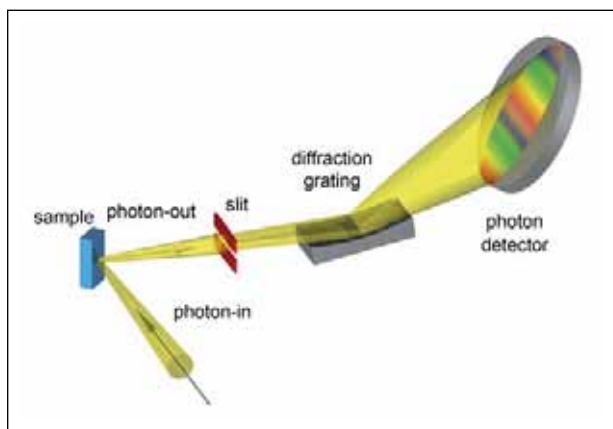


Figure 2: Sketch of the experimental setup.

The results

The spectra recorded for nickel oxide are summarised in Figure 3, showing the intensity of the scattered photons versus the energy transferred to the sample. Besides elastically scattered photons (zero transferred energy), well defined losses are detectable. They essentially resemble reorganisations of the nickel valence electrons within the shell, when some extra energy is available from the incoming X-rays (*dd* excitations). The fine details of spectral changes, when changing the incoming photon energy, can be explained based on theoretical calculations.

Basically the separation of the double structure visible in the high resolution spectra (Fig. 3, lower panel, see spectrum depicted with magenta line) allows the determination of the magnitude for magnetic interaction between nickel atoms,

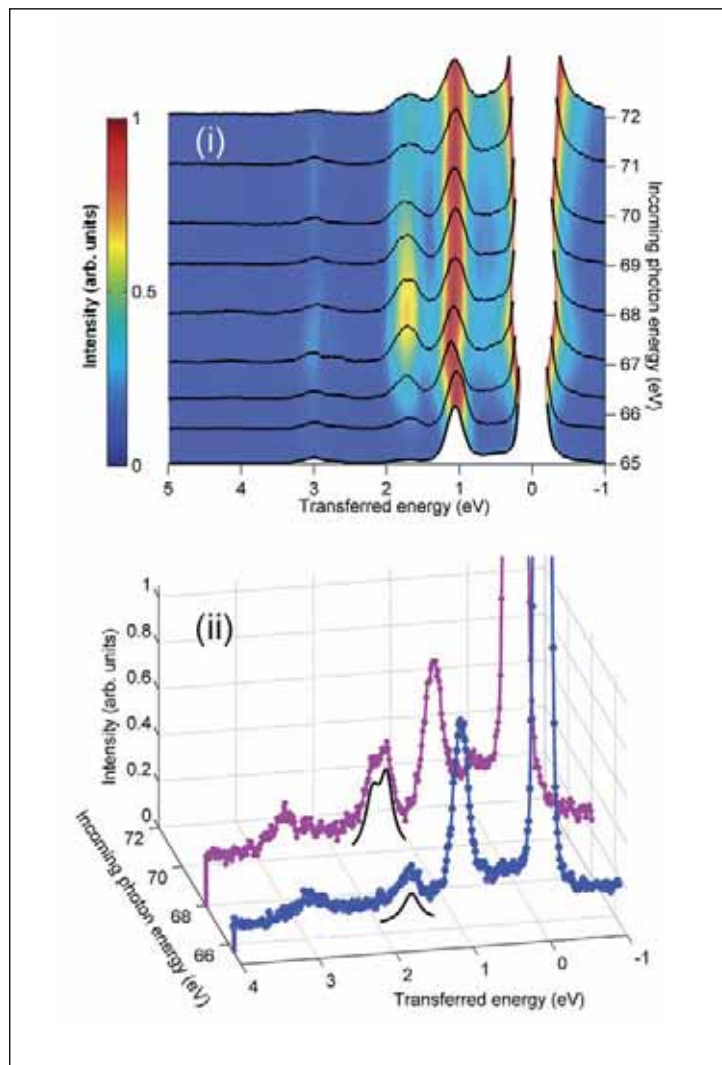


Figure 3: X-ray scattering results for nickel oxide with incoming photon energies encompassing Ni M absorption edges (i). For the spectra shown in the lower panel (ii) the resolution was increased by accessing the second diffraction order of the grating.

based on the good agreement between measured and computed data [1], it takes at least about 125 meV in order to flip one local nickel magnetic moment.

References

- [1] S.G. Chiuzaian, G. Ghiringhelli, C. Dallera, M. Gioni, P. Amann, X. Wang, L. Braicovich and L. Patthey, Physical Review Letters, 95, 197402 (2005)
- [2] F.M.F. de Groot, P. Kuiper and G.A. Sawatzky, Physical Review B, 57, 14584 (1998)
- [3] A. Kotani and S. Shin, Review of Modern Physics, 73, 203 (2001)

Induced magnetic ordering in a molecular monolayer

Andreas Scheybal, Trond Ramsvik, Rolf Bertschinger, Magali Putero, Frithjof Nolting, Thomas A. Jung,
Research Department Synchrotron Radiation and Nanotechnology, PSI

Chemically tuneable molecular magnets exhibit new and attractive properties, particularly in the field of spin-transport electronics or spintronics. In this work, the magnetic interaction between a magnetised thin film cobalt substrate and adsorbed manganese(III)-tetraphenylporphyrin chloride (MnTPPCI) molecules has been studied by X-ray magnetic circular dichroism (XMCD). For MnTPPCI submonolayer coverages circular dichroism is observed, which indicates that a net magnetisation is induced in the adsorbed molecules.

Surface and interface magnetism quickly evolved from basic research [1] to applications like GMR (giant magneto resistance) read-heads and MRAM (magnetic random-access memory) [2]. These applications rely on so-called spin transport electronics or spintronics, where the electron spin rather than the charge is employed to carry information [3]. Organic and semiconducting materials are capable spintronic materials, for example Xiong et al. showed that an organic semiconductor like tris(8-hydroxyquinoline) aluminium (Alq_3) can be used to prepare an organic spin-valve exhibiting GMR [4].

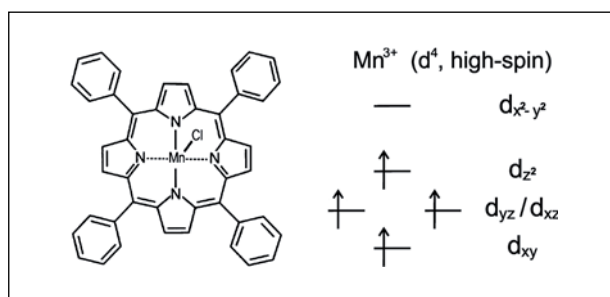


Figure 1: **(left) Chemical structure of the MnTPPCI molecule. A manganese atom is located in the center, surrounded by four basal pyrrole nitrogen atoms and an axial chloride ion. (right) Schematic energy level diagram of the Mn 3d-orbitals. The manganese ion is in III+ high-spin oxidation state with $S = 2$.**

Towards versatile magnetic materials with decreasing domain and layer dimensions, the understanding of local magnetic coupling in molecular monolayers is of utmost importance. Here we study the magnetic coupling between a ferromagnetic substrate and adsorbed molecules, e.g. manganese(III)-tetraphenylporphyrin chloride (Fig. 1), which is the parent compound of the [Mn(III)-porphyrin][Tetracyanoethylene] family of molecular magnets. Due to its chemical selectivity

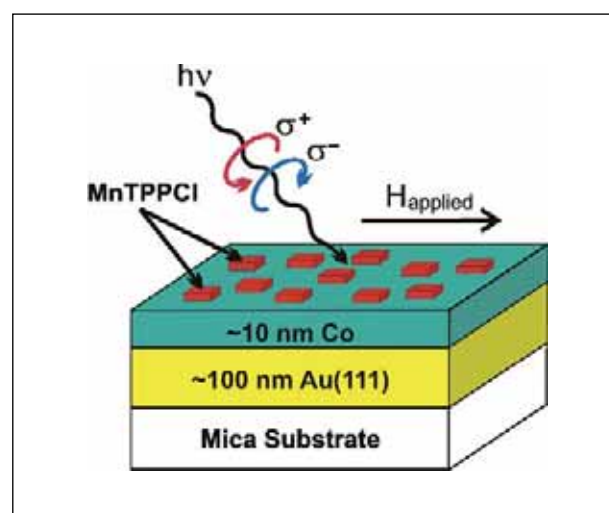


Figure 2: **Three-layer sample generated by controlled hetero-epitaxial growth. In the experimental setup σ^+ and σ^- symbolize right and left circular polarized light, respectively. H_{applied} denotes the in-plane orientation of the applied magnetic field.**

and submonolayer sensitivity, X-ray magnetic circular dichroism (XMCD) allows for the quantitative differentiation of surface and ad-layer magnetisation if different magnetic species are chosen.

Experiments were performed at the XMCD end station of the Surface / Interface: Microscopy (SIM) beamline at SLS. A cobalt film of about 10 nm thickness was evaporated in-situ onto a 100 nm Au(111) film on mica. An external magnetic field of 125 mT parallel to the surface plane assured single domain magnetisation along the easy axis. Finally, sub- and multi-layer coverages ranging from 0.15 to 6 monolayers MnTPPCI have been sublimed onto the cobalt film (Fig. 2). X-ray absorption (NEXAFS) and XMCD spectra at the Co and Mn $L_{\text{III,II}}$ -edges as well as at the N K-edge have been measured.

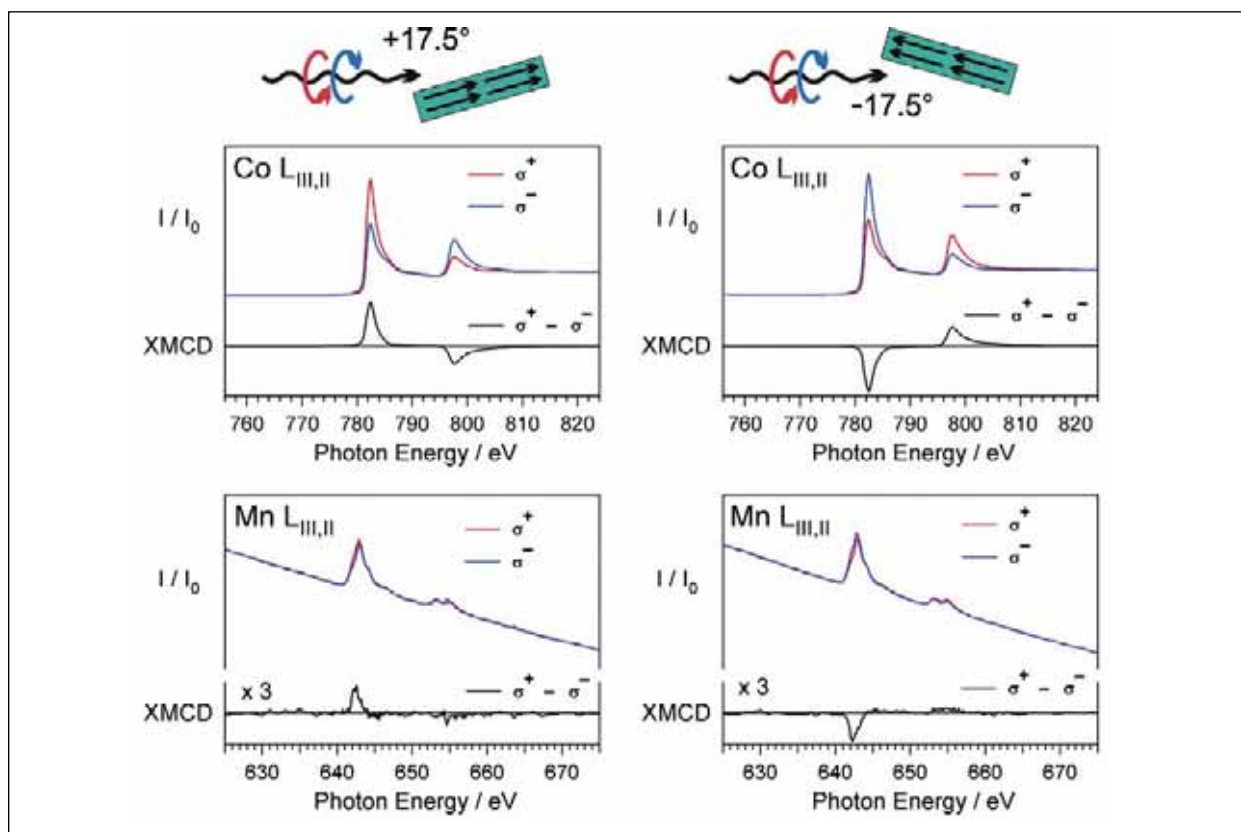


Figure 3: Confirmation of magnetic ordering in MnTPPCI at room temperature. The two upper figures show Co $L_{III,II}$ -edge NEXAFS and XMCD spectra and the two lower show Mn $L_{III,II}$ -edge NEXAFS and XMCD spectra for two grazing incidence angles $+17.5^\circ$ and -17.5° , measured from the surface plane as indicated in the sketches on top. I/I_0 is the X-ray absorption signal measured in the total electron yield mode and normalised to the incident photon flux. All the spectra are taken at remanence. The change in sign of the circular dichroism for the two geometries verifies the validity of the XMCD signal.

Figure 3 shows the room temperature measurement recorded at $\pm 17.5^\circ$ from the surface plane. A clear XMCD signal is observed at the Mn $L_{III,II}$ -edges, confirming a net magnetisation of the manganese ions in the adsorbed molecules [5]. By the application of the so-called sum rules spin and orbital magnetic moments can be deduced from the XMCD spectra. The manganese spin moment was found to decrease with increasing MnTPPCI coverage, reaching a maximum value of $(1.0 \pm 0.3) \mu_B$ at 0.15 monolayers, while the orbital moment scatters around zero for all coverages.

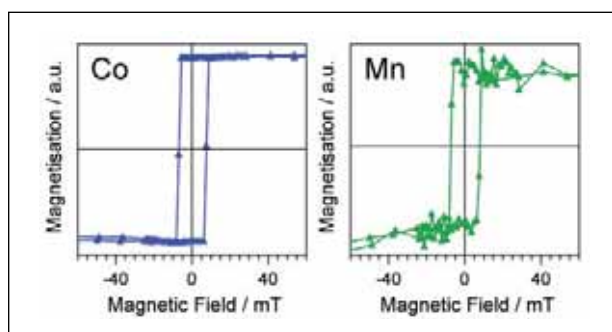


Figure 4: Element-specific hysteresis curves for the Co and Mn $L_{III,II}$ -edges for 0.75 monolayers MnTPPCI on cobalt recorded at 25° incidence angle.

An element specific hysteresis study (Fig. 4) shows that the magnetisation of the molecules mirrors that of the cobalt substrate. This provides clearly the evidence of a magnetic coupling between the MnTPPCI molecules and the substrate. Possible coupling mechanisms could be either magnetic dipole-dipole interaction or exchange interaction. As we observed already at room temperature rather high spin magnetic moments of the manganese ions (saturation magnetization $4.0 \mu_B$), we conclude that the magnetic coupling must be due to exchange interaction. Unreasonably high magnetic fields would be necessary at the manganese site (about 100 T) in case of magnetic dipole-dipole interaction. In conclusion, the magnetic coupling of a molecular magnet to the substrate depends on the details of chemical bonding and is thus tuneable by synthetic chemical methods.

References

- [1] P. Grünberg et al., Phys. Rev. Lett., 57, 2442 (1986)
- [2] S. Parkin et al., Proc. of the IEEE, 91, 661 (2003)
- [3] S.A. Wolf et al., Science, 294, 1488 (2001)
- [4] Z.H. Xiong et al., Nature, 427, 821 (2004)
- [5] A. Scheybal et al., Chem. Phys. Lett. 411 (2005) 214

Confinement induced short range order in liquids

Oliver Bunk, Ana Diaz, Franz Pfeiffer, Christian David, Celestino Padeste, Heilke Keymeulen, Philip R. Willmott, Bruce D. Patterson, Bernd Schmitt, Dominik Meister, Michael Lange, and J. Friso van der Veen, *Research Department Synchrotron Radiation and Nanotechnology, PSI, ETH Zurich*; Hua Guo, Gerard H. Wegdam, *Van der Waals-Zeeman Instituut, Universiteit van Amsterdam, The Netherlands*; Michael Sztucki, *European Synchrotron Radiation Facility, France*

The structure of thin films of confined liquids is of utmost importance in daily life. Engines would not work without a thin film of oil reducing the friction between the moving parts of the motor. By contrast, brakes work less efficiently with a film of moisture trapped between the brake disc and shoe. Ice is slippery due to a liquid-like surface layer, an effect utilized for ice-skating whereby the skate slides on a thin film of water; useful on some, dangerous on other occasions. These examples demonstrate why researchers investigate the structure of fluids confined between solids with nanometer sized spaces (1 nm = 0.000001 mm).

The consequences of ordering in thin liquid films are substantial. Very thin oil films confined in engines will have a different structure and therefore also different properties compared to the bulk liquid. This may eventually lead to solidification and rupture of the lubrication film and to abrasion and finally destruction of the moving parts. On the other hand this effect is desirable in brakes. If the humidity can not be removed by evaporation then it should at least reduce the friction and thereby the braking force as little as possible.

Hence, the motivation for research in the area of confined liquids is clear but in practice the experiment turns out to be rather difficult. A confined liquid film is hard to access, a well defined confinement is technically hard to produce and there

are very few techniques that are able to resolve structures in liquids on a molecular scale. X-ray scattering is a noticeable exception. Hard X-rays penetrate matter easily and can resolve structures of dimensions less than a nanometer.

Unique synergies

At the Paul Scherrer Institute (PSI), a combination of expertise is available which facilitates the study of microfluidic systems. In the Laboratory for Micro- and Nanotechnology (LMN) a new technique has been developed for fabricating microfluidic arrays [1]. These arrays are sample containers for liquid model systems. They are fabricated with high perfection and precise control of the individual dimensions. An example is shown in Figure 1.

The Swiss Light Source (SLS) provides brilliant synchrotron radiation, essential for investigations of structures within liquid and solid samples. The detector group develops X-ray detectors of unprecedented performance [2]. With the technical knowledge and unique detection systems at PSI we were able to study the ordering in liquid model systems such as colloids and emulsions on the nanometer scale.

Observing nanoscale order in colloids

X-ray diffraction patterns from the microfluidic array filled with a colloid (10 vol.% silica spheres of 112 nm diameter dissolved

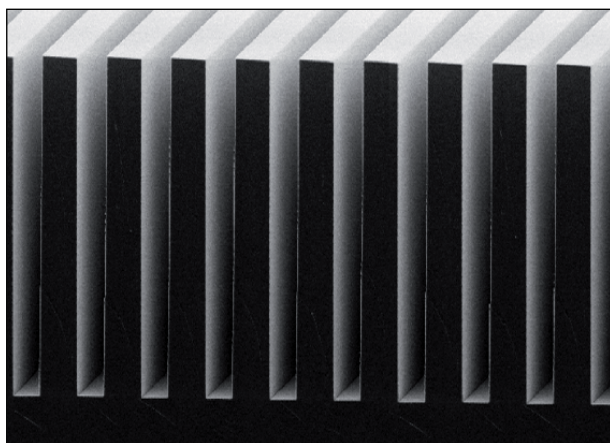


Figure 1: **Microfluidic array as sample container for liquid model systems. These structures of high perfection are made of silicon and typically have periods of one micrometer.**

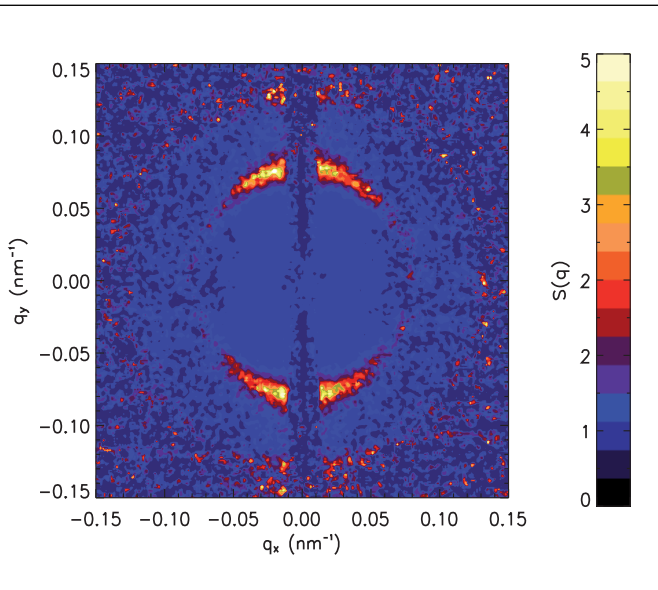


Figure 2: **Ordered liquid: the banana shaped anisotropy in the small angle X-ray scattering data is a clear fingerprint of confinement induced order.**

in alcohol) exhibit clear fingerprints of confinement induced order. The intensity of the signal caused by the ordered part in the liquid decreases with increasing distance between the confining walls, clear proof that the ordering in the colloid is induced by its confinement. An example of typical data is shown in Figure 2.

The data shown in Figure 2 were recorded at the small-angle scattering beamline ID2 at the ESRF in Grenoble. With the ESRF data the ordering effect was clearly observed but cannot be quantified easily due to insufficient resolution for this challenging system. At the Materials Science beamline at the SLS [3] a unique one dimensional microstrip detector has been installed [2]. The detector comprises 15000 pixels of 50 micrometer spacing. It has been developed in-house at the PSI. The data obtained with this detector were analysed in a novel, model independent way - iterative phase retrieval. Without assumptions of the internal structure of the confined liquid its phase profile across microfluidic channels of various gap sizes could be determined. Typical data and two examples are shown in Figure 3.

Conclusion

By using the combined expertise of several PSI groups, a specially tailored system was created, resolving a fundamental problem in the field of fluid physics. The confinement induced ordering in liquid model systems was determined in a model independent way with submicrometer resolution. This has important implications for the understanding of lubrication

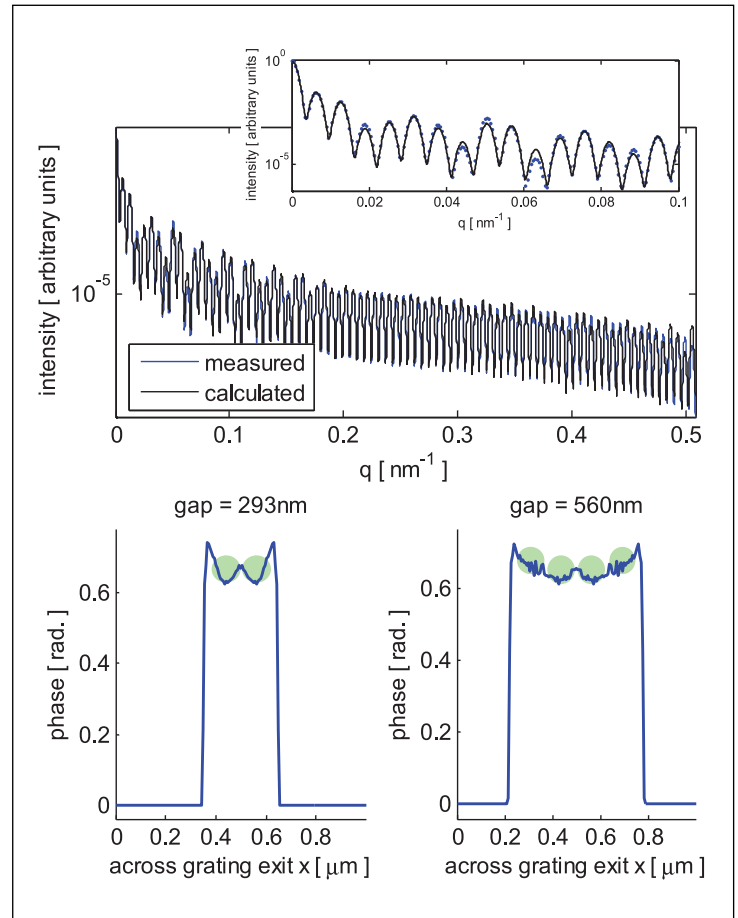


Figure 3: **Ordering for two film thicknesses. Top: An example for the high resolution 1D data recorded at the SLS. Bottom: One dimensional phase profiles across two microfluidic channels. The light green circles are to guide the eye, indicating ordered layers. The small gap (bottom left) induces much stronger order in the liquid than the larger one (bottom right).**

and friction phenomena on a nanoscopic level. Future experiments are planned to develop this technique from investigations of static systems as presented, here to research on microfluidic dynamics.

References

- [1] Diaz et al., Physica B 357, 199 (2005).
- [2] Schmitt et al., Nucl. Instr. and Meth. A 518, 436 (2004).
- [3] Patterson et al., Nucl. Instr. and Meth. A 540, 42 (2005).

New opportunities to create and study complex crystalline surfaces

Phillip R. Willmott, Christian Brönnimann, Oliver Bunk, Eric F. Eikenberry, Beat Henrich, Roger Herger, Miroslav Kobas, Philipp Kraft, Domenico Martocchia, Stephan A. Pauli, Christian M. Schlepütz, and Bruce D. Patterson, *Research Department Synchrotron Radiation and Nanotechnology, PSI*

Surface X-ray diffraction (SXRD) is capable of determining the atomic structure of crystalline surfaces with unsurpassed resolution. Complex metal oxides are of particular scientific interest in this context. High-quality surfaces of these can be prepared by growing thin layers using pulsed laser deposition. With SXRD at the SLS, we are now able to study in-situ the kinetics of the growth and the structures of these films. Also, the use of a novel photon-counting pixel X-ray detector developed at PSI has improved the reliability of data and dramatically increased acquisition rates.

Subtle changes in the atomic arrangements of strongly correlated electron systems such as the perovskites can lead to important alterations in their physical properties [1]. Because the atoms in the surface region of a crystal experience a different environment, due to the breaking of bonds when forming the surface, they will rearrange to minimise the surface energy. This region may therefore exhibit different physical properties from those of the bulk. This has important ramifications (a) on the ultimate downsizing of devices that utilise the material's bulk properties; (b) conversely, on potential nano-sized devices exploiting surface phenomena; and (c) on the interpretation of electronic band structure data from photoelectrons that largely originate from this surface region [2]. A technique that provides the necessary structural resolution would therefore be of great value.

Marriage of synthesis and analysis

The synchrotron-based technique, surface X-ray diffraction (SXRD), is uniquely capable of providing the resolution to meet these challenges [3]. Until recently, however, its applicability has been limited to relatively simple chemical systems, due on the one hand to the difficulty in producing atomically flat and clean crystalline surfaces, and on the other, to the long measurement times normally required to obtain reliable data. However, two innovations combined with SXRD at the PSI now promise a quantum leap in the complexity of chemical systems that can be reliably investigated: pulsed laser deposition (PLD) is capable of growing thin films of complex crystals with high purity and flatness [4], while the "PILATUS II" photon-counting

X-ray pixel detector developed at the PSI has accelerated data acquisition by over an order of magnitude [5], as well as ensuring any artefacts can be recognised and excluded (a source of significant error when using conventional "point" detectors).

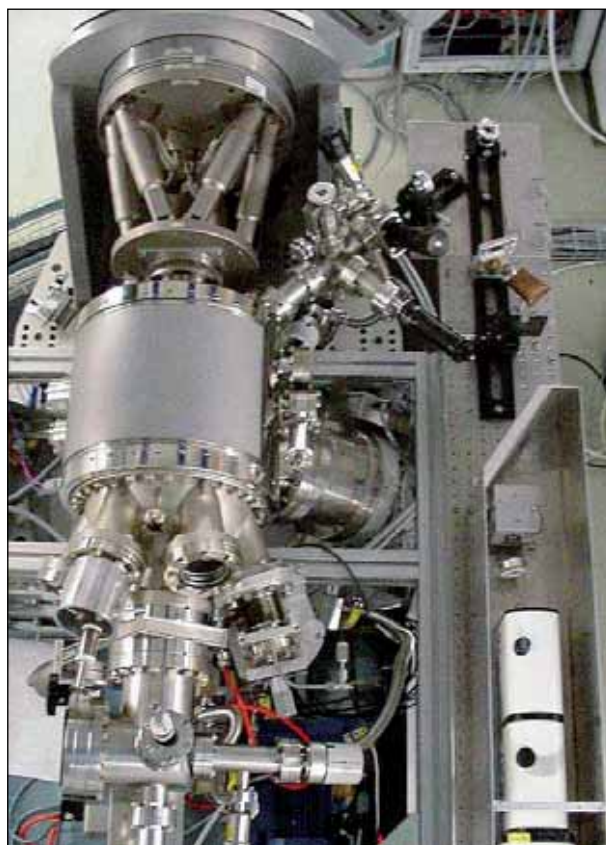


Figure 1: **View of the in-situ PLD chamber mounted on the diffractometer of the Materials Science beamline, SLS**

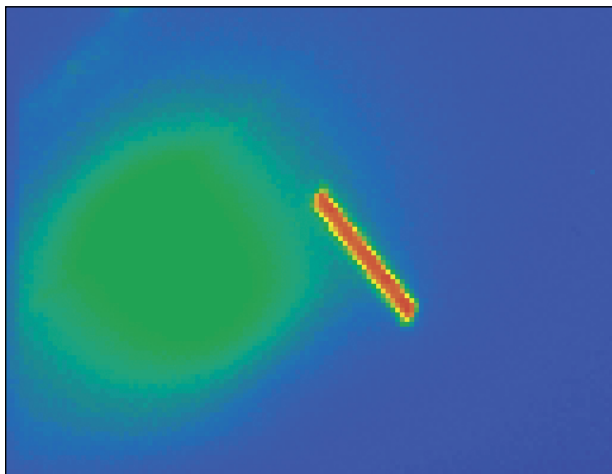


Figure 2: **Detail of a raw image of a 1s exposure using the PILATUS II pixel detector of a surface diffraction signal (sharp rod-like structure) approaching the (4 0 -4) Bragg peak (diffuse feature) of a NdGaO₃(110) substrate.**

This means that atomically flat surfaces can be prepared in an in-situ deposition chamber by growing high-quality films using PLD, while the large volume of data required to obtain a meaningful model of such complex systems can be collected within the limited time normally available to users of synchrotron beamlines.

Changing film thickness, changing surface

The PLD chamber is shown in Figure 1. Its most important feature is the large cylindrical section made from beryllium, covering nearly 180° [6]. Beryllium is transparent to hard X-rays. This, therefore, allows the user to maintain the vacuum quality required for film growth, while allowing him/her to simultaneously monitor the X-ray diffraction signal.

With this system, it is therefore not only possible to investigate the structures of surfaces, but also to study how these change during film growth, the kinetics of those changes [7], and the influence of the underlying material on which the film is grown (called the “substrate”) on the film’s atomic structure.

Figure 2 shows a portion of a typical image recorded using the PILATUS II pixel detector.

Because a 2-dimensional image is recorded, the signal of interest can be easily distinguished from other features or artefacts, while the background signal can be accurately subtracted using standard graphic manipulation software.

Deep complexity – SrTiO₃

SrTiO₃ (STO) is the prototypical substrate type used for thin film growth of perovskites. As such, it is widely used by ma-

terials scientists and solid-state physicists. Despite this, little is known or agreed upon regarding its surface structure. With this in mind, a large data set of the surface of STO was recorded using SXRD, at the Materials Science beamline of the SLS. It was found that the surface of STO consists of three different structures, which evolve from the common bulk structure. Analysis has shown that these structures and their relative contributions are mediated by the formation of a double layer of TiO₂ and the rearrangement of titanium atoms on the uppermost atomic layer [8]. Renditions of these are shown in Figure 3.

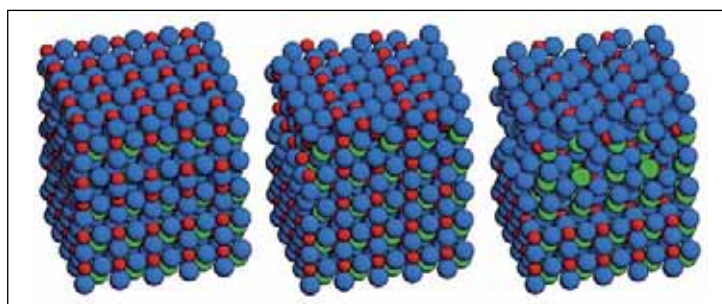


Figure 3: **Model fits of the three distinct surface structures of the perovskite SrTiO₃. Ti = red, Sr = green, O = blue.**

All three structures show significant shifts from the bulk atomic positions down to at 3 monolayers. This may have important consequences on unknown surface properties. For example, theoretical studies have suggested that STO may be ferroelectric at the surface [9], and indeed our own recent results suggest that regularly sized surface domains of a possibly ferroelectric nature may indeed exist [10].

Acknowledgements

The authors wish to thank F. Glaus, M. Lange, J. Lehmann, D. Lüthy, D. Meister, M. Naef, H. Rickert, and E. Schmid for their assistance in the construction of the PLD chamber and realisation of the pixel detector.

References

- [1] R.G. Moore et al., Phys. Stat. Sol., B 241, 2363 (2004)
- [2] H. Dulli et al., Appl. Phys. Lett., 77, 570 (2000)
- [3] R. Feidenhans'l, Surf. Sci. Reports, 10, 105 (1989)
- [4] P.R. Willmott and J.R. Huber, Rev. Mod. Phys., 72, 315 (2000)
- [5] C.M. Schlepütz et al., Acta Cryst. A, 61, 418 (2005)
- [6] P.R. Willmott et al., Appl. Surf. Sci., 247, 188(2005)
- [7] P.R. Willmott et al., Phys. Rev. Lett. Vol 96, 176102 (2006)
- [8] R. Herger et al., in preparation
- [9] N. Bickel et al., Phys. Rev. Lett., 62 2009 (1989)
- [10] R. Herger et al., unpublished

Solving structures of polycrystalline materials with the Si-microstrip detector

Lars Massüger, Christian Baerlocher, Lynne B. McCusker, *Laboratory of Crystallography, ETH Zurich*;
Bernd Schmitt, Fabia Gozzo, *Research Department Synchrotron Radiation and Nanotechnology, PSI*

Many technologically and industrially important materials are synthesized in polycrystalline form, and cannot be grown as single crystals. This means that conventional crystallographic methods of structure analysis cannot be applied. However, the crystal structures of such phases often determine their useful properties, so it is essential that methods for studying their structures be developed. In an attempt to address this problem experimentally, an approach that exploits both the preferred orientation of the crystallites in a textured sample and the high resolution of the Si-microstrip detector on the MS beamline has been devised.

Introduction

The initial experiments, which demonstrated the feasibility of the method, were performed in reflection mode [1,2], but these required three days of synchrotron beamtime per sample, extreme corrections to the data for the higher-tilt angles, and a large, homogeneously textured sample (ca 2 cm diameter flat plate). To circumvent these problems, the experiment was adapted to a transmission geometry using an imaging plate detector [3]. With the 2D detector, only 6h of beamtime was required per sample, no tilt corrections were necessary, and a very small sample (ca 0.2–0.3 mm sphere) could be used. However, these advantages were gained at the expense of

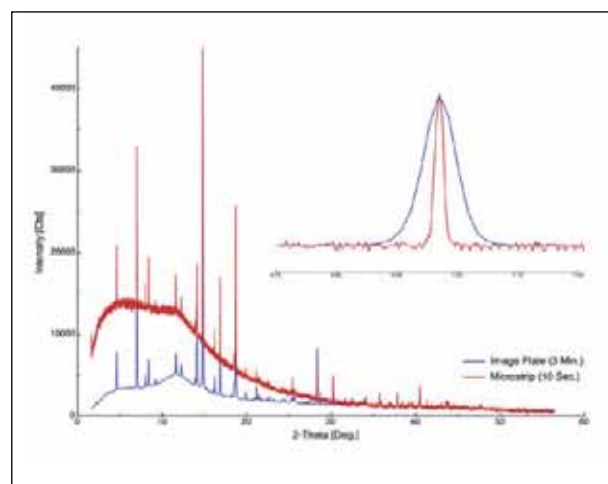


Figure 2: Comparison between imaging plate data (blue) and Si-microstrip data (red).

data resolution, both in 2θ range ($0\text{--}35^\circ 2\theta$) and peak width (ca $0.06^\circ 2\theta$). In order to study more complex structures, these limitations had to be overcome. With this in mind, the experiment was adapted to accommodate the newly developed 1D Si-microstrip detector at SLS.

Experimental setup

The experimental setup on the MS beamline is shown in Figure 1, and a comparison between data obtained from an imaging plate (SNBL at the ESRF) and those from the Si-microstrip detector in Figure 2. The resolution of the latter is much better (see inset), but it should be noted that the statistics are poorer and the background is higher.



Figure 1: Experimental setup showing (1) the Eulerian cradle (angles δ and ψ) for orienting the sample in the beam, and (2) the Si-microstrip detector.

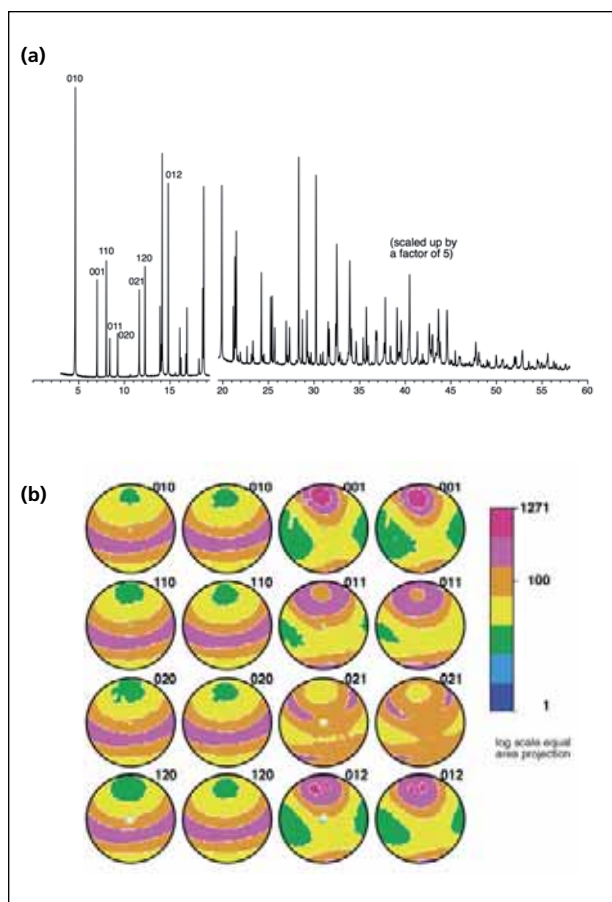


Figure 3: (a) Powder diffraction pattern of an untextured sample of the zeolite offretite with some non-overlapping reflections labelled, and (b) the corresponding pole figures for a textured sample (left measured, right calculated from the ODF).

Data collection and analysis

A powder diffraction pattern is collected for each sample orientation (rotation: $0^\circ \leq \Psi < 360^\circ$; tilt: $180^\circ \leq \delta < 270^\circ$; both in 5° steps) for a total of $72 \times 19 = 1368$ patterns (corresponding to 1296 unique orientations). The differences in the intensities in these patterns are directly related to the orientations of the crystallites in the sample. Data analysis is performed in two steps. First, the changes in the intensities of *non-overlapping* reflections as a function of sample orientation (pole figures) are used to determine how the crystallites are oriented in the sample (the orientation distribution function or ODF). As an example, a high-resolution powder diffraction pattern of the zeolite offretite ($a = 13.291 \text{ \AA}$, $c = 7.582 \text{ \AA}$, $P\bar{6}m2$) with some non-overlapping reflections labelled is shown in Figure 3a, and pole figures for these reflections from data collected on a textured sample in Figure 3b.

From the ODF, $P_{hkl}(\Psi, \delta)$ -values (fraction of the total intensity of reflection hkl observed for each orientation (Ψ, δ)) can be calculated for all reflections hkl . Then, a single set of (single-

crystal-like) reflection intensities (I_{hkl}) is extracted from all 1368 diffraction patterns simultaneously using the equation:

$$y(2\theta, \Psi, \delta) = \sum_{hkl} I_{hkl} P_{hkl}(\Psi, \delta) G(2\theta - 2\theta_{hkl})$$

where $y(2\theta, \Psi, \delta)$ is the intensity measured at step 2θ for the sample orientation (Ψ, δ) , and $G(2\theta - 2\theta_{hkl})$ is the standard peakshape function.

Test example offretite

To test the method, a textured sample of the zeolite offretite ($[KMgCa(H_2O)_{15}][Si_{13}Al_5O_{36}]$ -OFF) was prepared and data were collected and analysed as described above. Eight pole figures (Fig. 3) were used to determine the orientation of the crystallites in the sample (and thereby the $P_{hkl}(\Psi, \delta)$ -values), and then a single set of intensities was extracted from the 1368 diffraction patterns. With these data, the zeolite framework structure could be solved by direct methods without difficulty. The non-framework atoms were then found in subsequent difference Fourier maps.

Viologen vanadate

The structure of viologen vanadate ($C_{12}H_{14}N_2V_2O_5$) was unknown, and since the material crystallizes in the form of long, thin strands, it was considered to be well-suited for an attempt to apply the texture method to a real problem. A textured sample was prepared, data collected, and a set of intensities extracted ($C2/m$, $a = 21.232 \text{ \AA}$, $b = 6.318 \text{ \AA}$, $c = 3.585 \text{ \AA}$, $\gamma = 94.92^\circ$). These data proved to be sufficient to locate the V and O atoms in the structure using direct methods and default input parameters. The location of the viologen molecule could then be determined during the course of the structure refinement. The latter proved to require an eightfold expansion of the unit cell ($b' = 4b$ and $c' = 2c$, space group $P2$).

Thus, the method has been shown to be successful, and once the next edition of the Si-microstrip detector is ready, even better quality data can be expected, and more complex structures should become accessible.

References

- [1] T. Wessels, Ch. Baerlocher and L.B. McCusker, *Science*, 384, 477-479 (1999)
- [2] T. Wessels, Ch. Baerlocher, L.B. McCusker and E.J. Creghton, *J. Am. Chem. Soc.* 121, 6242-6247 (1999)
- [3] Ch. Baerlocher, L.B. McCusker, S. Prokic and T. Wessels, *Z. Kristallogr.* 219, 803-812 (2004)

Monitoring water flow in soils, using neutron and X-ray tomography

Andrea Carminati, Anders Kaestner, Peter Lehmann, Hannes Flühler, *Institute for Terrestrial Ecology, ETH Zurich*; Eberhard Lehmann, René Hassanein, Peter Vontobel, *Research Department Condensed Matter Research with Neutrons and Muons, PSI*; Marco Stampanoni, Amela Grosio, *Research Department Synchrotron Radiation and Nanotechnology, PSI*

Structures such as aggregates and fissures dominate the displacement of water, air, and solids in soil because they cause spatially non-uniform non-equilibrium flow. We can improve our understanding of these flow processes by making use of the recent advances in imaging techniques. Neutron radiography and tomography are efficient tools for real time monitoring of water distribution. X-ray tomography enables us to reconstruct the internal fabric of the soil at a resolution of a few microns. By combining the two methods, we discovered that micro-heterogeneities control the overall hydraulic behaviour of structured soils.

Introduction

Soil stores most of our water, supplies the nutrients to plants' roots and serves, for the purpose of humans, as a repository for industrial waste. The quality of groundwater and agricultural production depends on the capacity of the topsoil to retain water and, simultaneously, to let excess water pass into the aquifer. These hydraulic properties are strongly affected by the presence of structures like fissures, cracks, and aggregates that cause an extremely non-uniform flow field. The understanding of the hydraulic behaviour of structured soils has been substantially improved by the recent advances in non-destructive imaging techniques.

The soil components are often organised in aggregates with large pores in-between (i.e. in plough layers of tilled soils, biologically active forest soils, and humus-rich soils). The large pores between the aggregates are the primary pathways for rapid infiltration, while the aggregates are the storage com-



Figure 1: Soil aggregates are structural units frequently observed in top soils. The diameters range from one millimeter to a few centimeters.

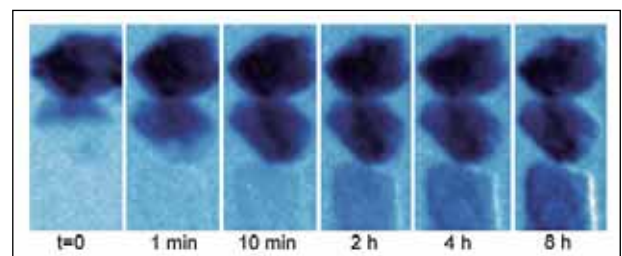


Figure 2: Time-series of neutron radiographs. Three aggregates were stacked onto each other; the samples were 5 mm wide and 20 mm long. The initial water input propagated downwards following gravity and capillary forces.

partment for the retained water and solutes. The hydraulic properties of such systems depend on the internal fabric of the aggregates and on their arrangement. Such relations have so far, not been quantified.

Neutron radiography

We studied the water infiltration into a packing of soil aggregates. In total, 15 samples were analysed. The infiltration was monitored in real-time, producing a time-series of neutron radiographs at NEUTRA.

Because the aggregates were smaller than typical samples inspected at NEUTRA and the flow process was relatively fast, with respect to the required exposure time, we chose the radiography position closest to the neutron source, with the smallest field of view and the greatest neutron flux. The smaller collimation was compensated by a custom-built sample holder, which allowed us to decrease the sample-detector

distance. The small pixel size and the limited exposure time resulted in poor neutron statistics. We used a scintillator developed at NEUTRA with a higher neutron efficiency, which improved the signal to noise ratio. With the use of digital detector systems the quantification of the water distribution at different times was possible. For a precise quantification, additional effects had to be taken into account. For example, neutrons scattered in the sample or at the instrumentation could reach the detector and blur the radiographs. Due to the poly-energetic neutron spectrum, beam hardening and the energy dependent detector sensitivity had to be considered. These effects were taken into account by a correction algorithm based on previously calculated point scattered functions [1]. The contacts between aggregates are the key factor in the infiltration process: the upper contact is highly conductive, while the second acts as a barrier limiting the flow. This different behaviour of the contacts was noticed in several samples. We observed that the contacts are highly conductive when wet, but after a small amount of drainage they become bottlenecks for the flow. The transition between these two hydraulic behaviours is abrupt. This is due to the presence of large pores within the contact region that are easily drained compared to the aggregate interior. After draining, the water flows through narrow and almost point-like hydraulic bridges. To verify this hypothesis the contacts were scanned with a higher resolution.

X-ray tomography

After monitoring the water infiltration at NEUTRA, the sample was transferred to the SLS for a closer X-ray inspection of the contacts. We measured with a photon energy of 20 keV and a resolution of 3.5 μm [2, 3]. One sample was scanned at different stages of drainage to analyze the spatial distribution of water in the contacts. In order to increase the visibility of the water we added CaI_2 at a concentration of 4%. The three phases (liquid, gas and solid) are visible. Before drainage, liquid menisci are visible in the contact region and the water can flow from aggregate to aggregate through a large water-filled cross section. After the drainage, the large pores are air-filled, and the remaining liquid contacts are sparse and almost point-like, thereby limiting the water flow.

Conclusion

Micro-heterogeneities, such as those in the contact region, affect the overall hydraulic properties of soils at larger scales. This conclusion is supported by images obtained with a very high accuracy. Neutron radiography and tomography are

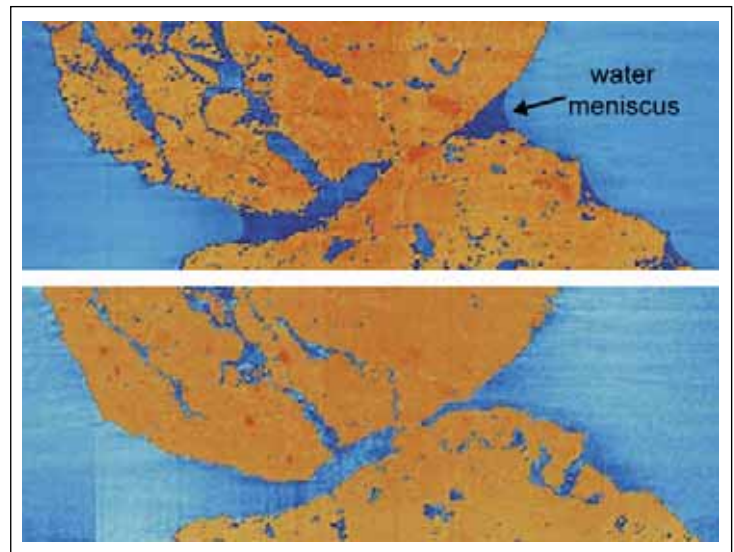


Figure 3: **Section of the contact between aggregates before and after drainage. The three phases are visible: air is blue, liquid is dark blue and solid red.**

efficient tools for monitoring the water flow distribution in real-time at a spatial-resolution up to 50 μm . By means of X-ray tomography it is possible to reconstruct the spatial distribution of the three phases at a resolution of 3.5 μm . For the analysis of flow processes in soils, neutron and X-ray tomography complement each other. Further joint experiments will enable us to optimize the applications of the two techniques.

References:

- [1] R. Hassanein, E. Lehmann and P. Vontobel, *Methods of scattering corrections for quantitative neutron radiography*, Nuclear Instruments and methods in Physics Research A, 37:1093-1106, 2005.
- [2] A. Kaestner, P. Lehmann, A. Carminati and H. Flüßler, *Analyzing the internal fabric of soil aggregates*, 2nd Italy-Canada workshop on 3D Digital Imaging and Modeling – Applications of: Heritage, Industry, Medicine and Land, Padova, Italy, 2005
- [3] M. Stampanoni, G. Borchert, P. Wyss, R. Abela, B. Patterson, S. Hunt, D. Vermeulen and P. Rüeggsegger, *High resolution X-ray detector for synchrotron-based microtomography*, Nuclear Instruments and methods in Physics Research A, 491: 291-301, 2002.

Single crystals of complex oxides

Kazimierz Conder, Ekaterina Pomjakushina, Andrei Podlesnyak, *Condensed Matter Research with Neutrons and Muons, PSI*

Single crystals have enormous importance for modern industry and science, because in a polycrystalline form, grain boundaries can have significant effects on the physical properties of a material. In order to learn more about these properties the travelling solvent floating zone (TSFZ) crystallization method was applied to the crystal growth of complex oxides like LaCoO_3 , $\text{SrCu}_2(\text{BO}_3)_2$, YMnO_3 , YFeO_3 , and Na_xCoO_2 ($0.5 < x \leq 1$).

Crystals have always been fascinating for their perfection, beauty and sometimes, extremely high costs. Systematic studies of crystalline minerals, especially the symmetry of their shapes, began as early as the 17th century. However, it was only at the beginning of the 20th century with the discovery of X-ray diffraction, that the internal structural symmetry was confirmed. At that time it was also realized, that the majority of solids have crystalline (ordered) internal arrangements of atoms. This order, however, very seldom perfectly extends throughout the whole volume of the material, making single crystals rare in nature and difficult to create artificially. Nevertheless, single crystals recently became one of the main pillars of modern technology. Further technological development greatly depends on the availability of suitably perfect and large single crystals for applications such as lasers, semiconductors, magnetic and optical devices.

Growing crystals

In the Laboratory for Developments and Methods at PSI, the travelling solvent floating zone (TSFZ) crystallization method is used. In this method a molten zone of the material is formed and held between two solid rods by its own surface tension (see Fig.1a). For insulating oxide materials, infrared image (IR) furnaces are used, which enable the focusing of the radiation of halogen lamps into a narrow band around the material. Once a small section of the rod has been melted, the molten (floating) zone (see Fig.2) is translated along the sample length by moving the material with respect to the radiation focus. As there is no need for crucibles, the impurity level in the crystals is reduced. A maximum operating temperature of 2400 °C can be reached, and the process can be performed in the controlled gas atmosphere from high vacuum up to 10 bars.

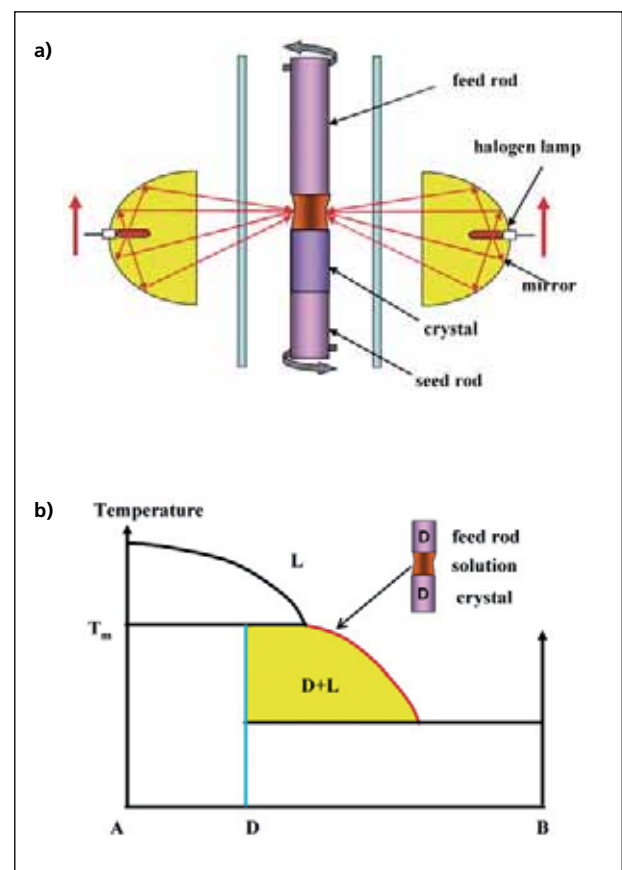


Figure 1: **a) Principle of TSFZ; b) Material of the composition D which decomposes during melting at T_m , can be crystallized from a solution L. The composition of this solution is shown with a red line in the phase diagram. When the solution zone is translated, solidification in the form of a single crystal, occurs at the crystal/solvent interface and the feed material dissolves at the feed/solvent interface.**

The TSFZ method enables even the growth of materials which decompose under melting – see Figure 1b. In order to grow such materials, a solution with low melting point (flux) is placed between the feed material and the seed crystal. During

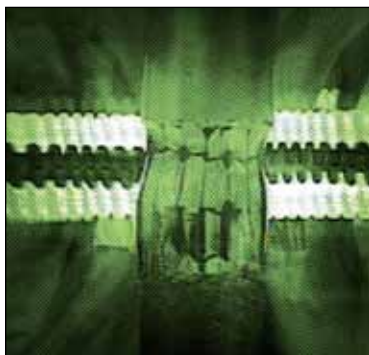


Figure 2: **The crystal can be observed "live" whilst growing. The central part of the rod is melted; the upper part is the feed rod, the lower part is the grown crystals. Perpendicular to the rod the halogen lamp filaments can be seen.**

the process, the feed material is dissolved in the solution zone and diffuses to the crystal/solution interface. The TSFZ method enables the growth of large crystals (\varnothing 7–8 mm, and a length of up to 100mm) and is applied predominately for oxide compounds. Our laboratory is equipped with instruments for preparation of the feed rods (hydrostatic press, vertical sintering furnace) and also for mechanical processing of the crystals (cutting and polishing).

In solid state science, a fundamental understanding of advanced materials often requires access to single crystals, as in polycrystalline form properties of the grain boundaries often manifest themselves more strongly than those of the material itself. The other reason is the anisotropy of many physical properties. This is observed only in single crystals and reflects the inner arrangements of atoms.

We have observed anisotropy of magnetisation and resistivity in layered cobalt oxide perovskite crystals $\text{RBaCo}_2\text{O}_{5+x}$ (R=rare earth atom). These materials have interesting proper-

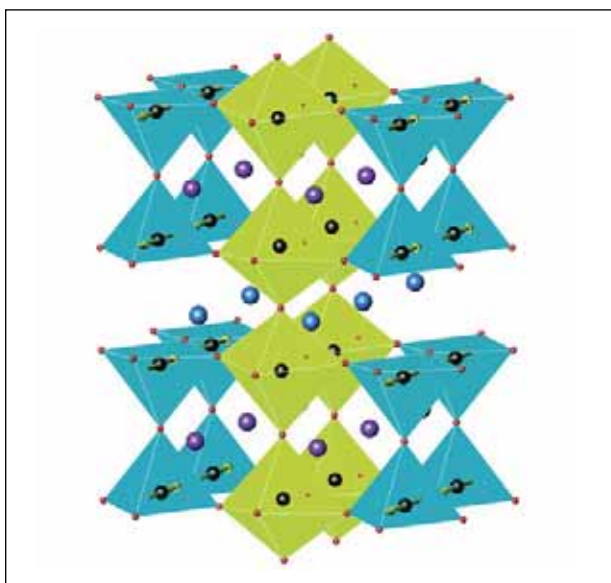


Figure 3: **Crystal structure of $\text{RBaCo}_2\text{O}_{5.5}$ (R=rare earth atom). The ions are drawn with the following colours: R-blue, Ba-violet, Co-black, O-red. Only pyramidal coordinated cobalt cations have magnetic moments depicted with arrows.**

ties, among others, magnetic and metal-insulator transitions and giant magnetoresistance. All these compounds are oxygen non-stoichiometric ($0 < x < 1$) and the cobalt cations can adopt different oxidation and spin states. In the structure of intermediate oxidized $\text{RBaCo}_2\text{O}_{5.5}$ cobalt cations exist in two oxygen coordination environments – pyramidal and octahedral - in both having oxidation state 3+ (see Fig. 3). It is believed that below room temperature only cobalt ions in a pyramidal environment have magnetic moments. However, the detailed magnetic structure is still not clear. There are many different models and Figure 3 shows one of them. This model assumes that all the magnetic moments are parallel to the ab plane. This is supported by the bulk magnetisation measurements made on single crystal. As can be seen in Figure 4, the magnetization signal is much higher when the applied magnetic field is parallel to the ab crystallographic plane. To clarify the magnetic structure neutron diffraction experiments will be performed this year.

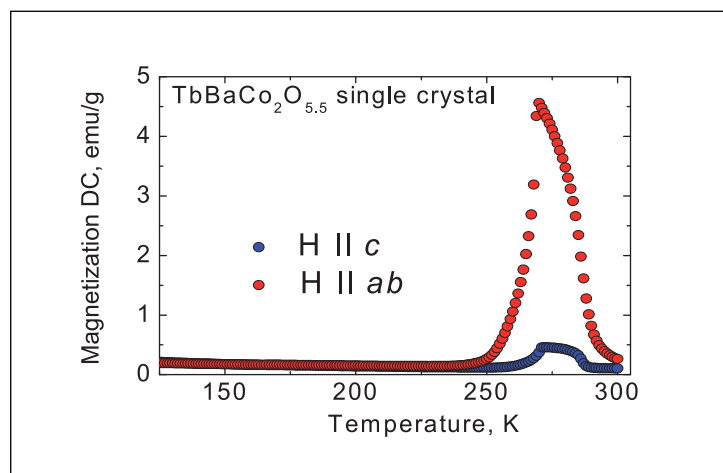


Figure 4: **Magnetization of $\text{TbBaCo}_2\text{O}_{5.5}$ single crystal measured in a magnetic field applied parallel to different crystallographic directions.**

In our laboratory high quality single crystals of LaCoO_3 (see Fig. 5), $\text{SrCu}_2(\text{BO}_3)_2$, YMnO_3 , YFeO_3 , ErFeO_3 and Na_xCoO_2 ($0.5 < x \leq 1$) have been grown. Crystals have been investigated by inelastic neutron scattering, neutron diffraction, X-ray absorption, ARPES, magnetisation under pressure and other techniques.



Figure 5: **LaCoO_3 single crystal.**

Characterization of nanomagnetic structures by polarized small angle neutron scattering

Joachim Kohlbrecher, *Condensed Matter Research with Neutrons and Muons, PSI*

The polarization option on the SANS-I instrument was implemented and made fully available to the users in 2005. This option, already in great demand, provides another valuable tool for investigation of magnetic properties on the nanometer scale. The topics ranged from nanostructures of metallic alloys to superconductivity, dynamic nuclear polarization, self-patterned structures on surfaces and development of grazing incident SANS techniques (GISANS) for magnetic surface structures.

Magnetism at the nanometer scale has, in recent years, provided a wealth of scientific interest and potential technological applications. These so-called nanomagnets form an excellent experimental laboratory for testing fundamental theorems in magneto-statics and micromagnetics. The very interest in the study of nanostructured magnetic materials is related to the basic notion that novel effects and properties may be expected whenever “crossing length scales” appear in a system, for instance, when the structural building units of a material (particle size, film thickness, dot size) are reduced below a characteristic intrinsic magnetic length scale of the system (domain wall thickness, magnetic exchange lengths, critical single domain size). Many of these length-scales are in the order of nanometers. For studies of magnetic phenomena that occur over this length-scale, magnetic small angle neutron scattering is appropriate.

Small angle neutron scattering (SANS)

This is a technique which allows characterizing of structures or objects on the nanometer scale, typically in the range between 1 nm and 500 nm. Besides the nuclear interaction, due to their magnetic moment neutrons undergo a magnetic interaction with matter, on the same order of magnitude as the nuclear interaction. With this dual interaction of neutrons with matter, they offer the opportunity to study both compositional and magnetic structures and correlations. Furthermore, by using a polarized neutron beam, very specific information on the magnetic structure or alignment of nanoparticles can be obtained, as well as on their response to an external magnetic field.

User experiments with neutron scattering

We report briefly on the outcome of a few of these user experiments.

The soft magnetic nano-composite Nanoperm ($\text{Fe}_{89}\text{Zr}_7\text{B}_3\text{Cu}_1$) is a two-phase composite material, which consist of ferromagnetic nanocrystalline bcc Fe particles embedded in an amorphous also ferromagnetic matrix. The magnetic contrast is related to the different magnitude of saturation magnetization of the Fe nanoparticles and the amorphous matrix with a Curie temperature of 345K which is much lower than the one of the Fe nanoparticles. The average size of the nanoparticle

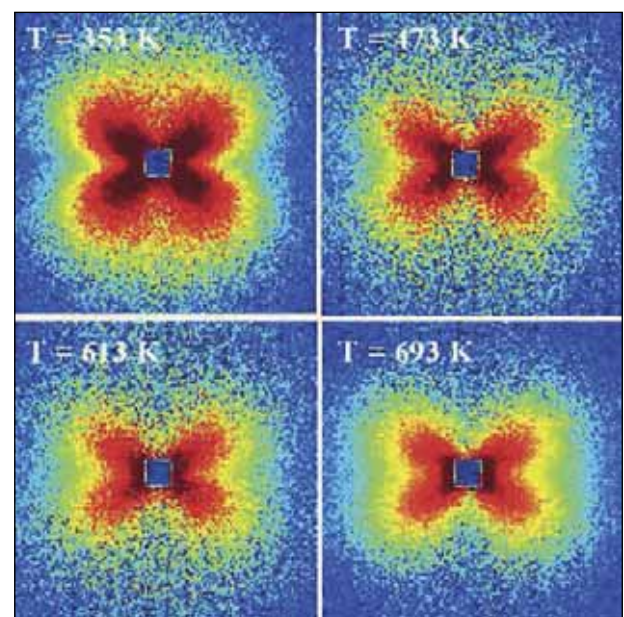


Figure 1: **Temperature variation of difference-intensity data of Nanoperm ($\text{Fe}_{89}\text{Zr}_7\text{B}_3\text{Cu}_1$) at $\mu_0H = 290$ mT (logarithmic scale). $d\Sigma/d\Omega$ has been subtracted from the respective $d\Sigma/d\Omega$ at 290 mT. Pixels in the corners have momentum transfer $q = 0.64$ nm $^{-1}$.**

is 12 nm which is considerably below the magnetic exchange length (~ 35 nm) in this material. Furthermore, they are exchange coupled to the amorphous magnetic matrix. This is believed to be the reason for their excellent soft magnetic properties. Michels et al [1] have recently observed an unexpected fourfold angular symmetry in the 2D SANS cross section in this material [2-4]. At an applied magnetic field of nearly two Tesla, the scattering signal is highly anisotropic with maximum SANS intensity in the direction normal to the field, whereas at the remanant state the pattern is isotropic, indicating a random domain orientation. At intermediate fields, they observe lobes of higher intensity at angles of about 40 degrees relative to the field axis. This feature becomes more pronounced when plotting difference-intensity patterns (Fig. 1). As the origin of the fourfold symmetry they have identified dipole fields which dress the individual Fe nanoparticles. In particular, the difference in the saturation-magnetization values between the Fe particles and the amorphous matrix, about 1.5 T for our Nanoperm sample, gives rise to a dipole field H_D whose magnitude is proportional to the difference in the magnetization values of the two phases and which reveals an angular symmetry according to $H_D \propto \sin\theta \cos\theta$, where θ is the angle between scattering direction Q and the external field H . The mismatch of the saturation-magnetization values between the nanosized Fe particles and the amorphous magnetic matrix gives rise to a dipolar stray field which induces spin disorder near the nanocrystals and manifests itself as a pronounced clover-shaped angular anisotropy in the magnetic small-angle neutron scattering cross section. The analysis of the experimental results is still ongoing, as are the efforts to understand the exact influence of the magnetic nanoparticles on the magnetisation in the surrounding ferromagnetic amorphous matrix.

Benefits of polarized neutrons

Another example where the dipolar stray field influences the surrounding ferromagnetic matrix was observed in CoCrPtB-based alloys in longitudinal recording materials, developed for use in high-density disk drives. [5]. Even though SANS is ideal for measuring magnetic structures in the relevant length scale it requires a sufficient large sample volume. In the case of recording material the magnetic nanostructure structure is located on a thin surface layer. The scattering of the substrate is therefore orders of magnitude larger than the scattering of the thin magnetic recording layer. To overcome this problem the use of polarized neutrons becomes essential. The small angle scattering signal from magnetic nanostructures depends on the spin state of the incoming neutron beam in contrast to a non-magnetic substrate which is independent of the beam

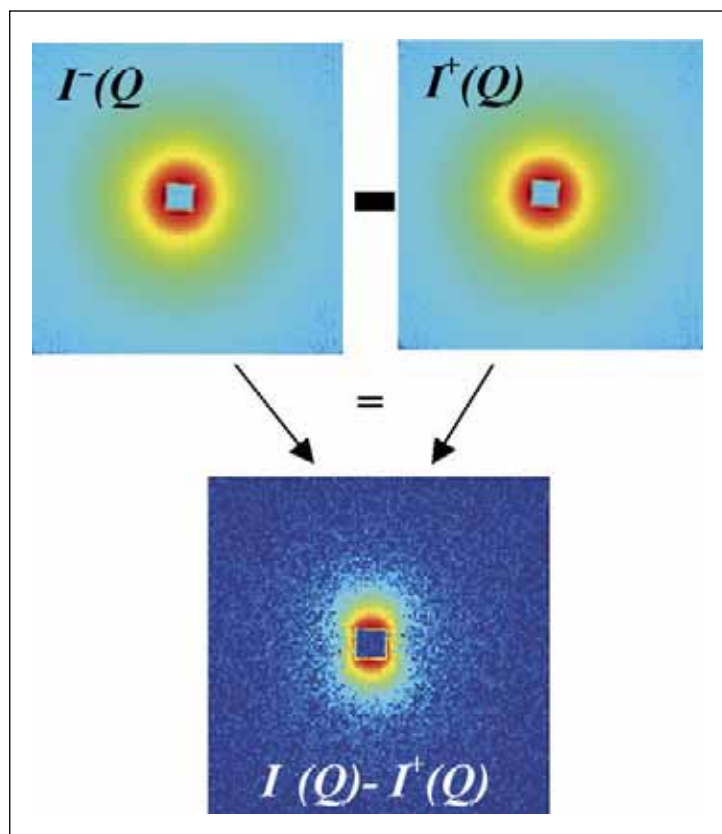


Figure 2: **SANS signal from magnetic nanostructures on a non-magnetic substrate. To extract only the scattering contribution of the thin magnetic layer the spin dependence of magnetic neutron scattering has been exploited. The difference intensity $I(Q) - I^+(Q)$ systematically suppresses the scattering of all non-magnetic structures and one can separate a clean signal from the thin (~ 15 nm) magnetic recording layer.**

polarization. Therefore the difference signal of both polarizations suppresses the scattering of all nonmagnetic substrates. This allows the systematic suppression of all disturbing signals by switching the polarization. The efficiency of this method is demonstrated in Figure 2. The difference signal shows a clean anisotropic scattering behaviour, which has its origin in the cross term between nuclear and magnetic form factor of the nano-structured magnetic recording layer.

References

- [1] Dr. Andreas Michels, Univ. Saarland, SINQ Proposal 20050264
- [2] A. Grob, S. et al., *phys. stat. sol. (a)* 201, 3354 (2004).
- [3] A. Michels et al., *Europhys. Lett.* 72, 249 (2005).
- [4] C. Vecchini et al., *Appl. Phys. Lett.* 87, 202509 (2005).
- [5] F. Y. Ogrin, S. L. Lee, M. Wismayer, T. Thomson, C. D. et al., (to be published)

Measuring quadrupolar orders by muon spin

Alexander Schenck, Fredy N. Gygax, *Institute for Particle Physics, ETH Zurich and PSI*; G. Solt, Oksana Zaharko, *Condensed Matter Research with Neutrons and Muons, PSI*; S. Kunii, *Department of Physics, Tohoku University, Japan*

Muon-spin spectroscopy studies performed on the strongly correlated system CeB_6 demonstrate that the careful determination of the μ^+ -Knight shift, that is, the difference between an externally applied magnetic field and the field inside a sample measured by the muon-spin precession frequency, precisely reveals some of the subtleties of the quadrupolar order present in this system. This result – which was a priori unexpected, as the muons are local spin- $1/2$ probes, believed to be insensitive to multipole features of the electric charge distribution inside the investigated sample – opens novel potential applications of the μSR technique.

Introduction

Positive muons (μ^+), as available at the Swiss Muon Source of the PSI, are considered excellent magnetic probes and can function in a complementary manner to neutrons in the sense that they are capable of resolving extremely weak magnetic moments, as well as disordered or short range magnetism. As the muons are local spin- $1/2$ probes, they are *a priori* not expected to be sensitive to multipole features of the electric

charge distribution inside the investigated sample. An example of such features is the so-called quadrupolar order, which reflects an ordering of the anisotropic electron orbitals around ions of the system.

The results reported below for the strongly correlated system CeB_6 [1] demonstrate that the careful determination of the μ^+ -Knight shift (i.e. the difference between an externally applied magnetic field and the field inside a sample measured by the μ^+ -spin precession frequency) reveals precisely some of the subtleties of the quadrupolar order present in this system.

CeB_6 crystallizes in the cubic CsCl-type structure, and the crystalline electric field splits the $4f^1\ ^2F_{5/2}$ multiplet into a Γ_7 doublet and a Γ_8 quartet, the latter being the ground state. What renders CeB_6 so interesting is the presence of multipolar (magnetic dipole-dipole, electric quadrupole-quadrupole, and magnetic octupole-octupole) interactions and their mutual interdependencies.

Phase diagram

The phase diagram consists of a low temperature double- \mathbf{k} anti-ferromagnetic phase ($T_N = 2.3$ K in zero applied field H_{ext}), followed by an antiferroquadrupolar (AFQ) phase [propagation vector $\mathbf{q}_Q = (1/2\ 1/2\ 1/2)$] up to $T_Q = 3.2$ K at $H_{\text{ext}} = 0$, and a paramagnetic Fermi liquid phase above T_Q . In particular, the AFQ phase has attracted much attention due to the observation that application of an external magnetic field induces an antiferromagnetic (AFM) dipolar order and stabilizes this phase, as seen by the monotonic increase of T_Q with \mathbf{H}_{ext} up to about 10 K at 35 T [2].

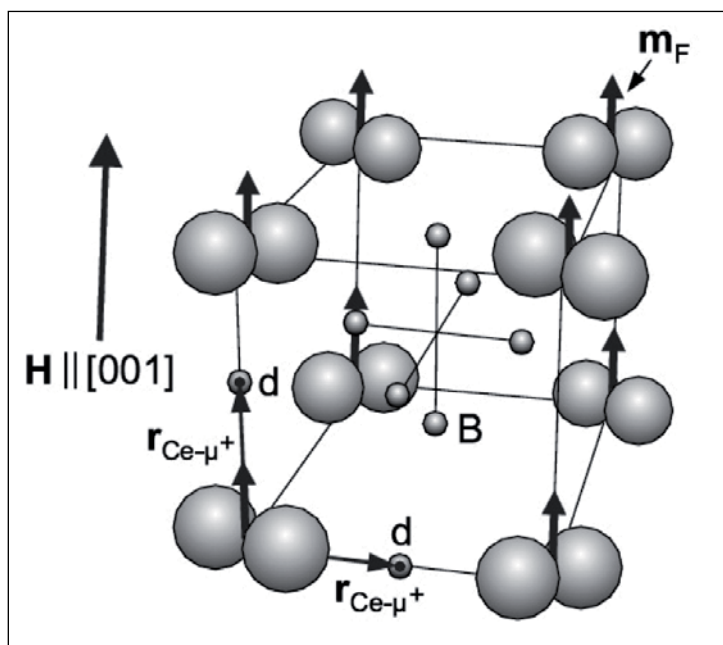


Figure 1: Schematic of the crystal structure of CeB_6 , with the direction of the external applied field and the ordering of the $4f$ orbitals of the Cerium ions in the AFQ phase. The muon position (d) is also marked.

The muon spin rotation measurements were performed at PSI using the low temperature instrument LTF and the general purpose spectrometer (GPS) on the π M3 beamline. In the GPS we used the same cylindrical sample as in Ref. [3]. Here we report only on measurements with $\mathbf{H}_{\text{ext}} \parallel [001]$ -axis. In the LTF we used a flat rectangular single crystal with the $[001]$ axis perpendicular to the flat face and parallel to \mathbf{H}_{ext} .

Results and outlook

From the high temperature μ^+ -Knight shift it can be concluded that the muons are located at the interstitial $3d$ site ($1/2 0 0$) situated symmetrically with respect to the nearest Ce neighbours (see Figure 1 and Ref. [3]). As a consequence, the dipole and also the associated contact hyperfine fields from the field induced AFM phase cancel at the $3d$ sites and do not contribute to the Knight shift. This feature allows one to perform μ^+ -Knight shift below T_Q despite the presence of the field induced AFM phase.

The contributions to the measured Knight shift are the dipole fields from the field induced ferromagnetically aligned moments $\mathbf{m}_{\text{FM}} = \chi \mathbf{H}_{\text{ext}}$ on the Ce sites and the contact hyperfine field due to the spin polarization of the conduction electrons at the μ^+ . The latter is induced also by the \mathbf{m}_{FM} via the RKKY interaction; χ is the isotropic bulk magnetic susceptibility due to the $4f$ electrons. As the crystallographically equivalent muon stopping sites become magnetically non-equivalent when an external field is applied to the samples, the μ^+ Knight shift can be expressed as the sum of two contributions:

$$K^{\perp}(T) = (A_{\text{con}}^{\perp} - \frac{1}{2} A_{\text{dip}}) \chi(T)$$

$$K^{\parallel}(T) = (A_{\text{con}}^{\parallel} + A_{\text{dip}}) \chi(T)$$

The remarkable characteristic of the obtained data, is the fact that the contact hyperfine field is *anisotropic* and *temperature dependent at low temperatures*, mainly below T_Q . This is illustrated in Figure 2, where we plot, for both contributions, $\delta A_{\text{con}}^i = A_{\text{con}}^i - A_{\text{con}}^i(T_Q)$ versus T/T_Q .

The observed smooth temperature dependence below T_Q which can be excellently reproduced by the equation:

$$A_{\text{con}}^i(T) = A_{\text{con}}^i(0) \left[1 - (T/T_Q)^{\gamma} \right]^{\beta} + A_{\text{con}}^i(T_Q)$$

The observed behaviour of $A_{\text{con}}^{\parallel}(T_Q)$ and $A_{\text{con}}^{\perp}(T_Q)$ as well as the extracted values of γ and β , show a striking resemblance with the temperature dependence of the quadrupolar order parameter $p(T)$ obtained by resonant and non-resonant X-ray scattering [4-6], suggesting that $\delta A_{\text{con}}(T_Q) \propto p \propto \langle O_{XY} \rangle$. In fact, in CeB_6 the only significant intrinsic temperature dependence below T_Q , as far as we know, is carried by the quadrupolar order parameter, and hence we conclude that indeed δA_{con}

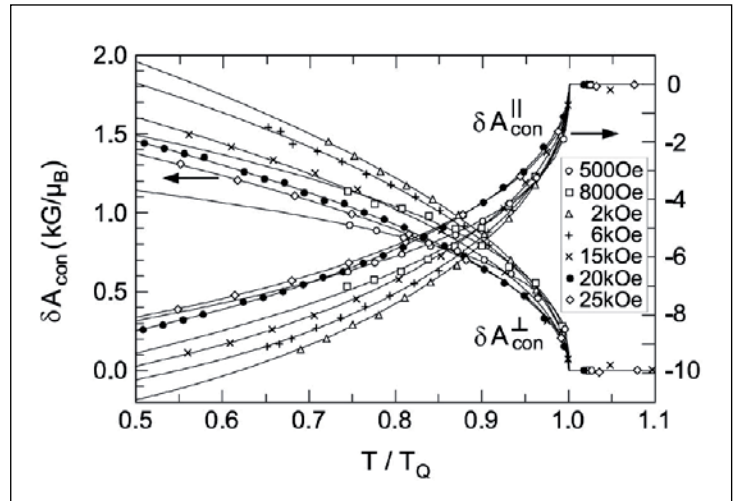


Figure 2: Plot of $\delta A_{\text{con}}^i = A_{\text{con}}^i - A_{\text{con}}^i(T_Q)$ versus T/T_Q . The solid lines represent fits as described in the text.

reflects directly the quadrupolar order parameter.

How is this possible? We attribute it to an anisotropic $4f$ moment induced RKKY mechanism, which depends on the orientation of the quadrupole moment, i.e., the nonspherical $4f$ charge distribution relative to the μ^+ position. Consistent with this interpretation is the fact that A_{con} becomes anisotropic. It is quite remarkable that μ^+ Knight shift measurements (a local probe technique) are able to provide the same information as X-ray scattering experiments. This needs to be exploited in future investigations.

References

- [1] A. Schenck *et al.*, Phys. Rev. Letters 93 (2004) 257601
- [2] R.G. Goodrich *et al.*, Phys. Rev. B 69 (2004) 054415
- [3] A. Schenck *et al.*, Phys. Rev. Letters 89 (2002) 037201
- [4] H. Nakao *et al.*, J. Phys. Soc. Jpn. 70 (2001) 1857
- [5] F. Yakhov *et al.*, Phys. Lett. A 285 (2001) 191
- [6] Y. Tanaka *et al.*, Physica B 345 (2004) 78

A new magnetic microprobe for hetero-structures

Elvezio Morenzoni, *Condensed Matter Research with Neutrons and Muons, PSI – Representing a collaboration of PSI and the universities of Birmingham, Braunschweig, Zurich, Leiden, Konstanz and St. Andrews University*

The new high-intensity muon beamline especially designed to serve the needs of the low-energy, polarized positive muon source (LEM) and the upgraded LE- μ SR spectrometer were put into operation in 2005. The high-flux of surface muons translates into a LEM rate of up to 8,000/s available for thin film studies. The sensitivity and depth dependent information is exemplarily demonstrated in the detection of a spin-density wave (SDW) coexisting with bulk superconductivity in a ferromagnetic-superconducting trilayer.

Introduction

Muons thermalized in matter act as a non-destructive, non-invasive, and microscopic probe of spins, magnetic moments or currents and provide unique information about magnetic, superconducting and other local properties of matter. The recently developed LE- μ SR technique where the implantation energy can be continuously varied from 0.5 to 30 keV extends the field of application of this probe allowing depth dependent μ SR-studies of thin films and multilayered structures in the range of ~ 1 nm to ~ 200 nm [1]. The potential offered by μ SR in conjunction with depth dependent studies led to the decision few years ago to build a new dedicated facility in order to achieve an increase in the intensity of available particles and to improve the experimental conditions.

The LEM beamline

In 2005 construction of the new LEM beamline was completed and first measurements taken. The system consists of a new high intensity surface muon beamline delivering up to 150 M/s polarized muons to the actual LEM setup where these particles are moderated to about 15 eV, re-accelerated to the desired energy, and then implanted in the thin film sample at a selected depth. LEM rates of 3000-8000/s can be delivered with the new apparatus, further strengthening the leadership of PSI in the use of muons for depth dependent study of thin films and multilayers [2].

An example is the study of the electronic properties of Pb in a Fe/Pb/Fe trilayer. Such artificially fabricated structures are ideal systems to study effects such as co-existence or competition of different order parameters or to see how the

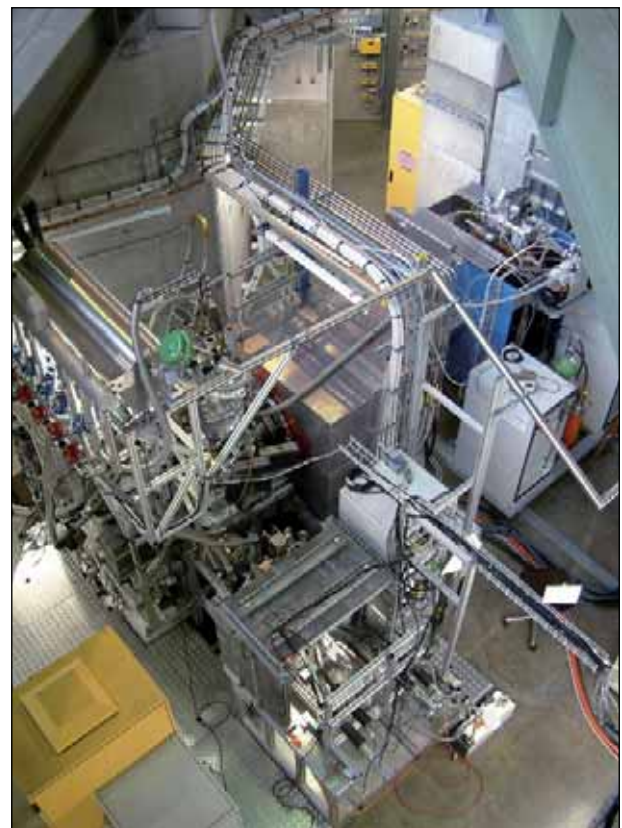


Figure 1: **The new LEM apparatus in the upgraded μ E4 area. The last section of the new surface muon beamline is visible, as is the actual LEM apparatus, which consists of the LE beam and μ SR spectrometer with sample chamber (lower part).**

electronic properties are modified by the proximity of materials with different ground states. For a normal metal-ferromagnetic multilayer, the exchange field can cause a periodic oscillation of the electron-spin density inside the normal layer. The period of this spin-density wave is determined by an enhance-

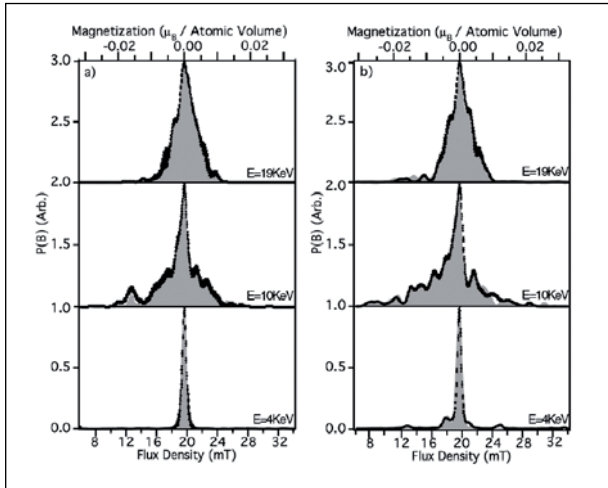


Figure 2: **The field probability distribution $p(B)$ for different implantation depths into the sample, revealing the presence of a spin-density wave inside the Pb layer. The points and shaded areas correspond to the data and fit, respectively. (a) Left side: normal state $T=10$ K and (b) Right side: superconducting state, $T=2.5$ K.**

ment of the wave-vector dependent susceptibility at external spanning vectors of the Fermi surface, as in the RKKY interaction [3,4]. LE- μ SR has recently been able to observe a SDW in Fe/Ag multilayers [5]. Replacing Fe with Pb a subtle effect of coexistence and interplay of this SDW with bulk superconductivity has been now found. The measurements were made in a field of 20 mT applied parallel to the film and perpendicular to the initial muon-spin polarization, at temperatures both above and below T_c . Insight can be gained from the frequency domain data of Figure 2, which shows the magnetic field distribution $p(B)$ sensed by the muons at different positions inside the Pb layer in the normal metallic state at a temperature of 10 K and in the superconducting state at 2.5 K. The unusual $p(B)$ reflects a flux density profile, arising from a SDW induced in the Pb layer by the exchange field from the Fe layers. The satellite peaks in the data are related to the turning points of the SDW.

The resemblance of the raw data between Figures 2(a) and 2(b) demonstrates that remarkably the SDW persists into the superconducting state. A detailed analysis performed by A. Drew from St. Andrews University [6] shows that the observed $p(B)$ s correspond to a magnetization $M(x)$ within the Pb spacer given by the addition of the magnetizations originating from each of the two Fe/Pb interfaces of the form:

$$M(z) = \sum_i A_i \frac{\sin(2k_i z + \phi_i)}{z^{n_i}}$$

where k_i are the wave vectors of the SDW, z the distance into the spacer layer, and A_i is an adjustable parameter for the coupling strength of the spin-density wave of wave vector k_i .

At a given temperature, an identical model is used for all energies. The fits were found to converge to two wave vectors, $k_1=2.3(2)$ nm⁻¹ and $k_2=15.8(2)$ nm⁻¹ in excellent agreement with those obtained from de Haas-van Alphen quantum oscillation measurements of Pb and which correspond to wave vectors that connect flat pieces of the Fermi surface along the (111) direction in reciprocal space.

In order to successfully model the field profiles inside the Pb/Fe film, one must also take into account the spatial phase of the oscillations. The fits shown in Figure 2(b) include a $\pi/2$ change in phase of one of the spin-density wave components compared to the value found in the normal state. The fits also require a 25% increase in amplitude for both oscillations to describe the data, suggesting an increase in the coupling of spins below the superconducting transition.

Conclusion

These results demonstrate the remarkable co-existence of a SDW with bulk superconductivity in the S layer in a FM/S/FM trilayer. Furthermore, the apparent enhancement of the SDW amplitude and $\pi/2$ phase shift of one component of the SDW below T_c indicates a profound coupling of these two forms of spin order. However, it remains a challenge to fully theoretically explain the persistence of the SDW and its accommodation to the onset of bulk superconductivity in these systems.

References

- [1] E. Morenzoni et al., J. Phys.: Cond. Matt. 16, S4583-(2004)
- [2] T. Prokscha et al., Physica B 374-375, 460 (2006)
- [3] K. Yosida, Phys. Rev. 106, 893 (1957)
- [4] M. A. Ruderman and C. Kittel, Phys. Rev. 96, 99 (1954)
- [5] H. Luetkens et al., Phys. Rev. Lett. 91, 017204 (2003)
- [6] A. Drew et al., Phys. Rev. Lett. 95, 197201 (2005)

Manganites and cobaltites: a playground for ideas in contemporary solid-state physics

Vladimir Pomjakushin, Andrew Podlesnyak, Marisa Medarde, Joël Mesot, Denise Sheptyakov, Sabine Streule, Kazimierz Conder, Ekaterina Pomjakushina, *Condensed Matter Research with Neutrons and Muons, PSI*; Anatoly Balagurov, *Laboratory of Neutron Physics, JINR, Dubna*; Maurits W. Haverkort, Daniil Khomskii, *Physics Institute, Köln University*

Currently of interest to modern solid-state physics is colossal magneto-resistance (CMR) in manganites and cobaltites which belong to the class of strongly correlated electronic systems displaying remarkable physical phenomena. Moreover, the interest in CMR-materials is naturally generated in view of their potential for new generations of magnetic devices for recording and sensors. The activity in this challenging field within the Laboratory for Neutron Scattering (LNS) is illustrated by two spectacular effects: a metal-insulator transition in $(\text{La}_{1-y}\text{Pr}_y)_{0.7}\text{Ca}_{0.3}\text{MnO}_3$ caused by oxygen isotope substitution, and a spin-state transition in LaCoO_3 induced by thermal excitations.

The manganese and cobalt oxides known as manganites and cobaltites belong to a well-known family of the 3d-transition metal (M) perovskite AMO_3 oxides. Due to 3d-electrons anisotropy and the mixed valence of the M-ions the charge, spin and lattice interactions are strongly coupled in manganites and cobaltites. A delicate balance of these interactions, which can be achieved by particular cation substitution on both A and M sites, provokes a plethora of physical phenomena which are of current interest in modern solid-state physics, such as M-I transition, mutually connected orbital, charge and spin state transitions/ordering, polaron formation and large isotope effects, microscopic and macroscopic phase separation.

effect cannot be attributed to a solely polaronic narrowing of the bandwidth within the double-exchange model. The effect has a percolate nature and requires an inhomogeneous phase separated state. The neutron diffraction studies (HRPT and DMC instruments at SINQ) allowed us accurate determination of the structure and magnetic parameters of the coexisting ferromagnetic metallic (FM) and anti-ferromagnetic insulating (AFM) phases. We have found that the ground state of LPCM can be characterized as an incoherent mixture of interpenetrating clusters of the FM and AFM phases with characteristic sizes of more than 10^3\AA across the whole phase diagram with the phase fraction ratio controlled by the effective bandwidth

Giant isotope substitution effect

The manganites show a peculiar isotope substitution effect: an increase in the mass of the oxygen atom by 12.5% leads to a change from a metallic to an insulating ground state[1-3]. The effect was first discovered in $(\text{La}_{1-y}\text{Pr}_y)_{0.7}\text{Ca}_{0.3}\text{MnO}_3$ (LPCM) for $y = 0.75$ and $(\text{La}_{0.5}\text{Nd}_{0.5})_{0.67}\text{Ca}_{0.33}\text{MnO}_3$, that is, in narrow charge carrier bandwidth W manganites and more recently in a wide bandwidth system $\text{Sm}_{1-x}\text{Sr}_x\text{MnO}_3$ ($x \approx 0.5$) as well (see [5] and references therein). In LPCM, the electron transfer integral strongly depends on the Mn-O-Mn bond angle, given by the Pr-concentration and thus the system can be switched from a metallic to a Mott insulating state at $y \approx 0.85$. The renormalization of W mediated by the anharmonic motion of the oxygen bridging the Mn ions is very large, and shifts the system towards the insulating state, but the “giant” isotope

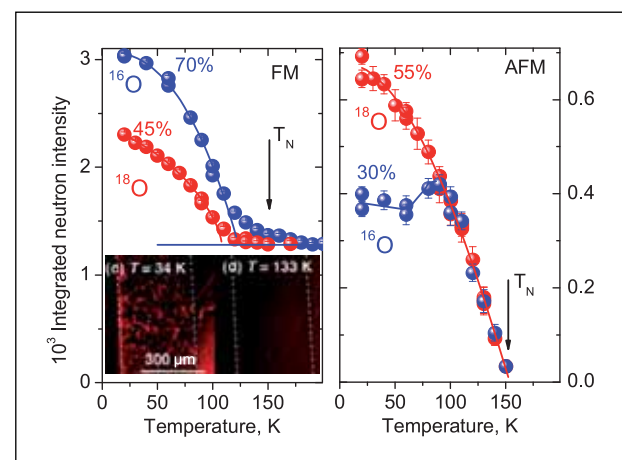


Figure 1: **FM and AFM diffraction peak intensities in LPCM samples ($y=0.8$) as a function of temperature. The insert shows magneto-optical images (taken from Ref. [6]) of the surface of the LPCM single crystal ($y=0.7$) providing visual evidence of the mesoscopic phase separation.**

W and also by the sample microstructure [2]. The AFM phase arises below $T_N=150\text{K}$ and then the FM phase starts to grow below 100K , reducing the volume occupied by the AFM phase as shown in Figure 1.

The decrease in W caused by the increase in the oxygen mass from ^{16}O to ^{18}O results in the redistribution of the phase volumes in favour of the AFM insulating phase, as indicated in the plot. If the volume of the FM metallic phase drops below the percolation limit of 16%, then the low temperature state changes from metallic to insulating providing a natural explanation of the giant isotope effect. The presence of the mesoscopic phase separation in the manganites is itself an unusual effect and needs special theoretical attention, since it is not a chemical kind of phase separation but is related to the properties of a strongly interacting system in the presence of so-called quenched disorder. The manganites $A_{0.7}A'_{0.3}\text{MnO}_3$ possess natural quenched disorder due to the A-cation radius dispersion and two charge states of the manganese ions. The theoretical study [7] of the competition between two ordered states in random field Ising model demonstrates the generation of the giant clusters of coexisting phases. This implies that the quenched disorder plays a key role in the formation of the phase-separated state in manganites.

Spin-state transition in LaCoO_3

LaCoO_3 displays two broad transitions [4] in the magnetic susceptibility occurring around $T_1 \sim 80\text{--}120\text{K}$ and $T_2 \sim 400\text{--}600\text{K}$, which were interpreted as spin-state transitions more than 40 years ago [8]. Although the vast majority of studies indicate that Co^{3+} ions display a nonmagnetic ground state (low spin (LS), $t_{2g}^6 e_g^0$, $S=0$) below 30K , the nature of the first and second excited states is still polemic. Hence, after the initial interpretation from Goodenough (high spin (HS), $t_{2g}^4 e_g^2$, $S=2$ [8]), the existence of Co^{3+} in the intermediate spin state (IS, $t_{2g}^5 e_g^1$, $S=1$) above T_1 has been proposed by several authors. Since the debate around the thermal sequence of spin states has not yet been settled, we decided to use inelastic neutron scattering to investigate the energy levels of the first thermally excited state of the Co^{3+} ion. The measurements, performed on the time-of-flight spectrometer FOCUS at the SINQ, indicated that a thermally-induced inelastic peak appears at an energy-transfer of $\sim 0.6\text{meV}$ (Fig. 2). The peak intensity strongly increases with temperature and follows the behaviour of the magnetic susceptibility, suggesting that the inelastic scattering occurs between thermally populated magnetic states. A clear shift of the transition to the higher energy $\sim 1.5\text{meV}$ was observed in magnetic field $H=6\text{T}$ compared to the zero-field spectrum, thus firmly establishing a g -factor of about 3.

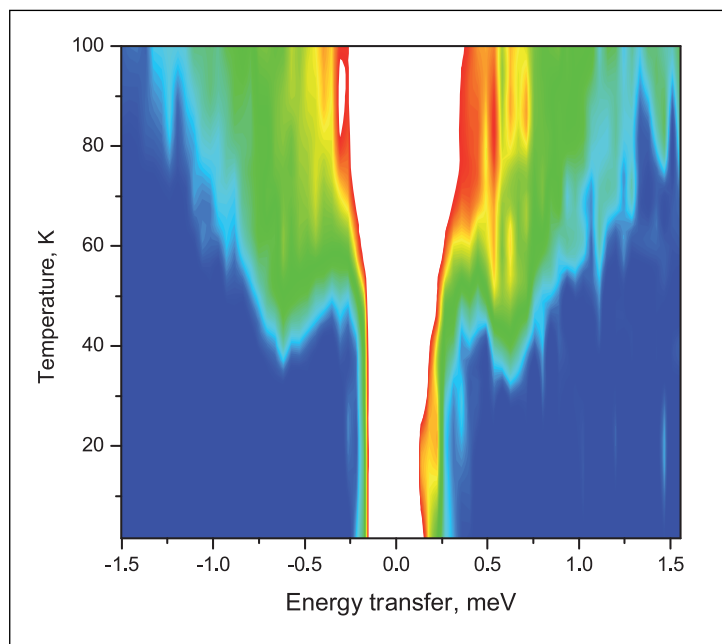


Figure 2: **Intensity contours visualizing the temperature renormalization of the energy spectra taken for LaCoO_3 .**

With these results in mind, we can now discuss the nature of the spin state giving rise to the observed inelastic peak. The HS state has, in a cubic CF, a half-filled shell $t_{2g}^3 e_g^2$ with spins up, and one extra spin-down electron on a triple-degenerate t_{2g} -level. Spin-orbit coupling splits this state into the lowest-lying triplet, the next state is a quintet, and the highest-lying state has $J=3$. The trigonal crystal field of LaCoO_3 can easily split the lowest-lying triplet into singlet and doublet with $\Delta E \sim 0.6\text{meV}$, in agreement with our measurements. Another possibility would be the IS state $dx^2-y^2 dxy$ with orbital ordering or strong non-cubic crystal-field. The lowest IS state has to create the maximum e_g -electron- t_{2g} -hole density overlap. The state has one hole in the t_{2g} shell and one electron in the e_g shell. However, such configuration would result in a system with a g -factor ~ 2.0 , a value difficult to reconcile with our experimental data. Thus, the first interpretation (HS excited state, in agreement with Goodenough's initial suggestion) seems more plausible to us.

References

- [1] A. Balagurov et al., Phys. Rev. B 64, 024420 (2001).
- [2] V. Pomjakushin et al., Phys. Rev. B, submitted, (2005).
- [3] A. Balagurov et al., JEPT Letters 82, 672 (2005).
- [4] A. Podlesnyak et al., Phys. Rev. Lett. accepted, (2006).
- [5] N.A. Babushkina et al., Phys. Rev. B 67, 100410 (2001).
- [6] M. Tokunaga, et al., Phys. Rev. Lett. 93, 037203 (2004).
- [7] J. Burgy et al., Phys. Rev. Lett. 87, 277202 (2001).
- [8] J.B. Goodenough, J. Phys. Chem. Solids 6, 287 (1957).

Polarized nuclei: from fundamental nuclear physics to applications in neutron science and NMR

Ben van den Brandt, Patrick Hautle, Ton Konter, *Condensed Matter Research with Neutrons and Muons, PSI*; Florian Piegsa, *Physics Department, Technical University Munich and PSI*; Juan-Pablo Urrego-Blanco, *Department of Physics and Astronomy, Univ. of Tennessee and PSI*

The methods of dynamically polarizing nuclei (DNP) have not only lead to the development of increasingly sophisticated polarized targets with which the role of spin in nuclear and particle interactions is investigated, but have also opened new possibilities in neutron science by exploiting the strong spin dependence of neutron scattering. Very recently NMR and MRI have been a driving force behind a surge of interest in DNP methods, as it has tremendous potential for sensitivity enhancement. The following is an overview of current projects with dynamically polarized nuclei.

A high nuclear spin polarization can be achieved in solid samples with various schemes, the simplest being the brute force method of high magnetic fields and millikelvin sample temperatures. Methods of dynamic nuclear polarization (DNP) [1], which can be applied to samples containing a small concentration of spatially immobile unpaired electrons (e.g. paramagnetic centres), in addition to the nuclear spins of interest, are advantageous due to their moderate experimental requirements. After irradiation with microwaves of frequency close to the electron paramagnetic resonance frequency, the polarization of the electron spin system, which at typical experimental DNP conditions of $T = 1$ K and $B \geq 2.5$ T is close to unity, can be transferred to the nearby nuclei, taking advantage of the dipolar interaction between the electrons and the nuclear spins. Proton polarizations close to unity can be achieved in certain substances.

Time-resolved polarized SANS

An interesting field of research using methods of DNP is opened by the spin dependence of neutron scattering. It is particularly strong for ^1H and thus concerns primarily soft matter. Low resolution measurements, as SANS, can benefit from polarized nuclei by selectively changing the contrasts, i.e. the scattering length density profiles. A recent technique combining time-resolved polarized SANS with DNP, tries to make use of the fact that the polarization of the sample proceeds in two steps. Firstly, the nuclei close to the paramagnetic centres are polarized and secondly, spin diffusion spreads it out to the bulk nuclei. Thus, in the first moments upon ap-

plication of the microwaves, polarized proton domains are created around the paramagnetic centres. They can be observed by SANS for short times compared to the spin diffusion, typically a few seconds. Such polarization domains can enhance considerably the scattering amplitude off free radicals and thus contribute to the determination of their positions inside a complex molecule. In a detailed study of the microscopic mechanisms of DNP by applying these techniques to model systems, we have shown that strong polarization gradients actually exist for a short time until spin diffusion equalises the polarization throughout the sample [2]. Both the possible use and the limitations of this method as a spectroscopic tool depends on the difference between the polarizing speed and the speed of spin diffusion.

Broad-band spin filters

Current techniques of neutron polarization analysis are based on neutron optical mirror reflection, and are systematically restricted in precision. Polarized nuclei are clearly a better way to provide broadband spin filters with a large acceptance. Optically polarized ^3He is often considered the best choice, however its energy-dependent absorption cross-section makes it impossible to optimise the filter thickness in a large range. A spin filter based on polarized protons does not have this drawback and as an example application, the polarization of the SANS I neutron beam has been determined to high precision for a broad wavelength spectrum with a polarized proton target.

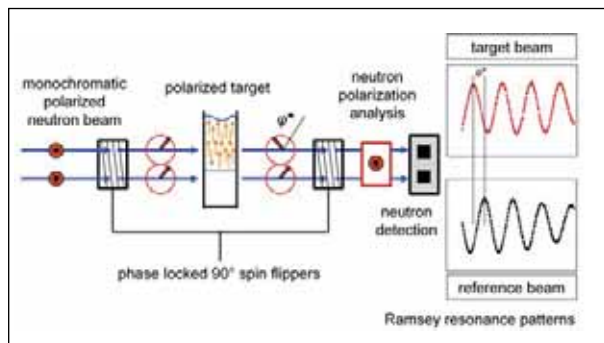


Figure 1: **Scheme of the Ramsey resonance apparatus as set up at FUNSPIN at SINQ.** The spins of monochromatic polarized cold neutrons are rotated by 90° in a first high frequency spin flipper and start to precess in a magnetic field perpendicular to the drawing plane. The spins of the neutrons passing the polarized target accumulate an additional precession angle φ^* compared to the ones in a reference beam passing below the target. The neutron spins are flipped back in a second phase locked spin flipper and a polarization analysis is performed with a supermirror polariser. The so called Ramsey resonance pattern is then obtained by measuring the neutron count rate in the detectors as a function of the frequency of the flippers.

Fundamental physics

In a classical field of use of polarized nuclei, an ambitious experiment is presently running which aims to precisely determine the poorly known spin-dependent doublet neutron-deuteron scattering length. This is a low energy parameter which is particularly well suited to fix three-body forces in novel effective field theories [3]. The understanding of such few-nucleon systems at low energies is essential, e.g. for accurate predictions of element abundances in big-bang and stellar fusion. The incoherent neutron scattering length $a_{i,d}$ will be determined directly using the phenomenon of pseudomagnetic precession. The spin of neutrons passing through a polarized target precesses around the axis of nuclear polarization with the precession angle being proportional to the polarization, the concentration and the incoherent scattering length a_i of the nuclear species present in the sample. The angle can be measured very accurately using Ramsey's atomic beam technique, adapted to neutrons [1]. A Ramsey apparatus (see Figure 1) has been optimised in order to reach the accuracy of 5×10^{-4} in precession angle measurement. A frozen spin type polarized target specially adapted for the use on a cold neutron beam, was constructed. To avoid the beam having to pass through the strongly absorbing ^3He , the target is contained in a separate cell filled with ^4He and is cooled by the mixing chamber of the dilution refrigerator via a sintered silver heat exchanger. In this device the polarizations of the proton and deuteron nuclei in the sample can be frozen at temperatures below 100 mK. First physics results from the experiment are expected at the end of 2006.

Increasing the sensitivity of NMR

Modern medicine, biology and chemistry would be unthinkable without the two main applications of NMR: spectroscopy and imaging. However, despite significant technological advancements (increasing field strength, open geometry), the sensitivity of NMR is fundamentally limited due to the low magnetic energy of nuclear spins compared with the thermal energy at room temperature. Considering that at the largest field strength available today for high resolution NMR (21 T) the polarization of the nucleus with the largest magnetic moment, ^1H , amounts to only 70 ppm, the potential gains obtainable by enhancing nuclear polarizations ($\sim 10,000$) becomes obvious. This prospect has triggered the investigation of several methods for enhancing nuclear polarizations, of which DNP is most promising. A project just started, bringing together the knowledge of DNP and NMR, aims to optimise classical DNP methods as applied to ^{13}C NMR spectroscopy in vitro and in vivo, especially in the field of intermediary metabolism [4].

Photo-excited triplet states

Creating nuclear polarization in solids is not restricted to the classical schemes and some more recent DNP methods are gaining interest. It was shown that it is possible to use photo-excited triplet states for DNP instead of radicals as source of the electron polarization with the same efficiency as classical DNP [5]. The beauty of a triplet experiment is that neither high fields nor very low temperatures are required, because the electron spin polarization of the triplet states is determined optically and not thermally, and a DNP scheme, known as integrated solid effect (ISE) can be used at moderate fields. A polarized target based on this approach has the potential to become the ideal solution for many nuclear and particle physics experiments. As a polarization analysis tool it could, in certain cases, be advantageous to the established methods. The necessary further studies are in progress. [4].

References

- [1] A. Abragam, M. Goldman, *Nuclear Magnetism: Order and Disorder*. Clarendon Press, Oxford, 1982.
- [2] B. van den Brandt, et al., *Europhys. Lett.* 59 (2002) 62; *Nucl. Instr. Meth. A* 526 (2004) 81; *Eur. Phys. J. B* 49 (2006) 157
- [3] B. van den Brandt, H. Glättli, H. Griesshammer, P. Hautle, J. Kohlbrecher, J. A. Konter, O. Zimmer, *Nucl. Instr. Meth. A* 526 (2004) 91; PSI Proposal R-03-01.1
- [4] J. van der Klink, B. van den Brandt, R. Gruetter, G. Bodenhausen, SNF Project 109479, 2005.
- [5] A. Henstra, P. Dirksen, J. Schmidt, W. Th. Wenckebach, *Chem. Phys. Lett.* 1990; 165: 6-10

Low temperature magneto-ferroelectrics

Severian Gvasaliya, Lukas Keller, Michel Kenzelmann, Bertrand Roessli, Juerg Schefer, Kazimierz Conder, Ekaterina Pomjakushina, *PSI, ETH Zurich*; M. Janoschek, *TU München*; Brooks Harris, *University of Pennsylvania*; S. Jonas, Collin Broholm, *John Hopkins University, USA*; Owen Vajk, Jeff W. Lynn, *NIST Gaithersburg*; S. B. Kim, C.L. Zhang, Sang-Wook Cheong, *Rutgers University, USA*

The coexistence of magnetism and ferroelectricity enables new applications such as magneto-electric sensors and electric generators, since magnetic properties can be controlled by an electric field or vice versa. TbMnO_3 and YMnO_3 represent two of the few examples where anti-ferromagnetism and ferroelectricity can be simultaneously observed. Neutron scattering is an efficient method for studying both magnetic and structural ordering, as a function of external parameters such as low temperature, pressure or magnetic field.

Magneto-electric applications depend on a strong coupling between the magnetic and ferroelectric order parameters. Recently, much progress has been made towards such applications with the discovery of a range of transition metal oxides that display strong magneto-electric effects [1].

The coupling of the magnetic and electric order parameters in these materials is not understood and there is currently increasing interest to understand these appealing properties. We applied neutron scattering methods on two model systems, the hexagonal YMnO_3 and the orthorhombic TbMnO_3 , to determine the symmetry and dynamics of their magnetism.

Magnetic inversion symmetry breaking

Orthorhombic TbMnO_3 is an insulating anti-ferromagnet in which competing interactions between the Mn^{3+} ions are suspected to be important for the ground state properties, and may make the material particularly sensitive to a coupling to the chemical lattice. The application of magnetic fields of only a few Tesla can switch the direction of the electric polarization [2] – proof of a strong direct coupling between the magnetic and electric polarization.

TbMnO_3 adopts long-range incommensurate magnetic order below $T_N = 41\text{K}$, and goes through a second magnetic transition at 28K into a second incommensurate phase. At 28K , there is also a sharp peak in the temperature dependence of the dielectric constant. Ferroelectricity is only observed below 28K .

Our neutron diffraction single crystal investigations show that the paraelectric, magnetically incommensurate phase has a sinusoidally-modulated collinear magnetic order (Fig.1a) that

does not break inversion symmetry; the moments all point along the b-axis. The ferroelectric phase, however, has a non-collinear incommensurate magnetic order described by two irreducible representations, which explicitly breaks inversion

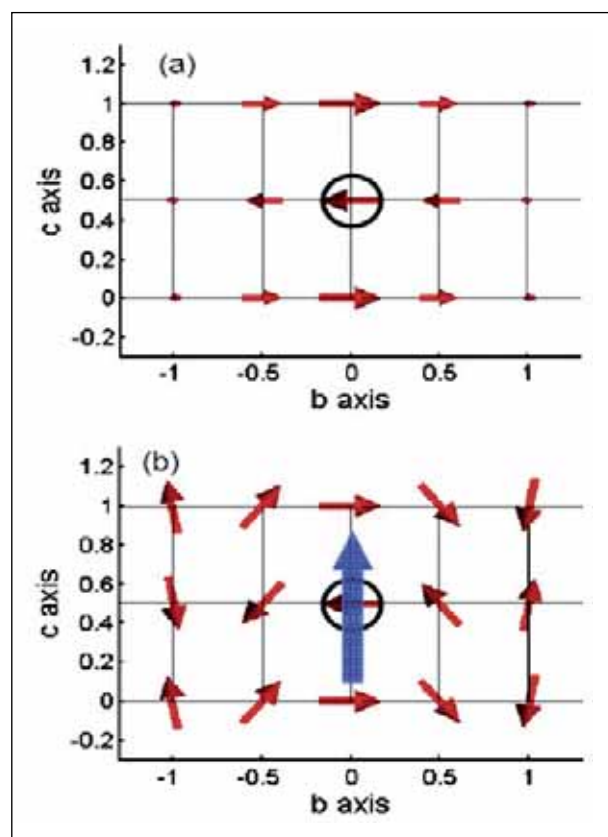


Figure 1: **Magnetic structure of TbMnO_3 at 35K (a) and at 15K (b) determined on TriCS/SINQ. While inversion symmetry is preserved in the longitudinally modulated structure at 35K, it is broken by the spiral structure at 15K, allowing an electric polarization to develop (blue vertical arrow).**

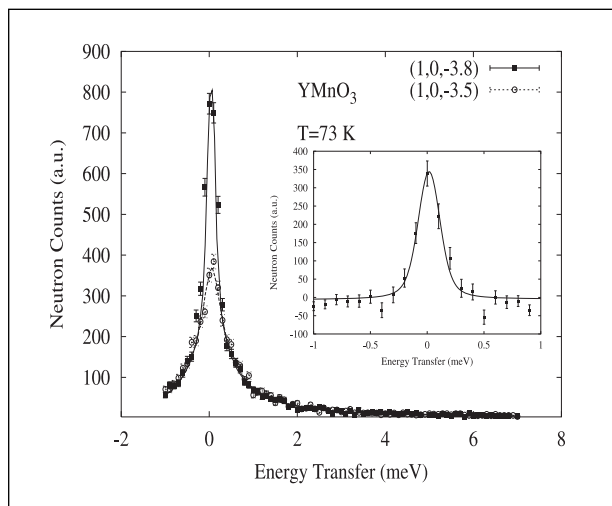


Figure 2: **Inelastic scan through diffuse scattering that shows the presence of the central peak in YMnO_3 . The insert shows the difference between scans measured at $(1, 0, -3.8)$ and $(1, 0, -3.5)$.**

symmetry (Fig. 1b) and thus gives rise to electric polarization: hence ferroelectricity and magnetism can coexist.

A Landau theory describing the tri-linear coupling between the two magnetic and the electric order parameter predicts that the ferroelectric polarization has to point along the c -axis, as observed in the experiment. Detailed results are published by Kenzelmann et al. [3]

Stacked-triangular anti-ferromagnet

Another promising candidate of this family is YMnO_3 which crystallizes in the hexagonal space group $P6_3cm$ below the paraelectric–ferroelectric phase transition (~ 900 K). In YMnO_3 , the Mn^{3+} ions form triangular layers well separated from each other by Y layers. Because the lattice is distorted in the ferroelectric phase, the Mn ions are slightly trimerized. The large separation between adjacent layers suggests that YMnO_3 forms a good candidate for a geometrically frustrated 2-dimensional (2D) anti-ferromagnet. The value of the critical exponent $\beta = 0.187$ is found to be close to the case of the 3D triangular Ising anti-ferromagnet [4]. In addition, two components in the spectrum of the fluctuations in YMnO_3 were observed close to T_N (see Fig.2), that correspond to two different time-scales [4]. This might be the signature for the coexistence of 2D and 3D fluctuations near T_N . Using polarized neutrons on TASP it was possible to separate in-plane and out-of-plane fluctuations in the paramagnetic phase of YMnO_3 .

The correlation length associated with the in-plane fluctuation diverges at T_N [4]. High-pressure powder diffraction study of YMnO_3 [5] complemented the above described single-crystal experiments. It was observed that the saturated ordered

magnetic moment in YMnO_3 is significantly reduced by application of pressure, while T_N is only marginally affected (Fig. 3). This may be attributed to the influence of the strain on the sub-lattice magnetization or/and to the enhancement of the 2D character of the magnetic properties of YMnO_3 [5].

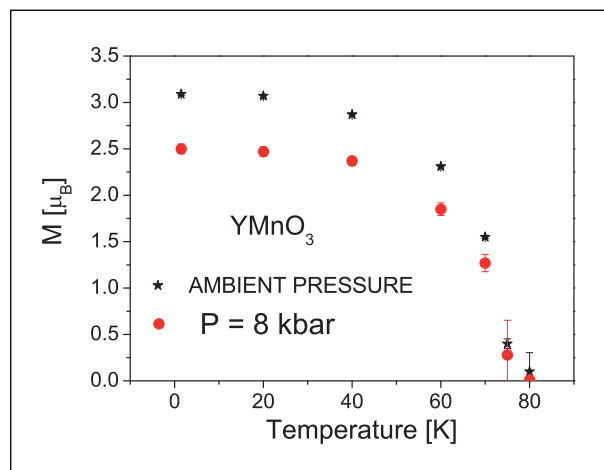


Figure 3: **Temperature dependence of the magnitude of the Mn magnetic moments for ambient pressure and for $P \sim 8$ kbar in YMnO_3 determined on DMC.**

Summary

In discussing some of the properties of two model magneto-ferroelectrics we would emphasize the value of neutron scattering as a tool to study the phenomena of long and short-range order, particularly in these rather complicated cases where different types of order coexist in a broad temperature range. In TbMnO_3 , lowering the temperature yields a symmetry breaking of the magnetic structure allowing ferroelectricity to develop. In YMnO_3 , increased pressure reduces the ordered magnetic moment at saturation significantly, while T_N is only marginally affected.

References

- [1] C. Ederer and N.A. Spaldin, *Nature* 3, 849 (2003), N. Hur et al., *Nature* 429, 392 (2004), Th. Lottermoser et al, *Nature* 430, 541 (2004)
- [2] T. Kimura et al., *Nature* 426, 55 (2003)
- [3] M. Kenzelmann et al. *Phys. Rev. Lett.* 95, 087206 (2005)
- [4] B. Roessli et al., *JETP Letters* 81 (2005) 287
- [5] M. Janoschek et al., *J. Phys.: Condens. Matter* 17, L425 (2005)

Does water always behave like water? Influence of the host medium on water in confinement

Fanni Jurányi, *Department Condensed Matter Research with Neutrons and Muons, PSI*; F. González, T. Gimmi, *Physical Chemistry, Saarland University, Germany*; Luc Van Loon, *Research Department Nuclear Energy and Safety, PSI*

Water in geometrical confinement or in contact with surfaces behaves differently from bulk water. As water is present almost everywhere in our life – often not in bulk state – it is crucial to understand the effect of a confining medium. At PSI, a research group in the Waste Management Laboratory is investigating clays, which have the potential to be used in barriers around radioactive waste repositories. Water located in the layered structure of clays plays an important role as a transport medium for radionuclides through the barrier. As we will show, neutrons can answer several questions about structure and dynamics, which is helpful for the understanding of the behaviour of the clay barriers.

Clays around waste repositories

Radioactive waste arises from the operation and decommissioning of nuclear power plants, from the fuel cycle of the power plants and from medicine, industry and research. Nowadays this waste is stored in interim storage facilities, but it is our responsibility to find a safe solution for the long term, (up to one million years). In Switzerland, there is a plan to dispose of radioactive waste in a deep geological repository. The safety of such a repository is assured by the interplay between the different barriers that surround a repository [1]. One of the barriers placed around a repository is made of bentonite, a natural clay consisting mostly of montmorillonite.

Clays belong to the so-called phyllosilicates and are built up from platelets which have a disc like shape, some micrometers

in diameter, and several nanometers thick. Platelets consist of several layers, which are stacked together directly or via interlayer cations and interlayer water, depending on the type of clay mineral (Fig. 1). The pore water in clays may be located between the layers (internal water) as well as between the platelets (external water) [2].

Water is the transport medium in which radionuclides can move in the clay. Its properties are influenced by geometrical constraints, by the cations in the clay, and by surface interactions [3]. Since understanding the movement of radionuclides in clay also requires the understanding of water dynamics in clay, we have started to investigate how different interactions affect, in particular, the water diffusion, but also other properties of water.

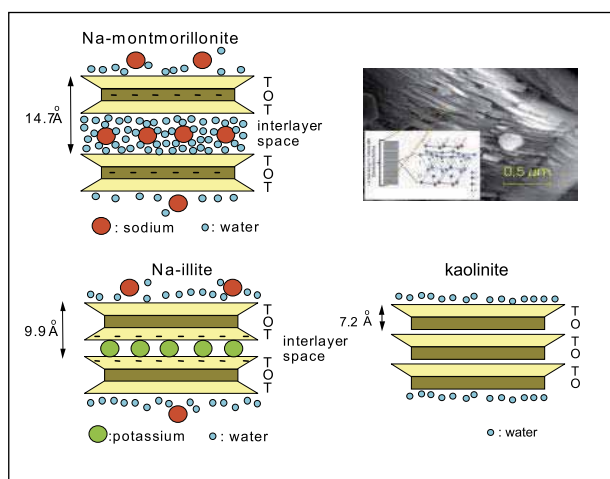


Figure 1: **Structure of clays and location of external and internal pore water.**

Neutron scattering

Neutron scattering techniques are able to provide insight into both the structure and dynamics of condensed matter at the atomic level. Neutrons interact very strongly with hydrogen and therefore also with water which makes them ideal for our research.

Water and ice in confinement

The freezing temperature is a characteristic property of a liquid. It may change due to confinement, therefore giving us feedback on the interactions of water with clay. Neutrons scatter on “static” atoms without energy exchange (elasti-

cally). It means that the intensity of the elastically scattered neutrons increases strongly, when the material freezes, i.e. when atoms become “static”. Figure 2 shows the intensity of the elastically scattered neutrons as a function of temperature for different types of compacted clay minerals. Water in kaolinite and pyrophyllite has a well defined freezing temperature, like bulk water, however it can be under-cooled (freezing lower than 0 °C) due to confinement. Other clays show a stronger influence, there is no longer a single freezing point, but instead a freezing temperature range.

Neutrons can also tell something about the structure of water or ice. Bulk water shows no periodicity over long distances, but for example in a mixture with cement, water shows long-range order [4]. This can be explained by the strong interaction between the internal water-cement surfaces. This was not observed for the clay structures we investigated so far (kaolinite and pyrophyllite). Furthermore, the structure of the ice in these clays has hexagonal symmetry, the same as for bulk water frozen under normal conditions (measurements on the diffractometer HRPT, PSI).

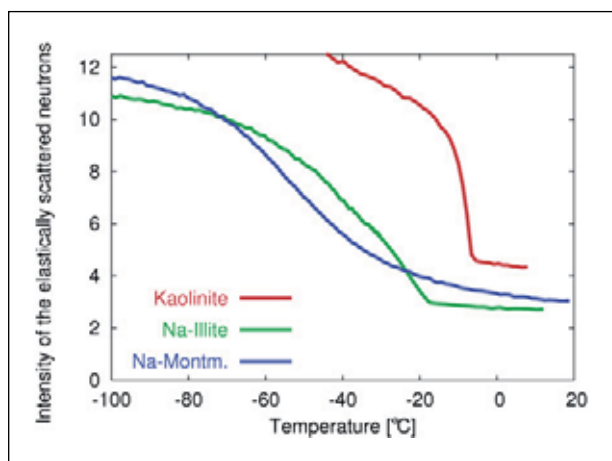


Figure 2: Freezing of confined water (IN16, ILL) for some of the investigated clays.

Diffusion of water in confinement

Water in clay is moving and therefore a neutron scattered on a water molecule may lose or gain energy, and also momentum, like in a classical collision of two hard spheres. A typical spectrum is shown in Figure 3. Such a spectrum can be analysed with different models, to see how the diffusion process takes place at the microscopic level. A water molecule typically rotates around the centre of the molecule, and also performs translational motion. Rotation is a localized motion; therefore it is in general not affected by the confinement. However the translational motion may slow down or even speed up due to the interaction with the surroundings. Diffu-

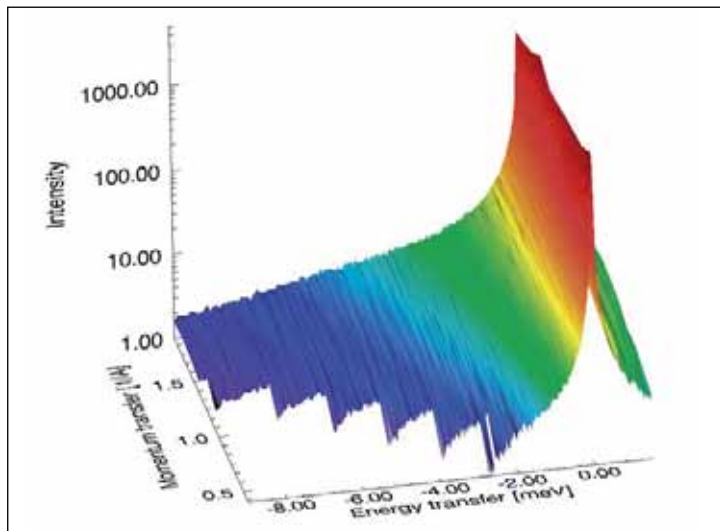


Figure 3: Typical neutron intensity as a function of energy and momentum transfer in the case of diffusive motion (FOCUS spectrometer, PSI).

sion of water confined in uncharged clays such as kaolinite was only slightly affected according to our measurements. Confinement in charged clays, however, results in a slowing down of the diffusive motion of the water molecules.

What did we learn?

Both the measurements on the freezing behaviour of water and on the dynamics show a consistent picture and indicate that water confined in uncharged clays such as kaolinite and pyrophyllite possesses mainly bulk water properties. In contrast, water in charged clays such as montmorillonite and illite shows properties (e.g. diffusion coefficients) different from those of bulk water. Knowing these properties helps to interpret the results of macroscopic transport experiments that are performed to assess the barrier function of clays; a function relevant for waste repositories.

References

- [1] www.nagra.ch;
- [2] K. B. Krauskopf: Introduction to Geochemistry. Mc Graw-Hill (1979)
- [3] R. Bergman, J. Swenson: Nature 403 (2000) 283-286; proceedings of the international workshops on dynamics in confinement: http://www.ill.fr/YellwBook/IN6/confit2006/confit_2006.html
- [4] M. P. Fang et al.: J. Porous Materials 6 (1999) 95-99

Footprints of plastic deformation

Helena Van Swygenhoven, Peter M. Derlet, Steven Van Petegem, Uwe Stuhr, Zeljka Budrovic, Stefan Brandstetter, *Condensed Matter Research with Neutrons and Muons, PSI*; Bernd Schmitt, *Synchrotron Radiation and Nanotechnology, PSI*

The neutron source (SINQ) and synchrotron light source (SLS) at PSI are excellent tools for investigating the structural and mechanical behaviour of materials. Experiments performed at the materials science beamline MS4 of the SLS and at the pulse overlap time-of-flight diffractometer (POLDI) of SINQ allowed us to shed light on the deformation mechanism in materials. We investigated materials in the sub-micron or nanometer range, and by doing so, contributed to the body of research in size-dependent plasticity.

Materials deformation mechanism

The desire to develop materials where strength and functionality are combined, has driven materials research into the development of microstructures that are characterized by length scales typically in the sub-micron range or even in the nanometer range. Examples are nanocrystalline (nc) metals with nanosized grains, multilayered structures with each layer being a few nanometers thick or composite materials with submicron-sized inclusions. Much to materials scientist's surprises, size effects in mechanical behaviour were evidenced, and deformation properties can not be understood by simply extrapolating our knowledge from conventional plasticity laws. The research field has benefited a lot from large scale atomistic computer simulations. Experimental verification requires new and appropriate measurement techniques, allowing the measurement of mechanical behaviour, at the same time providing information on structural characteristics, i.e. so-called in-situ mechanical testing techniques. Such an approach has been recently developed at the SINQ as well at the SLS.

Nanocrystalline metals

With a reduction of the grain size to the nanometer scale and a corresponding increase in the fraction of grain boundary atoms, the traditional view of dislocation driven plasticity in polycrystalline metals needs to be reconsidered, since the limited size offered by nanograins does not allow the operation of conventional dislocation sources. Large scale molecular dynamics computer simulations suggest that grain boundaries (GBs) can act as source and sink for dislocations in nc metals,

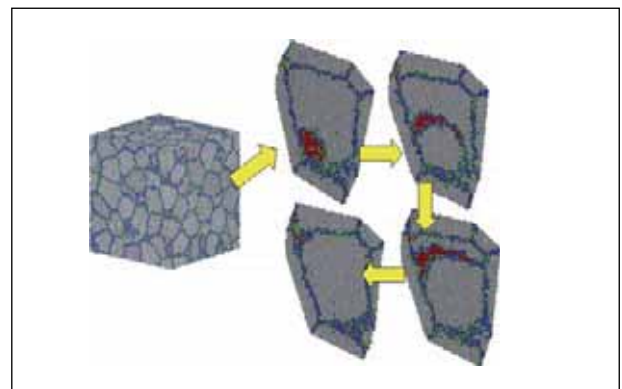


Figure 1: **Computer simulated nanocrystalline Ni sample, and enlarged view of a dislocation travelling through a grain (gray=fcc atoms in grain interior, red=hcp part of dislocation, green and blue resp. other-12 and non-12 coordinated atoms).**

a mechanism where each dislocation is absorbed in opposite grain boundaries after having propagated through the grain, in other words, leaving no footprint in the grain interior [1]. Figure 1 shows a computational nc-Ni sample and enlarged view of a dislocation travelling through a grain.

The existence of such a mechanism has been verified by in-situ X-ray diffraction measurements performed at MS4, where a miniaturized tensile machine is mounted on the goniometer, as shown in Figure 2. By following the peak width during deformation it has been demonstrated that broadening due to the presence of inhomogeneous strain is totally recoverable upon unloading at room temperature [2,3]. When performing the same experiment at lower temperatures peak broadening is unrecoverable. Warming up the sample to room temperatures allows again complete recovery [4]. Such behaviour is entirely compatible with the dislocation mechanism suggested by simulations.

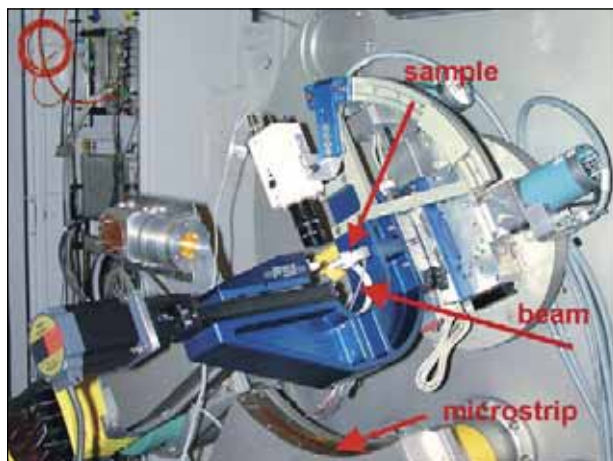


Figure 2: **Miniaturized tensile machine for in-situ measurements at the SLS.**

Another important microstructural aspect influencing deformation behaviour is the presence of texture, and this parallel as well as perpendicular to the tensile direction, an issue that is successfully addressed by combining light and neutron scattering experiments. The latter have the advantage of providing information on the entire sample volume.

Nanocomposites

Another example of a material where size effects play a key role in the mechanical behaviour is nano-filamentary copper/niobium (Cu/Nb) wires, envisaged for possible application as winding material in resistive magnetic cores, where besides functionality the mechanical properties are also extremely important. Figure 3 shows a cross-section of a Cu/Nb wire, consisting of Nb nanofilaments embedded in an assembly of multi-scale Cu channels.

In-situ deformation under neutron beam allowed evidencing size dependent strengthening in the Cu components where

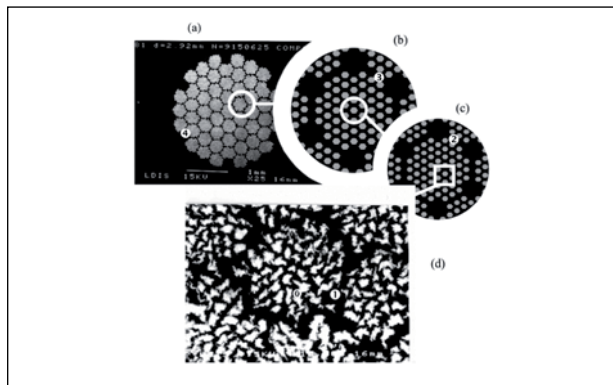


Figure 3: **Cross-sections of nano-filamentary Cu/Nb wires. Nb filaments appear in white on highly magnified SEM micrograph (d) (conductor with $d_{Nb}=524\text{nm}$ and $d_{Cu-0}=89\text{nm}$).**

load sharing between Cu and Nb starts only at the yield strength of the smaller Cu component. Upon initial loading, both the Cu and Nb phases are deforming elastically until the largest Cu channels yield. At that stage, the finest Cu channels are still in the elastic regime as well as the Nb nanofilaments. Once the whole Cu matrix is in the plastic regime, a strong load transfer is observed onto the Nb fibers. This feature can be attributed to the impenetrable character of fcc/bcc interfaces. During further loading the Nb filaments continue to deform elastically up to macroscopic fracture, confirming their whisker-like behaviour.

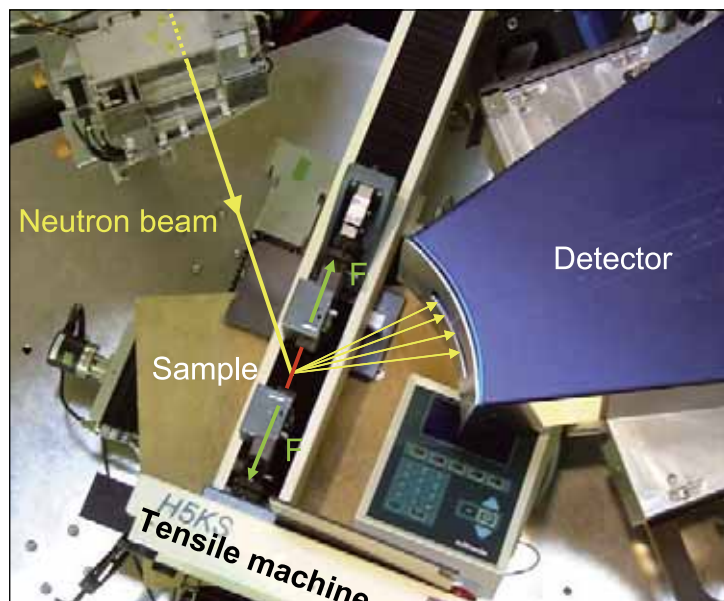


Figure 4: **Set-up of the in-situ tensile test at POLDI for diffraction at planes perpendicular to the tensile axis.**

Research in size dependent plasticity using atomistic computer simulations implemented on the large parallel computing platforms available in Switzerland and using in-situ mechanical testing with neutrons and light, is supported by the Swiss National Science Foundation and the 6th EU Framework programme.

References

- [1] H. Van Swygenhoven et al., *Nature Mater* 3, 399 (2004)
- [2] Z. Budrovic et al., *Science* 304, 273 (2004)
- [3] Z. Budrovic et al., *App. Phys. Lett.* 86, 231910 (2005)
- [4] S. Brandstetter et al., *App. Phys. Lett.* 85, 132910 (2005)
- [5] L. Thilly, V. Vidal and F. Lecouturier, Université de Poitiers, France

The ultracold neutron source at PSI

F. Atchison, A. Baechli, M. Baumann, B. Blau, H. Blumer, B. van den Brandt, T. Brys, F. Chapuis, M. Daum, R. Doelling, K. Dreyer, P.-A. Duperrex, U. Ellenberger, P. Fierlinger, A. Fuchs, D. George, E. Gisler, W. Gloor, P. Hautle, G. Heidenreich, F. Heinrich, R. Henneck, S. Heule, Th. Hofmann, M. Horvat, F. Jenni, St. Joray, R. Kaech, M. Kasprzak, K. Kirch, S. Kistryn, K. Kohlik, J. Kohout, J. A. Konter, M. Kuzniak, A. Magiera, Ch. Perret, A. Pichlmaier, R. Reiser, U. Rohrer, S. Teichmann, M. Wohlmuther, S. Zelenika, G. Zsigmond, J. Zuellig, *PSI*; K. Bodek, *Krakow*; P. Geltenbort, *ILL*; S. Grigoriev, *Efremov*; J. Zmeskal, *SMI*

A new type of ultracold neutron source based on the spallation process is under construction at PSI. The essential elements of this source are a pulsed proton beam with a highest intensity of ($I_p > 2\text{mA}$) and a low duty cycle ($\sim 1\%$), a Lead spallation target, a large D_2O moderator and a solid D_2 ($s\text{D}_2$) converter system. Spallation neutrons are thermalized in the D_2O , further cooled in the $s\text{D}_2$ and, finally, some of them are down-scattered into the ultra-cold neutron range ($T_{\text{kin}} < 250\text{ neV}$). The expected UCN density in the new source is $3000\text{ UCN}/\text{cm}^3$, almost two orders of magnitude higher than with the best source currently available (at ILL).

In 2005, the Ultracold Neutron (UCN) project at PSI has made big steps towards the realization of the source. The safety report has been reviewed by the Federal Office of Public Health

(FOPH). No major concerns were reported by the Swiss authorities. In total, 30 licensing requirements were requested, the fulfilment of which is within the normal development of the project.

An important milestone was the start of the civil engineering in August 2005. In the first phase, the foundation for the large source tank, see Figure 1, was built using steel beams from stock; the thickness of this steel layer is $\sim 1.5\text{m}$ in order to prevent the soil below it from being activated. In total, about 300 tons of steel was installed.

Impressive civil engineering

The concrete shielding walls have been built around the experimental area, and the civil engineering for the infrastructure has started; for example the pumping station for the heavy-water moderator circuit, the room for the storage and leakage tanks for the heavy water circuit, etc. Finally, housing for the air conditioning was installed in a spectacular action shortly before the end of the year, see Figure 2. This housing also contains the roll-up door, which is required for crane access and the exchange of large components in the experimental area.

The construction of the deuterium system continues to make good progress. This system is contained in a helium blanket at 1.2bar in order to avoid any possible contamination of the gas, even in the case of leakage. Therefore, the pumps, valves

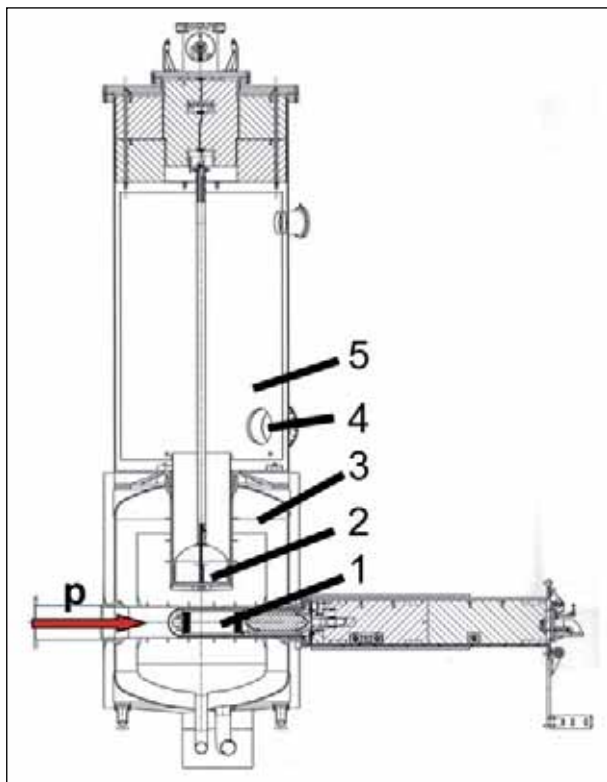


Figure 1: UCN source tank; p: proton beam; 1: neutron spallation target; 2: cold source (30dm^3 solid deuterium); 3: heavy water moderator; 4: neutron guide; 5: UCN storage volume.



Figure 2: **Positioning of the air conditioning housing on the roof of the experimental area.**

etc. are enclosed in boxes filled with helium. Many of the components for the gas circuit have been delivered, e.g. (i) the four gas reservoir tanks with an integral volume of 30m^3 , (ii) the valve box between the gas reservoirs and the collector box for filling and draining of the system, and (iii) the vacuum box with all the pumps and valves for the evacuation of the UCN tank, which contains the storage volume for UCN and the UCN extraction guides, items 4 and 5 in Figure 1. Other components such as the cryo-box for liquefying and para-to-ortho-conversion of the deuterium outside the source have been designed. Different components of this cryo-box have been tested successfully for pressure and overpressure performance.

For the liquefying and solidification of the deuterium in the source, item 2 in Figure 1, a closed-loop cooling cycle of supercritical helium has been designed. This component is required for safety considerations because of tritium production by spallation of the helium coolant near the neutron production target. The cold source containment has been designed and first pressure tests with a prototype are scheduled for early 2006.

The layout of the warm moderator containing the cooling circuit of the target and the heavy water moderator with about 4m^3 volume is in the design phase. A particularly important aspect is to find the most cost effective way of keeping the dose-rate to personnel within statutory limits. Solutions such as delay tanks require more heavy water, and local shielding causes access problems.

For the proton beamline, new “harp” monitors for the measurement of the intensity distribution in front of the spallation neutron target have been delivered. The corresponding electronics have been in operation, e.g. in the LISOR project, since 2002. The spallation neutron target, item 1 in Figure 1, has been developed in close collaboration with NUM and GFA. A “cannelloni” target based on lead enclosed in zircaloy cylinders such as is already in test at SINQ, has been designed. Calculations show that the design will withstand the rather higher mechanical loading during operation: while the beam inten-

sity at SINQ is increased to the full intensity in about 30 seconds, the beam for UCN is pulsed and switched instantly with full intensity onto the UCN target.

Results from source-related R&D experiments have been published in scientific journals [1-12]. A special highlight was the experimental demonstration that diamondlike Carbon has very similar UCN storage properties, (Fig. 3), compared to the more commonly used Beryllium, which is toxic and far more expensive.

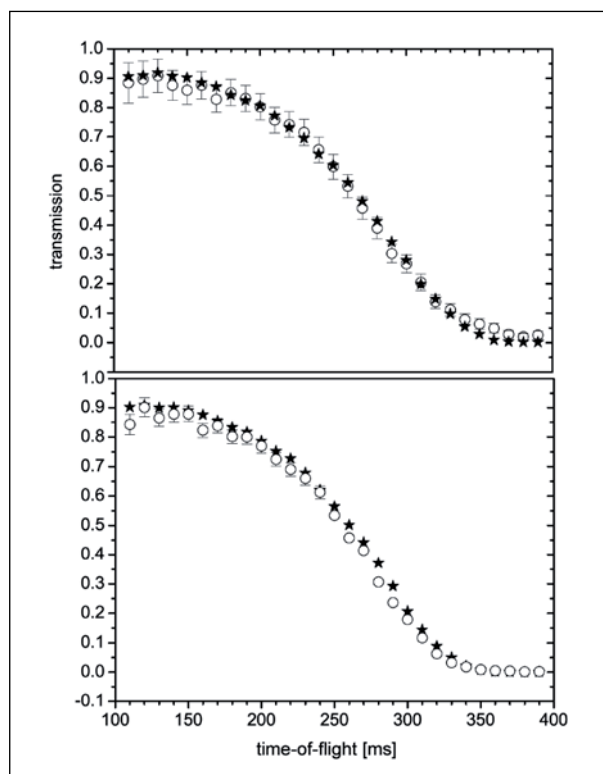


Figure 3: **Measured (open circles) and simulated (stars) data for the transmission of ultracold neutrons through material foils. Top: 150 nm DLC on 0.18mm Aluminium. Bottom: 200 nm Beryllium on a 0.525 mm Silicon wafer. The length of the flight path was 2270 mm. From the decrease in transmission, the critical velocities for both materials are found to be 6.9 m/s.**

References

- [1] F. Atchison et al., Phys. Rev. Lett. 95, 182502 (2005)
- [2] F. Atchison et al., Phys. Rev. Lett. 94, 212502 (2005)
- [3] F. Atchison et al., Phys. Lett. B 625, 19 (2005)
- [4] F. Atchison et al., Phys. Rev. C 71, 054601 (2005)
- [5] S. Groeger et al., Appl. Phys. B, 645 (2005)
- [6] T. Brys et al., NIM A 554, 527 (2005).
- [7] F. Atchison et al., NIM A 552, 513 (2005)
- [8] T. Brys et al., NIM A 551, 429 (2005)
- [9] T. Brys et al., NIM A 550, 637 (2005)
- [10] D. Anicic et al., NIM A 541, 598 (2005)
- [11] J. Zejma et al., NIM A 539, 622 (2005)
- [12] F. Atchison et al., NIM A 539, 646 (2005)

A new search for the neutron electric dipole moment

G. Ban, T. Lefort, O. Naviliat-Cuncic, G. Rogel, *LPC Caen*; K. Bodek, S. Kistryn, J. Zejma, *JUC Cracow*; N. Khomutov, B. M. Sabirov, *JINR Dubna*; P. Knowles, M. Rebetez, A. Weis, *University of Fribourg*; C. Plonka, *ILL Grenoble*; G. Quemener, D. Rebreyend, M. Tur, *LPSC Grenoble*; M. Daum, P. Fierlinger, S. Groeger, R. Henneck, S. Heule, M. Kasprzak, K. Kirch, M. Kuźniak, A. Pichlmaier, *PSI*

If time reversal symmetry holds, then particle electric dipole moments (EDMs) will be zero. However, strong theoretical arguments suggest that they may not be zero after all and may be intimately connected to an explanation of the matter-antimatter asymmetry of the universe. The best upper limit for the neutron EDM is still orders of magnitude higher than the Standard Model expectation. Improved experimental sensitivity requires a better control of systematic effects and increased statistics, which will be available at the new PSI ultracold neutron source. The first issue is being studied using and upgrading the existing Sussex/RAL/ILL EDM apparatus at ILL.

Many particle properties and processes are symmetric under reflections in space, P , and in time, T , and when exchanging particles with anti-particles, C . Purcell and Ramsey first pointed out [1] that, although based on “suggestive theoretical symmetry arguments”, the general assumption that “nuclei and elementary particles can have no electric dipole moment” should be experimentally tested. Electric dipole moments (EDM) would violate both, P and T . With the discovery of P -violation in the weak interaction [2, 3] questioning T -symmetry was a next step [4] but very speculative, until the discovery of CP -violation [5]. Invariance under the combined transformation, CPT , is supported by the rather general CPT -theorem [6], thus CP -violation also implies T -violation and connects EDM to CP -violation. Sakharov [7] showed that the observed baryon asymmetry of the universe (BAU), i.e. the dominance of matter over antimatter, can only be explained with, among other things, CP -violation.

CP-violation and baryon asymmetry

The CP -violation [5] is well integrated in the Standard Model (SM) of particle physics, but seems insufficient to explain the BAU. It can thus be expected that additional (non-SM) sources of CP -violation will be identified at some point and the neutron EDM is one of the most sensitive places to look for it. The present best upper limit on the EDM value, 3×10^{-26} e cm [8], is still about 6 orders of magnitude from the electro-weak SM-expectation [9] but considerably constrains theories beyond the SM, see e.g. [9,10].

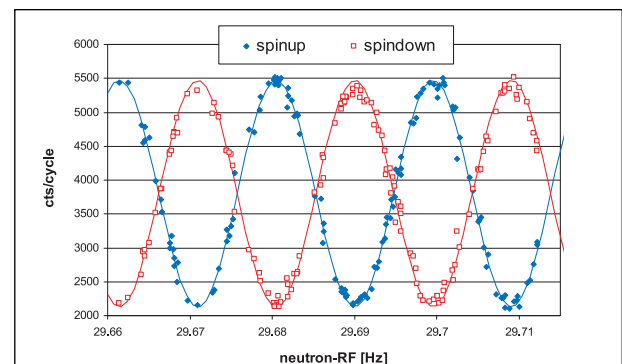


Figure 1: **Central Ramsey fringes obtained for 50s precession time: counts per measurement cycle as a function of the applied spin flip frequency after correction using the (unstabilized) HgM.**

The EDM limit [8] was obtained in an experiment at the Institute Laue-Langevin (ILL). Ramsey’s basic idea is to prepare polarized neutrons, bring them into a region with collinear magnetic and electric B - and E -fields, apply a $\pi/2$ spin flip, have a free spin precession period, apply another spin flip and analyze the polarization. This method of separated oscillatory fields [11] results in an interference pattern, “Ramsey fringes”, and is more sensitive the longer the free precession is.

Neutron EDM experiment

Using ultracold neutrons (UCN) allows storage and precession times exceeding 100s. A finite EDM would shift the position of the fringes, i.e. the precession frequency, with the E -field parallel to the B -field compared to the reversed configuration.

Stability of the B-field while reversing the E-field is crucial. The EDM limits have been pushed down over the decades, by improving sensitivity and suppressing systematic effects. Further reduction of the statistical uncertainties requires higher UCN densities. The dominant systematic effects are the B-field homogeneity and stability and, in particular, B-field gradients [12, 13]. The most significant step in [8] was the implementation of a Hg co-magnetometer (HgM) [14] occupying the same volume as the UCN and measuring the B-field simultaneously with almost the same spatial average. The co-magnetometer allows off-line corrections of the UCN data for field drifts. Our collaboration makes use of this apparatus [8] at ILL. In 2005, we put the equipment back into operation and were able to measure Ramsey fringes (Fig. 1). The B-field homogeneity had not been tuned, explaining the sub-optimal visibility of the curve, and no E-field was applied. One major improvement for the future EDM experiment should come from using an array of laser pumped Cs-magnetometers (CsM) [15, 16] inside the magnetic shield. Figure 2 shows a prototype array of 8 CsM mounted around the UCN volume and the HV-electrodes.

Data from inside (HgM) and outside (CsM) the UCN chamber were measured simultaneously and digitized with the same system [17]. The much faster CsM can be used to stabilize the B-field magnitude and gradients in feedback loops. The potential for this is seen in Figure 3, which displays two time series of the HgM frequency determined for the 180s free precession period of successive measurement cycles (223s each). The series were measured during separate nights, and each represents about 8h of data, the bottom (top) trace with (without) a prototype B-field magnitude stabilization using CsM. The Allan variance of $10\mu\text{Hz}$ ($73\mu\text{Hz}$) for 180s integration



Figure 2: The inside of the EDM vacuum chamber showing the newly installed 8 CsM (black cylinders).

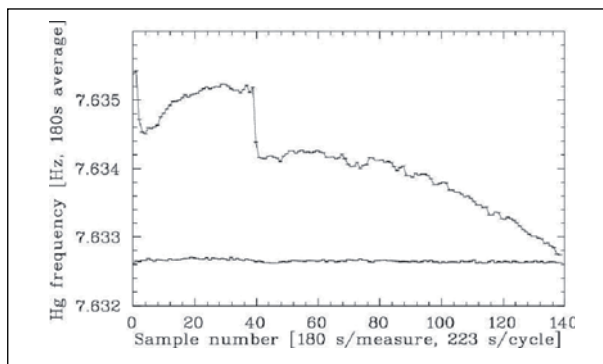


Figure 3: Time series of the HgM precession frequency under unstabilized (top trace) and CsM feedback-stabilized (bottom) conditions.

represents well the gain in system stability. The precision per point is $2\text{-}5\mu\text{Hz}$.

Other ongoing R&D is connected to “double resonance alignment” CsM [18], UCN detectors [19], new materials with high reflective potentials [20, 21] and HV-compatibility, and EDM related analytic and simulation [22] tasks. Our aim is to run a first EDM test measurement at ILL by the end of 2006; the UCN become available at PSI in 2008.

We gratefully acknowledge the support from various workshops, fruitful discussions with members of the Sussex-RAL-ILL EDM collaboration and for allowing us to use their apparatus.

References

- [1] E.M.Purcell and N.F.Ramsey, Phys. Rev. 78, 807 (1950)
- [2] C.S.Wu *et al.*, Phys. Rev. 105, 1413 (1957)
- [3] R.M. Garwin *et al.*, Phys. Rev. 105, 1415 (1957)
- [4] J.H.Smith *et al.*, Phys. Rev. 108, 120 (1957)
- [5] J.H. Christenson *et al.*, Phys. Rev. Lett. 13, 138 (1964)
- [6] G.Lüders, Dansk. Mat. Fys. Medd. 28, 17 (1954)
- [7] A.D.Sakharov, JETP Lett. 5, 24 (1967)
- [8] P.G.Harris *et al.*, Phys. Rev. Lett. 82, 904 (1999)
C.A. Baker *et al.*, hep-ex/0602020
- [9] X.-G.He *et al.*, Int. J. Mod. Phys. A 4, 5011 (1989)
- [10] M.Pospelov, A. Ritz, Ann. Phys. 318, 119 (2005)
- [11] N.F.Ramsey, Rev. Mod. Phys. 62, 541 (1990)
- [12] J.M.Pendlebury *et al.*, Phys. Rev. A 70, 032102 (2004)
- [13] S.K.Lamoreaux and R.Golub, Phys. Rev. A 71, 032104 (2005)
- [14] K.Green *et al.*, Nucl. Instr. Meth. A 404, 381 (1998)
- [15] S.Groeger *et al.*, Appl. Phys. B 80, 645 (2005)
- [16] S.Groeger *et al.*, J. Res. NIST 110, 179 (2005)
- [17] S. Groeger *et al.*, Eur. Phys. J. AP 33, 221 (2006)
- [18] S.Groeger *et al.*, submitted to Phys. Rev. A
- [19] G.Ban *et al.*, J. Res. NIST 110, 283 (2005)
- [20] F.Aitchison *et al.*, Phys. Lett. B625, 19 (2005)
- [21] T.Brys *et al.*, Diamond Rel. Mat., in press
- [22] F.Aitchison *et al.*, Nucl. Instr. Meth. A 551, 429 (2005)

First calculation of electroweak corrections for a process with 6 external particles, $e^+e^- \rightarrow 4$ fermions

Angsar Denner, Lars H. Wieders, *Research Department Particles and Matter, PSI*; Stefan Dittmaier, Marcus Roth, *Max Planck Institute, Germany*

Precision tests of the Standard Model of particle physics require, besides accurate measurements, precise calculations. Recently we obtained a breakthrough in the field of precision calculations for many-particle reactions. Using newly developed methods we evaluated the complete first-order electroweak corrections to charged-current 4-fermion production in electron-positron annihilation. This is, in particular, important to measure the mass of the W boson at a linear collider with a relative accuracy below 0.01 per cent. Our calculation was the first calculation of first-order corrections to a process with six external particles.

Much progress in our understanding of the fundamental laws of nature comes from experiments at high-energy colliders. In 2007, the Large Hadron Collider will start operation, and proposals for an electron-positron collider, the International Linear Collider (ILC), are being studied. Although the Standard Model of particle physics presently provides a good description of experiments, these colliders will allow further testing of the model and searching for physics beyond. While the primary focus of these tests will be the search for, and the investigation of, the Higgs boson, other parts of the Standard Model will also be tested with higher accuracy or at higher energies.

Testing the Standard Model

Precise tests of the Standard Model require, besides accurate experiments, precise theoretical predictions. As these are obtained in perturbation theory, higher orders have to be calculated in order to match the experimental precision. In turn, this permits testing the Standard Model as a Quantum Field Theory. Since future colliders allow studying processes involving many external particles, adequate predictions for such processes are required. The calculation of higher-order corrections to processes with four external particles has been routine for many years. In the last decade techniques for processes with five external particles have been developed and used to calculate perturbative corrections to processes both at hadron and lepton colliders. Processes with six external particles set the current technical frontier in this highly competitive field.

New methods

Last year we succeeded in establishing the first complete calculation of first-order corrections to a process with six external particles, i.e. the production of four fermions in electron-positron annihilation [1,2]. This required the development of various new techniques and concepts. Firstly, we introduced the complex-mass scheme for the treatment of unstable particles in higher orders of perturbation theory. In this scheme the masses of unstable particles are consistently treated as complex quantities. As a consequence perturbative calculations are straightforward, and gauge invariance is exactly conserved in this universal scheme. Secondly, in order

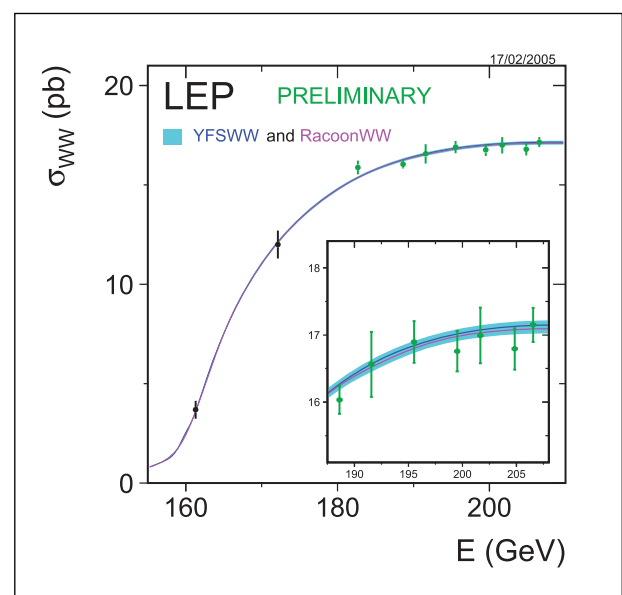


Figure 1: Total cross section for W-pair production at LEP2 [4].

to get numerically stable results in all parts of the complicated many-particle phase space, we have devised new methods for the calculation of appearing integrals.

To this end, we used appropriate expansions or numerical integration of suitable well-behaved master integrals in problematic regions of parameter space. These methods are independent of the considered process and applicable to arbitrary processes with six external particles and can be generalized to processes with more external particles. Finally, we developed techniques to simplify the spinor structure of the matrix elements. The constructed algorithms allow reducing the more than thousand appearing spinorial objects to only a few. These algorithms are applicable to similar processes with external massless fermions.

Physical motivation

We have chosen the process $e^+e^- \rightarrow 4$ fermions, because it can be studied with very high precision at the ILC. It contains W-pair production as dominant contribution and will allow the measurement of the mass of the W boson with an accuracy of 6 MeV from a scan of the cross section in the threshold region. This cross section and the couplings of the W boson can be measured at the per-mille level. These measurements rely on adequate theoretical predictions. The tools used to analyse this process at the Large Electron-Positron (LEP) collider are based on approximations like the double-pole approximation (DPA), which has a theoretical uncertainty of 0.5% sufficiently far above threshold, or the improved-Born approximation (IBA) with a theoretical uncertainty of 2% in the threshold region. Evidently these approximations are not accurate enough for the envisaged experimental accuracies at the ILC.

Figure 1 shows the theoretical predictions for the W-pair-production cross section in the LEP2 region with the error band of the DPA approximation and the experimental data points with errors. At the ILC this error will be reduced by an order of magnitude above threshold and by two orders of magnitude in the threshold region.

Results

The relative corrections to the leading-order prediction for the cross section of the process $e^+e^- \rightarrow u\bar{d}\mu^+\nu_\mu$, which is a specific final state of W-pair production, are shown in Figure 2. The red curve corresponds to the complete corrections, the green one to the DPA, and the blue one to the IBA. The difference between the full calculation and the DPA is of the order of half a per cent in the LEP2 energy region. It gets larger with increasing energy and reaches 2% at 2 TeV. In the threshold

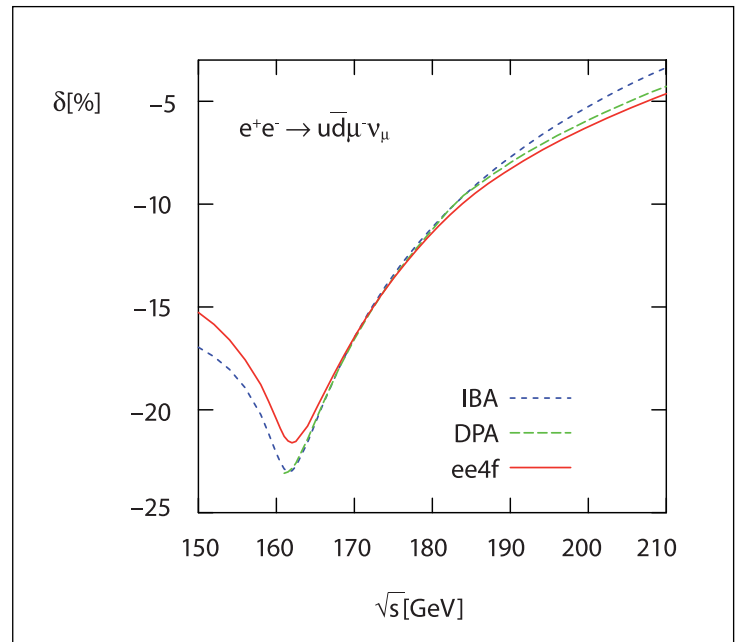


Figure 2: **Relative corrections to the cross section for $e^+e^- \rightarrow u\bar{d}\mu^+\nu_\mu$ from the complete $\mathcal{O}(a)$ calculation, in DPA and in IBA.**

region, where the DPA is unreliable, the full corrections differ from the IBA by almost 2%. Our calculation reduced the theoretical uncertainty to some per mille, which is a sizeable improvement and necessary for the ILC, in particular in the threshold region, where it was previously 2%.

Since our calculation has been implemented in a Monte Carlo generator, we can also calculate differential distributions. It turns out that the corrections beyond the DPA distort the angular distribution of the produced W bosons and can thus fake effects of non-standard W boson couplings, if not taken into account. Similarly, these corrections have a significant effect on the invariant-mass distribution of the virtual W bosons, which can affect the determination of the W boson mass from the decay products. In summarising, our calculation is crucial for the full exploitation of the potential of the ILC for the measurements of the properties of the W boson.

References

- [1] A. Denner, S. Dittmaier, M. Roth, L.H. Wieders, Phys. Lett. B612 (2005) 223
- [2] A. Denner, S. Dittmaier, M. Roth, L.H. Wieders, Nucl. Phys. B724 (2005) 247
- [3] J.A. Aguilar-Saavedra et al., TESLA Technical Design report Part III: Physics at an e^+e^- Linear Collider, hep-ph/0106315
- [4] The LEP Collaborations ALEPH, DELPHI, L3, OPAL, and the LEP Electroweak Working Group, LEPEWWG/2005-051, hep-ph/0511027

New results on radiative pion decay

Wilhelm Bertl *on behalf of the PIBETA Collaboration*
(Virginia – PSI – Dubna – Swierk – Tbilisi – Arizona – Zagreb)

Measurements of radiative decays are used to determine the form factors of the decaying particle, which in turn can be predicted by the Standard Model of particle physics. A large data sample of radiative pion decays was obtained at the PSI accelerator leading to much improved form factors and eliminating earlier deviations from the Standard Model.

The radiative decay of charged pions $\pi^+ \rightarrow e^+ \nu_e \gamma$ (RPD) is described by two main processes: a) radiation from propagating charged particles (“inner bremsstrahlung” IB), and b) radiation off weak hadronic currents directly from the interaction vertex (“structure dependent part” SD). The latter process is the interesting one as it allows the study of strong interaction physics. According to the Standard Model of particle physics (SM) only vector and axial-vector currents should contribute to the structure term which is parameterized by the phenomenological form factors F_V and F_A , respectively [1]. The contour

plot in Figure 1 shows the dependence of the structure term on the energy of the positron and the photon, respectively. The IB contribution, which peaks along the diagonal boundary and dilutes the structure dependent information, has been omitted for clarity. Early experiments suffered from low event rates, high background and acceptance limited to region A shown in Figure 1. In experiment R-89-01, a precision measurement of the pion beta decay $\pi^+ \rightarrow \pi^0 e^+ \nu_e$ performed between 1999 and 2001 at PSI [2], the RPD process became accessible in a much enlarged phase space, indicated as regions B and C in Figure 1.

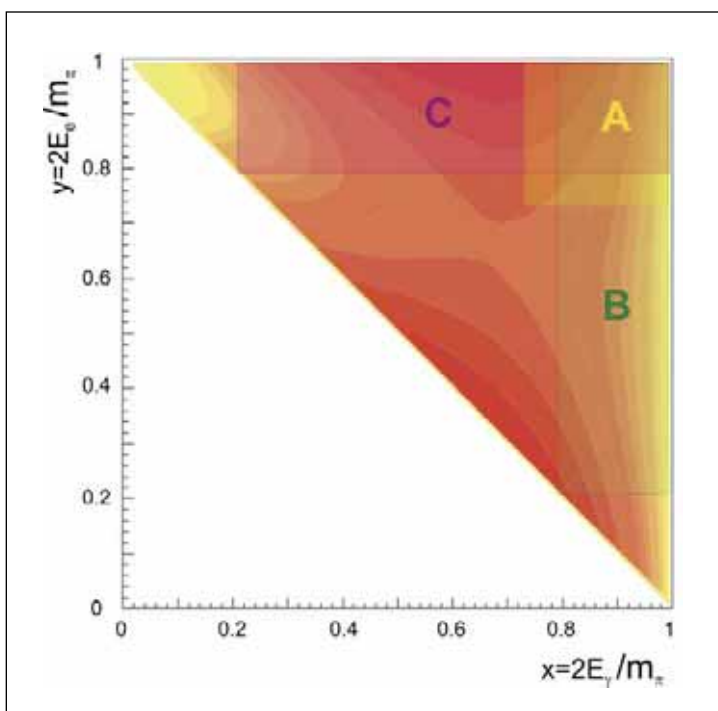


Figure 1: Intensity distribution of the structure dependent part of the $\pi^+ \rightarrow e^+ \nu_e \gamma$ decay. Regions A, B and C accessible by the measurement are indicated.

Unexpected previous results

Surprisingly, the analysed branching ratio showed a significant deficit compared with theoretical predictions in region B while the results for region A and C agreed very well. [3] A similar, albeit statistically less significant deviation was previously reported by the ISTR collaboration [4] and attributed to a nonzero tensor form factor F_T clearly at variance with the SM predictions. It was shown by Herczeg [5] that the existence of a form factor F_T of order 10^{-3} could not be excluded based on other measurements to date. Disturbingly, no similar effect was seen in the decay $\mu^+ \rightarrow e^+ \nu_e \bar{\nu}_\mu \gamma$ measured simultaneously. Experiment R-04-1 was set up to clarify this anomaly using the same spectrometer (PIBETA), an optimized beam rate (10^5 π -stops/s) and slightly simplified electronics. The experiment was carried out in 2004 and first results are now available [6,7,8].

Normalisation of the RPD rate was achieved by simultaneously recording $\pi^+ \rightarrow e^+ \nu_e$ decays whose branching ratio is known to 0.4%. After careful rejection of various background sources results for the weak form factors were obtained using

a global fit procedure simultaneously minimizing the error-weighted difference between experimental and theoretical branching ratios for all kinematic regions as a function of parameters $\gamma \equiv F_A/F_V$ and a . Parameter a represents the momentum dependence of the form factors assuming a general form like $F(q) = F(0)(1+a \cdot q^2)$. The large number of observed RPD events (approximately 28000) makes it possible to subdivide the 3 regions into 8 smaller bins and, consequently, to use more parameters (F_A , F_V , a) in a global fit of all 8 regions.

Results confirm theory

The result of all those fits using different sets of parameters and kinematic regions, respectively, were all in agreement within their uncertainties. Averaging the fit results from the 8 region analysis and those of the 3 regions we conclude for:

$$\gamma \equiv F_A/F_V = 0.450 \pm 0.082 \text{ and } F_V = 0.0262 \pm 0.0015.$$

From which it follows that:

$$F_A = 0.0118 \pm 0.0003.$$

The final result for the q -dependence parameter a was obtained averaging the fit results received from all independent methods:

$$a = 0.241 \pm 0.093.$$

The branching ratios for the original 3 regions were determined using the best-fit results from the 8 region analysis. They are now in very good agreement with theoretical predictions based on standard (V-A) assumptions (see Table 1).

Region	Theoretical BR ($\times 10^8$)	Experimental BR ($\times 10^8$)
A	2.6410 ± 0.0005	2.655 ± 0.058
B	14.490 ± 0.005	14.59 ± 0.26
C	37.900 ± 0.028	37.95 ± 0.60

Table 1: **Theoretical and experimental branching ratios for best values of γ obtained from the 8 regions analysis.**

Figure 2 shows a comparison between experimental and theoretical data of the kinematic variable λ evaluated in region B. Theoretical predictions were calculated with the best fit values of γ assuming validity of the SM. The shape of this distribution is rather sensitive to the suggested tensor form factor, but no deviation from the SM prediction is visible. Evaluating the tensor term based on either the 8 or the 3 region analysis resulted in $F_T = (0.8 \pm 3.95) \times 10^{-4}$ which is equivalent to an upper bound of $F_T < 5.1 \times 10^{-4}$ at the 90% confidence limit.

The above values for the weak form factors of the pion represent the currently most accurate measurements available, and

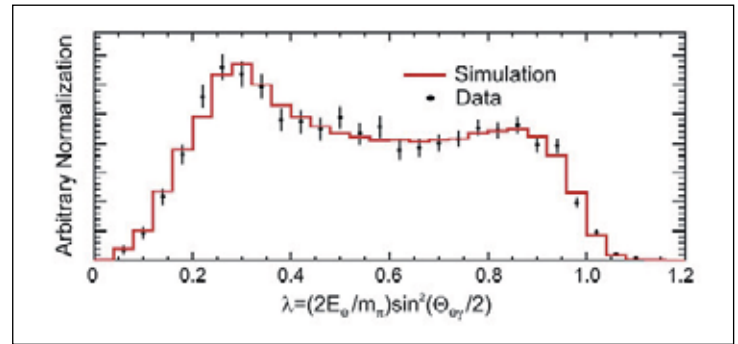


Figure 2: **Shape fit (sensitive to FT) of kinematic variable λ for region B. No deviation from the simulation based on standard model assumptions are visible.**

exceed the precision of previously published values by typically 5–6 times. The momentum dependence parameter a has been determined for the first time. No indication for the existence of an exotic current contribution (e.g., a tensor component) has been seen, either in the radiative decay of pions, or in the corresponding muon decay. In order to understand the observed deficit of the RPD branching ratio in region B in our previous measurement [3] we have started to reanalyze those data. The higher beam rate caused a significant increase of the background, which complicates the analysis. However, once the analysis of the first data set is corrected, the overall statistics will be significantly increased. Region A received much more data in the first run than in the 2004 run. Combining the data of both experiments will lead to almost equally populated regions with a total of more than 60000 events, which will further improve our weak form factor uncertainties.

References

- [1] D.A. Bryman, P. Depommier and C. Leroy, Phys. Rep. 88, 151 (1982).
- [2] D. Počanić et al., Phys. Rev. Lett. 93, 181803 (2004).
- [3] E. Frlež et al., Phys. Rev. Lett. 93, 181804 (2004).
- [4] V.N. Bolotov et al., Phys. Lett. B243, 308 (1990).
- [5] P. Herczeg, Phys. Rev. D 49, 247 (1994).
- [6] M. Bychkov, Ph.D. thesis, University of Virginia, Charlottesville, Virginia, 2005.
- [7] B. Vandevender, Ph.D. thesis, University of Virginia, Charlottesville, Virginia, 2005.
- [8] All published papers, theses, status reports and conference contributions of the PIBETA collaboration are available at <http://pibeta.phys.virginia.edu/docs/>

Chemical separation of Rf/Db nuclides produced in the $^{48}\text{Ca}+^{243}\text{Am}$ reaction

Dorothea Schumann, Horst Bruchertseifer, Robert Eichler, B. Eichler, *Research Department Particles and Matter, PSI*; Heinz W. Gäggeler, *Uni. Berne*; S. N. Dmitriev, Yu. Ts. Oganessian, V. P. Utyonkov, S. V. Shishkin, A.V. Yere-min, Yu. V. Lobanov, Y. S. Tsyganov, V. I. Chepygin, E. A. Sokol, G. K. Vostokin, N. V. Aksenov, M. Hussonnois, M. G. Itkis, *JINR Dubna, Russia*

An experiment was performed at the Flerov Laboratory of Nuclear Reactions in Dubna to support the previously observed evidence for element 115. Using a chemical procedure developed at PSI on the basis of 15 atoms it was possible to confirm that element 115 decays by consecutive emission of alpha particles to element 105 (dubnium), or via electron-capture decay of dubnium to element 104 (rutherfordium). The separated 15 atoms of dubnium (or rutherfordium) decayed by spontaneous-fission with a half-life of about 32 hours.

Introduction

In 2003 an experiment was carried out at the U400 cyclotron (FLNR, JINR Dubna, Russia) aimed to synthesize element 115 in the $^{243}\text{Am}(^{48}\text{Ca}, xn)^{291-x}115$ reaction. Three decay chains were found with 5 consecutive α -decays, detected in time intervals of about 20 s and terminated by a spontaneous fission (SF) with a high energy release after 16-28 h [1]. This SF activity may thus be assigned directly to isotopes of Db. Assuming long-lived EC-branches for the Db decay the observed SF can be assigned to isotopes of Rf. The idea of the present experiment was to confirm this result by chemical identification of Db and/or Rf as a long-lived decay product. The chemical separation system should guarantee high separation factors from transfer products in transplutonium region like Cm, Cf, or Fm, which may interfere with the detection of the expected long-lived transactinides. Moreover, conditions were selected, which allow the collection of both Db and Rf in one fraction. Earlier results showed that the most promising chemical separation system for elements of the 4th and 5th group is ion exchange from HF containing solutions [2-6]. Anionic fluoride complexes are formed, which are not adsorbed on cation exchangers, whereas actinides can be adsorbed with high distribution coefficients, due to the formation of insoluble fluorides.

Experimental setup

The experiment was performed at FLNR (JINR) U400 cyclotron in June, 2004. The 32-cm² rotating target consisted of 1.2 mg/cm² of ^{243}Am (enriched to 99.9%) in the oxide form de-

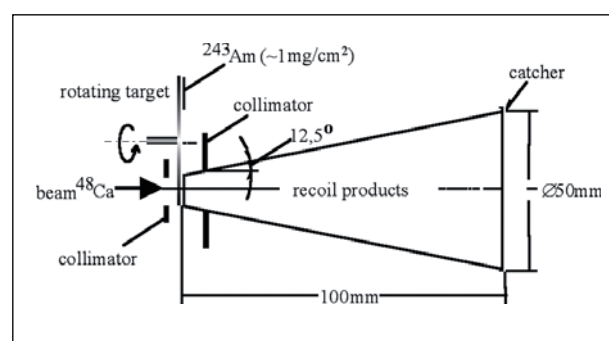


Figure 1: **Schematic setup of the irradiation.**

posited onto 1.5- μm Ti foils. The target was bombarded by ^{48}Ca ions with energy of 247 MeV at the middle of the target layer. The average intensity of the beam was $5 \cdot 10^{12}$ ion/s. A collimator, 10 mm in diameter, limited the irradiated area. The recoiling nuclei of the reaction products passed through a second 12 mm collimator, 10 mm behind the target, and were stopped in a 50 mm diameter copper catcher positioned 100 mm behind the target. The efficiency of collecting the compound nucleus in such a geometry (collecting angle $\pm 12^\circ$) was close to 100%. The range of recoils in the copper catcher was approximately 3-4 μm .

About 7-10 μm from the catcher surface (100-150 mg Cu) were removed mechanically by means of a micro-lathe. The copper chips were dissolved in 10 ml 7M HNO_3 . Carrier-free tracers ^{177}Ta , $^{92\text{m}}\text{Nb}$, ^{88}Zr , ^{175}Hf , $^{88\text{Y}}$, ^{167}Tm and ^{169}Yb for monitoring the separation and 700 μg La-carrier were added and the hydroxides were precipitated with concentrated NH_3 solution. Under these conditions Cu remains in solution as ammine complex, whereas group 4 and 5 elements as well as La and actinides precipitate. The procedure was repeated twice. The precipitate

was dissolved in 2M HNO₃ and adsorbed on a DOWEX50x8 column (8x20 mm, 150-200 mesh). The group 4/5 fraction was eluted with 2 ml 1 M HF. Finally, the solution was evaporated on PE foils (30 µg/cm²) for detection of SF in 4π geometry between 2 PIPS detectors inside a neutron counter. Yields for group 4 and 5 elements of ~ 65+–20% were achieved.

To model the chemical behaviour of transactinides with $Z \geq 106$ the separation procedure was also applied to ¹⁹²Ir, ¹⁹¹Pt, ^{199/198}Au, ¹⁹⁷mHg, ²⁰⁰Tl, and ²⁰³Pb tracers under identical conditions as in the real experiment. After twice dissolving the precipitation in HCl and precipitating again, no γ-lines of the corresponding nuclides could be detected in the lanthanide precipitate containing the group 4/5 elements, which refers to a separation of > 95%.

For the registration of α-particles and spontaneous fission fragments we used a detection module which combines 4 identical chambers, each equipped with two opposite semiconductor detectors with an active area of 5 cm², mounted at a distance of 5 mm. All counting chambers were inserted into a neutron detector consisting of 72 ³He counters, which were positioned in three layers apart from the cylinder axis in order to register prompt neutrons. The detection efficiency for fission fragments was about 90% and for neutrons ~40%. In the course of a 330-hour test run prior to the experiment no coincident background events were detected.

Eight identical experiment runs were performed, measurement times of which were up to 960 hours. A ninth experiment was carried out under identical experimental conditions but without chemical separation (direct catch). The catcher surface was cleaned from ²⁴³Am carrying aerosol particles and put in contact with solid-state track detectors in order to determine the overall amount of spontaneously fissioning nuclei.

Results and discussion

After eight irradiations (with a total dose of $3.4 \cdot 10^{18}$) we measured 15 spontaneous fission events in the final samples. The results are listed in Table 1.

The value of the total kinetic energy (TKE), calculated from the 13 measured coincidences, with respect to pulse height defects of the PIPS detectors and correcting for the energy loss in the samples was about 235 MeV. A half-life of 32(+11;-7)h and a production cross section of the long-lived SF decaying nuclide from the ⁴⁸Ca+²⁴³Am reaction of 4 pb could be determined. The observed overall SF rate in the direct catch was 2 events per day in the first 30 days and 1.9 events in the following 36 days. With the obtained separation factor from lanthanides (and actinides), the probability for detecting a SF event from actinides within 174 h is less than 0.1%. With respect to the physics experiment in 2003 [1] the observed SF

N	t _{irr} [h]	beam dose	E _{bot} +E _{top} [MeV] +. ν (t _n [µs])	t _{det} [h]	t _m [h]
1	20	2,5 · 10 ¹⁷	98+96+2n (5;64)	20	429
2	22	3,7 · 10 ¹⁷	– +51 +1n (57)	74	186
3	22	3,4 · 10 ¹⁷	111+94 +1n (3)	15	
			95+92+2n (8;16)	72	385
4	22	2,9 · 10 ¹⁷	74+91 +1n (2) 74+95+1n (151) 76+99+1n (89)	22 29 51	358
5	38	6,7 · 10 ¹⁷	96+87+2n (6,98) 87+76+3n (4,31,43) 102+67+0n – + 35 +2n (6,41)	6 9 15 68	861
6	23	3,9 · 10 ¹⁷	97+84 +2n (2,2)	39	933
7	22	3,6 · 10 ¹⁷	–	–	957
8	45	7,4 · 10 ¹⁷	95+80 +2n (5;33) 95+75 2n (72,165) 40+27+3n (12,19,29)	5 93 174	910

Table 1: Measured SF events without corrections.

activity can be assigned to a Db or Rf isotope with high probability. Due to its chemical behaviour in our study the measured nuclide neither can be an actinide nor a transactinide with $Z \geq 106$. Hence this chemical study can be assumed as a confirmation of the formation of element 115 in the nuclear reaction ⁴⁸Ca with ²⁴³Am. For the exact assignment of the observed activity to a defined Z, further chemical studies are necessary.

References

- [1] Y. T. Oganessian et al., Phys. Rev. C 69, 021601(R) (2004)
- [2] Z. Szegłowski et al. Radiochim. Acta 51(1990)71-76
- [3] D. Schumann et al. Radiochim. Acta 72 (1996) 137
- [4] D. Schumann et al. J. of Alloys and Compounds 271-73 (1998) 307-311
- [5] G. Ter-Akopian et al. J. Nucl. Phys. 29(3), 608 (1979)
- [6] H. Bruchertseifer et al. Radiochim. Acta 47, 41(1989)

High rate test-beam results with CMS pixel module prototypes

Wilhelm Bertl, Wolfram Erdmann, Kurt Gabathuler, Roland Horisberger, Hans-Christian Kästli, Stefan König, Danek Kotlinski and Tilman Rohe, *Research Department Particles and Matter, PSI*; Urs Langenegger, Beat Meier, Andrey Starodumov and Peter Trüb, *Institute for Particle Physics, ETH Zurich*; Christoph Hörmann, *Physics Institute of the University of Zurich and Research Department Particles and Matter, PSI*

The compact muon solenoid (CMS) is one of the two general purpose detectors being built for the Large Hadron Collider (LHC), the 15 TeV proton-proton collider at CERN. The main research goals are to find the Higgs particle and look for effects of supersymmetry. The pixel detector will be the innermost tracking device of the CMS experiment. A Swiss collaboration is responsible for the construction of the pixel barrel. Bombarding prototype pixel modules with high rate, low energy pion beams at PSI represents the best simulation of the expected environment at the LHC and is therefore the best possible performance test.

Pixel barrel modules for CMS

The core of a pixel module consists of a sensor, which is segmented into pixels by appropriate implantation, with 16 readout chips (ROC) bump-bonded to it (see Fig.1). This bare module is glued onto silicon nitride base strips to provide mechanical strength. A high-density interconnect (HDI) flex

print is glued on top of the sensor. Wire bonds connect the readout chips to the HDI, which distributes the readout and control signals appropriately and routes them to a flat flexible cable, glued and wire-bonded to the HDI. The power for the chips and the sensor bias voltage are brought to the HDI by a ribbon cable soldered to the HDI.

The total thickness of a pixel module does not exceed 0.8 mm, owing to back-thinned readout chips and an ultra-thin HDI. This minimizes the multiple scattering of charged particles traversing the pixel detector.

At the LHC, bunch crossings will occur with a frequency of 40 MHz with several hundred charged particles (mostly pions) produced inside the acceptance of the pixel detector at each crossing. In order to simulate these conditions as closely as possible, a prototype module was operated at the end of 2006 in a high intensity 300 MeV/c pion beam at PSI. This beam has a 50 MHz bunch structure, quite similar to the 40 MHz LHC bunch crossing frequency. The main purpose of this test was to measure the efficiency of a pixel barrel module with stochastic hit rates as a function of particle flux.

Test setup in the $\pi E1$ beam

The module was placed in the middle of a row of four single-ROC pixel devices, each device covering an area of $8 \times 8 \text{ mm}^2$, two upstream and two downstream of the module, serving as a beam telescope (see Fig.2). This allowed the selection of straight tracks with four hits in the telescope and to check whether a corresponding fifth hit was present in the module. A small

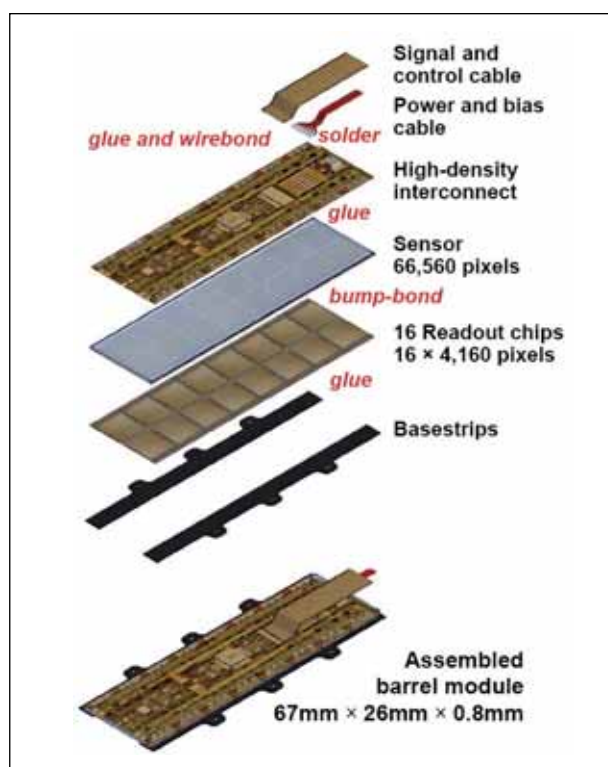


Figure 1: Structure of a CMS pixel barrel module.

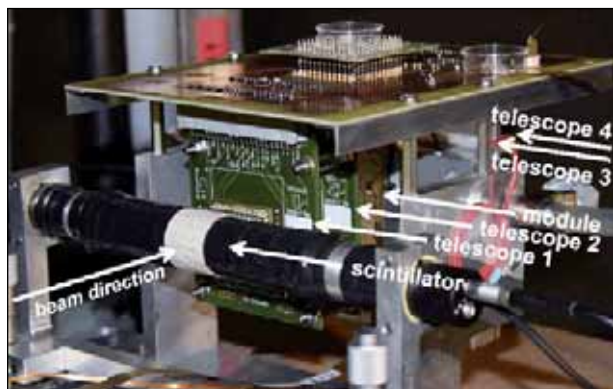


Figure 2: **Beam test setup showing the arrangement of scintillator, telescope and module in the π E1 area.**

plastic scintillator covering an area of $2 \times 2 \text{ mm}^2$ mounted upstream of the pixel telescope provided particle triggering. Module and telescope were operated with a 40 MHz clock (LHC frequency). Triggers were only allowed in one out of five beam bunches where it lined up with a 40 MHz clock cycle. This ensured that triggered particles had the correct timing relative to the 40 MHz clock. The trigger rate was tuneable by randomly selecting among scintillator pulses. The beam intensity was varied, using an adjustable collimator, between 1 MHz/cm^2 and 100 MHz/cm^2 .

Triggered event hits consisting of the analogue coded pixel address and the analogue pulse height of each hit pixel were digitized in a local 12-bit ADC and written into a large local memory. Upon termination of a data taking run, the data was copied via a USB link from the memory onto a remote hard disk for data analysis.

Inefficiency results

Figure 3 shows the inefficiency of the module in the region covered by the telescope, as a function of particle flux. The beam had perpendicular incidence and its intensity was roughly uniform over the entire module. The average cluster size of the hits was 1.2 pixels. The trigger rate in the shadow of the scintillator was chosen at 20 kHz. The results are compared in Figure 3 to a Monte Carlo simulation which follows particle hits through the entire architecture of the readout electronics. Compared to the simulation, the data exhibits an additional constant inefficiency of about 1 % whose origin is, for the time being, not explained. The simulation does however not take into account the sensor performance which could explain part of this discrepancy. Without the constant term the slope of the data is quite well reproduced by the simulation. Therefore it is possible to quite reliably predict with this simulation program the inefficiencies expected in the CMS experiment.

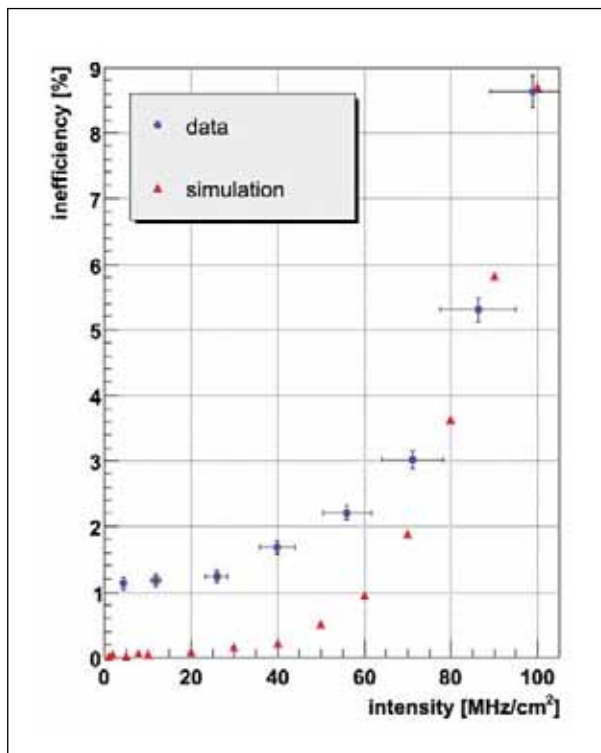


Figure 3: **Measured inefficiencies compared to a Monte Carlo simulation. Trigger rate 20 kHz. The data show a pedestal of $\sim 1\%$, which could partly be attributed to the sensor which is ignored in the simulation.**

Cluster charge results

The CMS pixel detector has an analogue readout scheme. The pixel charge is stored in arrays of capacitors in the ROC's during the trigger latency. Figure 4 shows Landau distributions for different angles of incidence. The pions are close to minimal ionising.

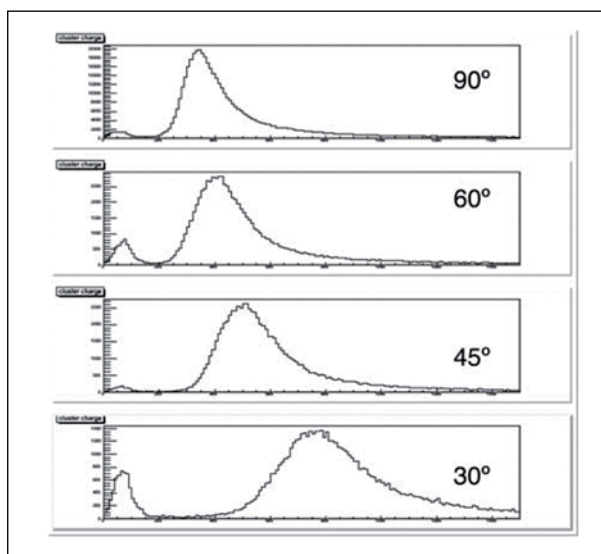


Figure 4: **Hit cluster charge in pixel module for different angles of incidence.**

Status of the MEG experiment

Peter-Raymond Kettle, *Research Department Particles and Matter, PSI; (Representing the MEG-Collaboration: BINP Novosibirsk – Russia, Univ. California Irvine – USA, ICEPP Univ. Tokyo – Japan, INFN and Univ. Genova, Lecce, Pavia, Pisa, Rome I – Italy, JINR Dubna – Russia, KEK – Japan, PSI – Switzerland, Waseda Univ. – Japan)*

In order to search for signatures of “new physics” the MEG experiment utilizes a combination of the highest intensity surface muon beam together with state-of-the-art detector technology. The manifestation of such a signal in “lepton-flavour violating muon decay” is the coincident appearance of a 52.8 MeV positron and photon, travelling in opposite directions. Significant progress was made in 2005 in many aspects of the experiment’s design and construction phase, culminating, at the end of the year, in the injection and phase space measurement of the first muon beam inside the COBRA detector magnet.

Since the first search for the $\mu^+ \rightarrow e^+ \gamma$ decay in cosmic rays, by Hincks and Pontecorvo now some sixty years ago [1], both theory and experimental techniques and technologies have made significant advances, making it likely for so-called “forbidden decays” in the Standard Model to be seen: that is if the expectations of Supersymmetry (SUSY) or Grand Unification

(SUSY-GUT) prove to be reality. The goal of the MEG experiment is to improve detection sensitivity by about two orders of magnitude compared to the most sensitive search to date, that of the MEGA Collaboration $B_R(\mu^+ \rightarrow e^+ \gamma) \leq 1.2 \cdot 10^{-11}$ in 1999 [2].

International collaboration

In order to achieve this ambitious aim, both the highest intensity beam of stopping muons and a detector capable of distinguishing such events from a sea of combinatorial normal and radiative muon decays, is required. In 2005, significant progress was made towards the goal of commissioning the experiment in 2006, both from the point of view of hardware implementation and design completion. Besides commissioning beam time and background/calibration studies in the πE_5 zone at PSI, tests were also undertaken at the Frascati National Laboratory LNF in connection with the Timing Counters and at the Legnaro National Laboratories LNL in Padua, to test calibration techniques for the liquid xenon photon calorimeter. A few notable highlights are mentioned below.

Beam related

In July, the eagerly awaited superconducting beam transport solenoid (BTS) arrived at PSI, after its 6500 km journey from Novosibirsk where, prior to which, the performance tests had successfully been completed (see Fig. 1). This, together with the completion of the new MEG vertical 200 kV WIEN filter ($\vec{E} \times \vec{B}$ separator) marked the hardware completion of the

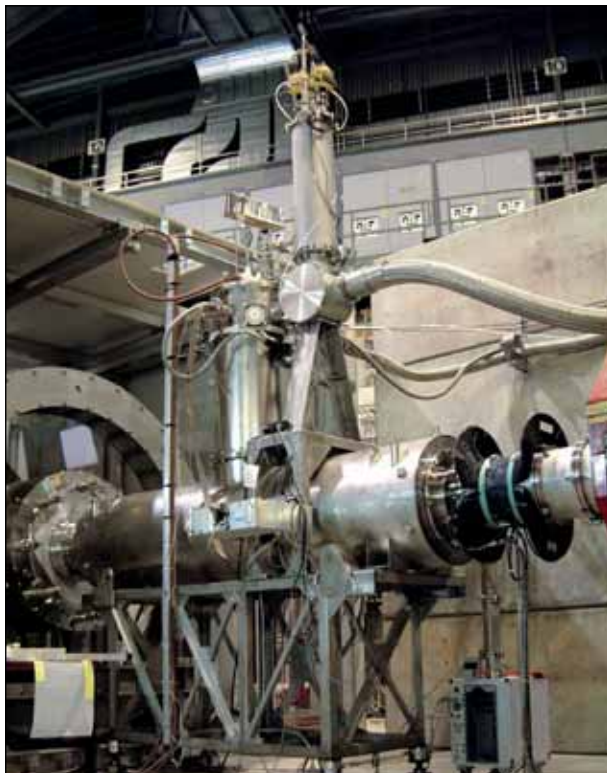


Figure 1: Shows the BTS coupled to the COBRA magnet, just inside the opened detector housing to the left of the picture. On the right is the steering magnet/collimator system.

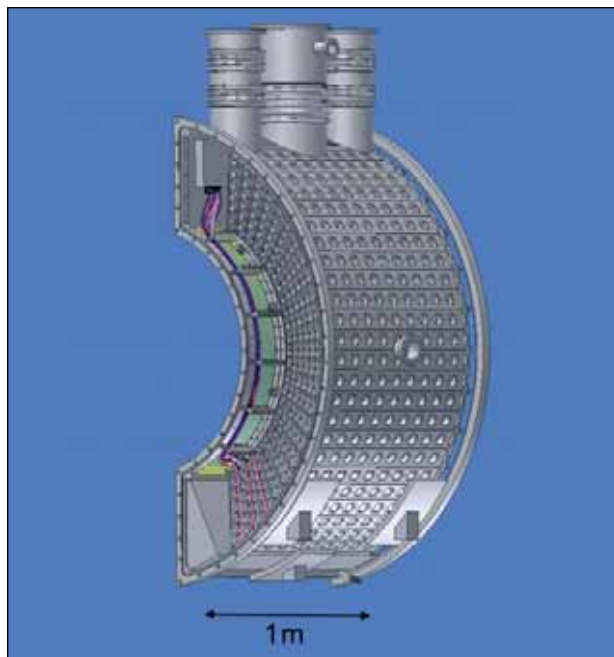


Figure 2: **Schematic of interior of LXe photon calorimeter, showing the PMT support structure.**

major beamline elements for the experiment. During the two beam commissioning periods, the BTS underwent exhaustive trials including magnetic field measurements, quench tests, with final integration and automatic cryogenic operation in conjunction with the PSI cryo-plant and the MEG-own slow control system MSCB (Midas Slow Control Bus) [3]. Several beam-optics injection schemes into the COBRA detector solenoid were tested, as well as phase space measurements of the beam at the target location, centred in COBRA. This involved constructing a provisional Helium-bag environment of ~ 2000 litres volume, together with a 3 mm diameter APD-detector mounted on a 3-D automated measuring machine, some 3 m long. These first results, without a degrader, gave beam-spot sizes and rates totally consistent with simulation i.e. $R_{\mu} = (1.15-1.19) \cdot 10^8 \mu^+/s$ at 1.8 mA beam intensity and 4 cm Target E (dependent on BTS optics). Final measurements with the degrader will follow in 2006.

Detector related

Significant advances were also made with the liquid xenon (LXe) calorimeter, with delivery expected mid- 2006. A schematic of the cryostat interior is shown in Figure 2, along with the holders for 850 photomultiplier tubes (PMT), which will be immersed in 800 litres of LXe, at 167 K and will view the scintillation light produced by a photon conversion. To ensure the LXe purity, a new liquid-phase purification scheme was successfully introduced allowing an in situ operation with a purification rate of 100 litres/hr. The delivery of a 1000 litre

storage vessel, as part of the system, has further ensured a minimum of contaminants. An extensive programme of PMT testing in LXe was done at both PSI (600) and Pisa (300) using different techniques, resulting in most of the 1000 PMTs being classified in the database.

Calibration and monitoring techniques are of essential importance to the experiment, with extensive time invested in developing these techniques. One improvement made was the replacement of the short-lived ^{210}Po multi-spot wire α -sources by long-lived ^{241}Am ones. Tests for a future photon monitoring source using a moderated neutron source/generator to produce a 9 MeV photon line from Nickel were shown to work. Finally, the implementation of a Cockcroft-Walton proton accelerator into the MEG experiment for calibration purposes was tested at the Legnaro Laboratory's Van de Graaff generator facility. The feasibility of producing 17.6, 14.6 MeV γ -lines from $\text{Li}(p,\gamma)\text{Be}$ and 4.4, 11.7, 16.1 MeV γ -lines from $\text{B}(p,\gamma)\text{C}$ using self-constructed targets was confirmed, with an expected calibration rate (17.6 MeV line) of 1.8 kHz/ μA current.

The first of the final drift chamber (DC) modules of the positron tracker was also completed and quality controlled (see Fig. 3) indicating that the complex mechanical structure problems of the light-weight materials involved could be mastered. The overall precision limit of 0.1 mm on the complete structure could be maintained. Significant work was also invested in the design of the support structure and gas-control system. Initial tests of the first 128 channels of 2GHz waveform digitizing electronics, based on the DRS2 chip[4], showed a good performance with noise characteristics of ≤ 0.5 mV, indicating that a 50 ps timing accuracy can be achieved.



Figure 3: **First completed drift chamber module, showing inner anodes/cathodes and hood module (top).**

The major components of the scintillator-bar part of the timing counters are now completed, with work continuing on the APD readout and the scintillating fibre layers.

References

- [1] E. P. Hincks and B. Pontecorvo, Phys. Rev. 73, 257 (1948)
- [2] M. L. Brooks et al., Phys. Rev. Lett. 83, 1521 (1999)
- [3] MSCB <http://midas.psi.ch/mscb>, PSI Scientific Report 2001, vol. 1, 34
- [4] PSI Scientific Report 2004, vol. 1, 12

Timing of glacier variations in the Alps with cosmogenic ^{10}Be , ^{26}Al and ^{36}Cl

Susan Ivy-Ochs, *Institute of Particle Physics, ETH Zurich and Geography Institute, University of Zurich*;
Peter W. Kubik, Hans-Arno Synal, *Research Department Particles and Matter, PSI*; Hanns Kerschner,
Geography Institute, University of Innsbruck, Christian Schlüchter, *Geology Institute, University of Berne*

More than a century of detailed geomorphological mapping both in the Alps and the foreland provides a unique opportunity throughout the world for exposure dating of former ice margins in a well-constrained field situation. Surface exposure dates based on ^{10}Be , ^{26}Al , and ^{36}Cl have allowed us to constrain the timing of fast glacier variations. From the last glacial maximum (LGM) to the early Holocene, glacier volumes in the Alps have varied in tune with North Atlantic Ocean climate oscillations (Heinrich event 1, Younger Dryas, Preboreal oscillation and 8.2 kyr events).

Introduction

Cosmogenic nuclides build-up predictably within mineral lattices of exposed rock surfaces due to reactions of target nuclei with cosmic rays. Therefore, measuring their concentrations allows the calculation of how long a rock surface has been exposed. Glaciers are very sensitive indicators of climate change, responding rapidly and markedly to changes in both temperature and precipitation, with changes in volume. The exposure dating of boulders on moraine crests allows the determination of how much time has passed since the glacier abandoned that position and the moraine stabilized. The introduction of the exposure dating method and the direct dating of moraines with cosmogenic nuclides marks a turning point in the science of glacial geomorphology and the reconstruction of the timing of past fluctuations in glacier volume.

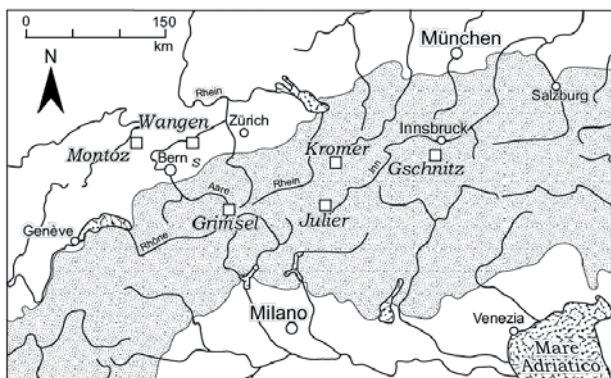


Figure 1: **Index map showing site locations, the Alps are indicated by the grey shaded area.**

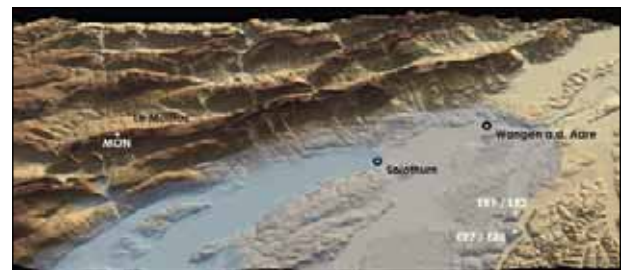


Figure 2: **Digital elevation model based on DHM25 data set (used with permission of Swisstopo©) showing the generalized extent of the Rhône Glacier during the LGM at Wangen an der Aare and Solothurn LGM stadials. Vertical exaggeration is 3 times. Scale varies with perspective.**

Here, we summarize the present state of knowledge on periods of glacier expansion in the Alps (Fig. 1) which have been temporally constrained using the cosmogenic nuclides ^{10}Be , ^{26}Al , and ^{36}Cl [1]. The upper few centimeters of boulder surfaces were sampled. Be, Al and Cl were extracted from the rock samples at the Institute of Particle Physics (ETH-Zurich) and radionuclide concentrations were determined with accelerator mass spectrometry at the PSI/ETH AMS facility.

Dating with cosmogenic nuclides

First results of ^{10}Be from one boulder at the Montoz site (Jura Mountains, Switzerland) (Fig. 2) bear out the concept that the most extensive glaciation(s) of the Alps occurred before the last interglacial. A reasonable minimum age estimate is 155 ± 18 kyr. During the LGM, piedmont lobes of the glaciers from



Figure 3: **Erratic boulder ER1 located on the outermost moraine at Wangen an der Aare (Solothurn, Switzerland).**

the Alps reached their maximum extent synchronous with the global ice volume maximum. Deglaciation began no later than 21.1 ± 0.9 kyr as shown by the exposure age on the Steinhof boulder located near Wangen an der Aare (Fig. 3). Notably, ice melted back out of the foreland regions early in the last termination.

Based on relative moraine position, moraine morphology and equilibrium line altitude depressions, a system of families of moraines (stadials) was constructed for glacier re-advances after recession of LGM glaciers, during the Lateglacial. The stadials are known as Gschnitz, Daun, Clavadel, Egesen, Kromer and Kartell. During the Lateglacial, surface exposure dating has proven especially useful for constraining the timing of glacier expansions. The first clear re-advance of independent glaciers in the Alps is represented by moraines of the Gschnitz stadial. Surface exposure ages from boulders on the Trins Gschnitz moraine (Tyrol, Austria) point to moraine stabilization no later than 15.4 ± 1.4 kyr. Based on the age and the cold, dry climate we suggest that the Gschnitz glacier advance was the response to cooling of the North Atlantic Ocean related to Heinrich event 1. The most impressive moraines formed during the Alpine Lateglacial were deposited during the Egesen stadial. In Figure 4 surface exposure ages from nine different boulders at the Julier Pass Egesen stadial moraine complex (Graubünden, Switzerland) are shown.

Excellent agreement between exposure ages based on ^{10}Be , ^{26}Al and ^{36}Cl in individual boulders is seen. The ages show clearly that Egesen moraines were formed as glaciers advanced in response to the Younger Dryas cold event, which occurred between 12.7 and 11.6 kyr. The outer moraine at Julier Pass stabilized right around (12.3 ± 1.5 kyr based on ^{10}Be). This age is indistinguishable from the ^{10}Be age of 12.2 ± 1.0 kyr based on four boulders from the Egesen I moraine at Schönferwall (Tyrol, Austria). The coincidence of exposure ages from correlative Egesen stadial moraines hundreds of kilometers apart illustrates the power of the exposure dating method.

Towards the end of the Egesen stadial glaciers waned and rock glaciers formed. This indicates that conditions remained cold yet became progressively drier. This is especially well exemplified by the inner moraine deposits at the Julier Pass site, which date to 11.3 ± 0.9 kyr. The date of 10.8 ± 1.0 kyr from moraines located less than a kilometer in front of Little Ice Age moraines in the Kartell cirque (Tyrol, Austria) shows that in certain catchments small glaciers re-advanced during the earliest Holocene, likely during the Preboreal oscillation. Before 8.4 ± 0.7 kyr, in Kromer Valley (Vorarlberg, Austria), small cirque glaciers advanced to a position several hundred meters to one kilometer in front of the little ice age position [2]. This is the first absolute age evidence for glacier advance in the Alps during the 8.2 kyr cold event.

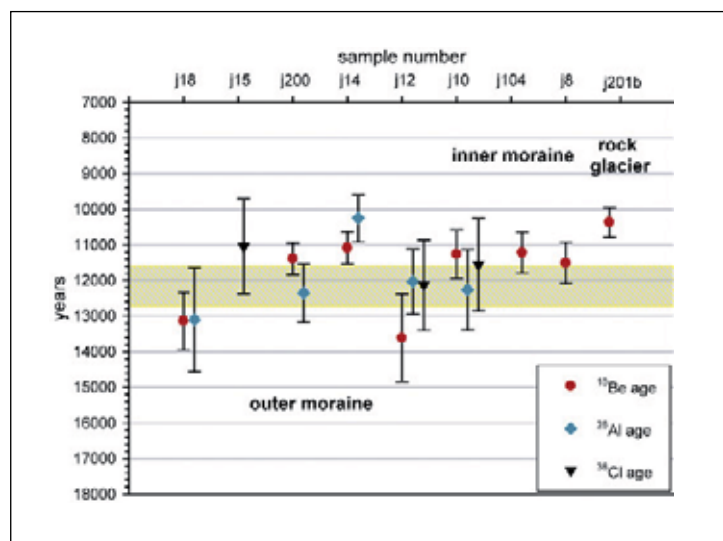


Figure 4: **Plot of ^{10}Be , ^{26}Al and ^{36}Cl surface exposure ages from nine boulders at the Julier Pass Egesen moraine complex. The shaded band indicates the Younger Dryas cold interval (12.7-11.6 kyr).**

Summary

Glacial landforms, thus glacier advances, that were previously undatable have been dated directly with cosmogenic nuclides. Expansions of glaciers in the European Alps show marked synchrony with climatic downturns such as Heinrich event 1, Younger Dryas, Preboreal oscillation and 8.2 kyr event as recorded in North Atlantic Ocean sediment cores.

References

- [1] S. Ivy-Ochs et al., Geological Society of America Bulletin special volume (in press) (2006)
- [2] H. Kerschner et al., The Holocene vol. 16, 7-15 (2006)

Hubble goes infrared

Ulrich Langer, Adrian Glauser, Manuel Güdel and Alex Zehnder, *Research Department Particles and Matter, PSI; And the European MIRI Consortium, 17 Institutes in 11 European Countries*

In 2013 NASA, ESA and the Canadian Space Agency will replace the Hubble Space Telescope by its successor – the James Webb Space Telescope (JWST). JWST is designed to study the first light stemming from the earliest galaxies formed after the big-bang, as well as signals from Earth-like planets. Predicted by Einstein, this first light is shifted to infrared (IR) wavelength due to the expansion of the universe. Moreover, the thick dust, in which forming stars are embedded, can be penetrated by infrared light. JWST will provide unprecedented access to imaging and spectroscopy of extra-solar planets. On JWST, there are four IR sensitive instruments, PSI is actively involved in building one of them, the Mid-InfraRed Instrument MIRI.

It is probable that in 2010, after twenty years in orbit, NASA will end the extremely successful Hubble Space Telescope mission. This does not end an era of astronomical discovery; it merely extends it. Three years later, NASA, ESA and CSA plan to launch the James Webb Space Telescope (JWST, see Figure 1), which in many ways is Hubble's scientific and technological successor.

Equipped with a large, 6.5-meter-class deployable mirror and a suite of revolutionary, infrared-sensing cameras and spectrometers, JWST will allow us to see even farther into space than is currently possible with Hubble and help us analyse the miniscule specks of light that Hubble cannot even detect. These nascent stars and galaxies are so distant that by the time their light reaches us, it has stretched into the longer, redder wavelength bands and is invisible to the human eye (infrared light).

Consequently, no one has ever observed this cosmic “dark zone” before because they did not have the tools to do so. But with this “first-light machine,” we will finally see what the

universe looked like when it was merely a fraction of its current age and size, when the first stars and galaxies were just beginning to take form. The physics of star formation itself can be studied in nearby, galactic star forming regions ideally in the infrared range, because light at shorter wavelengths is strongly absorbed by thick dust clouds. Here again a telescope like JWST is required to make the forming stars visible at spatial resolutions never achieved before. By observing planets around nearby stars JWST will measure the composition of their atmospheres, potentially discovering pivotal molecules for the origin and sustenance of life. Altogether JWST will tackle four major objectives over the course of its 5–10 year lifetime:

- First-light after the Big Bang
- Assembly of first galaxies
- Formation of stars and planetary systems
- Evolution of planets and origin of life

Technological requirements

These demanding scientific goals lead to challenging technical requirements and solutions (see Table 1). First of all the extension into the infrared requires that the main mirror has to be significantly enlarged to nearly maintain the spatial resolution of Hubble (0.1 arc seconds). To reduce the thermal radiation of the mirror itself the whole telescope has to be cooled below 50K. This is achieved by going to the Lagrange point L2 at a distance of 1.5 million km from Earth. Their thermal radiation will be shielded by multilayer insulation the size of a tennis court. When fully opened, the large 6.5-meter mirror and the sunshield will not fit into the launcher, an ESA

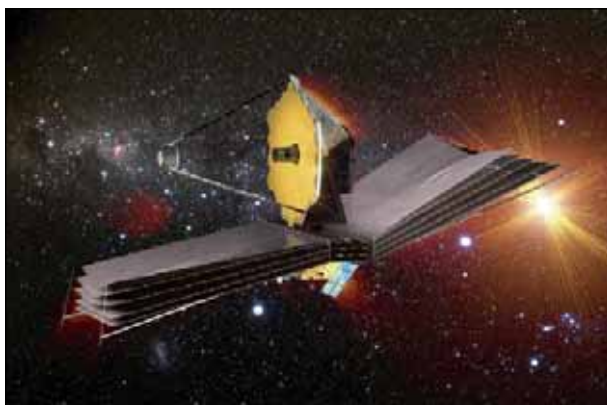


Figure 1: Artist's view of the James Webb Space Telescope.

Features	Hubble	James Webb
Primary Mirror	2.4m, monolithic, lightweight glass	6.5m, 18 segments, deployable, Beryllium
Wavelength	0.1–1.1 μ m (since 1997 up to 2.5 μ m)	0.6–28 μ m
Operating temperature	~20°C	-230°C
Mass	11t	6.2t
Launch	1990 by Space Shuttle	2013 by Ariane 5
Orbit	Low Earth Orbit (600km)	Lagrange point L2 (1.5 million km)
Duration	~20 years	5–10 years
Service	By astronauts	Not possible

Table 1: Comparison of Hubble and James Webb.

delivered Ariane 5 rocket. The mirror and sunshield will fold up and open only once JWST is in outer space. This induced a complex deployable telescope/spacecraft system with more than 50 mechanisms and actuators.

JWST will be equipped with four instruments, which are designed to work primarily in the infrared range of the electromagnetic spectrum, with some capability in the visible range:

- NIRCam: a wide field (2.2' x 4.4') near-IR camera covering wavelengths 0.6 - 5 μ m.
- NIRSpec: a wide field (3.5' x 3.5') multi-object near-IR spectrometer covering wavelengths 0.6 - 5 μ m at spectral resolutions of R~100, R~1000 and R~3000.
- MIRI: a combined mid-IR camera (1.4' x 1.9') and coronagraph as well as spectrometer (R~3000) covering wavelengths 5 - 28 μ m.
- FGS (Fine Guidance System) will include a near-IR tuneable filter imaging capability (2.3' x 2.3'; R~100) covering wavelengths 0.6 - 5 μ m.

Mid-InfraRed Instrument

The Mid-InfraRed Instrument (MIRI) will provide unique capabilities to probe the deeply dust-enshrouded regions of the universe, thereby investigating the history of star formation both near and far. MIRI will have enormous advantages in image quality, field of view, low background light, and environmental stability over any previous ground or space-based observatory. The mid infrared (5-28 μ m) region is particularly important because it contains unique spectral and diagnostic features for studying both galaxy and planet formation.

Optically the instrument is divided into two channels: an imager channel, with one 1kx1k Si-As detector array and a spectrometer channel, which is further subdivided into two modules each with a 1kx1k Si-As detector array. The imager

channel provides broad and narrow band filters covering the range 5 to 27 μ m with 0.11"/pixel and a 1.3' x 1.7' field of view, coronagraphs at 10.65, 11.4, 15.5, 23 μ m and incorporates a slit for R ~100 spectroscopy from 5 to 10 μ m. The spectrometer channel provides medium resolution integral field spectroscopy at R ~ 3000 and covers the full 5 to 28.3 μ m contiguously in 3 exposures. The spectrograph is subdivided into four image slicer inputs with fields of view of the sky of 3.5x3.5 - 7x7 arc seconds providing the inputs to a short and a long wavelength spectrometer. MIRI will be actively cooled by a cryo-pump to cryogenic temperatures of 7K. This is necessary to reduce the dark current and background in order to meet the stated sensitivity for the Si-As detector arrays.

Swiss expertise

MIRI is jointly developed by US and European institutes with the latter being responsible for the complete optical bench assembly, the cryo-mechanisms, calibration sources and the related electronics. PSI is contributing three components and one test facility to MIRI:

- Contamination control cover
- Cryo harness
- Temperature sensors
- A cryo test facility

The contamination control cover will be used to protect the highly vulnerable optical surfaces against external particular and molecular contamination. The cryo harness provides the delicate electrical link for all components of the cold instrument and the temperature sensors are used to verify the thermal requirements. The cryo test facility simulates the prevailing space environment to test all MIRI cryo mechanisms at the nominal operating temperature of -265°C.

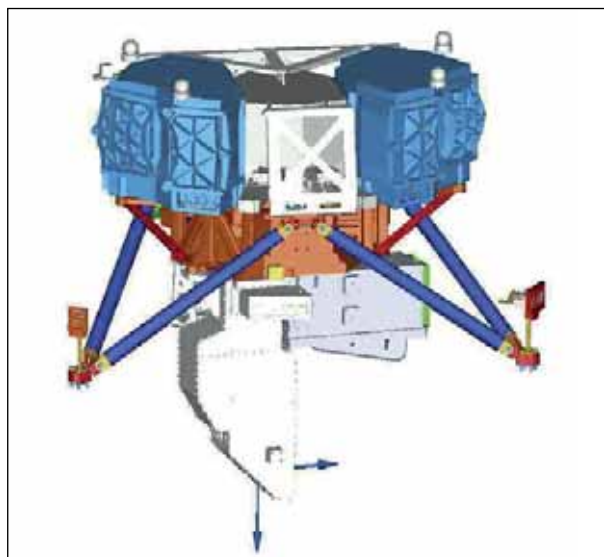


Figure 2: CAD model of the Mid-InfraRed Instrument.

Star formation in the solar neighbourhood: a long-term study in X-ray and infrared radiation

Manuel Güdel, Alessandra Telleschi, Adrian Glauser, Kaspar Arzner, Kevin Briggs, Owen Matthews,
Research Department Particles and Matter, PSI

The study of star formation in nearby galactic molecular clouds is of prime importance for understanding the origin of the elements, the early history of the solar system, the structure and evolution of the galaxy, and the basic physics involved in ionization and accretion processes together with a wide variety of induced chemistry. We are studying a wide array of star-formation processes observationally, numerically and theoretically, concentrating in particular on a unique, long-term investigation of the Taurus star-formation region.

The physics of star formation has evolved as one of the central topics in astrophysics, of general interest not only to stellar astronomy but equally relevant to research fields ranging from solar system studies to cosmology. The formation history of the solar system is of prime interest for our understanding of the present conditions on our planet and it serves as a test bed of theories with which to interpret planet formation elsewhere.

An X-ray and infrared survey

We have obtained large amounts of observing time on the XMM-Newton and Spitzer satellites to conduct a comprehensive survey of the nearest star-formation complex, the Taurus Molecular Cloud, in X-ray and infrared radiation, respectively. X-rays are thought to be produced predominantly by plasma trapped in stellar magnetic fields. The X-ray survey has detected nearly every targeted object and has, for the first time, allowed us to characterize the thermal structure of the emission sources in detail [1]. Clear evidence is found that stars accreting gas supposedly from a circumstellar disk along magnetic field lines produce X-rays less efficiently than non-accretors. The same magnetic fields, connecting the inner edge of the disk with the star, may in fact slow down the stellar rotation, weakening the internal magnetic dynamo and therefore the magnetically induced X-ray output [2].

On the other hand, the survey uncovered a new type of X-ray spectrum to which two spatially distinct plasma sources contribute [3]. A very hot (50-100 MK) component is strongly absorbed presumably by gas streaming toward the star, while a much cooler (1-5 MK) plasma component reveals very little absorption by gas, suggesting that it is formed in shocks at the base of polar jets that can be seen in the optical, albeit at

much larger distances. X-ray production in jets may be important because the photons can efficiently irradiate the surface of the circumstellar disk, thus ionizing it and inducing chemical reactions.

The large infrared survey is presently being analyzed. It probes the entire star-formation region, sensitively recording the presence of dust in circumstellar disks that are eventually becoming important for the formation of planets. It is also contributing to our understanding of the large-scale distribution of dust in the entire region.

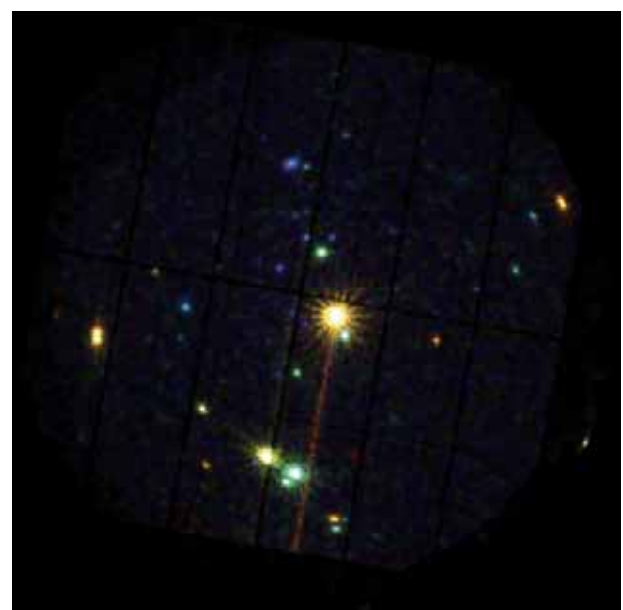


Figure 1: **One of 28 exposures of the XMM-Newton X-ray survey of Taurus. The sources in this half-degree field are colour coded from red to blue, red indicating soft and blue indicating hard emission.**

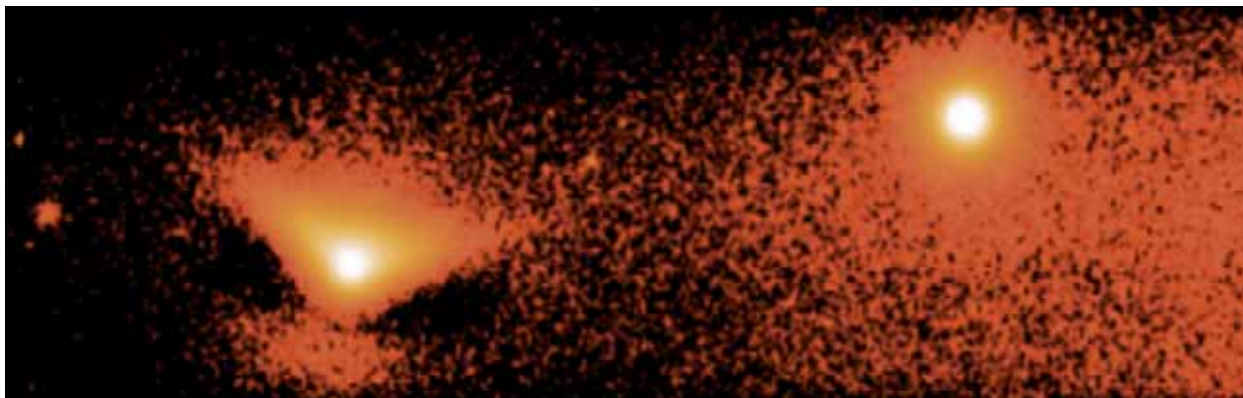


Figure 2: Near-infrared image of a dusty disk around a young, forming star, seen nearly edge-on (left).

Dust content of circumstellar disks

We are studying dusty accretion disks around young stars in Taurus seen nearly edge-on [4]. This configuration permits a detailed interpretation of the disk geometry (thicker disk at larger radii) and, with the help of scattered-light images and infrared spectra, a measurement of the size distribution of the dust grains. The analysis makes use of high-resolution images obtained with the Very Large Telescope and the France-Canada-Hawaii Telescope in the near-infrared range, and flux measurements across the mid-to-far infrared range. A radiative transfer code is used to simulate images and spectra with the goal of finding the fundamental properties of the dust disk. We also use X-rays that penetrate the disk gas to measure the total gas column toward the star. We have thus derived the total mass of this disk (0.1-0.2 times the stellar mass, which itself is 0.1-0.2 times the solar mass), where the gas mass was found to comprise about 99.5% of the total mass. The disk studied here is outstanding for its very large radius, given the small mass of the star. We plan to continue this pilot project toward a systematic study of gas and dust disks in the Taurus region accessed by our surveys.

Instabilities in gaseous accretion disks

Further insight into the behaviour of circumstellar accretion disks can be gained by performing fluid dynamic simulations. Such computations allow us to better predict the evolutionary behaviour of these disks, which is critical to understanding the planet formation process. Our work focuses on the effect of stellar magnetic fields [5], on disk outburst mechanisms [6], and on the physical source of the viscosity which drives accretion.

We use smoothed particle hydrodynamics (SPH), a Lagrangian particle technique, and the FLASH code of the University of Chicago to calculate hydrodynamic and magneto-hydrody-

namic models. Recent results include the first ever successful model of the magneto-rotational instability – a leading candidate for disk viscosity – in SPH [7], and a new way of triggering dust collapse in the inner solar system [8]. Future work will combine a new renormalized viscosity model with advanced cooling in order to model disk outbursts with unprecedented accuracy.

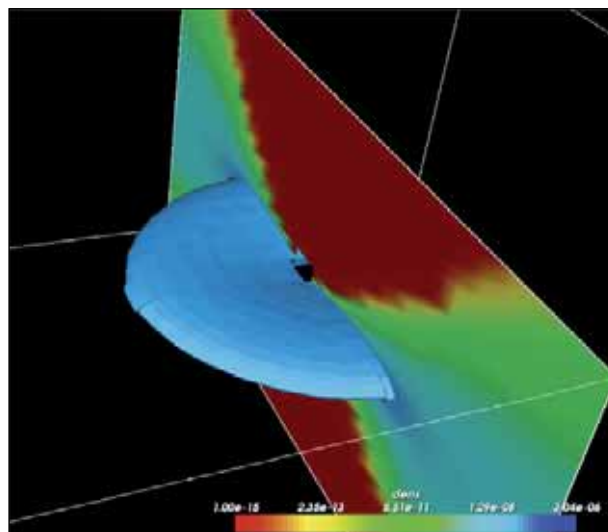


Figure 3: Simulation of a magnetized gas disk. The image is colour-coded, red and blue indicating low and high densities, respectively.

References

- [1] Telleschi, A., et al. 2006, *Astron. Astrophys.*, in prep.
- [2] Briggs, K.R., et al. 2006, *Astron. Astrophys.*, in prep.
- [3] Güdel, M., et al. 2005, *Astrophys. J.*, 626, L53
- [4] Glauser, A., et al. 2006, *Astron. Astrophys.*, submitted
- [5] Matthews, O.M., Speith, R., Truss, M.R., Wynn, G.A. 2005, *Mon. Not. Roy. Astron. Soc.*, 356, 66
- [6] Matthews, O.M., Speith, R., Wynn, G.A. 2004, *Mon. Not. Roy. Astron. Soc.*, 347, 873
- [7] Price, D., Matthews, O.M., Fouchet, L., in prep.
- [8] Fouchet, L., Matthews, O.M., in prep.

Smaller – faster – smarter: new paths for nanoelectronics using templated self-organisation

Detlev Grützmacher, Harun Solak, Christian Dais, Philipp Käser, Elisabeth Müller, Eugen Deckhardt, Yasin Ekinci, *Research Department Synchrotron Radiation and Nanotechnology, PSI*

The demand to increase the circuit density and speed in microelectronics requires the development of new device concepts, since standard complementary metaloxide semiconductor CMOS technology may hit its limits once the gate length of transistors enters the 10–30 nm regime. Quantum information technology relying on information transfer among quantum dots is foreseen as a potential route for beyond CMOS technology. Here we use templated self-organization to prepare 3-dimensional quantum dot crystals containing Ge dots in a Si host crystal. The process involves patterning of Si (100) substrates by X-ray interference lithography at the SLS and reactive ion etching and subsequent overgrowth by molecular beam epitaxy.

Combining the advantages of conventional top-down lithographic techniques with bottom-up approaches like self organization, templated self assembly of semiconductor nanostructures may develop into a potential technology to overcome some of the problems occurring during the scale down of conventional microelectronics. This technology will allow us to deposit semiconductor nanostructures with a narrow distribution in size at predefined sites. Hence, the technology offers the possibility of adjusting structural and electronic properties locally. This way Ge islands can be used as local stressors to fabricate tensile strained Si in the gate area of a transistor increasing the switching speed [1]. The Si/Ge system is of special interest, since it is compatible to Si technology and offers a variety of paths for the realization of spintronics [2,3] and maybe even quantum computing [4]. Si is a particular interesting host material for emerging information technology since the fabrication processes for integrated circuits are so well developed. Moreover, Si naturally consists predominantly of an isotope (Si^{28}) which has no nuclear spin, thus the spin orbit interaction is small leading to spin population lifetimes and coherence times approaching hours and milliseconds, respectively [5,6]. Indeed, several Si compatible spin-based designs for qubit operation have been suggested [2, 7, 8, 9, 10].

Ge dot arrays

In particular, the Si-Ge material system provides promising, scalable architectures for quantum information technology using Ge dots [4]. This may include lateral as well as vertical coupling of Ge dots, thus dense arrays of Ge quantum dots at

specified locations are required. Consequently the deposition of ordered Ge dot arrays at predefined sites, which allow for addressing of single dots, has found quite a lot of attention recently. E-beam lithography [11], ion-beam lithography [12] and optical interference lithography [13] have been performed to fabricate pre-patterns on Si substrates. Whereas the first two approaches write the pattern sequentially for the nucleation site for each individual dot, the optical interference technique allows us to pre-pattern large areas with 2-d arrays in a single exposure. However, optical interference lithography is only able to achieve periodicities of the pattern equal to $\lambda/2$ (λ : wavelength of light). For e-beam and ion-beam lithography the determination of the location of each nucleation site is limited to the resolution of the instrument, which might be in the range of 5 nm, thus interdot distances may vary by a few nanometers. Moreover, the 2-d Ge dot arrays reported so far, have reasonably large inter-dot distances, thus lateral coupling between dots will be too weak [11-13].

Interference lithography

Here the fabrication of ordered Ge dots in 2-dimensional and 3-dimensional arrays, providing structures suitable for vertical and lateral coupling of Ge dots, have been studied using X-ray interference lithography (XIL) to pre-pattern the Si substrates. Interference lithography allows for a very accurate precision and pattern control in the sub-nanometer regime has been achieved [14]. Moreover, the method allows the formation of patterns with less than 30 nm periodicity, improving the lateral coupling strength in densely packed Ge dot arrays.

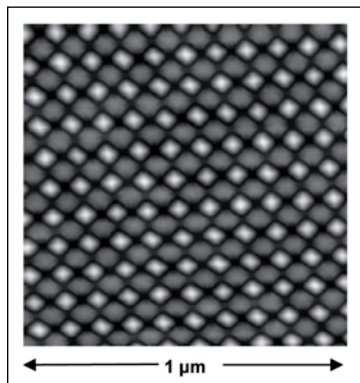


Figure 1a: **AFM image showing a regimented array of Ge dots (bright) on a Si substrate pre-patterned by X-ray interference lithography.**

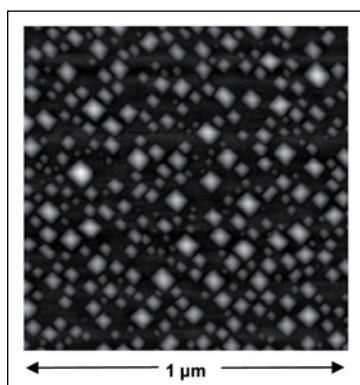


Figure 1b: **AFM image taken from the same wafer as Fig. 1a, but from an unpatterned area.**

In our experiments a Si pattern with a periodicity of typically 90×100 nm was first fabricated by XIL exposure and subsequent reactive ion beam etching (RIE). Next, a 50 nm thick Si buffer layer was deposited at 300°C by molecular beam epitaxy (MBE). After the deposition of the buffer layer, the square like depressions etched into the Si surface by RIE transform into narrow inverted tip like holes of 3-4 nm depth. The deposition of 7 monolayer (ML) of pure Ge at 450°C leads to the formation of (105) faceted islands on the surface as shown in the atomic force microscopy (AFM) image in Figure 1a.

The islands have only been formed at the places where the holes had been fabricated into the Si surface. Clearly, a very uniform array of Ge dots has been formed. For comparison, Figure 1b shows an AFM scan on the same sample, but on a surface area without pattern. Here, the dots nucleate randomly, exhibiting a broad distribution in size. Thus the growth of Ge dots on the pre-patterned surface not only led to close to perfectly regimented arrays of dots but also to a dramatic improvement of the size distribution.

The Ge dots were overgrown with low temperature Si, ramped from 300 - 450°C during deposition, to reduce intermixing of the Ge dots with the Si cap layer, followed by a second Ge dot layer using 5 ML of Ge. Figure 3 shows a high resolution z-contrast transmission electron microscopy cross sectional view of a multiple dot layer structure. The Ge dots appear bright and the Si matrix is dark in this image. Clearly it can be seen that Ge dots in the first layer fill the holes prepared by XIL and RIE. Most likely this can be attributed to capillarity forces.

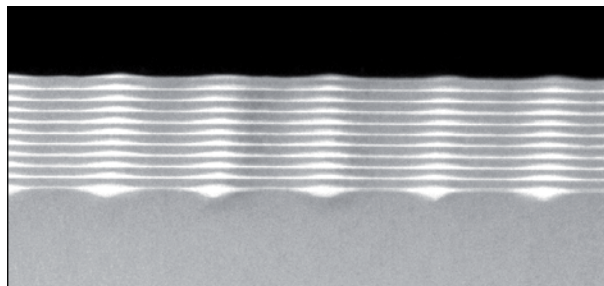


Figure 2: **TEM image (z-contrast) showing a cross section through a 3-dimensional quantum dot crystal of Ge dots (bright) embedded in a Si matrix.**

The Si layer of 7 nm thickness covers these dots and leads to a flat surface. In the second dot layer the dots nucleate on top of the buried dots due to the strain fields of the buried dots [15]. This self alignment of the dots in subsequent layers can be used to build up 3-dimensional quantum dot crystals with high lateral and vertical periodicity.

Acknowledgements

This work is supported by the Swiss National Science Foundation and by the European Commission.

References

- [1] O.G. Schmidt, K. Eberl, IEEE Trans. on Electron Devices, 48, 1175 (2001)
- [2] R. Vrijen, E. Yablonovitch, K. Wang, H.W. Jiang, et al. Phys. Rev. A, 62, 012306 (2000)
- [3] A.M. Tyryshkin, S.A. Lyon, W. Jantsch, and F. Schäffler, Phys. Rev. Lett., 94, 126802 (2005)
- [4] M. Friesen, P. Rugheimer, D.E. Savage, M. Lagally, et al., Phys. Rev. B, 67, 121301 (2003)
- [5] H. Honig and E. Stupp, Phys. Rev. Lett., 1, 275 (1958)
- [6] Jantsch W, Malissa H, Wilamowski Z, H. Lichtenberger, et al., J. of Superconductivity, 18, 145 (2005)
- [7] D. Loss, D.P. DiVincenzo, Phys. Rev. A 57, 120 (1998)
- [8] B.E. Kane, Nature, 393, 133 (1998)
- [9] D. Mozysky, V. Privman, and M.L. Glasser, Phys. Rev. Lett., 86, 5112 (2001)
- [10] J. Levy, Phys. Rev. A, 64, 052306 (2001)
- [11] O.G Schmidt, N.Y. Jin-Phillipp, C. Lange, et al., Appl Phys. Lett., 77, 4139 (2000)
- [12] Karmous A, Cuenat A, Ronda A, et al. Appl. Phys. Lett., 85, 6401 (2004)
- [13] Z.Y. Zhong, A. Halilovic, T. Fromherz, et al. Appl. Phys. Lett., 82, 4779 (2003)
- [14] L.J. Heyderman, H.H. Solak, C. David, et al. Appl. Phys. Lett., 85, 4989 (2004)
- [15] M.G. Lagally, J. of Chemical Education, 75, 277 (1998)

Radiation grafted polymer brushes: a versatile route to functional materials

Celestino Padeste, Patrick Farquet, Harun H. Solak, *Research Department Synchrotron Radiation and Nanotechnology, PSI*; Selmiye Alkan Gürsel, Günther G. Scherer, *Research Department General Energy, PSI*

Polymer brushes are densely packed layers of polymer chains attached at one end to a surface. These materials have attracted tremendous attention as they enable tailoring of physical and chemical surface properties. We have fabricated functional polymer brushes patterned with nanoscale resolution through radiation grafting on polymer substrates exposed at the X-ray interference lithography beamline of the SLS. Such designed surfaces have a high potential for applications in sensors and bio-analytic devices.

The interface between materials defines their interaction to a high extent. Adhesion, friction, wettability, and biocompatibility are typical examples of macroscopic effects determined by physical and chemical surface properties. Polymer brushes provide a special type of interface in that they extend from the surface to which they are bound into the adjacent liquid or gas phase. Due to the flexibility of the grafted chains the contacting phase can penetrate the brush resulting in an intense interaction. The anchoring of the polymer chains on the surface enables their chemical modification in order to achieve defined properties.

In nanopatterned brushes the accessibility of the polymer chains is further increased, a great advantage for biochemical applications, where nanometer sized molecules have to diffuse to specific binding sites. Periodically structured brushes are expected to show strong optical effects when their morphology reacts to changes in the environment. Furthermore, it should be possible to design layers of nanostructured brushes that open and close depending on the environmental conditions.

Patterned brushes on polymer surfaces

Polymer brushes can be grafted onto various polymer substrates in a relatively simple two-step process. In the first step, radicals are created near the polymer surface by exposure of the base polymer to energetic radiation. In the second step, these radicals serve as initiators in a radical polymerization reaction, by which the brush grows directly from the surface. At PSI we take advantage of the interference lithography setup available at the SLS to create large area micro- and nanopatterns of polymer brushes [1]. At this beamline PSI

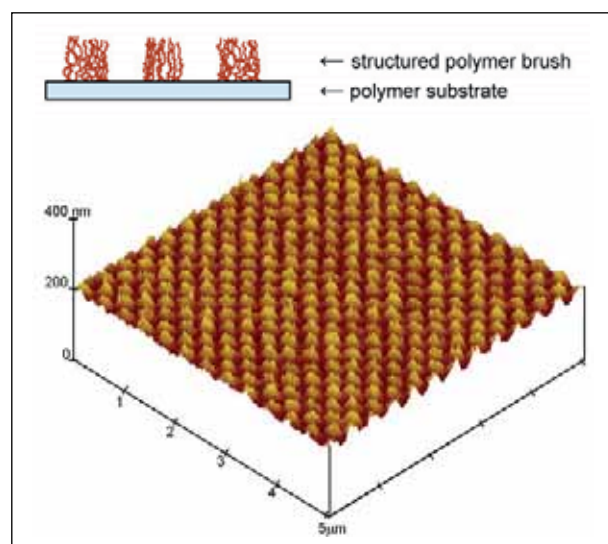


Figure 1: **Schematic view of a patterned polymer brush, and atomic force micrograph of a periodic nanopattern of poly-GMA brushes grafted onto a fluoropolymer using RAFT-polymerization.**

currently holds the world record in resolution (16 nm) of patterns created by photons [2]. The used photon energy of 92 eV is ideal for creation of radicals used for polymer grafting: It is high enough to break chemical bonds but it penetrates only the top few tens of nanometers of the exposed polymer.

Controlling polymer growth

The simplest way of growing brushes is to introduce the exposed samples into solutions of monomers such as acrylates, methacrylates or styrene and to initiate the polymerization reaction by heating. The thickness of the grown brush can be

influenced by a number of parameters including exposure dose, monomer concentration and temperature [1]. However, it was found that this “free radical” polymerization proceeds very quickly, typically leading to a relatively low density of grafted chains. Moreover, the chains grow to be up to several micrometers long, which limit the pattern resolution of such grown brushes. In order to improve the resolution, “living” radical polymerization schemes such as “reversible addition fragmentation chain transfer” polymerization (RAFT) were examined. In this reaction the active radicals are trapped by added RAFT agents, limiting the time available for chain growth. This causes a much slower but more uniform and controllable polymerization and allowed resolution of 100 nm period patterns.

Brush functionalization

We chose to fabricate our brushes out of poly-(glycidyl methacrylate) (poly-GMA) which can be functionalized in a simple way, since many molecules bind to the epoxide group present in every unit of this polymer. For example ionic groups such as sulfonates could be introduced turning the brush into a poly-electrolyte brush which in contrast to the poly-GMA is highly hydrophilic (Fig. 2). Nanopatterns of such modified brushes could be used as a base for the layer by layer deposition of poly-electrolytes to fabricate three-dimensional nanostructured assemblies.

In the current trend of bio-analytics towards highly integrated arrays, structured, functionalized polymer brushes may be of particular importance, because they can provide more binding sites per surface area compared to the usual direct functionalization of the surface, thus increasing the sensitivity of such

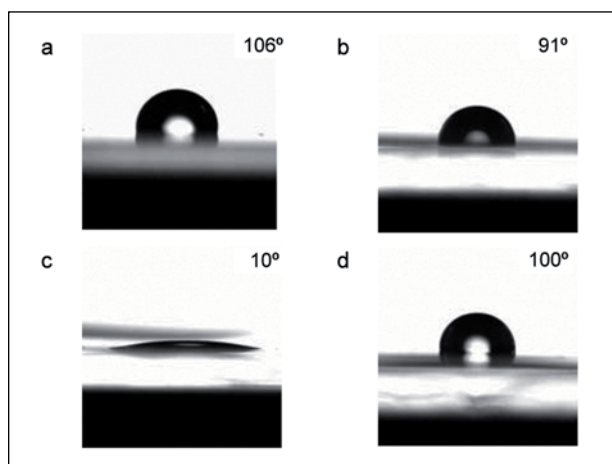


Figure 2: H₂O droplets reveal the wetting behaviour of different surfaces: a) the fluoro-polymer ETFE, b) with grafted poly-GMA brush, c) after sulfonation of the brush, d) after binding dodecylamine. Determined contact angles are indicated in the pictures.

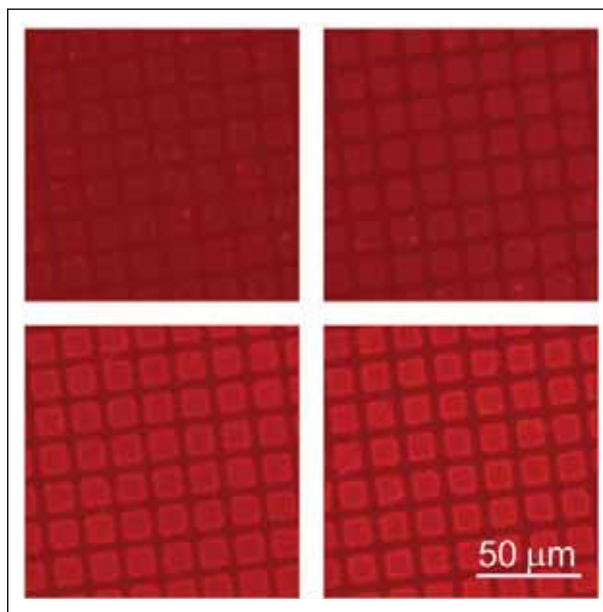


Figure 3: **Fluorescent images of grafted microstructures with increasing amounts of bound fluorescence labelled streptavidin bound in a competitive assay.**

arrays. As a test for bio-functionalization of the patterned brushes, we have attached biotin to grafted poly-GMA. The protein streptavidin selectively and quasi irreversibly binds to biotin. After contact of the biotin-functionalised brushes with solutions of fluorescent labelled streptavidin the grafted micro-structures were clearly observed in a fluorescent microscope, proving the bio-functionality of the system.

Towards smart surfaces

Materials whose properties can be significantly altered by external stimuli are called smart materials. Polymer brushes have the ability to react sensitively to environmental conditions. For example, a reversible switching between high and low wettability has been demonstrated in co-polymer brushes, caused by rearrangement within the polymer layer when it is exposed to different solvents [3]. Nano-structured brushes provide additional degrees of freedom for controlled chain rearrangement, which makes them very promising materials for creating “smart” interfaces with adaptive properties.

References

- [1] C. Padeste et al., J. Vac. Sci. Technol. B, 22, 6, 3191 (2004)
- [2] H. Solak et al., submitted to EIPBN '06
- [3] J. Ruehe et al., Adv. Polym.Sci, 165, 79 (2004)

Dithiocarbamates: functional and versatile linkers for the formation of self-assembled monolayers

Peter Morf, Thomas A. Jung, *Research Department Synchrotron Radiation and Nanotechnology, PSI*;
 Fabio Raimondi, Bernhard Schnyder, *Research Department General Energy, PSI*; Heinz-Georg Nothofer,
 Akio Yasuda, Jurina M. Wessels, *Sony Germany, Materials Research Laboratory*

Self-assembled monolayers (SAMs) are versatile systems used to tune surface properties. The general concept of SAM formation involves the selective binding of molecules to a flat surface followed by periodic rearrangement of the molecular backbone. Here, an alternative binding group, the dithiocarbamate (DTC) group is introduced and new structural and electronic properties are demonstrated. Such conductive SAM linkers have potential for applications in organic electronics and lithographic applications based on SAM.

The unique affinity of sulphur containing functional groups to the almost inert gold surface makes the Au-sulphur-group system a very interesting playground for fundamental studies and applications in the context of the engineering of surface properties. An overwhelming variety of thiol-functionalised molecules has been used to form SAMs [1].

In collaboration with Sony Germany, Materials Research Laboratory Stuttgart, an alternative functional binding group; the dithiocarbamate (DTC) group (see Fig. 1) has been carefully characterized in the context of SAM layer formation. The chemistry of this group differs much from the thiol linker, which is predominantly used in the field of self-assembly on gold. For DTC, the entire N-C-S₂ group forms a resonant structure (Fig. 1a, b). This leads to characteristically different physical and chemical properties like e.g. the metallic behaviour described for 3D nanoparticle assemblies interlinked by aromatic bifunctional DTCs [2]. In our work, DTCs are investigated on their SAM formation abilities and the electronic structure of mono-functional acyclic and bifunctional cyclic DTC derivatives on flat gold surfaces.

Physical chemistry of monolayer formation

In these assessments, the physics and the chemistry of the bond formation at the DTC-gold interface needs to be explored in detail. For this purpose, X-ray photoelectron spectroscopy (XPS) and Cyclic Voltammetry (CV) are used. The properties of three selected compounds, thiram, DEDT and PBDT have been compared to the corresponding properties of the well-known octanethiol molecule (see Fig. 1). The Au-sulphur interaction and the total amount of sulphur abundant on the

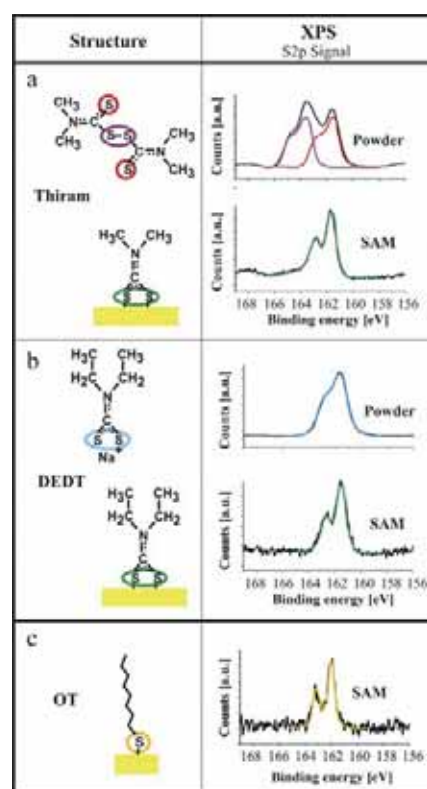


Figure 1: **Acyclic dithiocarbamate and thiol assemblies: XPS data obtained for thiram and Diethyl-dithiocarbamate (DEDT), in comparison to octanethiol (OT) on flat gold surfaces.**

surface has been analyzed using XPS. CV reveals the electrochemical binding characteristics i.e. the reductive desorption of DTCs and thiols from gold substrates.

Self-assembly of DTC

The reactive chemisorption of thiram is evident from the changes of the XPS-sulfur signal of DTC powders compared

to DTC assembled on gold. The disulfide bridge in thiram cleaves at the Au surface, leading to a bidentate state where both sulfur atoms of the dimethyldithiocarbamates (DMDT) bind symmetrically to the surface and are recognized by only one XPS peak corresponding to one chemical species in Fig. 1. Comparing the powder and the monolayer preparation of DEDT, a dithiocarbamate sodium salt reveals that the sodium ions are fully exchanged upon chemisorption of DEDT onto gold.

Through reductive desorption in cyclic voltammetry (CV) we verify (see Fig. 2) the binding properties of thiram disulfides and dithiocarbamates to gold. For DMDT, DEDT and OT SAMs a characteristic desorption and re-adsorption behaviour is observed: The first, reductive sweep is exhibiting a pronounced desorption peak at a characteristic potential. While sweeping back in potential, a small re-adsorption peak occurs. This is related to the fraction of molecules that did not diffuse into the solution and are re-adsorbing on the electrode. Consequently, a second reductive sweep shows a lower desorption peak: a behaviour which is well known from the thiols and provides complementary evidence for SAM formation from thiram and DEDT. The quantitative analysis of the first CV cycle provides a measure for the number of charges involved in the desorption process of the studied SAM. In combination, XPS and CV reveal the desorption stoichiometry: 1 ± 0.2 electron are required to desorb each molecule (for DMDT and DEDT).

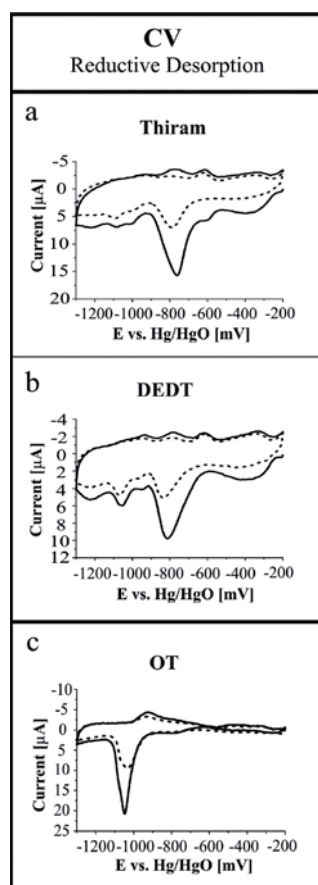


Figure 2: **Reductive desorption in cyclic voltammetry (CV) of acyclic dithiocarbamate and thiol assemblies. CV data obtained for SAMs formed from thiram and diethyldithiocarbamate (DEDT), in comparison to octanethiol (OT) on flat gold surfaces. Two potential cycles (second scan: dotted line) show the electrochemical characteristics.**

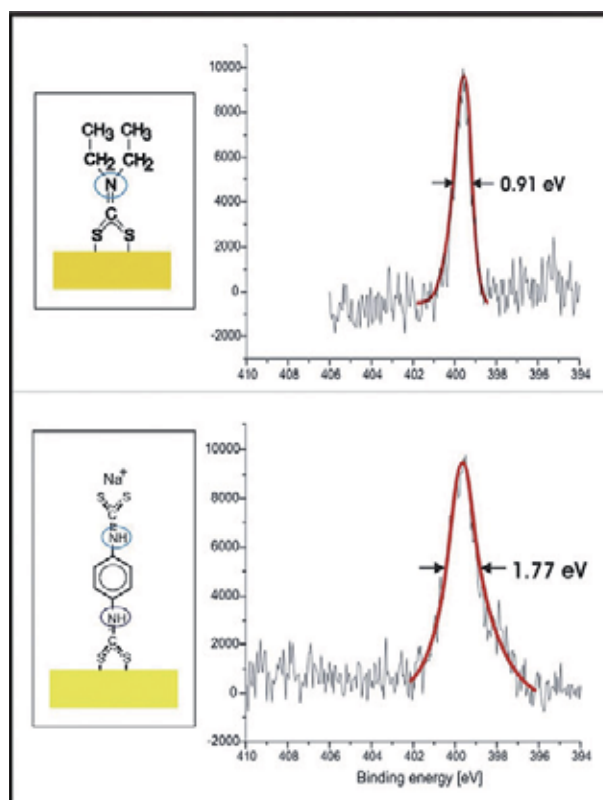


Figure 3: **The N1s XPS peaks of DEDT (top) and PBDT (bottom) show FWHM of 1.0 eV and 1.8 eV resp., which can be assigned to one and two chemical nitrogen species.**

DTCs as linkers for molecular electronics

Bifunctional cyclic dithiocarbamates (see Fig. 3 bottom) likewise form Self Assembled Monolayers, as evidenced with the above mentioned methods. The symmetric DTC-Au bond contains one delocalized electron which is the structural basis for electron exchange with the substrate. A possible consequence of an electronic coupling can be detected in the N1s XPS signal: Comparing the peak shape of monofunctional DTCs and bifunctional DTCs a significant broadening of the N1s peak of the latter (PBDT) can be detected in Figure 3. This is a strong indicator that the electron density on the two nitrogen species in the PBDT SAMs are modified by transferred charge along the molecular backbone from either Au to DTC or Na to DTC. Thus, DTC is a potentially conductive chemical linker between functional molecular layers and metallic substrates and thus offers itself for a large number of applications in organic devices and molecular electronics.

References

- [1] Ed. Ulman A., *Thin Films, Volume 24, Self-Assembled Monolayers of Thiols*, Academic Press, Boston (1998)
- [2] Wessels et al., *J. Am. Chem. Soc.*, 126, 3349 (2004)

The MEGAPIE target commissioning and tests

Friedrich Gröschel, Sergejs Dementjevs, Waihung Leung, Hajo Heyck, Werner Wagner, *Research Department Condensed Matter Research with Neutrons and Muons, PSI*; Marc Diercks, *SCK-CEN, Mol, Belgium*

The MEGAPIE project to design, build, and operate a 1 MW liquid metal target in the SINQ facility is a key experiment on the road to an experimental accelerator driven system (ADS) for transmutation of nuclear waste [1] and for the development of liquid metal spallation targets. The project is supported by an international group of nine research institutes. With the irradiation scheduled for 2006, the target will be one of the first high-power liquid metal targets coupled to a proton accelerator and operating in a spallation source under full service conditions. The target system has been extensively tested out-of-beam.

The MEGAPIE experiment

The target is designed for a beam power of 1 MW and 6 Ah of accumulated current. It will contain about 90 l of lead-bismuth eutectic serving as target material and primary heat-removal fluid. The heat deposited by the proton beam will be removed by forced convection using an in-line electromagnetic pump with 4 l/sec capacity. The heat will be evacuated from the target through 12 mono-wall cooling pins via intermediate oil and water cooling loops. The beam window made of the martensitic steel T91, will be cooled by a jet of cold LBE of about 1 m/sec extracted at the heat exchanger exit by a second EM pump from the LBE mainstream.

Test programme and results

The goal of the test programme was to prove the proper functioning of the system and the thermal hydraulic performance. The tests should allow the validation of the design assumptions and model calculations and should also extrapolate to the behaviour in SINQ. Figure 1 shows the target installed in the test facility at PSI.

The tests carried out comprised

1. EM pump performance and flow meter calibration tests, during which the target was equipped with a small calibration loop in the beam window position as shown in Figure 1.
2. Thermohydraulic tests to determine the heat removal capacity and the ability to comply with thermal transients imposed



Figure 1: **View of the target in the test facility. The target is thermally insulated and equipped with a small bypass flow calibration loop at the bottom.**

by beam trips or interrupts. In this campaign, the target was equipped with a 200 kW heater rod bundle at the beam window location to simulate the heat deposition of the proton beam. Figure 2 shows a typical recording during a test campaign.

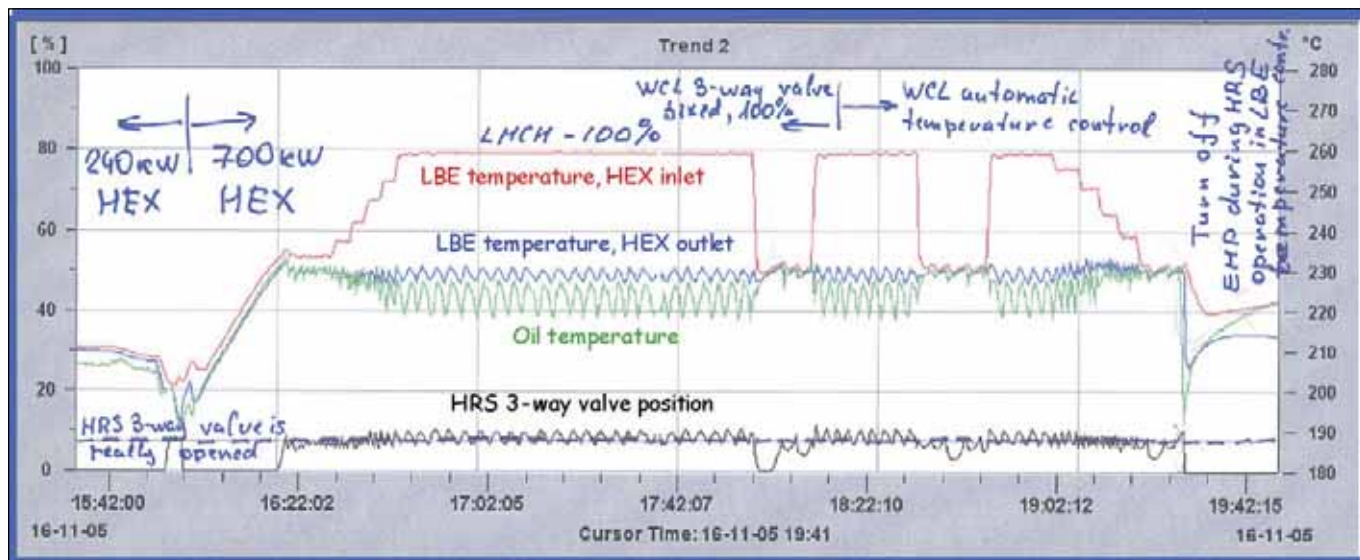


Figure 2: Test sequence recording to check the performance of the 700 kW intermediate heat exchanger and the temperature control of the system.

3. Operational tests, during which preheating, filling and draining as well as standard operation of the target in its final configuration was practised. In this configuration, the beam-window-cooling by the bypass jet-flow was visualized by infrared thermography. Figure 3 shows a radiograph of the beam window area of the target and the IR-image of the beam window.

The tests confirmed:

- The good functioning of the target with liquid lead-bismuth. All operations to run the target could be properly executed.
- The performance of the electromagnetic pumps according to design specifications. The integrated electromagnetic flowmeters, however, did not meet the specified accuracy. The effect of temperature fluctuations and electric fields induced by the nearby pumps could not be fully eliminated.
- Adequate hydraulic performance and the capacity to extract the expected heat deposited by the beam. The control to maintain a constant LBE temperature during thermal transients by regulating a flow bypassing the intermediate heat exchanger in the oil loop functioned properly at full heater power. At low power input, the strong non-linearity of the 3-way valve led to an open-close characteristic causing temperature fluctuations in the system which were however still acceptable.

predictions made during the design phase. Based on these findings, proper functioning in beam can be expected when the system goes into operation.

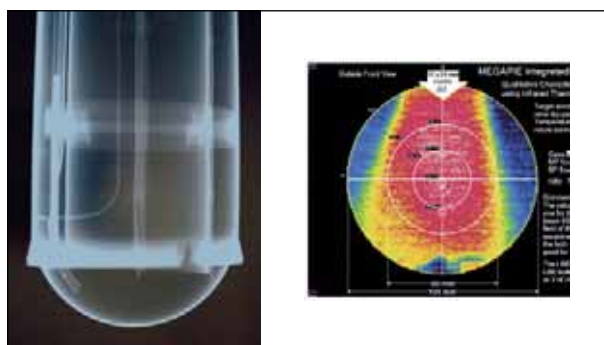


Figure 3: Radiograph of the beam entrance window area (left). The beam will enter from below. On the left side, the bypass flow tube is directed to the centre of the beam window. Right: infrared image of the beam window with strong bypass flow, demonstrating the good coverage of the beam entrance window and hence a good cooling function.

References

- [1] G.S. Bauer, M. Salvatores., G. Heusener: MEGAPIE, a 1 MW pilot experiment for a liquid metal spallation target; J. Nuclear Mat. 296 (2001) 17-35

Conclusions

The target commissioning and tests confirmed the proper functioning of the system. The performance was close to the

Release of mercury from liquid eutectic lead-bismuth alloy under different gas atmospheres

Jörg Neuhausen, *Research Department Particles and Matter, PSI*

The quest for neutron sources of ever increasing intensity is driven by various scientific applications as well as technologies such as accelerator driven systems (ADS) for the transmutation of long-lived nuclear waste. The construction of high power spallation neutron sources requires the development of new technologies such as the use of heavy liquid metal targets. Knowledge about the behaviour of volatile radioactive species in the liquid metal is of utmost importance with respect to the safe operation of such systems.

Spallation targets have numerous applications ranging from spallation neutron sources for scattering experiments, to Radioactive Ion Beam (RIB) facilities, to new technologies such as the transmutation of long-lived nuclear waste using accelerator driven systems (ADS) [1]. In an endeavour to design more intense neutron sources, the use of heavy liquid metals as spallation targets has many advantages. For example, radiation damage does not play a role in the liquid metal, and the target material itself is used as the primary coolant for heat removal. However, the liquid metal also acts as a solvent and reaction medium for nuclear reaction products that are formed by spallation and fission reactions. These products comprise practically the complete periodic table of the elements from hydrogen up to the element with the atomic number $Z+1$, where Z is the atomic number of the heaviest target component. A prototype of such a liquid metal target is planned for operation in the spallation source SINQ at PSI during the irradiation period 2006.

MEGAPIE

The MEGAPIE (Megawatt Pilot Experiment) [2] is a liquid metal spallation target using liquid lead-bismuth eutectic (LBE) as target material. The objective of the experiment is to demonstrate the feasibility of liquid metal target technology. Nuclear reaction products formed in this system range from hydrogen up to polonium. Since the liquid alloy can act as solvent, chemical reactions among these elements will occur to a much larger extent, than compared to a solid target. Possible reactions include formation of intermetallic phases, corrosion processes and formation of oxides with the oxygen contained in the liquid alloy and in oxide surfaces of the construction materials. These products, when transported within

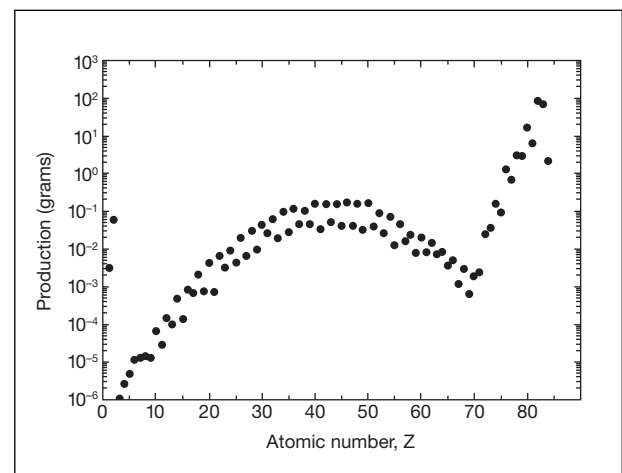


Figure 1: **Element production in a liquid LBE target. Irradiation for 200d with 1.25 mA proton current [3].**

the target system, may form precipitates that can influence the system behaviour. For example, suspended particles may cause abrasive effects on construction materials, or plating can lead to changes in heat transfer. Therefore, a basic understanding of the chemistry in liquid LBE is important. From the radiation safety point of view, the volatilization of radioactive materials is by far the most critical process that occurs in such a target system. According to nuclear calculations [3], volatile elements such as Po, Tl, Hg, Br, I, Rb and Cs are produced in up to gram-amounts (see Fig. 1).

For the licensing of MEGAPIE, an assessment of the volatility of these elements dissolved in liquid LBE is crucial. Among these elements, polonium is prominent because of the high radiotoxicity of the isotope ^{210}Po . Mercury is of high importance because of its rather high volatility. The volatility of non carrier-added amounts of polonium [4], thallium, mercury [5] and iodine [6] dissolved in LBE were studied earlier in our labora-

tory under a reducing (Ar/7%H₂) atmosphere. This atmosphere corresponds to normal operation conditions of a spallation target, where substantial amounts of spallation hydrogen are present. For the assessment of accident scenarios, where the target material can be exposed to air, the influence of oxygen on the release of volatiles has to be examined. In this work we extend our previous studies of mercury release to gas atmospheres with varying oxygen potential. In contrast to previous investigations, realistic concentrations of mercury are used.

Experiments

Mercury samples containing radioactive ²⁰³Hg were prepared by irradiation of a solid Cd-Hg alloy at SINQ and subsequent distillation of Hg. LBE samples containing an amount of Hg similar to MEGAPIE conditions were prepared by a two step dilution series. Finally, a mole fraction of $x_{\text{Hg}} = 6.81 \cdot 10^{-5}$ was obtained. A defined sample geometry for γ -spectrometry was achieved by melting in a quartz boat.

Evaporation experiments on these samples were performed using a method described in [4]. Experimental conditions are compiled in Table 1, γ -ray spectroscopic measurements were performed using an HPGe-detector. A γ -ray spectrum of the sample was recorded before and after each 1h-heating experiment and the fractional release of mercury was calculated from the integrated peak areas of the ²⁰³Hg γ -ray signal at 279.20 keV before and after heating.

Gas composition	p(H ₂ O) [Pa]	Temperature range [K]	Sample weight [g]
Ar/7%H ₂	370±170	474 – 622	10.6 – 11.2
N ₂	1700	448 – 649	7.81 – 11.0
N ₂ /5%O ₂	1700	477 – 935	5.69 – 6.17
N ₂ /20%O ₂	3170	441 – 988	8.06 – 8.38

Table 1: **Experimental conditions for release experiments: duration of each experiment; 1 h.**

Results and Discussion

Visual inspection of the samples shows that under oxygen containing atmosphere a surface oxide layer is formed. The rate of formation of this oxide layer strongly increases with increasing temperature. Figure 2 shows the results of the evaporation experiments compiled in Table 1, together with the results obtained from similar experiments using non carrier-added amounts of ²⁰³Hg dissolved in LBE and an Ar/7%-H₂ atmosphere [5]. Both series of experiments under Ar/7%-H₂ atmosphere show good agreement, with more than 50 % of

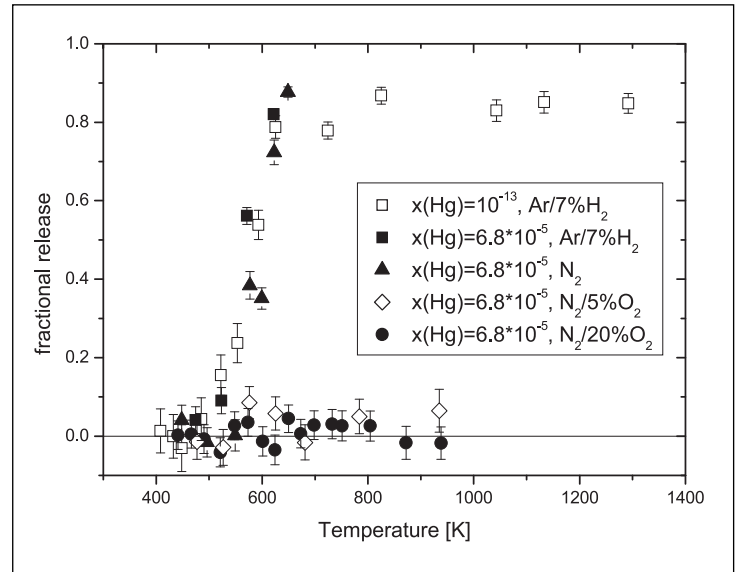


Figure 2: **Comparison of the fractional release of Hg from liquid LBE under different gas atmospheres and different Hg concentrations.**

the mercury released in 1h at 571 K, indicating that the release rate of Hg from LBE scales linear with concentration in the range $10^{-13} \leq x_{\text{Hg}} \leq 10^{-5}$.

The release behaviour under a moist N₂ atmosphere is very similar to behaviour under reducing conditions. When changing to an oxidising environment, however, a drastic reduction of the evaporation rate is observed, together with the formation of the oxide layer. Within the limits of error no significant release of Hg is found for temperatures up to 935 K for both oxygen concentrations. The fact that a relatively low oxygen concentration such as 5% O₂ substantially decreases the evaporation rate of mercury is valuable information in context with safety assessments. For the MEGAPIE target a partial inertisation (reduction of the oxygen content to 12 %) of part of the target complex is discussed for fire protection reasons. The results of this study indicate that even under these conditions a strong reduction of mercury release can be expected due to the formation of an oxide layer.

References

- [1] B. F. Gromov et al., Nucl. Eng. Des. 173 (1997) 207.
- [2] M. Salvatores, G. S. Bauer, G. Heusener, PSI-Report Nr. 00-05, Paul Scherrer Institut, Villigen, Switzerland, 2000.
- [3] L. Zanini et al., PSI Report Nr. 05-12, Paul Scherrer Institut, Villigen, Switzerland.
- [4] J. Neuhausen, U. Köster, B. Eichler, Radiochim. Acta 92, 917 (2004).
- [5] J. Neuhausen, B. Eichler, Radiochim. Acta 93 (2005) 155.
- [6] J. Neuhausen, B. Eichler, Radiochim. Acta, in press.

Low emittance gun project (LEG) – X-ray free-electron laser

René Bakker, Stefan Adam, Andreas Adelman, Ake Andersson, Alexander Anghel, Michael Böge, Micha Dehler, Romain Ganter, Chris Gough, Sladjana Ivkovic, Simon Leemann, Kevin Li, Martin Paraliiev, Marco Pedrozzi, Frédéric Le Pimpec, Jean-Yves Raguin, Leonid Rivkin, Thoms Schilcher, Volker Schlott, Lothar Schulz, Andreas Streun, Albin Wrulich, *Department of Large Research Facilities, PSI*; Robin Betemps, Walter Pfister, Daniel Rossetti, Sasa Zelenika, Charles Zumbach, *Department of Logistics, PSI*; Jens Gobrecht, Gerhard Ingold, Eugenie Kirk, Harald Sehr, Daniel Sütterlin, *Research Department Synchrotron Radiation and Nanotechnology, PSI*; Arno Candel, *ETH Zurich*; Evelyne Meier, *EPF Lausanne*

In 2003 the PSI initiated the low emittance gun project (LEG) with the aim of constructing an ultra-bright electron source based on field-emission. This development is particularly interesting for the realization of the next generation of X-ray light sources, because it paves the way for a more economic approach to their construction and operation. At present the fabrication and tests of the electron source are in progress and complemented with a case study for an X-ray free-electron laser light source. This could grant the SLS science community access to the femto-second time domain with atomic resolution.

Introduction

The X-ray free-electron laser (XFEL) is presently considered to be the most promising candidate for extending the capabilities of synchrotron light sources. That is, they may provide six orders of magnitude more peak power and offer the opportunity to perform experiments with femto-second resolution. The successful operation of an X-FEL (target 0.1 nm or 12.4 keV) depends on the combination of high peak current (~kA) and a low emittance of the electron beam. Especially the latter is challenging since state of the art electron-gun technology inhibits operation in the X-ray spectral range with a short undulator period and low electron beam energy. Consequently this precludes a small size and hence, cost effective construction of such a device.

For this reason PSI pursues a series of innovative developments, which are crucial for the economics of an X-FEL facility, i.e., the low emittance gun (LEG) project. Work is being undertaken in the following fields:

- Field emission electron source – single-tip field-emitters and field-emitter arrays are investigated as low emittance electron sources.
- High gradient acceleration – a fast acceleration of the beam into the relativistic regime is mandatory to minimize space charge effects.
- Acceleration concept – only RF accelerators can provide the necessary beam energy. Care must be taken to maintain the low emittance in the acceleration process.

The electron source

Field emitters have an intrinsic low transverse emittance but are sensitive to electric breakdowns when operated at high current. Pushing the peak current is therefore important for LEG. Figure 1 depicts the progress obtained.

The graph is a compilation of single field-emitter tips (FE) and arrays (FEA). The latter reduces the current from a single tip and is more likely to provide the ultimate low emittance. Figure 2 shows an example of the FEA production process, which is in progress at the laboratory for micro- and nanotechnology at the PSI.

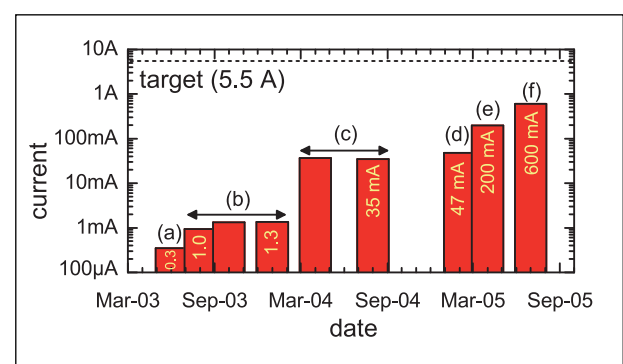


Figure 1: **Peak current obtained: (a) initial DC tests with (b) improvement of the experimental setup, (c) 100-ns pulsed arrays (Spindt) with (d) improved cleaning, (e) modification of the arrays to sustain 8 ns pulses, and (f) a single tip with laser induced field-emission.**

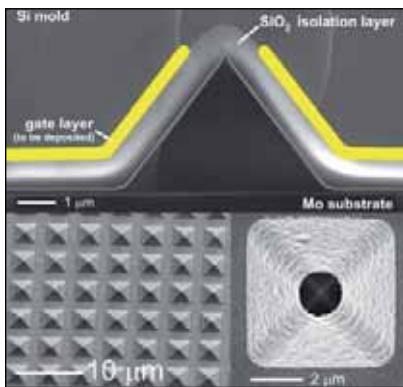


Figure 2: **Examples of FEA production at the PSI.** Top: slice image of single emitter under production. Bottom left: an array of uncovered Mo tips. Bottom right: single tip covered with a Ta gate layer.



Figure 3: **100 kV DC test setup for first beam-diagnostics of field emitters: current, transverse profile and emittance.**



Figure 4: **High voltage tank of the 200 ns, 500 kV pulser.** The machining is designed as a test-environment that feeds pulses to a cathode and also permits a fast replacement of them in the case of electrical breakdowns.

2005 saw a significant improvement in the available diagnostics to characterize the performance of field-emitters. The example presented in Figure 3 is a test setup to diagnose the electron beam at an energy of 100 kV.

High gradient acceleration

The low emittance from field-emitters can only be maintained if the electrons are accelerated fast enough to relativistic energies. The tank depicted in Figure 4 houses a 500 kV pulsed diode configuration, which will permit acceleration gradients that exceed the values that can be obtained with RF accelerators. Major parts of this setup were constructed in 2005 and initial operation is planned for the first half of 2006.

Roadmap to an X-FEL

Even after the first pulsed acceleration the electron beam remains fragile and requires a sophisticated acceleration scheme to preserve the low emittance. Figure 5 shows the first acceleration cavities, specifically designed at double frequency to maintain the emittance while boosting the energy to 4 MeV. A prototype of this cavity is presently under construction. It is intended to mount it at the exit of the pulser shown in Figure 4.

However, in view of the performance of an X-ray FEL, the first 250 MeV of acceleration are critical because most of the potential emittance dilution can take place in this section of the machine. As a next step of acceleration the LEG project therefore concentrates on the design of a 250 MeV test accelerator. This accelerator, which incorporates the existing hardware of LEG, is intended to eventually serve as an injector for a future X-FEL. Prior to this task it should first serve as an experimental test-environment to evaluate the technological risks of the

construction of such a FEL before full investment in the project. The intention is to finalize the technical design of an X-FEL user-facility after the appropriate experience has been obtained.

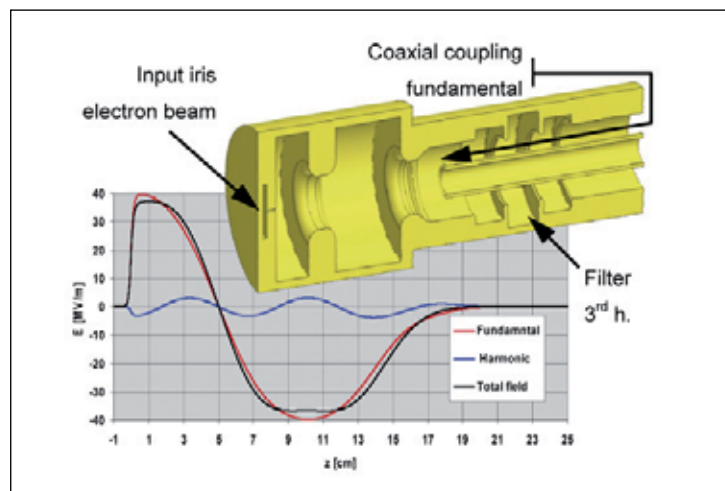


Figure 5: **Development of a double-frequency RF gun (1.5 and 4.5 GHz) for improved emittance preservation in the initial phase of the acceleration process.**

Further information:
<http://leg.web.psi.ch>

Electron beam stabilization for the European X-FEL

Volker Schlott, Micha Dehler, Boris Keil, Andrei Lunin, Goran Marinkovic, Patrick Pollet, Thomas Schilcher, Peter Spuhler, Daniel Treyer, *Department of Large Research Facilities; PSI*

Electron beam stabilization represents the Swiss contribution to the preparatory phase of the European X-FEL project. In this context, an ultra fast feedback system is presently being developed at PSI for bunch-by-bunch correction of the electron beam position after the main accelerator of the European X-FEL to a micrometer level.

The construction of the European X-ray Free Electron Laser (X-FEL) facility [1] is presently proposed at the Deutsche Elektronen Synchrotron (DESY) in Hamburg, Germany. As a user facility based on superconducting linear accelerator technology, it will provide X-rays of unprecedented properties in terms of peak and average brilliance, coherence, pulse duration, and time structure at a target wavelength of 1 Å. Switzerland, together with eleven other countries, has joined the preparatory phase of the European X-FEL project by signing a memorandum of understanding that allows Swiss research institutes to participate in the project with so called “in-kind” contributions. In this context, PSI has taken over the responsibility in the field of electron beam stabilization by developing a so-called “intra bunch train” feedback (IBFB) system for the European X-FEL. A prototype IBFB is designed and fabricated throughout the funding period from 2004 until 2007 and will be tested under real SASE operating conditions at the VUV-FEL test facility at DESY, Hamburg.

Beam stability requirements for the IBFB

First start-to-end simulations of the European X-FEL and the VUV-FEL test facility indicate that transverse bunch-by-bunch beam motions up to the order of one tenth of the rms beam sizes ($\sigma/10$) along the undulators are still acceptable for

stable SASE (self amplified spontaneous emission) operation at the target wavelengths of 1 Å for the X-FEL and 6 nm for the VUV-FEL. The rms beam sizes at these locations will be in the order of 30 – 50 μm . The specific time structure of the superconducting drive accelerator will provide very long bunch trains of up to 800 μs with bunch spacing between 200 and 1000 ns at repetition rates of up to 10 Hz. Table 1 summarizes the specifications for the transverse IBFB system as presently designed in a prototype version by the European X-FEL project group at PSI.

Trans. IBFB Specifications	VUV-FEL	X-FEL
required bunch-by-bunch stability – at location of IBFB – along undulators	$< \sigma/10$ 5 – 15 μm < 5 μm	$< \sigma/10$ 3 – 10 μm < 3 μm
maximum beam position offset * – at location of the pick-ups	$< 10 \cdot \sigma$ < 1500 μm	$10 \cdot \sigma$ < 1000 μm
bunch-by-bunch resolution	$\leq 2 \mu\text{m}$	$\leq 1 \mu\text{m}$
system latency	< 1000 ns	< 200 ns

* this defines the maximum range of beam offset from bunch train to bunch train, where the IBFB will still be able to apply corrections to the specified values

Table 1: **Specifications for the transverse IBFB system.**

Both parameter sets define the requirements for an active beam stabilization system, which needs to be a low latency feedback capable to correct the electron beam position on a bunch-by-bunch basis to the micrometer level.

Design concept of the transverse IBFB

One of the most stringent requirements for the IBFB to achieve effective suppression of beam motion along the bunch trains of the VUV- and European X-FEL is the ultra fast response time

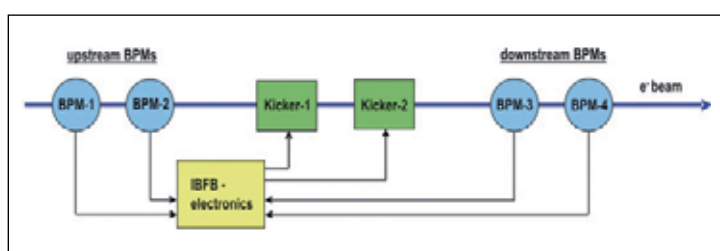


Figure 1: **Topology of the transverse IBFB system.**

of the complete feedback chain of < 200 ns. In this respect, the topology of the transverse IBFB (see Fig. 1) uses two pick-ups (BPM-1 and BPM-2) upstream of the electromagnetic correction kickers for horizontal and vertical beam position measurements. The BPM signals travel in the RF cables in the same direction to the IBFB electronics as the electron bunches in the beam pipe, thus minimizing the latency of the overall system. The corrections are calculated in the IBFB electronics and applied to the following electron bunches by two electromagnetic kickers. Instant verification of the corrected beam positions can be achieved by the two downstream BPMs (BPM-3 and BPM-4). Thus, static and dynamic effects like kicker scaling errors or inaccuracies of the optics model can be detected and eliminated by dynamic adaptation of the applied feedback model. Moreover, it will be possible to predict long range beam movements from bunch train to bunch train and correct repetitive disturbances through slow adaptive feed forwards using look-up tables. The main IBFB components and sub-systems are listed below:

- BPM pick-ups
- Electronics:
 - analogue signal conditioning (RF front end)
 - high speed digitization of RF front end signals (ADC)
 - digital signal processing unit using fast programmable logic and high throughput data links
 - high speed digital-to-analogue conversion to set the kick amplitudes for beam corrections
 - power amplifiers to drive the electromagnetic kickers
- Electromagnetic kickers

A modular design approach will be chosen for the IBFB electronics, allowing the use of similar hardware for all correction planes. Gigabit optic links based on the Rocket I/O standard will provide the possibility of sharing all relevant beam-based information with other accelerator sub-systems such as low level RF or other electron and photon beam diagnostics devices on a real time basis. In this respect, the IBFB can be considered as the most central part of a general beam stabilization concept for the European X-FEL.

Status of IBFB sub-systems

Based on electromagnetic interference measurements at the VUV-FEL test facility, two types of pick-ups are designed to obtain sub- μm single bunch beam position resolution. A resonant strip-line BPM at 1.625 GHz (see left side of Fig. 2) will be used for the IBFB prototype tests at the VUV-FEL, while a cavity BPM at an operating frequency of 4.3875 GHz is designed to meet the more stringent requirements at the European X-FEL. Detailed measurements of the electromagnetic properties

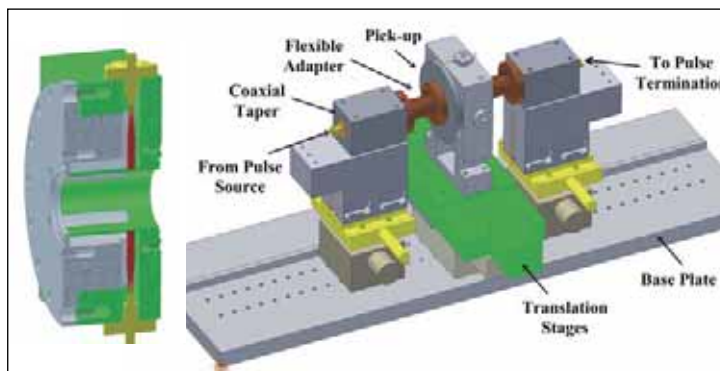


Figure 2: 3-D mechanical drawings of the IBFB resonant strip-line BPM and the pick-up test-bench.

of the pick-ups in combination with the analogue signal conditioning electronics (RF front end) and the analogue-to-digital converters (ADC) will be performed on a pick-up test-bench (see right side of Fig. 2) in the SLS diagnostics lab.

To account for the low latency requirement of the IBFB, the RF front end will deliver flat-top pulses of only 10 – 20 ns duration to the digital processing unit. Large beam excursions and bunch current variations will be eliminated through automatic gain adjustment and programmable offsets. In this way, the ADC – a state-of-the-art AT84AS001TP from ATMEL with 12 bit resolution at 500 MS/s and 3 GHz analogue bandwidth – will always operate at its full range providing the highest resolution. The digital processing units will be implemented in VME-bus technology representing the latest control system and diagnostic standard at PSI. A modular design approach for the digital electronics will allow the use of similar hardware for all correction planes (both transverse and a future longitudinal) of the IBFB. For each plane, eight ADCs will be needed for sampling of the beam position sensitive signals provided by the RF front ends. The final topology of the digital electronics is still under investigation and depends strongly on the heat dissipation and the form factor of the high speed ADCs. The calculation of beam position corrections will be performed on an upgraded version of the VPC carrier board [2] developed at PSI by using digital signal processors (DSP) and field programmable gate arrays (FPGA). In this way, low latency and highest flexibility to adapt the accelerator optics model can be guaranteed to achieve optimum electron beam stabilization.

References

- [1] See e.g. web-page: <http://xfel.desy.de/>
- [2] B. Keil et al., Proc. DIPAC'05, June 2005, Lyon, France, 140 (2005).



- 84 Swiss Light Source
SLS
- 88 Spallation Neutron
Source SINQ
- 92 Swiss Muon Source
 μ S
- 94 Proton accelerator
- 100 Tandem accelerator

PSI provides excellent facilities and support for competitive research and development in condensed matter research. These are used for in-house research, for collaboration with external partners and by the international user community. The research departments involved are Synchrotron Radiation and Nanotechnology (SYN); Condensed Matter Research with Neutrons and Muons (NUM); Particles and Matter (TEM). The research departments and user labs are supported with the technical expertise of the Department of Large Research Facilities (GFA). Continually developing infrastructure and equipment, the GFA and user labs report here on upgrades to the proton accelerator, new instruments at the Swiss Muon Source (μ S) and operating developments at the Swiss Light Source (SLS), Spallation Neutron Source (SINQ) and the Tandem accelerator facilities. The new COMET cyclotron came into operation in 2005 and the Swiss contribution to the European X-ray Free Electron Laser facility is in the prototype phase.

This report only highlights a selection of the work done at PSI in the past year; for more information about these, and many other ongoing projects or to apply to the user lab as a visiting scientist, visit our website (<http://www.psi.ch/forschung/benutzerlabor.shtml>).

Operation of the Swiss Light Source in 2005

Andreas Lüdeke, Anton C. Mezger, *Department of Large Research Facilities, PSI*

The Swiss Light Source was very successfully operated in 2005. All key statistics such as availability, beam integral or mean time between failures, have improved in comparison with previous years. While the facility continues to be extended by the implementation of new equipment, some activities had to be delayed due the late delivery of critical components.

Operation

In 2005 the SLS again succeeded in improving in terms of availability and mean time between failures, as it has done so in each year since the start of operations in 2001. The total downtime was only 82 hours or 1.6% of the scheduled user operation. Therefore we had more than twice as much reserved compensation time as downtime.

In some aspects, this year had fewer activities than expected. The installation of the FEMTO chicane and the super-bend dipole magnets was postponed to the first half of 2006, due to a delay in the magnet delivery.

We succeeded in doubling the vertical storage ring acceptance by a careful realignment. This leads to an increase of beam lifetime from 12 to 15 hours for our standard operating mode.

An improved beam based alignment now allows us to reduce the coupling close to the design value. This enables us to provide a twofold enhanced brightness for micro focus experiments.

A new power-save mode was introduced for the ramped booster power supplies that will save about 1 GWh per year. The PSI digital controllers of these power supplies facilitated this mode.

Further enhancement of the filling pattern feedback now allows an electron source charge modulation during a refill. This new filling mode helps to suppress the higher order modes of the cavities and will allow us to reach stable operation at the design beam current of 400 mA. This will become the default for user operation after the shutdown in April 2006.

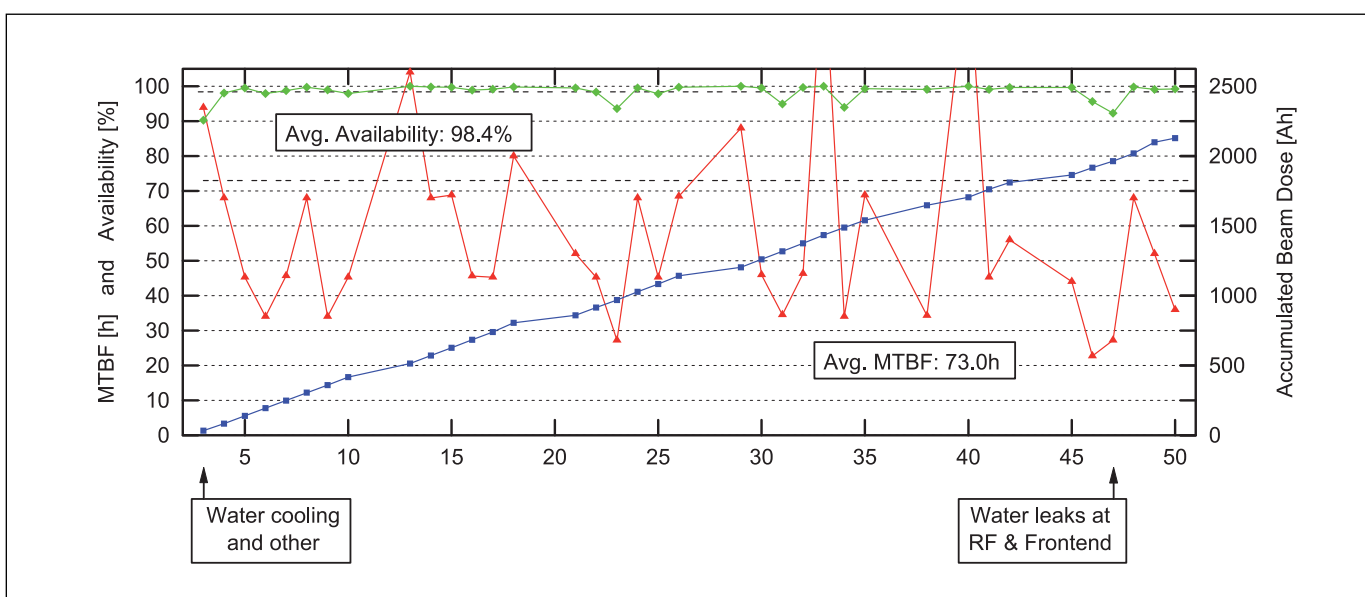


Figure 1: SLS weekly availability, mean time between failures and accumulated beam dose.

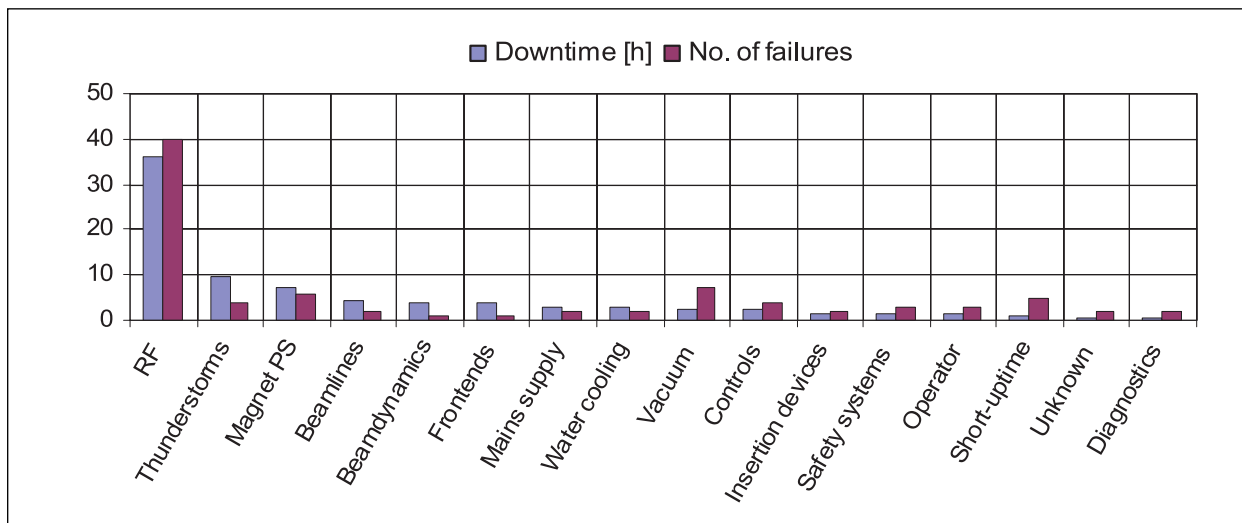


Figure 2: Beam downtimes per system in 2005.

Statistics

The main statistics of the SLS operation are shown in Figure 1. An outstanding average availability of 98.4% was reached during the user beam time. The mean time between failures (MTBF) of the storage ring reached more than three days. The remaining outages were analysed for the failure sources (see Fig. 2). The RF contributes to about 40% of the downtime but these 36 hours compare very well to the 98 hours of RF outages in 2002.

The mean time to recover (MTTR) after a beam loss went down drastically from 2.2 hours in 2004 to 1.2 hours in 2005. Figure 3 shows the distribution of the duration of downtimes in 2005. Downtimes below 10 minutes were delayed starts of user operation or unusable short uptimes. In more than 2/3 of the cases the downtime was below 30 minutes.

The injector outage decreased to 30 hours. In contrast to the previous year the booster was the main contributor to the injector outage this year. The outages were caused by a vari-

ety of minor failures: ramped power supplies, Booster RF, gun control problems and others.

The operational data is summarized in Table 1. Since the beginning of 2005 each beam loss is automatically documented and individually analyzed. This allows us to identify transient failure sources quickly and to fix them before they reoccur.

Beam Time Statistics Swiss Light Source	2005		2004	
	h	%	h	%
Total beam time	6608 h	75%	6616 h	75%
• User operation	4952 h	56%	5116 h	58%
– incl. compensation time	175 h	2%	175 h	2%
• Beamline commissioning	792 h	9%	696 h	8%
• Setup + development	864 h	10%	804 h	9%
Shutdown	2152 h	25%	2168 h	25%
User operation downtimes	67		85	
• unscheduled outages	82 h	1.6%	190 h	3.7%
• injector outage	30 h	0.6%	46 h	0.9%
Total beam integral	2129 Ah		1845 Ah	
Availability	98.4%		96.3%	
Availability after compensation	101.6%		99.7%	
MTBF	73.0 h		59.5 h	
MTTR (mean time to recover)	1.2 h		2.2 h	

Table 1: SLS Operation Statistics.

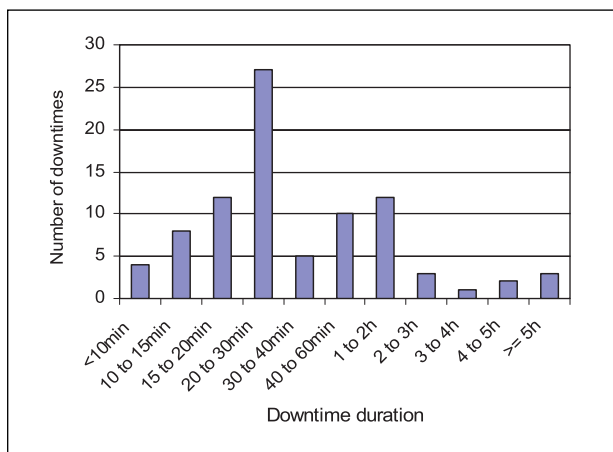


Figure 3: Distribution of the duration of downtimes.

Outlook

The commissioning of the FEMTO chicane is planned for April 2006. The installation of three super-bends will follow in July. Both are major changes to the machine and will be demanding for SLS operation. In addition we will install two insertion devices and five dipole beamlines will start commissioning in 2006. This doubling of the number of beamlines will be the major challenge for the SLS operation in 2006.

Short pulses at SLS: sources for ultrafast science

Leonid Rivkin for the SLS team,
Large Research Facilities and Synchrotron Radiation and Nanotechnology, PSI

Short pulses of tuneable energy X-rays are used routinely at the SLS beamlines to follow physical and chemical processes on picosecond scale. With the FEMTO project scheduled for commissioning for the first half of 2006 the researchers will gain access to thousand times shorter pulses, allowing them to study the dynamics on femtosecond scale.

Very short X-ray pulses make it possible to see the time evolution of small structures at the atomic scale. In static pictures the fast motion is averaged out and the structures look blurred. Nature stands still during the short time exposures, posing for a picture. Taking lots of such snap shots, making movies, we advance our understanding of *function*, based on *structural* studies.

The time scales for some of the fundamental processes involved in the major fields of applications of synchrotron light are represented in the figure below.

How short are short pulses from SLS?

The synchrotron light pulses emitted from the SLS storage ring are as short as the length of the stored electron bunches. The energy lost by the electrons to synchrotron radiation at every turn is restored to them in radiofrequency (RF) 500 MHz

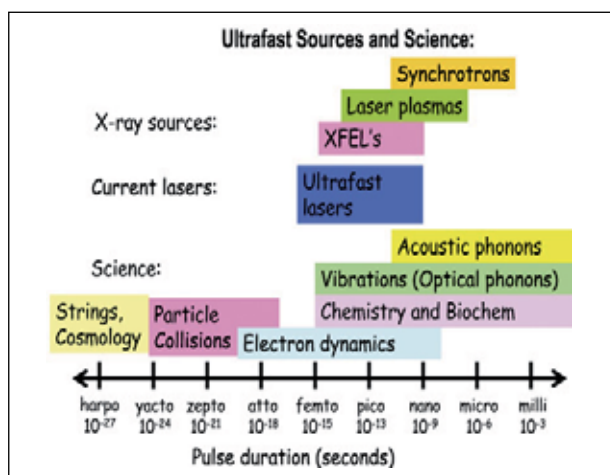


Figure 1: **Relevant time scales and some of the sources of short light pulses.**

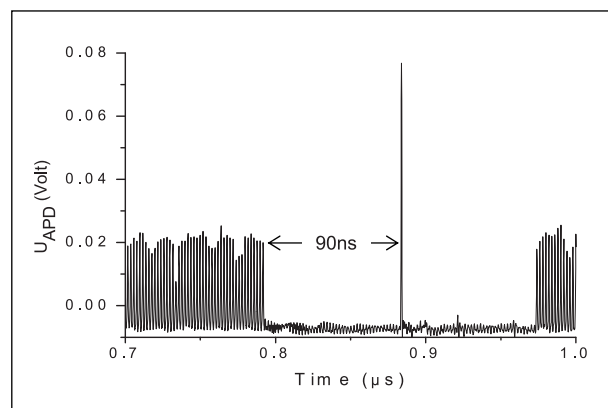


Figure 2: **Fill pattern in the SLS storage ring with a single bunch in the middle of the bunch train gap.**

accelerating cavities. This process imposes a natural time structure on the electron beam. There are maximum of 480 equidistant bunches that can be stored in the ring. Their length is about a centimeter (Full Width Half Maximum, FWHM) or 30 picoseconds and they are separated by a gap of 2 nanoseconds. The standard filling pattern of the SLS storage ring leaves a gap of 90 empty bunches or 180 ns in the bunch train. This gap is one of the measures needed to insure the stability of the electron beam at high current, the other being a higher harmonic superconducting RF system that lengthens the electron bunches by almost a factor of 3. A single bunch in the middle of the gap is then routinely used by the experimenters interested in time resolved studies. This arrangement provides enough time between the light pulse from the single bunch and the light from the rest of the bunch train to make sure that measurements can be performed with 100 ps resolution. The total stored current in the machine as well as the current in the single bunch is kept constant in time with top-up injection.

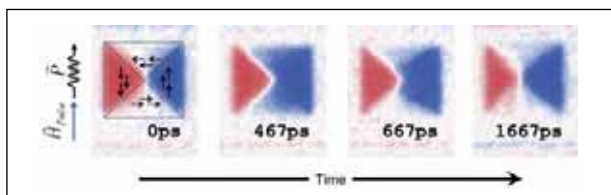


Figure 3: The “dance of magnetic domains” seen with synchrotron light.

In an experiment that investigated the dynamics of micron size magnetic domains it was possible to record the time evolution of the magnetization of these domains after they have been excited by pulsed magnetic field [1], as illustrated in the figure below.

Several other experiments at SLS were able to perform time resolved studies with 100 ps resolution. An important aspect for the success of these studies was the fact that the single pulses were available during the normal user operation, without the need for dedicated single bunch running time. Machine studies have been performed to optimize the length and intensity of single pulses in this “parasitic” operation, allowing improvement of the time resolution down to 70 ps. Further reduction down to 30 ps is possible in a dedicated single bunch mode of operation without the bunch lengthening cavity.

FEMTO in 2006 and beyond

In the next large step in resolution, a thousand times shorter X-ray pulses will be produced at the FEMTO beamline [2] in 2006. In this scheme a very short slice out of an electron bunch is separated from the main bunch and is directed to the “radiator” undulator magnet, where it emits tuneable wavelength hard X-ray pulses of 100 femtoseconds duration. The slicing is achieved with the help of a powerful femtosecond laser pulse that interacts with the electron bunch in the “modulator” magnet. Since only a small fraction of the total stored electron current is used in this scheme, the photon flux and brightness are much lower than in the rest of the SLS beamlines.

The storage ring optics had to be changed to implement this scheme. Some of the additional magnets have been installed and successfully commissioned. The rest of the ring modifications are scheduled for installation in the first half of 2006. The FEMTO laser system has been installed and commissioned. A pump-probe technique for characterizing of femtosecond X-rays has been developed and demonstrated at the SLS μ XAS beamline on a picosecond time scale [3].

The experience with very short, tuneable X-ray pulses, gained at the SLS will also contribute to the detailed specifications and scientific case for the future X-ray Free Electron Laser

(XFEL) planned at PSI. Based on a new concept of Low Emittance Gun (LEG) [4], presently under development at PSI, this XFEL will provide fully coherent, tuneable wavelength X-ray pulses of femtosecond duration. The XFEL is a unique source that translates the properties associated with the classical laser systems into a spectral regime, which is presently only accessible with synchrotron radiation.

The development of short pulse synchrotron radiation sources at PSI follows the world-wide trend towards high peak brightness sources (Figure 4 above). These will add time as an additional dimension in the three dimensional structure studies with atomic resolution.

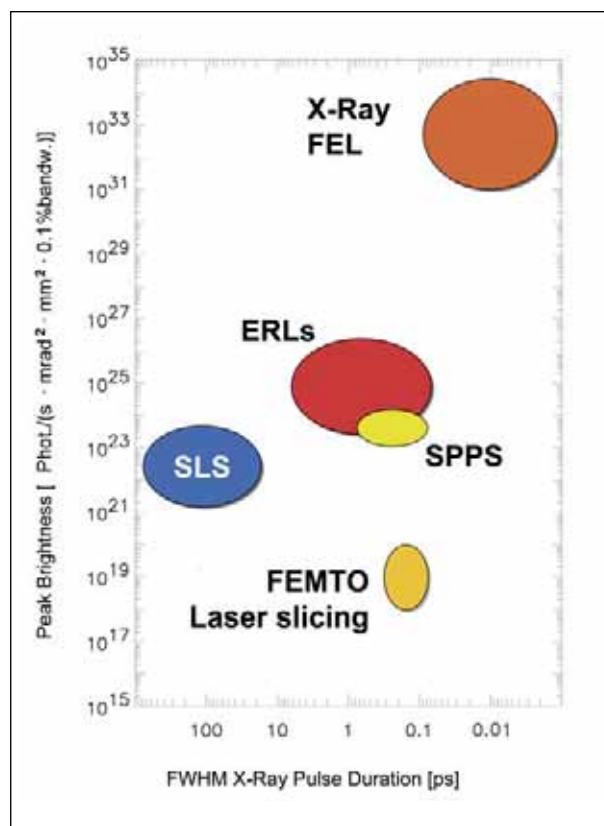


Figure 4: The world-wide trend towards higher peak brightness, short pulses synchrotron radiation sources (after H.-D. Nuhn and H. Winick).

References

- [1] J. Raabe et al., PRL 94, 217204 (2005)
- [2] G. Ingold et al., PSI Scientific Report 2003 and 2004, VII
- [3] G. Ingold and S. Johnson, private communication
- [4] R. Bakker, this volume

Swiss Spallation Neutron Source – SINQ

Stefan Janssen, Werner Wagner, Joel Mesot, Peter Allenspach, Kurt Clausen, *Research Department Condensed Matter Research with Neutrons and Muons*

The year 2005 was very successful for SINQ and its user operation: the high availability of the source together with the reliable performance of the instruments allowed 351 experiments to take place. Two new instruments were inaugurated and the MEGAPIE liquid metal target was prepared for installation and operation in SINQ in 2006 [1].

Stable operation and high availability

2005 was the 7th year of full user operation at the Swiss spallation neutron source SINQ. Receiving a proton current of approximately 1.3 mA, SINQ is the most powerful accelerator driven source worldwide and is well established in the international user community as one of the major European neutron facilities. The success of the facility is mainly based on three pillars: (1) the high availability and stability, (2) the suite of modern and state-of-the-art instruments as well as sample environment devices and (3) the competence and the enthusiasm of the PSI staff in charge of the accelerator and neutron source operation on the one hand and neutron scattering instruments on the other.

The neutron source was operated almost without interruptions whenever the proton accelerator was available. In total the SINQ solid Pb target accumulated a charge of 5822 mAh in 2005 (Fig. 1), which is approximately 800 mAh higher than in 2004 and a new record of accumulated charge per year since the inauguration of SINQ in 1996. The total availability of SINQ was 87 % and 99 % relative to the effective production of the proton accelerator.

351 experiments, 550 user visits

Ten diffractive instruments were operational over the entire year. They delivered a total of 1618 experimental days. An-

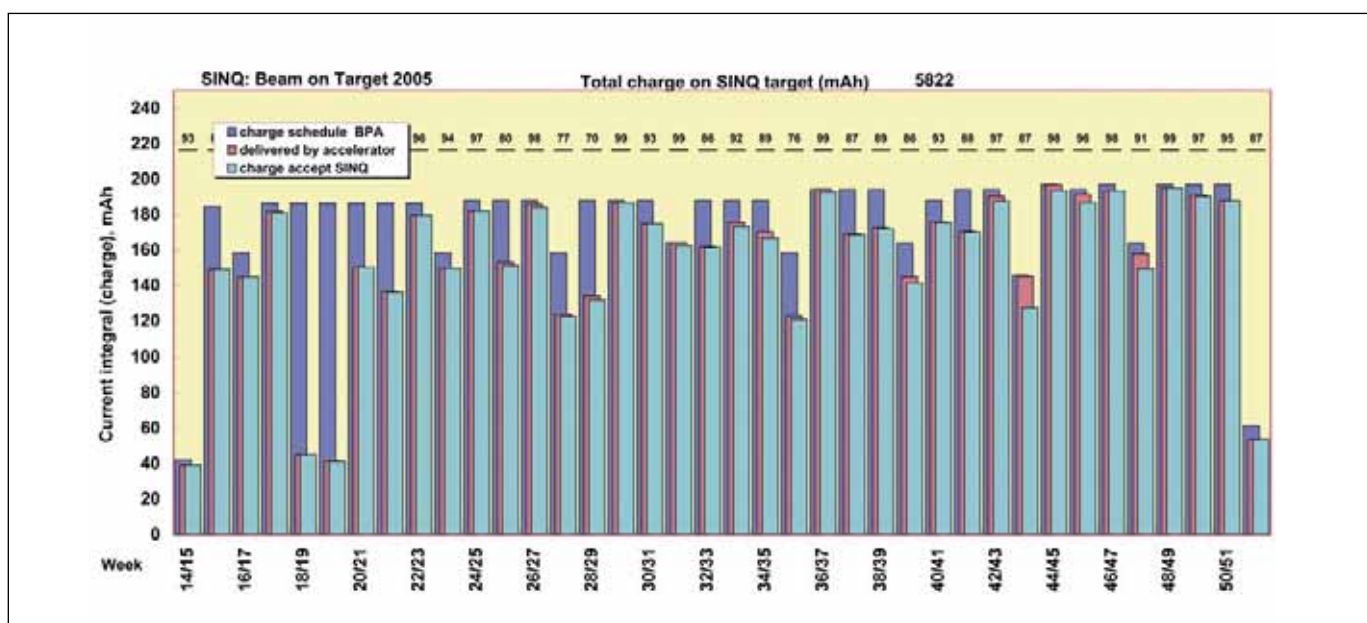


Figure 1: History of charge accumulation in 2005, the total delivered charge amounts to 5822 mAh, a value that has never been obtained so far.

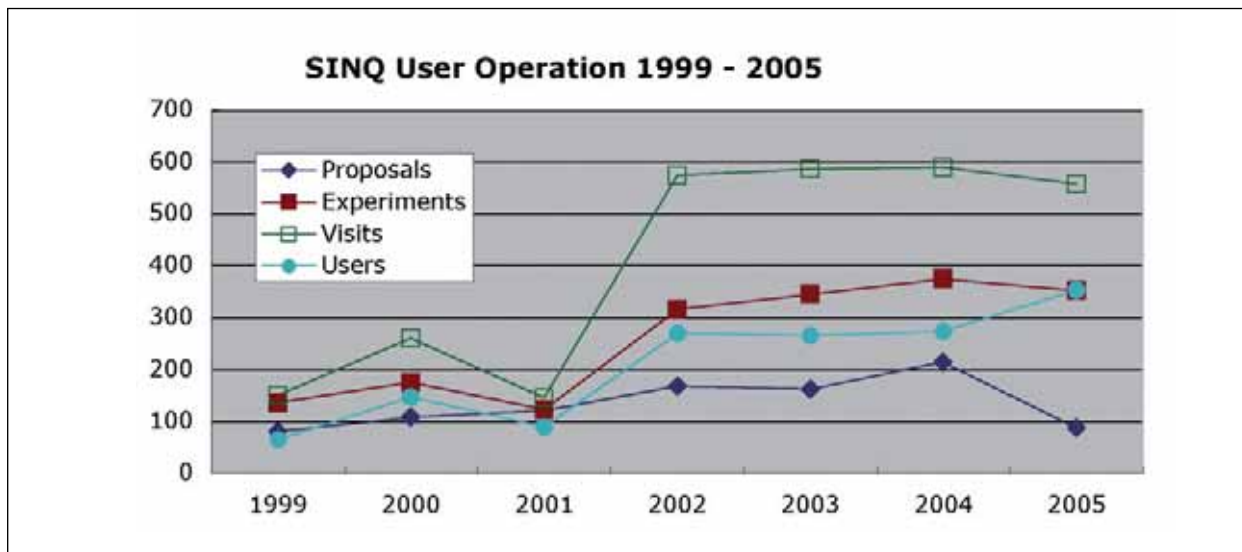


Figure 2: Key numbers of the SINQ user programme since the start of the user operation. Due to the extended shutdown in 2006 only one call for proposals was launched in 2005. Normalized to the amount of available beam time or the number of proposal rounds the number of proposals has remained constant.

other 137 days were used for development of the SINQ instruments. The interest of the international user community remained very strong: the PSI user office counted more than 550 visits from users. As some scientists performed more than one experiment per year – e.g. in the course of a long term project at SINQ – the number of individual visitors amounted to 352, a number that was never previously reached. The high efficiency of the SINQ instruments is well documented by the large number of experiments in 2005, namely 351. The average duration of an experiment at SINQ in 2005 was 4.6 days. Due to the extended shutdown of SINQ in 2006 for the installation of the Megapie liquid metal target, one of the two calls for proposals was cancelled and consequently the number of new proposals received in 2005 decreased accordingly. The overbooking of the instruments was again in the order of a factor of two.

Figure 2 shows the history of the user operation key numbers since 1999. Since 2002 the number of visits, users and experiments has been maintained at a high level and has almost doubled compared to previous years. One of the reasons for that is the impact of the EU access programmes at SINQ, which have been in action since 2002.

Strong impact of EU access programme

The EU access programme is essential for the scientific user community. It enables the facility to make user friendly instrumentation available for the users and provide them with scientific and technical support during the experiment. In addition the users receive financial support for their travel and subsist-

ence (T&S) costs. Since 2004 SINQ has been a full partner within the EU trans-national access activity NMI₃ (Neutron and Muon Integrated Infrastructure Initiative, EU Framework Programme 6). Within the programme it was possible to fund 77 different projects at SINQ in 2005. 80 users could be supported directly by T&S funds, another 66 participated in the funded experiments without T&S support.

Home base for Swiss neutron scattering

SINQ is the home base for the Swiss neutron scattering community: 43% of the instrument days were used by Swiss groups: 17% by peer reviewed in-house research and 26% by external Swiss groups mainly from universities. The remaining half of the instrument days was used by groups from EU

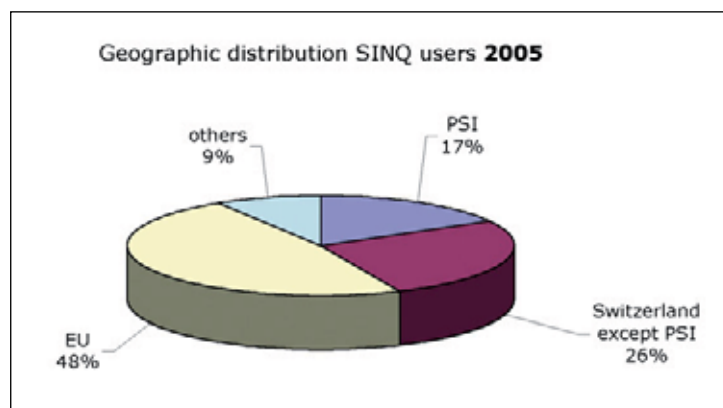


Figure 3: Geographic distribution of SINQ users in 2005 weighted by the number of instrument days.

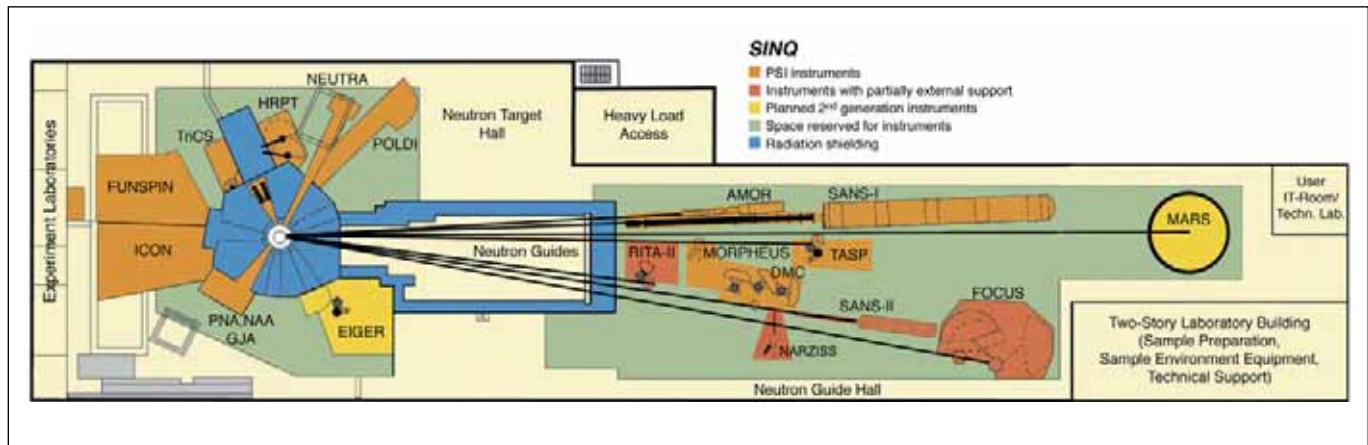


Figure 4: Sketch of the SINQ halls with the instrument suite and infrastructure

member countries and associated states. Here the 403 days of access provided in the NMI3 programme are directly reflected. In total, users from 19 different countries made use of SINQ in 2005 (Fig. 3). The largest foreign user community comes from Germany (14%), closely followed by British (12%) and Danish users (11%). 9% of the SINQ users came from Russia, United States and the Far East.

Non-diffractive applications at SINQ

2005 was also an important and successful year for the non-diffractive applications of neutron beams from SINQ. A milestone was reached when the new cold neutron radiography station ICON was inaugurated on the occasion of a radiography workshop at PSI in October. The instrument has already proven to be particularly powerful for low contrast samples and coherent phase contrast imaging. It will also be used for miniaturized tomography, high-resolution imaging and energy-selective imaging, and ensure that PSI can continue to play a leading role worldwide in the development of imaging with neutrons.

On both radiography stations NEUTRA and ICON again a large number of experiments were performed: 139 projects could be realized by 88 users. 22 experiments were performed in collaboration with partners from industry. This documents fairly well the huge community interest in non-diffractive applications.

The Digital User Office

In 2005 the Digital User Office (DUO) software tool – already known to the users of the Swiss Light Source – was adapted and implemented for use at SINQ. DUO is a web interface that allows online submission of proposals and for an easy man-

agement of experiments at SINQ. DUO sends out the notifications and feedback to the proposal authors after the evaluation round and allows the facility management to easily handle the user operation and create statistics. DUO is under continuous support and development by the PSI User Office, which serves as central contact point for the users of SINQ, SLS and μS . By the extension of DUO from SLS to SINQ and μS in 2005 the users of muon, neutron or X-ray beams at PSI see the same entry portal for their access to the facilities.

Instrument developments in 2005

In addition to ICON another new instrument was inaugurated by the end of the year: NARZISS. This horizontally scattering reflectometer is partly financed by industry and is intended for standard testing of neutron optical components. In this way the complementary but much more flexible MORPHEUS facility will be fully available for more sophisticated applications.

In addition to the inauguration of ICON and NARZISS two projects in the field of neutron spectroscopy made significant progress: MARS, a high-resolution time-of-flight backscattering spectrometer and EIGER, a thermal neutron triple-axis spectrometer. The MARS instrument is almost completed: Commissioning is foreseen for summer 2006 when neutrons will be available again. The instrument makes use of a pulsed polychromatic neutron beam tailored by five disc choppers. The secondary branch of the instrument consists of 10 mobile analyzers equipped with mica (phlogopite) crystals. The energy resolution ΔE can be tuned between 1 and 170 μeV . EIGER (Enhanced Intensity and Greater Energy Range) will be the first thermal neutron spectrometer at SINQ. Together with MARS it will increase the accessible dynamic range of the SINQ instrument suite significantly. Energy transfers of up to 70 meV will be accessible (status quo: 15 meV). EIGER will be

equipped with a sophisticated shielding concept to optimize background conditions. The instrument will allow for an automated exchange of various crystal monochromators (pyrolytic graphite and polarizing Heussler). Another important feature is the non-magnetic design, which enables the use of high-field cryo-magnets with applied fields of up to 15T. The commissioning of EIGER is envisaged for 2007.

MEGAPIE and a look into future

SINQ produced its very first neutrons in December 1996. Hence 2006 will be the year of its 10th anniversary. 1017 proposals have been submitted over these years and 1815 experiments have been performed during almost 9000 user visits. With the existing instruments and the ongoing upgrade programme SINQ is well prepared for the demands of the user community.

2006 will also be the year of the implementation of the first liquid metal target at a 1MW spallation neutron source. MEGAPIE (Megawatt Pilot Experiment) is a joint initiative of six European research institutes together with JAERI (JP), KAERI (CO) and the US Department of Energy. From summer 2006 onwards SINQ neutrons will be produced by a liquid metal target on the basis of lead-bismuth eutectic. The operation of that target is – in the first instance – limited for a

period of 6-7 months (up to the end of 2006). After that a detailed inspection will have to provide information if and how the liquid metal technology will be used in the future. A gain in neutron flux by a factor of 1.3-1.4 is expected, making some compensation for the necessary extended shutdown in 2006. The other compensating factor is that MEGAPIE will be a milestone for the development of liquid metal target technology in general.

Another very important contribution for the development of neutron scattering at PSI was the decision to start a 4-5 year upgrade programme for the proton accelerator. The main goals are to improve the reliability of the accelerator and at the same time to increase the proton current in steps from the existing 1.8 mA towards 2.4 mA and ultimately 3.0 mA. With these enhancements the accelerator will remain state-of-the-art and the world's highest power proton accelerator for the foreseeable future. SINQ will benefit from this long term programme directly by a proportional gain in reliability and allow the PSI neutron facility to remain competitive and attractive.

Reference:

- [1] W. Wagner, J. Mesot, P. Allenspach, G. Kuehne, H.M. Rønnow, proceedings of ICNS 2005, in press

Swiss Muon Source S μ S

Dierk Herlach, *Condensed Matter Research with Neutrons and Muons, PSI*

For the S μ S the year 2005 is best characterized by a number of important instrumental developments which may well herald a new era of μ SR at PSI. Despite the personnel intensive activities, the year was also very successful in terms of scientific output generated by PSI scientists and a strong international user community which substantially benefited from the S μ S partnership within the European Framework Programme FP6.

Towards a new era of μ SR at PSI

The successful completion and commissioning of the new, highest intensity μ E4 muon beamline and the inauguration of the completely refurbished low energy muon (LEM) apparatus towards the end of 2005 constitutes an important milestone in the history of μ SR at PSI. The gain in LEM intensity of almost an order of magnitude and improvements to the instrument strengthen PSI's leading position in the field of materials research on thin films, multilayers and interfaces, with the unique tool of depth resolved μ SR on the nanometer scale [1]. This is nicely demonstrated by the fact that the mere prospect of this facility becoming available to users in 2006 has triggered the submission of 21 research proposals by groups from Switzerland (8), the EU (10), Israel, Russia and South Africa (1 each), asking for significantly more beam time than will be available.



Figure 1: **First tests of the new GPD instrument at the μ E1 beamline in December 2005.**

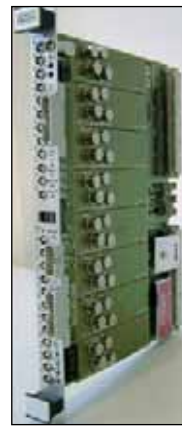


Figure 2: **Constant fraction discriminator CFD950.**

Another instrument development highlight is the design and almost completed construction of a new decay channel μ SR spectrometer (Figure 1) which will replace the oldest instrument of the bulk μ SR facility, GPD, in 2006. Equipped with a modern sample environment, including a ^3He cryostat from Oxford Instruments (base temperature 240 mK) with custom designed tail and a new generation of pressure cells developed at the Technical University of Braunschweig, this instrument will meet the rapidly growing demand for μ SR measurements under high pressure.

Other important projects aimed at further modernization of the facility have been making good progress. Ongoing studies aimed at the preparation of a PSI High Magnetic Field (10 T) μ SR Facility project will also benefit μ SR techniques in general. Some of these studies such as the simulation of μ SR instruments using Geant4, or the development of novel detector systems based on microchannel avalanche photodiodes (AMPDs) [2,3], are part of a Joint Research Activity (JRA8-MUONS) within the Neutron and Muon Integrated Infrastructure Initiative (NMI3, 6th European Framework Programme). Significant progress has been made in the field of data acquisition hard- and software. Besides the completely new hard- and

software system (based on MIDAS and the MIDAS slow control bus) developed for the LEM apparatus in collaboration with the PSI experimental electronics group and Stefan Ritt, a new, platform independent data acquisition software based on MIDAS with graphical user interface and improved visualization software has been developed and tested, and the plan is for it to be implemented on the bulk μ SR instruments for user operation starting in April 2006. On the hardware side, a fully programmable, fast timing, 8 channel VME constant fraction discriminator module developed in collaboration with the TEM electronics group (Figure 2) will replace the commercial NIM modules used up to now. The CAEN company has shown interest in this module and entered into licensing negotiations with PSI.

Successful user lab

Although – due to the construction and commissioning of the new μ E4 beam – the LEM beamline has not been fully operational, and two of the bulk instruments (ALC and DOLLY, which have to share their beamlines with particle physics experiments) were only available part time, 2005 was a very good year for the users of our facility: in total, 482 instrument days were delivered to 100 experiments. We counted over 400 visits of 148 individual users (many scientists are involved in different experiments). If all scientists involved in the approved proposals are counted, we can see that about 230 individuals from 19 countries have benefited from the use of the S μ S facility. Figure 3 shows the geographical distribution of the delivered instrument days, sorted according to the country of the main proposer. The diagram shows that in contrast to previous years, with a share of 30% of the total beam time, Switzerland has become the biggest user of the S μ S, followed by Germany (19%) and the United Kingdom (15%). Projects with main proposers from 9 other countries (France, Russia, Italy, Romania, Japan, Portugal, Netherlands, Israel and Greece) had shares of less than 10% each.

Swiss muons for Europe

Since 2004, the S μ S is a full partner of the European Neutron and Muon Integrated Infrastructure Initiative (NMI³). The Transnational Access Activity, which is part of the NMI³ provides financial support for travel and subsistence (T&S) costs for European users. Substantial additional funds (beam fees) granted within NMI³ enable the facility to keep the instruments up to date and user friendly and to give scientific and technical support to the users. In 2005, 28 different projects could be funded, and 176 instrument days of access delivered. Within these projects, 27 users benefited from the T&S funds.

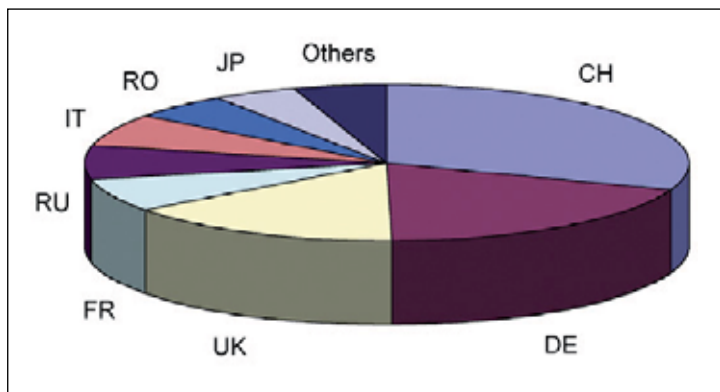


Figure 3: **Distribution of instrument time according to country of main proposer.**

Rich scientific harvest

Regarding scientific output, 2005 has been a very good year: 45 papers (of which 29 with PSI authors) based on work performed at the S μ S were published in peer reviewed journals. Among these, there is a significant proportion of publications in highly reputed journals such as Physical Review Letters (6), Physical Review B (14), Journal of Physics: Condensed Matter (3), Europhysics Letters, Nuclear Instruments and Methods A, Journal of Physical Chemistry B, and Inorganic Chemistry (1 each), as well an invited contribution to the Encyclopedia of Condensed Matter Physics.

References

- [1] E. Morenzoni *et al.*, this report p. 36
- [2] A.V. Stoykov, R. Scheuermann and Z.Ya. Sadygov, PSI Technical Report TM-35-05-02, 2005
- [3] V.V. Zhuk, A.V. Stoykov and R. Scheuermann, PSI Technical Report TM-35-05-01, 2005

Operation of the proton accelerator in 2005

Anton C. Mezger, Pierre A. Schmelzbach, *Department of Large Research Facilities, PSI*

The proton accelerator facility continues to meet the high requirements of a large user community. However, a few incidents shadowed the 2005 period of beam production. While the availability was raised to 95% in the last two months of the year, the loss of about two weeks of beam time in May caused this figure drop to 84% for the full year. The integrated charge was 8.4 Ah on Target E and 5.8 Ah on SINQ.

Operation

In the first half of the 2005 production period the routine beam current was between 1.8 and 1.85 mA. Later, the operation of the copper cavity 100 kV above the other ones allowed the slight reduction of the number of turns in the ring cyclotron and thus allowed us to gradually increase the routine beam intensity up to 1.9 mA while keeping the extraction losses at the low level suitable for long term operation. However, due to a few long interruptions, the delivered integrated charge has not increased as expected with the larger beam current and longer production period.

During the shutdown period of 2005 the central region of the ring cyclotron was modified, such that the injection optics had to be adjusted during the machine setup.

Unfortunately, due to the misalignment of two magnetic elements, this procedure took an undue amount of time, delaying

the start of the production by one week. After solving this problem, it was possible to reach the scheduled beam intensity of 1.8 mA in the record time of only one week.

The main features of the 2005 production period are shown in Figure 1. A severe incident occurred in week 18, with consequences influencing the quality of the beam production during several months. Due to a leakage of an oil-filled high voltage insulator, surfaces in the ring cyclotron became contaminated, leading locally to critical vacuum conditions for the operation of the injection and extraction electrostatic elements. The resulting malfunction, followed by their breakdown and replacement in the weeks 19/18 and 22, caused the loss of about two weeks of beam time. In addition, the self-cleaning of the systems was slow. As seen in Figure 1 the frequency of beam trips which are mainly due to discharges in these elements only returned to satisfactory values after week 33. Three interruptions of approximately one day were due to a

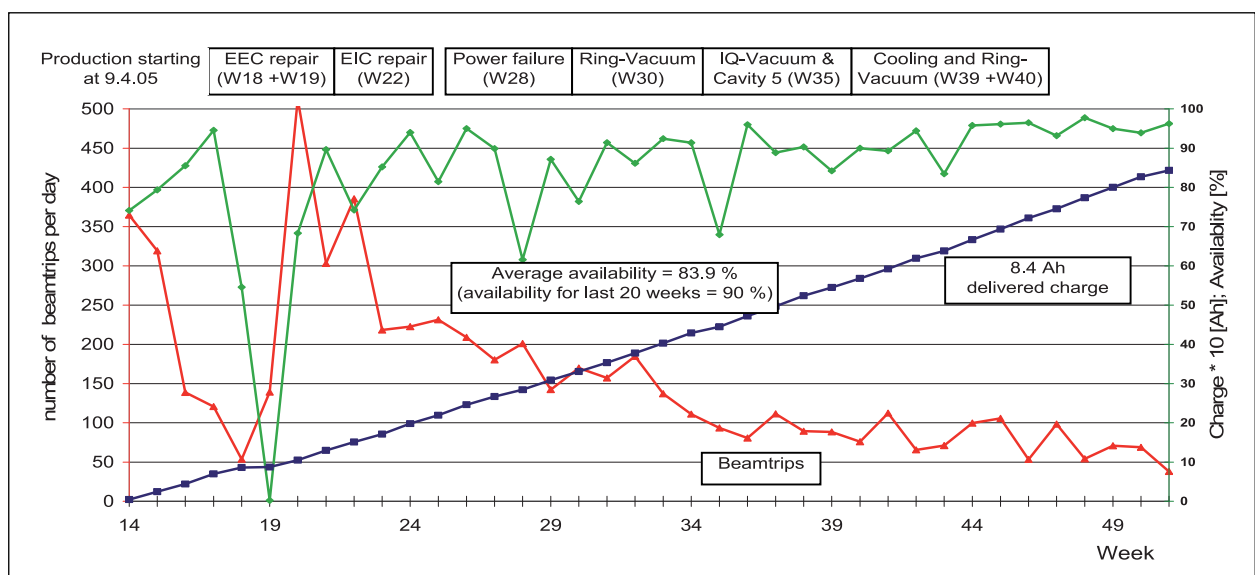


Figure 1: Operation of the proton accelerator: availability, main failures, delivered charge and beam trips.

site power failure and vacuum leaks that were difficult to detect at the ring cyclotron and the ion source, respectively. Two interruptions of the cooling water supply in weeks 39 and 40 were partly compensated by shifting a service day. Besides the good availability, the last two months were also characterized by a more efficient restart after a beam interruption. Past difficulties have been overcome by the application of an improved algorithm and a faster centering while ramping up the beam current. Table 1 shows details of the beam usage in 2005 compared to the figures of the previous year.

Beam Time Statistic	2005		2004	
Ring Cyclotron (590 MeV)				
o production for experiments				
• meson production	5420 h	62 %	4710 h	54 %
... with SINQ	5310 h		4460 h	
... with proton therapy	1784 h		1480 h	
... with PIF	280 h		0 h	
• parasitic beam programs served with direct primary beam	60 h	1 %	80 h	1 %
o setup	170 h	2 %	160 h	2 %
o beam development	120 h	1 %	120 h	1 %
o unscheduled outage	550 h	6 %	282 h	3 %
o service	360 h	4 %	320 h	4 %
o shutdown	2080 h	24 %	3380 h	38 %
Injector II (72 MeV)				
o production for experiments				
• production for Ring cyclotron	5490 h	63 %	4800 h	55 %
... with isotope production	1120 h		1680 h	
• parasitic beam programs (IP2) served with direct primary beam	68 h	1 %	210 h	2 %
o setup	220 h	3 %	200 h	2 %
o beam development	160 h	2 %	300 h	3 %
o unscheduled outage	195 h	2 %	206 h	2 %
o service	280 h	3 %	250 h	3 %
o shutdown	2307 h	26 %	3180 h	36 %
Total beam integral delivered				
o to meson production targets	8400 mAh		7100 mAh	
o to SINQ	5800 mAh		5100 mAh	
availability	83.9 %		84.2 %	
Injector I (variable energy)				
o production for experiments				
• NE-experiments	1820 h	21 %	1140 h	13 %
• OPTIS	400 h	5 %	360 h	4 %
o setup	200 h	2 %	240 h	3 %
o beam development / training	330 h	4 %	350 h	4 %
o no production	6010 h	69 %	6770 h	77 %

Table 1: Overview of beam uses.

The table also displays the statistics of the operation of the Philips cyclotron which continues to be used internally on a limited basis for eye cancer therapy (OPTIS) and for tests of research instrumentation.

Failure analysis

The various relative contributions to the downtimes in 2004 and 2005 are shown in Figure 2. Most contributions were in the range to be expected based on past experience. The largest single contribution comes essentially from the ramping-up

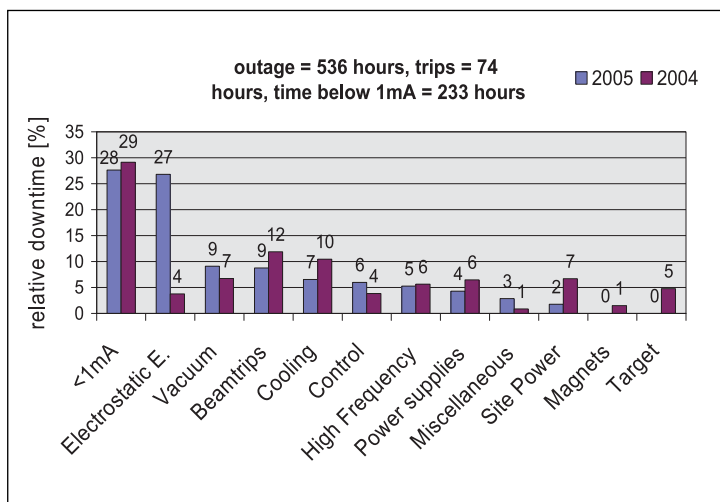


Figure 2: Characterization of the downtimes.

procedure requested by SINQ when the beam current is put back on target after an interruption.

The major exceptional event was the damage of the electrostatic elements discussed above. The contributions from the beam trips diminished thanks to a faster restart procedure. The reliability of the water cooling plant improved, and by chance, a remaining margin of a few centimeters saved the pumping station from a switch-off during the floods which ravaged Switzerland in August. The unusually large contribution of the control system was mainly due to the fact that fans and power supplies of the control crates failed more often this year. Some improvement will be expected by making spare parts available to the operation crews. The long site power breakdown in 2004 was a single event in the laboratory history. The excellent performance of the targets observed in the last years was confirmed. The damage to Target M in 2004 was not a proper failure but the consequence of a vacuum accident in the beamline to an experimental area.

The downtime from interventions shorter than 6 hours is quite constant over the years and reflects the overall quality of the equipment and the fast reaction of operation and maintenance crews. The longer downtime periods are mostly due to unpredictable single events of which the nature differs from year to year. They lower the availability of the facility by 5 to 10%. The background due to the most common failures contributes by 2 to 3%, as does the restart and ramp up time after beam trips. Some sources of failure are well identified. The renewal of aging components like vacuum equipment, power supplies and diagnostic elements is under way within the bounds of the available resources. However, the prototype character of important systems and continuous developments like the beam power upgrade in parallel with the beam production will still remain in variance with the call for highest possible availability.

Upgrade of the PSI Megawatt proton accelerator

Pierre A. Schmelzbach, Andreas Adelman, Stefan Adam, Markus Bopp, Hans-Rudolf Fitze, Martin Humbel, Jean-Yves Raguin, Peter K. Sigg, Lukas Stingelin, *Department of Large Research Facilities, PSI*

The status of the upgrade programme of the proton accelerator is described. The main effort in 2005 was dedicated to the development and construction of new bunchers for the 870 keV injection line of Injector 2 and for the 72 MeV transfer line to the ring cyclotron. Significant progress has also been made in the development and application of new computational beam dynamics tool.

Introduction

Following the demand for higher beam intensities a goal of 3 mA (1.8 MW) has been set for the future performance of the proton accelerator. The installation of the second copper rf-cavities in the ring cyclotron and the implementation of new bunchers is foreseen for 2006. In parallel with the development of new equipment, simulations of the beam properties when space charge effects are dominant are underway, especially to settle the most efficient acceleration mode in the ring cyclotron.

Operation with a new ring cavity

After demonstrating on the test bench that the prototype of the new copper rf-cavity fulfils all specifications it was installed in the ring cyclotron, as shown in Figure 1, and has been used without problems since 2004 [1]. While the future operation voltage will be 1 MV, beam dynamical reasons due to the asymmetric configuration, limit this figure to 830 kV. It was nevertheless possible to test the electromagnetic compatibility with other cyclotron components, to achieve a modest reduction of the number of turns and thus to reduce the beam losses at the extraction. A second cavity has been successfully tested and is ready for installation during the 2006 shutdown.

Improved bunching for Injector 2

The beam quality in Injector 2 depends crucially on the properties of the injected bunches. A judicious balance between beam compression and counteracting space charge forces



Figure 1: **Installation of the first new copper rf-cavity in the ring cyclotron.**

allows for a good matching of the longitudinal phase space to the acceptance of the accelerator and the application of a genuine mode of acceleration suitable for high intensity beams.

The present first harmonic two-gap sine buncher will be replaced during the shutdown 2006 by two bunchers operated at the first and third harmonics, respectively. The expected performance predicted by a one dimensional bunching model is shown in Figure 2. Confirmation by a full simulation is underway. The possibility to inject more beam out of a reduced DC beam will also result in a more stable operation of the Cockcroft-Walton pre-injector.

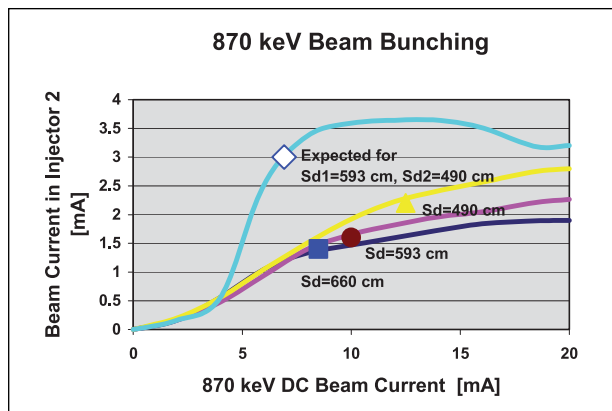


Figure 2: Beam intensities accepted by Injector 2 for a one and a two-buncher system. The lines are smooth interpolations between calculated values, the solid symbols are operational data for different locations of the single buncher used up to now.

Bunching of the 72 MeV beam

The 2 degree phase width of the beam extracted from Injector 2 increases to about 16 degree at the entrance of the ring cyclotron, which requires the use of a flat-top cavity in this machine. A recompression of the bunch relaxes the conditions imposed on the matching of the operating voltage of this device to one of the new accelerating cavities. It might even make the use of this artefact obsolete, thus reducing costs and development work. After a comparative study [2] a 10th harmonics two-gap drift-tube buncher (500 MHz) has been designed for this purpose. It will be ready for installation as soon as satisfactory power tests have been performed in 2006. Figure 3 illustrates the selected design.

New resonators for Injector 2

The basic design of the additional accelerating rf-cavities (named resonators in Injector 2) is close to completion and has resulted in the choice of single-gap systems fitting the available space at the location of the obsolete flat-top resonators. The achieved field distribution is well suited to increase



Figure 3: Components of the 500 MHz buncher to be installed in the 72 MeV beam transfer line to the ring cyclotron.

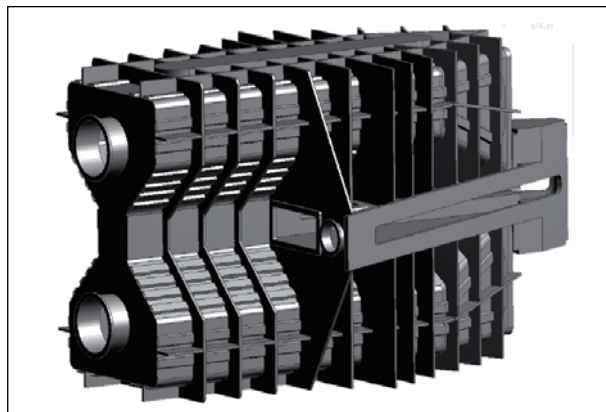


Figure 4: Engineering model of the planned new Injector 2 resonators.

the turn separation at the extraction. The mechanical layout is illustrated in Figure 4.

Beam dynamics

The space charge aspects of the injection and of the acceleration of the beam in our accelerators are extensively investigated using simulation tools developed in our laboratory [3]. A new, preliminary investigation of the injection of the re-bunched beam suggests that the “round beam” mode of operation we developed for Injector 2 might also be applicable in the ring cyclotron.

The investigation of the beam distortions due to high-order rf-modes induced by the beam itself in a high power cyclotron showed that these effects remain small in our accelerator [4]. Finally, the remaining question of the influence of overlapping turns in the ring cyclotron can now be addressed by means of newly developed codes.

References

- [1] H.R. Fitze et al., Operation of the First Copper Cavity in the PSI Ringcyclotron, Proc. 17th Int. Conference on Cyclotrons and their Applications. Tokyo, Japan, Oct. 18-22, 2004, p. 67
- [2] J.-Y. Raguin et al., Comparative Design Studies of a Super Buncher for the 72 MeV Injection line of the PSI Main Cyclotron, Proc. European Accelerator Conf., EPAC'04, Lucerne, Switzerland, July 5-9, 2004, p. 1162
- [3] A. Adelman et al., Recent Results on Simulations of High Intensity Beams in Cyclotrons, Proc. 17th Int. Conference on Cyclotrons and their Applications. Tokyo, Japan, Oct. 18-22, 2004, p. 425
- [4] L. Stingelin, Beam-Cavity Interactions in High Power Cyclotrons, EPFL, Thèse N° 3169 (2005)

Commissioning of the new proton therapy facility – PROSCAN

Marco Schippers, Damir Anicic, Jacques Cherix, Rudolf Dölling, Jürgen Duppich, Timo Korhonen, Markus Kostezzer, Peter Meyer, Anton Mezger, Marco Negrazus, Hans Reist, Wolfgang Tron, *Department of Large Research Facilities*; Beat Amrein, *Department of Logistics*; Terence Boehringer, Martin Jermann, Benno Rohrer, *Research Department Life Sciences*; and the PROSCAN team.

The new cyclotron COMET for PSI's new proton therapy facility PROSCAN has been installed and the commissioning and acceptance tests have started. The beamline to the test area, and the control system are being commissioned simultaneously.

Introduction

During the year 2005 the commissioning of the first major components of the PROSCAN facility (the superconducting cyclotron COMET and the beamline to the test area) began and first acceptance tests of COMET were performed at the end of the year.

Commissioning of the cyclotron

After commissioning of the 72 MHz HF-amplifier, it was possible to obtain the required 110 kW HF-power on the cyclotron cavities in March 2005. In order to observe the first turns of the protons in the cyclotron, a phosphor screen was mounted near the centre of the cyclotron. Figure 1 shows the light spots caused by the first few orbits.

This intermediate milestone demonstrated that the central region was properly designed in order to stand the high voltage. After having observed the beam in the central region, we were able to accelerate protons until just before extraction. Using a radial probe equipped with a phosphor screen and a CCD camera, we observed intensity and shape fluctuations as



Figure 1: Light spots on a screen, showing the first few turns in the centre of the cyclotron, measured with two different settings of the HF-power.



Figure 2: Light intensity on the radial probe, as a function of radius.

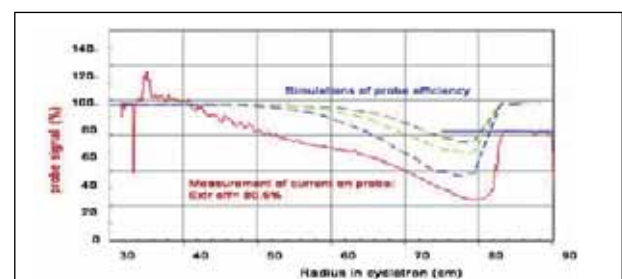


Figure 3: The measured current on the radial probe as function of radius shows the extraction efficiency ($I_{r=82}/I_{r=30}$). The probe efficiency varies with radius, but simulations with different beam sizes (dashed lines) show it is 100% at $r=30$ cm and at $r=82$ cm.

a function of radius due to precessions of the beam. A video-analysis program [1], allowed a quantitative evaluation of the video images. The intensity fluctuations could then be minimized by centering the beam using the inner trim rods in the cyclotron, see Figure 2.

On April 1st (no joke!) the beam centering was optimized such, that the first protons could pass through the coupling resonance, reach extraction radius and be detected by the first beam profile monitor in the beamline. Re-adjustment of the balance of the HF-power on the four “dees” improved the reliability and centering, so that further beam dynamical optimizations were possible. Also slight adjustments of the position of the SC-coil were made [2]. In October the important specification

of 80% extraction efficiency has been reached, see Figure 3. It is important to note that this specification is now reached routinely. This is an important property of a cyclotron of this type, and a specification which has never been achieved before. After improvements to critical HF-amplifier parts, beam intensities up to 500 nA could be extracted routinely to perform the first acceptance tests: beam energy (250.4 MeV, see Fig. 4), energy stability and extraction efficiency, as well as to commission the beamline to the test area.

Commissioning of the beamline

The beamline components between cyclotron and degrader have been used to study the beam properties from the cyclotron. For this purpose several tools in the machine control system, based on existing applications for the other cyclotrons at PSI, have been used. An example (emittance measurement) is shown in Figure 5.

During the summer of 2005 the beamline to the test area (the vault before the future Gantry2 area) was completed and a first beam of 250 MeV protons has been transported to the test area on July 28. A first study of the beam transport with the new profile monitors, showed a good agreement with the calculated beam widths (Fig. 6). Beamline settings can be saved and reloaded using a newly developed tune handler. A first measurement of the transmission through the degrader and collimator system shows that the losses due to multiple scattering in the degrader are a few percent larger than expected (Fig. 7). For 70 MeV a transmission of 2% is observed before the momentum analysis. The momentum selection will reduce the intensity by another factor of 4-5. The operation is performed either from the main control room, or from the newly dedicated control room in the medical pavilion. Also the Run-Permit system, which performs machine safety checks, is in operation now. PSI's radiation safety group has started to monitor the activation in the vaults and, during a full day with beam, the concrete shielding has been checked.

Outlook

The commissioning and acceptance tests will be continued in 2006 until mid February. Then, the existing gantry will be connected to COMET. The commissioning is planned to be resumed in June 2006 and first patient treatment is expected in the fall of 2006. In 2007 the new Gantry2 and the eye treatment room will be installed.

We would like to acknowledge the ACCEL crew for the excellent collaboration during the installation and commissioning of COMET.

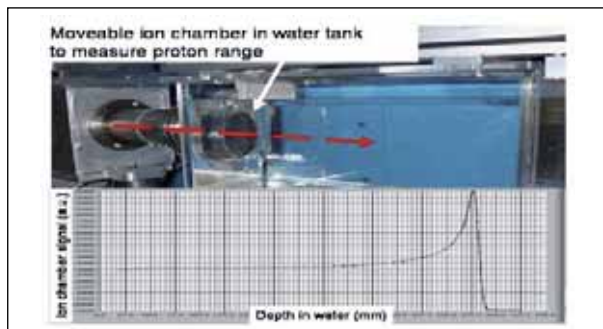


Figure 4: Measurement of dose as function of depth in water. The beam energy is derived from the range.

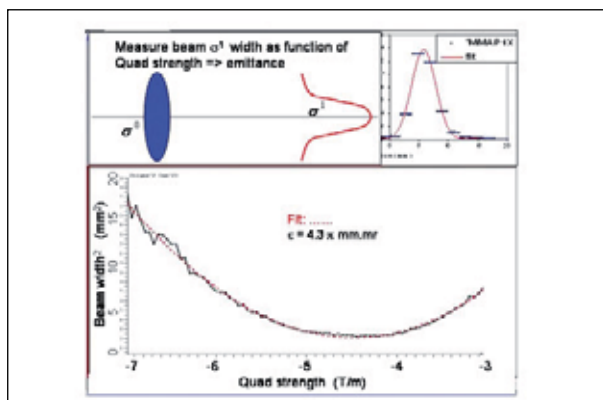


Figure 5: Emittance measurement with the "varying quadrupole" method.

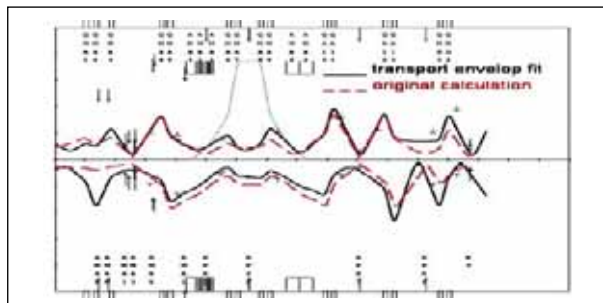


Figure 6: Calculated and measured beam envelopes of the undegraded 250 MeV beam to the test area.

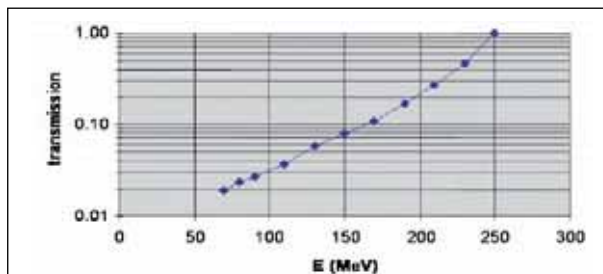


Figure 7: Transmission through the degrader, with the collimator system set for eye-treatments.

References

- [1] R. Geus, private communication
- [2] J.M. Schippers, V. Vrankovic, D.C. George, Proc. 17th Int. Conf. Cycl. Appl., Tokyo, October 2004, p. 435

New developments in ion beam physics

Hans-Arno Synal, Vasily Alfimov, George Bonani, Marcus Christl, Max Döbeli, Michal Grajcar, Irka Hajdas, Christian Kottler, Peter W. Kubik, Marc Mallepell, Arnold Müller, Guo Sun, Martin Suter, Martin Stocker, Emanuel von Wartburg, Lukas Wacker, *Research Department Particles and Matter, PSI, and Institute of Particle Physics, ETH Zurich*, Susan Ivy-Ochs, *Institute of Particle Physics, ETH Zurich and Geography Institute, University of Zurich*

Based on experimental knowledge gained during the height of atomic and nuclear physics research, physics of ion beams has become an independent research field and its application is now established in many different areas of modern research. Ion beam physics can be regarded as a key technology essential for many present research programmes and for future developments in those fields. The Laboratory for Ion Beam Physics has three accelerator facilities in operation, which provide charged particle beams for a vast variety of research projects. Here, we focus on new developments and on operational aspects.

The PSI/ETH Laboratory for Ion Beam Physics, one of the world's leading facilities in this field, conducts research in accelerator mass spectrometry (AMS) and in the materials sciences (MS). To accommodate the experimental requirements of our research programmes we have three accelerator systems in operation. The backbone of our extensive application programme is still the 6 MV EN tandem accelerator. Our research programme for methodological and instrumental developments relies on the 500 kV Pelletron based AMS system and on our latest instrument, the 200 kV radiocarbon detection system.

EN tandem accelerator operation for the year 2005 is summarized in Table 1. We spent 67 % of the beam time on AMS,

17% on materials sciences projects and only 16% on machine conditioning and tests. The small fraction of beam time spent on accelerator maintenance is an indication of the good condition of our accelerator. The reduction in total beam time is due to the transfer of the Ca-41 and I-129 measurement programmes from the EN tandem accelerator to the 500 kV AMS system (TANDY).

Pushing detectors to their limits

The TANDY system was predominantly used in connection with our ongoing research programme to push the AMS detection techniques to their physical limits [1-2]. Several improvements in the detection of low energetic heavy ions have been made. The advent of very thin, extremely homogeneous silicon nitrate detector windows [3] improved the particle identification capability of our gas ionisation detectors significantly. The use of cooled FET preamplifier units combined with an elaborate detector design yielded a relative energy resolution of less than 6 % for 430 keV ^{14}C ions. This goes beyond traditional models to describe energy loss and energy straggling in materials, but it can be explained with more elaborate approaches. The enhanced resolving power of such gas-ionisation detectors make it possible to clearly identify low energetic heavy ions. This is, in particular, important for the detection of other radio-nuclides such as ^{10}Be , where the isobaric interference of ^{10}B has to be suppressed, or for the detection of heavier nuclides such as ^{129}I and actinides (Pu, Pa, and U isotopes), where

EN Tandem Accelerator Operational Hours			
AMS	2003	2004	2005
Be-10	616	855	738
C-14	800	805	804
Al-26	91	102	33
Cl-36	193	160	265
Heavier Elements	137	136	
MS			
Materials Science	411	490	438
SSIMS	167	96	42
Maintenance			
Conditioning/Tests	800	424	428
Total	3215	3068	2748

Table 1: Beam time statistics 2003–2005.

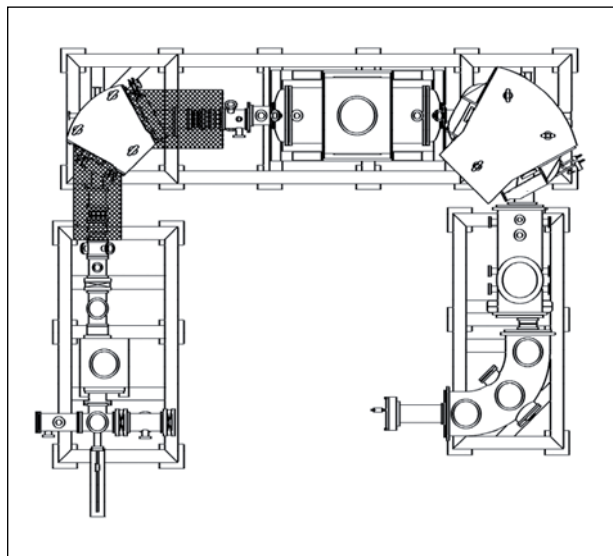


Figure 1: **Overview of the latest PSI/ETH AMS system. It has overall dimensions of 2.3 x 3 m².**

molecular break-up products have to be separated. The potential of measuring those nuclides with the latest generation of AMS instruments is under investigation within the framework of various Ph.D. and diploma theses.

Applications for materials sciences

The progress made with the detection of heavy ions is also exploited for materials science research. In particular, the newly built elastic recoil detection analysis (ERDA) spectrometer performs better with silicon nitrate detector windows [4]. Due to a higher energy resolution at lower recoil energies, particle identification has improved and it became possible to reduce the energy of the initial beam particles. The strong dependence of the scattering cross section on particle energy resulted in a higher counting rate at the detection system and as a consequence has enhanced the sensitivity of the method significantly.

We have also focused our activities on instrumental developments. Based on the systematic investigations to understand and model the processes involving ion atom collisions, it became possible to design a tabletop sized AMS spectrometer (Mini Carbon Dating System: MICADAS, Figure 1).

The system is operational and routine measurements of radiocarbon samples have been made in unattended, fully automated operation mode. Results of these measurements clearly demonstrate the capability of the MICADAS system to obtain high quality radiocarbon dates from samples with natural activity levels. This can be regarded as a big step towards the ultimate goal in AMS development to simplify the measurement technique and to make it easier to operate the instrumentation.

Continual demand for radiocarbon analysis

Within the framework of our AMS application programme we have analysed more than 4700 individual samples (Figure 2). The number of radiocarbon measurements has remained at a level of about 1900 samples, which has been reached over the last five years. The fraction of archaeological samples is about 25%. With our compact AMS systems we can now analyse very small samples of less than 100 µg carbon and measurements in connection with research on the atmospheric carbon cycle have been made. To extend our capabilities in this field we are developing an interface to the MICADAS ion source to perform direct measurements of small gaseous CO₂ samples.

The requests for ¹⁰Be measurements are equally as high as the demand for radiocarbon analyses. Polar research, oceanography and exposure dating projects are responsible for about 25% of the total number of measured samples. More and more external research groups are setting up their in-house sample preparation laboratories, which generate an ever-increasing number of samples. In 2005, ⁴¹Ca and ¹²⁹I measurements have been measured exclusively at the compact 500 kV Pelletron based AMS spectrometer. With ⁴¹Ca, we are now using CaF₂ as target material, which is much easier to handle than the CaH₂ material used in earlier experiments. The background levels are not as good as with the hydride target material but the advantage of the new measurement procedure is tremendous. The performance of this method is best suited for biomedical research projects.

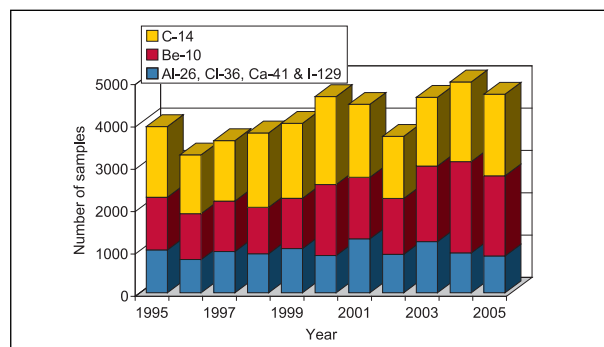


Figure 2: **Compilation of measured AMS samples at the PSI/ETH AMS facilities over the last 10 years.**

References

- [1] M. Suter, S.W.A. Jacob, H.-A. Synal, Nucl. Instr. and Meth. B 172, 144 - 151 (2000).
- [2] M. Stocker, M. Döbeli, M. Grajcar, M. Suter, H.-A. Synal, L. Wacker, Nucl. Instr. and Meth. B 240, 483-489 (2005)
- [3] M. Döbeli, C. Kottler, M. Stocker, S. Weinmann, H.-A. Synal, M. Grajcar, M. Suter, Nucl. Instr. and Meth. B 219-220, 415-419 (2004)
- [4] M. Döbeli, C. Kottler, F. Glaus, M. Suter, Nucl. Instr. and Meth. B 241, 428-435 (2005)



Technology transfer 103

Patents and licenses

The PSI technology transfer office aims to transfer inventions stemming from new research results or new technologies for industrial use, with the goal of either adding competitiveness to existing companies, or to create new jobs. This process has to be adapted for each technology transfer case because the majority of cases require person-to-person business where the specific needs of the industrial company have to be anticipated.

The most effective method of technology transfer is the transfer of persons, who not only carry specific know-how but also the spirit of transforming an invention into an innovation. Along with this method, the transfer of know-how or protected intellectual property rights (IPR) mostly in connection with a collaboration is a good way to sustain a successful transfer.

As we are a user lab operating large and complex research facilities, we generate not only scientific results but also new technological solutions, necessary for operating the facilities at the scientific vanguard. Experience has shown that these technologies can be beneficial in other fields of applications.

We always strive to generate a win-win situation for both the industrial customer and the scientific community. In 2005, PSI filed forty-two new applications for IPRs and completed seven new licence agreements.

The bubble-jet injector developed at PSI will provide advanced control of fluid injections for a wide range of applications in the chemical industry.

(Photo: Rade Milenkovic)

New dimensions in neutron imaging

Eberhard H. Lehmann, Peter Vontobel, René Hassanein, Gabriel Frei, Mirko Estermann and Guido Kühne,
Spallation Neutron Source Division ASQ, PSI

Neutron imaging has demonstrated a tremendous potential for industrial use, especially in the area of non-destructive testing. Using thermal neutrons, at the NEUTRA facility (SINQ) [1], high image contrast has been obtained for adhesives, lubricants, water and explosives, all contained in metallic structures. To overcome some limitations in respect to contrast, spatial resolution and quantification, a new facility (ICON) was built in 2004/2005 which uses cold neutrons for imaging purposes. We have already demonstrated that ICON [2] can be used to successfully apply sophisticated new methods such as phase-contrast enhancement and energy selection. A new micro-tomography system will be available in 2006 providing the opportunity for many industrial partners and users to profit from these recent improvements.

Introduction

In most cases neutrons are able to transmit metallic structures better than X-rays. Furthermore, organic materials such as adhesives, lubricants, moisture and even explosives can be visualized and quantified even with small sample size. At the NEUTRA facility it has been shown that when properly applied these state-of-the-art imaging techniques have a high potential for industrial applications [3].

However, there are new challenges in this field with respect to better spatial resolution, higher contrast and more precise quantification - also driven by industrial demand. In order to meet this challenge a new beamline, with the acronym ICON (**I**maging with **C**old **N**eutrons), came into operation in 2005.

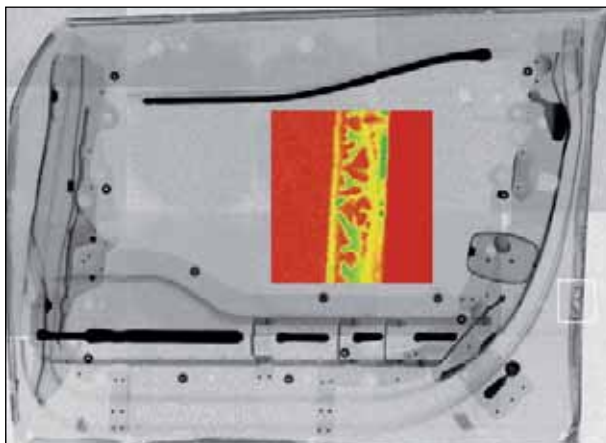


Figure 1: **Transmission neutron image of a car door, where the adhesive connection can clearly be inspected through the metal (the insert is a cut-out from the right side as indicated).**

Industrial applications for neutron imaging

Very prominent in the uses of neutron imaging is the in-situ diagnosis of the behaviour of electric fuel cells [4]. Here, we can see and measure the amount of the produced water in-situ and its time evolution.

Because gluing is increasingly replacing welding in manufacturing processes, a reliable and non-destructive testing method is required. Neutron imaging can contribute to such inspections, at least as a referencing procedure. For the case of a car door, the determination of the adhesive distribution is demonstrated in Figure 1. Similar tests can be performed for different metallic connections, especially when safety, reliability and costs will play an important role, for example; air and space industry and nuclear technology.

The new beamline ICON

A second beamline at the spallation neutron source SINQ was implemented for neutron imaging purposes with a cold neutron spectrum from the D₂ moderator at 25 K. The advantages of cold neutrons are the higher probability of interaction with matter and higher contrast in neutron images in the end. The layout of the ICON beamline is shown in Figure 2.

The large space inside the shielded room around the beamline will enable the inspection of sizable objects at the end position (a sample weight of up to 500 kg can be manipulated in the beam). It is also possible to bring additional equipment such as experimental infrastructure up to the beamline.

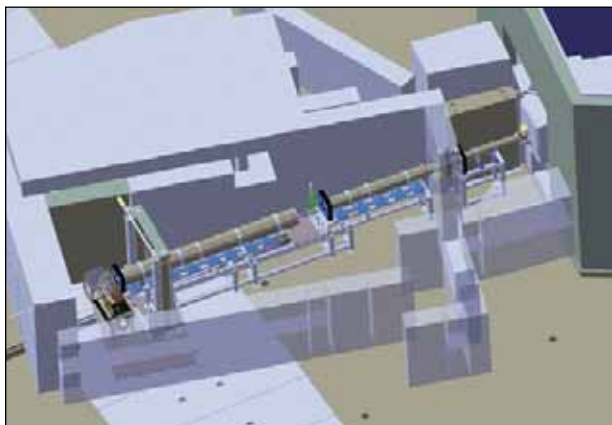


Figure 2: **Layout of the ICON facility at SINQ, where cold neutrons are used for imaging purposes.**

An important new feature of ICON is the variability of the inlet aperture from 8 cm down to 0.5 mm. In this way, the beam collimation, intensity and field of view can be adapted to the required experimental conditions. With the very small aperture, so-called phase-contrast enhancement can be pushed. This option is important, when weakly absorbing materials with small size or structure should be visualized. An example is given for a titanium screw of only 3 mm diameter in Figure 3, comparing the direct transmission with the new phase feature. Another approach in phase-sensitive radiography was successfully tested at ICON very recently [5].

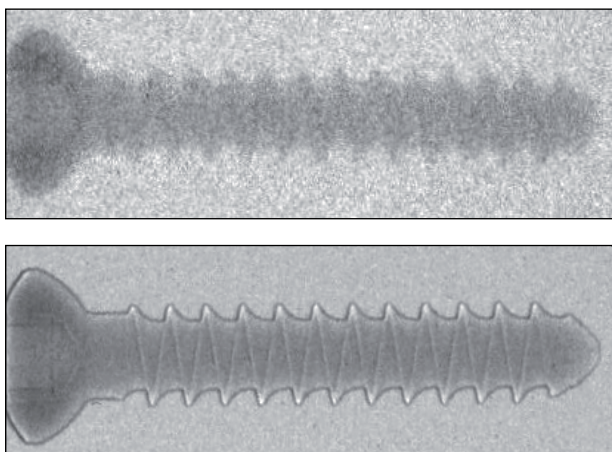


Figure 3: **Neutron images of a Ti screw (diameter 3 mm) in normal transmission mode (above) and with the pin-hole phase-contrast enhancement (below).**

Future activities

After the successful test phase in 2005, where we established the specific properties of ICON under standard imaging conditions and with an energy selector and a chopper for narrow band studies, we now intend to complete the facility to enable the full user support such as at the existing NEUTRA beamline.

One of the first tasks will be the setup for a new apparatus for micro-tomography (see Fig. 4), where we try to reach a resolution in the order of 20 μm for object of size up to 3 cm. Another option of industrial relevance will be the scanning performance of sizeable objects at the end position of the beamline (to the left in Fig. 2). With an inherent resolution of 0.1 mm we will be able to visualize an area of interest of 1.5 m.

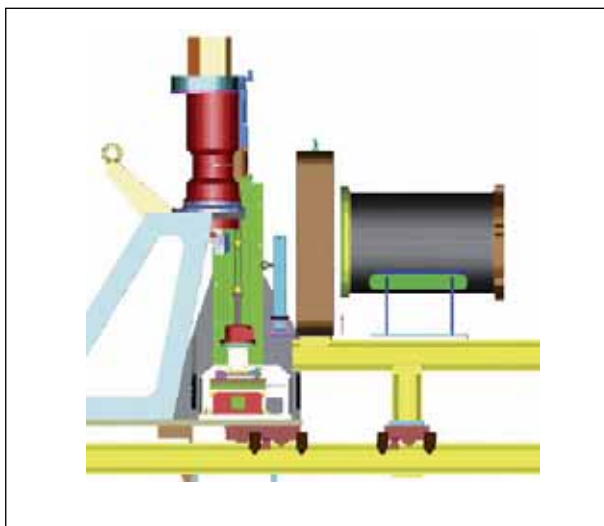


Figure 4: **The micro-tomography setup at ICON.**

Conclusion

The capability for new and improved options in neutron imaging with ICON for scientific and industrial applications was successfully demonstrated during its installation phase in 2005. There will be potential for further enhancement when the test setup for the determination of the differential phase contrast will be transferred into a permanent device.

References:

- [1] E.H. Lehmann et al., Non-destructive Testing and Evaluation, Vol. 16, No. 1-6 (2001), pp. 191-203
- [2] G. Kühne et al., NIM A 524 (2005) 264-270
- [3] E. H. Lehmann, Neutron imaging – Detector options and practical results, NIM A 531 (2004) 228-238
- [4] D. Kramer et al., An on-line study of fuel cell behavior by thermal neutrons, NIM A 542 (2005): 52-60
- [5] F. Pfeiffer et al., this volume, p.

High speed waveform digitizing with the DRS chip

Stefan Ritt, *MEG Experiment, Laboratory for Particle Physics, PSI*

The MEG experiment [1] is currently being built at the πE_5 area of the PSI proton accelerator within the framework of an international collaboration. This precision experiment requires high speed waveform digitizing in the range of several GHz on all its 3000 detector channels, at an affordable cost. For this purpose a new chip is under development at PSI, based on a previous design [2]. Partners for commercialization have been contacted and they will have the chance to provide input into the last design step, in order to make the chip more attractive for other applications.

The Domino Ring Sampling (DRS) chip is based on a switched capacitor array (SCA). It contains ten channels each with 1024 cells and can record analogue waveforms with a speed of up to 4.2 GHz. The capacitors are read out at a speed of 40 MHz and digitized with a 12-bit flash ADC [3]. The DRS chip is based on the same technology as the CMS Pixel Detector [4] and is therefore radiation hard. Due to its small power consumption of less than 10 mW per channel, it also becomes attractive for space applications. After a first test version, the second version of the chip (DRS2) has been produced and successfully tested.

Four chips are mounted on piggy-back boards on a VME board recently developed at PSI and licensed to industry [5]. Each VME board contains 32 channels. The DRS2 chip already works well enough to be used in all channels of the MEG experiment.

As high speed waveform digitizing becomes more and more important in modern particle physics experiments, many re-

quests for this technology have already been received from other laboratories. Besides particle and astrophysics, many industrial applications could benefit from this development, such as test equipment or handheld oscilloscopes.

Collaboration with industry

To make this technology easily available to other laboratories, collaboration with industrial partners has been started. CAEN S.p.A. in Viareggio, Italy, has expressed an interest in integrating the DRS chip into its line of high speed waveform digitizer VME boards. This company has extensive experience in instrumentation for nuclear physics and aerospace and a worldwide distribution network. To increase the value of the technology for commercialisation, PSI will offer CAEN the opportunity to incorporate requirements and features into the design of the DRS3 chip, which is going to be submitted in spring 2006. A patent is pending on the technology of the DRS chip. It is expected that the combination of the chip design competence of PSI, together with the industrial experience of partner companies will result in a successful deployment of this technology in both particle physics experiments and commercial applications.



Figure 1: Picture of the DRS2 chip.

References:

- [1] PSI research proposal R99-5
- [2] C. Brönnimann et al., NIM A 420, 264 (1999)
- [3] PSI Scientific Report 2004, vol. 1, 12
- [4] W. Erdmann et al., NIM A 549,153 (2005)
- [5] PSI Scientific Report 2005, vol. 1, p. 80

Technology transfer by mechanical engineering sciences

Alfred Waser, *Technology Transfer, PSI*;

Heinrich Blumer, *Department of Mechanical Engineering Sciences, PSI*

The Department of Mechanical Engineering Sciences at PSI is a rich source of novel services which, although primarily developed for internal purposes, can also be very successfully applied and transferred to industry.

Mechanical engineering sciences

The mission of PSI's Department of Mechanical Engineering Sciences (MES) is to support the needs of PSI research departments by developing and producing advanced products for the infrastructural and experimental field. In consequence MES incorporates specialized skills in the field of mechanical engineering as well as in production engineering and fabrication.

It is therefore not surprising that MES is a potential source for advanced technologies and services to be made available to industry.

Electron beam welding

A major Swiss player in pressure sensing, producing pressure sensors for diesel engines and hydraulic equipment was looking for an outsourcing opportunity for the friction welding process. PSI has been demonstrating a stable high quality process by using its electron beam welding installation and competence. In case of availability of production resources PSI is interested in implementing similar cooperation in order to (a) exploit its knowledge and make it available for industrial use and (b) to use such opportunities to improve its production technologies.

High vacuum capable diamond window

For application at an optical beamline at PSI's Synchrotron Light Source a novel diamond window has been developed and manufactured. The window consists of a very thin CVD (Chemical Vapor Deposition) foil mounted into a cupreous window frame by applying a high temperature soldering technique. As a result this diamond window shows very high

mechanical and thermal stability. This results in better optical performance and lower production costs and therefore the diamond window will replace the beryllium windows frequently used for the above mentioned application.

This diamond window production technology was licensed in 2005 to Diamond Materials GmbH, a spin-off company of the Fraunhofer Institute in Freiburg (Germany).

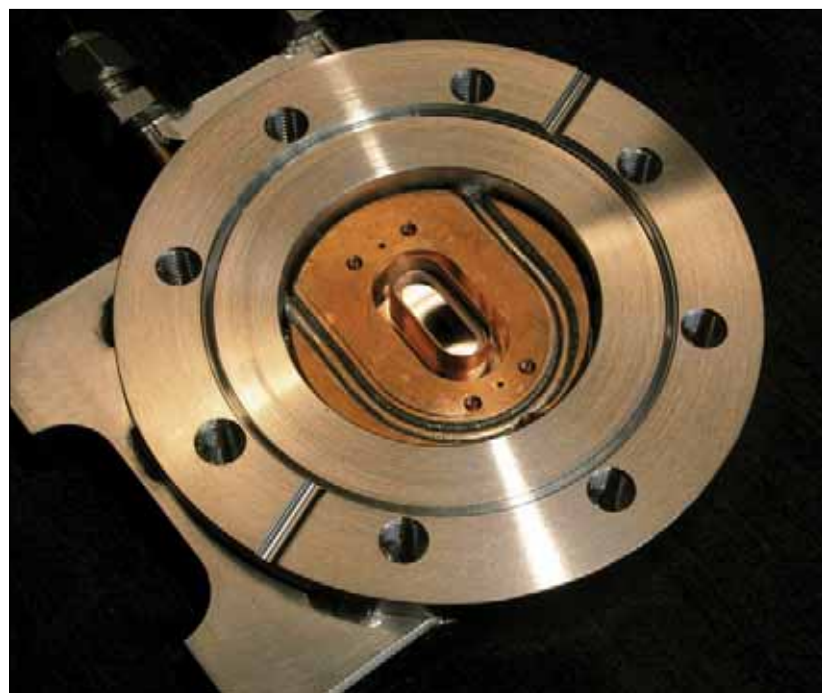


Figure 1: **The CVD window.**

A new production technology: X-ray interference lithography

Harun H. Solak, Ahed Al-Adwan, Qianhong Chen, Christian David, Yosin Ekinci, Uwe Flechsig, Fredy Glaus, Jens Gobrecht, Yves Hemmerling, Marcus Kropf, Luc Patthey, *Research Department Synchrotron Radiation and Nanotechnology*

Since its inception several years ago the X-ray Interference Lithography (XIL) beamline at the SLS has been producing nanostructures with unrivalled resolution, quality and throughput. The structures produced are used in diverse research fields. The XIL facility has been recognized by the industry as the international standard for high-resolution lithography in the development of new technologies for the production of semiconductor devices. EULITHA GmbH has recently been founded as a spin-off company of the PSI to bring the benefits of this technology to the international market.

Lithography is the technology used for producing the extremely small circuit elements found on semiconductor chips. This technology is the main force behind the tremendous advances realized in information technology. Nowadays, this basic technology is applied in diverse fields from the fabrication of micromechanical systems to DNA chips. Miniaturization in lithographically fabricated patterns is desired for achieving more functionality and higher speed, with less material. The XIL beamline at the SLS has been pioneering the use of a new

technology based on soft X-rays (Extreme Ultraviolet, EUV) for producing nanostructures.

The nanostructures produced at the XIL beamline are periodic in nature, such as line-space type gratings or two-dimensional arrays of dots (see figure). The structures produced in this way at the PSI are among the smallest ever produced by the lithographic method, going down to 25 nm in period. Such patterns will be increasingly required in future nanotechnology applications. For example data storage devices with one-hundred times higher capacity than today's hard discs could become a reality through the use of such patterns.

Impact on the semiconductor industry

The leading companies and research laboratories in the microelectronics industry have been testing candidate photoresist materials to evaluate their suitability for use in EUV lithography, which is expected to be used in the production of future integrated circuits. Currently PSI has the most advanced facility for performing high-resolution exposures at the EUV wavelength. Through these tests the lack of photoresist materials that can address the production challenges has become apparent. These results have contributed significantly to the recognition of the photoresist problem as the number one critical issue facing EUV lithography, as came to light at a recent industry conference.

The performance of the innovative patterning technology developed at the PSI has led to important results in both basic and applied research. This technology will be further developed and adapted for commercial use by the recently founded spin-off company EULITHA GmbH.



Figure 1: Exposure system at the XIL beamline. Inset shows a 50 nm period dot pattern.

Institute for Polymer Nanotechnology: a new path for technology transfer

Jens Gobrecht, *Laboratory for Micro- and Nanotechnology, PSI*

For an efficient transfer of scientific results into practical applications a substantial engineering effort is required. In order to facilitate this transfer in the area of nanotechnology, the PSI established a joint venture with the University of Applied Sciences Northwestern Switzerland; and thus the Institute for Polymer Nanotechnology, known as "INKA", was established.

For a number of years nanotechnology has produced spectacular scientific results. Accordingly, there are high expectations concerning future applications such as smart clothing, quantum computers or personalised drugs. A major challenge is the development of fabrication processes to produce the nano-objects, patterns and devices reliably and at a reasonable cost. Most scientific results today are achieved with laboratory equipment, which fulfils neither of these conditions.

In order to fill this gap and to facilitate the transfer of scientific knowledge into useful applications, the Institute for Polymer Nanotechnology (in German: "Institut für nanotechnische Kunststoff-Anwendungen, INKA") was started in early 2005 as a joint venture between PSI and the University of Applied Sciences Northwestern Switzerland (FHNW).

Mission of INKA

The mission of INKA is threefold: firstly to provide an efficient channel for the application of knowledge generated in PSI's nanotechnology research. Secondly, to establish a platform

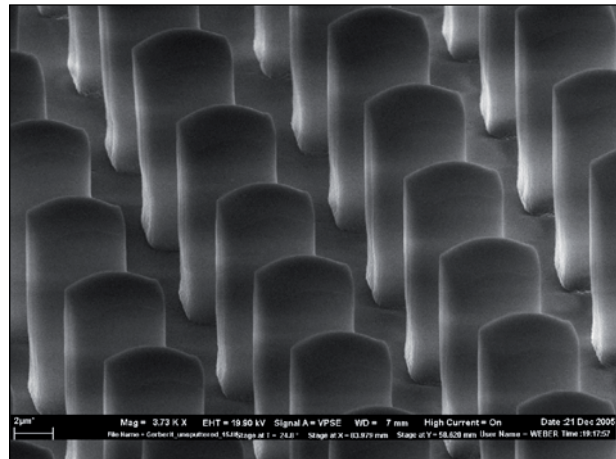


Figure 2: Is a SEM of an array of high aspect ratio microcolumns produced by hot embossing in polycarbonate. Shrinking the dimensions by an order of magnitude will yield a superhydrophobic surface. The engineering challenge here is to achieve the same structures by means of injection molding, which is by far the more economical process for production of large quantities. There are obvious applications for this in bioanalytical equipment.

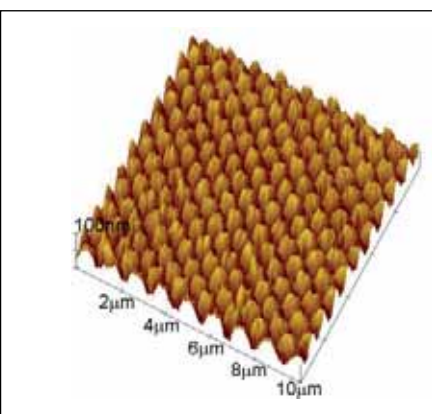
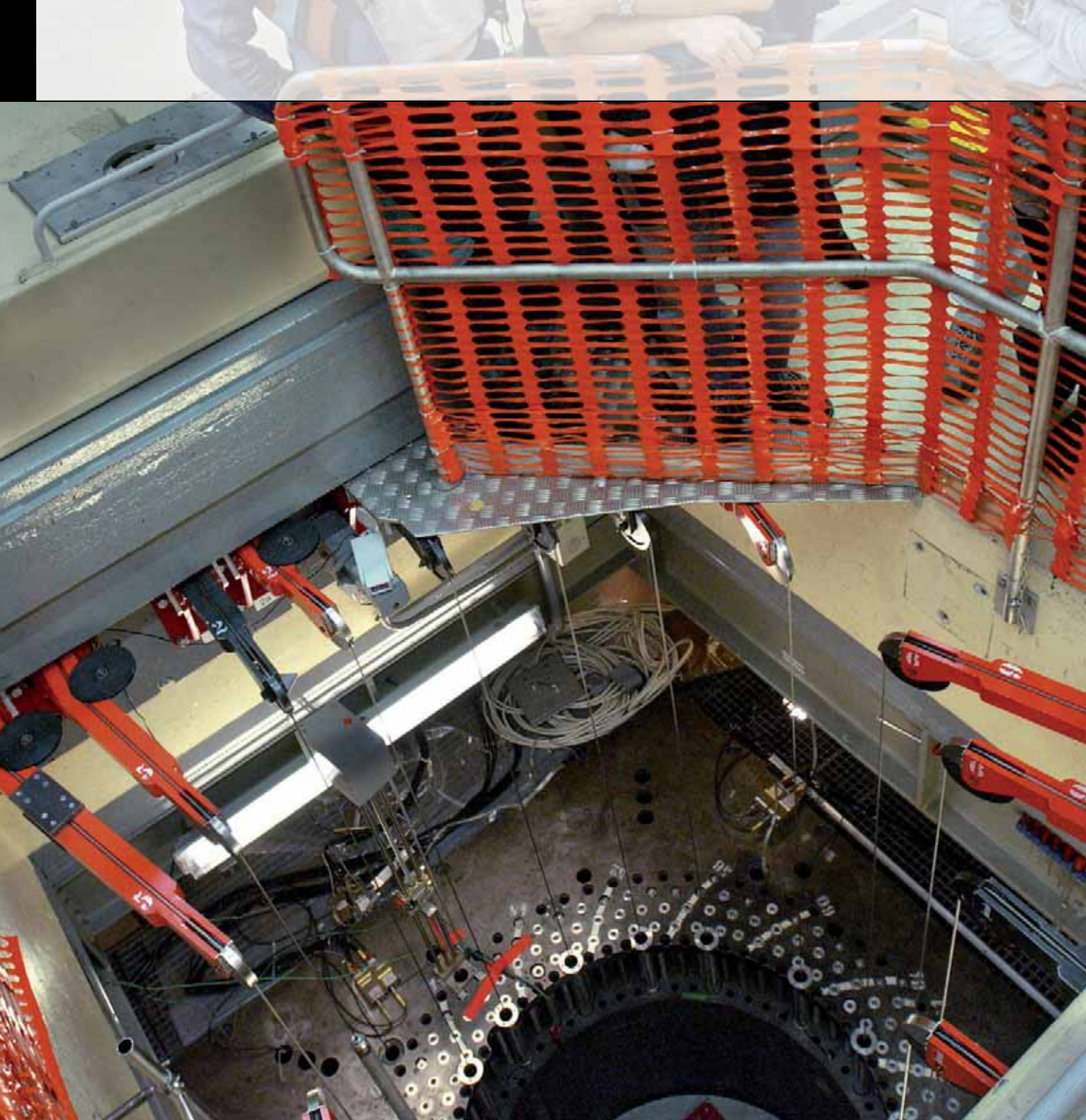


Figure 1: Shows a foil of ETFE (ethylene-tetrafluorethylene) which has been locally overgrown with polystyrene, a polymer to which biomolecules can be coupled. This "nanografting" process is made possible by irradiating the foil with a holographic pattern of soft X-rays at the SLS prior to the grafting. Surfaces of this type may allow a tailored biocompatibility of polymer materials.

for better research and development service to SMEs, who are traditionally well networked with the universities of applied sciences. Thirdly, allowing access to motivated engineering students and providing a platform for modern professional education in a highly promising high-tech area.

In 2005 INKA focused on getting some projects launched with initial industrial partners, on completing its technological capabilities and on making itself known within the community. The main scientific/technical focus lies on the functionalisation of polymer surfaces by controlled nanopatterns. This may be, for example, the wetting behaviour, the optical, or the biochemical properties of the surface. Two examples are illustrated.



Facts and figures 111

Research and user labs

Commission and committees

The Paul Scherrer Institute (PSI) is a multi-disciplinary research centre for natural sciences and technology. Research priorities lie in areas of basic and applied research, particularly in fields which are relevant for sustainable development, as well as of major importance for teaching and training, but which are beyond the capabilities of a single university department. In national and international collaborations with universities, other research institutes and industry, PSI is active in solid state research, materials sciences, elementary particle physics, life sciences, nuclear and general energy research, and energy-related ecology.

The institute is committed to future generations by paving the way for sustainable development of society and economy. Through its research, PSI acquires new basic knowledge and actively pursues the application of this knowledge within industry.

With 1,200 employees, it is the largest national research institute and is unique in Switzerland. PSI develops and operates complex research installations which call for especially high standards of know-how, experience and professionalism, and is one of the world's leading user laboratories for the international scientific community.

Nearly 10,000 visitors poured through the doors at the PSI open day in 2005. The chance to glimpse into the experimental facilities, such as the PROTEUS reactor, was fascinating for all who came.

(Photo: Béatrice Devènes)

Research and user labs

PSI's total expenditure on R&D, construction and operation of research centres, infrastructure, and services in the year under review amounted to CHF 269.3 million. The Swiss Federal Government provided 83% of this sum.

Investments amounted to CHF 43.9 million (16%); HR costs (including scheduled work) comprised CHF 163.3 million (61%). Third party funding rose by some CHF 10 million on the previous year. As federal funding remained virtually constant (increasing by CHF 2.3 million or 0.1%), the increase in total expenditure to CHF 269.3 million represents funding provided by the private sector.

Third party funding in 2005 amounted to CHF 40 million, 63% of which came from private business and 20% from federal Swiss research programmes (Swiss National Science Foundation, Federal Office of Energy); 16% was linked to EU programmes.

PSI Financial Statement (in CHF millions)		
	2005	
Expenses		
Operations	225.4	84 %
Investments	43.9	16 %
Total	269.3	100 %
Thereof from:		
Federal government funding	224.3	83 %
Third party revenue	45.0	17 %
Third party revenue		
Private industry	25.5	64 %
Federal Research Fund	8.1	20 %
EU programmes	6.4	16 %
Total	40.0	100 %
HR (incl. trainees, staff continual-education and scheduled work)	163.3	61 %

High-end user lab

Some 70% of total expenditure in 2005 was again associated with our user laboratory. High pressure from the largely external body of users is currently restricting PSI's own research activities. Yet these activities are essential, because PSI can

only provide support and consultative services for external users if its own research remains competent and attractive. At year-end 2005 some 1200 people were employed at PSI. Most of these (77%) live in Canton Aargau; 11% live in Canton Zurich and 8% outside Switzerland. Women account for 14% of employees, and well over a third of all employees (37%) hold a foreign passport.

User lab 2005						
	SLS	SINQ	SμS	Particle physics	PSI Total	(2004)
No. of beamlines/instruments	8	10	6	11	35	(31)
No. of experiments	677	351	100	13	1141	(930)
No. of user visits	1805	557	433	230	3025	(2516)
No. of users	830	352	148	102	1432	(1399)

Training facilities in high demand

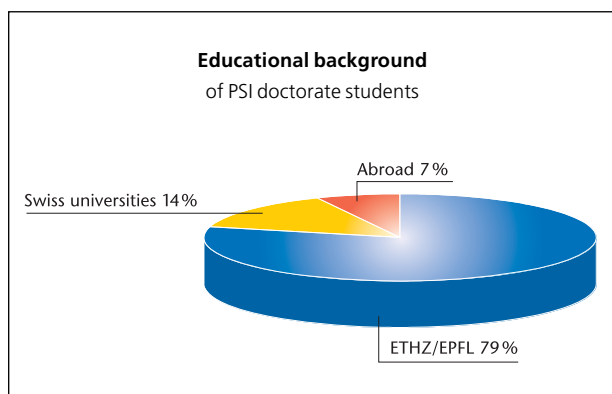
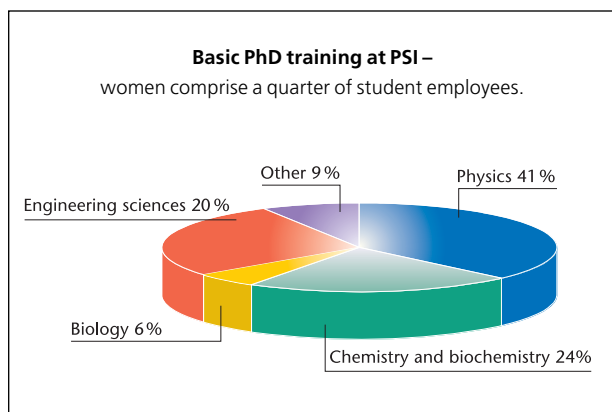
Approximately 270 PhD students are currently working in various internal and external PSI research groups. Of these some 170 are funded by PSI. The young doctoral students are mostly physics, chemistry or engineering graduates from the Swiss Federal Institutes of Technology (ETH) in Zurich and Lausanne, the Universities of Bern and Zurich or from abroad. In this way PSI provides a major input to ETH postgraduate programmes.

The largest group (58 students) are researching in the general energy (ENE) sector. Chemistry and biochemistry achieved the highest growth-rate in completed theses in 2005 (up 20% on the previous year); PhD's in biology, on the other hand, dropped 25%.

Thirty-two students, nine women and twenty-three men, completed their doctorates at PSI in 2005 with topics ranging from "Water Soluble Substances in the Atmosphere" and

“Experimental Investigations into Air Bubbles” to “Special Phase Transitions in Spin Liquids”.

As well as these PhD students, more than 40 graduates from classical or universities of applied sciences (Fachhochschulen), completed their final diploma or MSc dissertation at PSI in 2005. The institute is also a popular place for internships, with 76 students, some 70% from abroad and a third of them women, doing a laboratory trainee programme in the year under review.



With its commitment to doctoral education, as well as to teaching at the two Federal Institutes of Technology and at the classical and universities of applied sciences, PSI is a major source of input to graduate schools in the ETH sector. Our cutting-edge research, recognized the world over, as well as our globally networked user lab, guarantee that students are trained at internationally competitive levels. More than 70 PSI scientists had teaching commitments at classical and universities of applied sciences in 2005.

Support for Swiss universities

In 2005 PSI spent just over CHF 25 million on training and infrastructure facilities for PhD students and on university teaching. Some 80% of this outlay was allocated to post-graduates from Swiss universities and from the ETH institutes

in Zurich and Lausanne. By providing research training and lab facilities for external research groups, PSI takes a considerable financial and academic load off the shoulders of the Swiss universities.

Alongside academic and vocational training – PSI currently employs 77 apprentices in 12 different trades – the institute also offers courses on radiation protection and reactor technology. The special schools established for that purpose were attended by more than 2200 people in 2005.

Publications and impact score

Research at PSI is closely linked to the design, development and operation of large, complex research facilities. Unique in Switzerland, we are also, thanks to this specialty, the biggest national scientific research institute. Indications of our success and standing are on the one hand the number of papers published by our scientists in refereed journals, and on the other the impact score that tells how often publications are cited by other researchers.

Bibliometric data supplied by the University of Leiden shows that the output of scientific articles from PSI has risen slightly in recent years, reaching over 500 per year as against a ten-year average of 425. The impact score has likewise risen and currently stands at 2500 per year. In other words each paper is referred to on average five times by other scientists.

An attractive cooperation partner

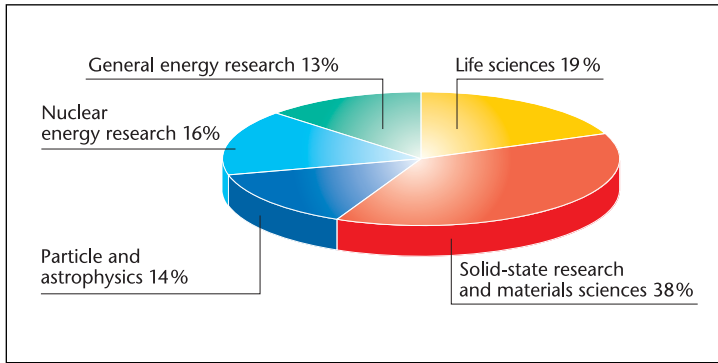
The main focus of this impact score coincides with our principal research fields – solid-state, particle and astrophysics, nuclear medicine and energy research. Some 80% of our



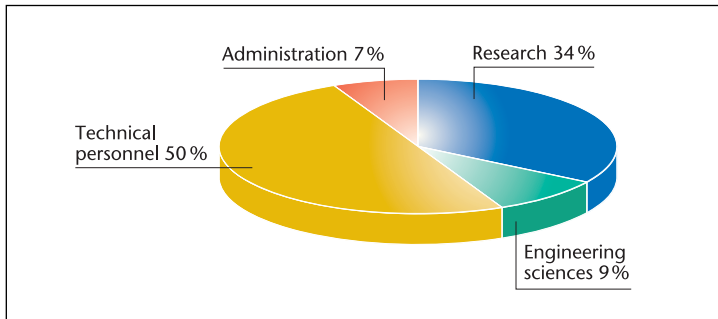
SLS

The Swiss Light Source (SLS) is a massive microscope and giant X-ray machine all in one. It accelerates electrons to nearly the speed of light and steers them with special magnets so that the characteristic high intensity synchrotron light is generated

straight ahead. This electromagnetic radiation spanning the wavelengths from infra-red to hard X-ray light is ideally suited to structural analysis of matter as well as spectrometry and to the ultra-fine structuring of material surfaces in the nanometer range.



Total budget distribution for 2004 (incl. non-governmental funding) across PSI's main research fields. The research facilities – in particular the accelerator, SLS and SINQ – were allocated to the various departments.



HR structure clearly reflects PSI's function as a user lab: the large scale facilities and complex research equipment require a large number of technical staff.

publications are in these areas. Analysis of publication activities shows that PSI is an attractive partner above all at the international level. Here too PSI achieved an impact score that puts us among the world leaders.

PSI as a user lab

PSI aims to continue attracting the best international scientists in their fields. This means that our employees, our research spectrum and infrastructure as well as our vital research culture must all meet the highest demands.

Nationally as well as internationally, PSI has established itself as a leading user laboratory. In 2005 we had some 3000 visits (previous year 2500) from more than 1400 scientists from 50 different countries. This meant one fifth more experiments than in 2004. Approximately 40% of lab users are from PSI and the Swiss universities, and more than half are from EU countries. Results of the research from the large facilities; SLS, SINQ, and S μ S resulted in 280 scientific publications, among them a larger number than ever in top journals like *Science*, *Nature*, *Cell*, *Langmuir* and *Physical Review Letters*. The Swiss Synchrotron Light Source (SLS) at PSI has been operating since 2001. In the year under review 830 scientists have conducted 677 experiments with this giant microscope, profiting from the exceptional qualities of a facility that is among the world's best.

Current research projects using the synchrotron's beamlines cover a wide area. They include the investigation of protein structures – crucial for the development of pharmaceuticals as well as for research into the function of the human genome – or the creation of 3-D reconstructions of biosystems, or the investigation of structures and properties of new materials and material surfaces.

Intense demand for SLS beam time

The high stability of the SLS beamlines has resulted in intense demand for user time, and we are stepping up our provision



SINQ

The **Spallation Neutron Source (SINQ)** is another oversized microscope. It produces neutrons, which at PSI are mostly used for experiments in materials research, solid-state physics (e.g. superconductors, magnetic and ferroelectric materials) and technology (neutron radiography). The neutrons are produced via spallation reactions induced by bombarding heavy metals (e.g. lead) with a proton beam from the accelerator.

The neutrons are produced via spallation reactions induced by bombarding heavy metals (e.g. lead) with a proton beam from the accelerator.



S μ S

Harnessed to the proton accelerator the **Swiss Muon Source (S μ S)** produces muons by directing the proton beam on a carbon target. When implanted in matter, these unstable elementary particles function like minute gyroscopes, providing precise information about local internal magnetic fields. Thanks to their spins, muons serve as highly sensitive probes used widely in materials and solid state research.

Thanks to their spins, muons serve as highly sensitive probes used widely in materials and solid state research.

to meet this as rapidly as possible. Eight beamlines were in use at the SLS in 2005, and a further eight were in various stages of planning, construction and commissioning.

Proton accelerator in demand on all fronts

The proton accelerator was originally developed more than 30 years ago for research into the basic physics of elementary particles. Today it is mostly used to produce neutrons in the Spallation Neutron Source (SINQ), the most powerful of its kind in the world. The facility comprises ten instruments for neutron experiments, used in 2005 by more than 350 scientists from Switzerland and other countries.

Central to SINQ are solid-state and soft matter research and materials sciences. Significant for future applications are high-temperature superconductors (HTS), which at certain temperatures can conduct electricity without losses. At the moment the upper temperature limit is minus 125 degrees Celsius. In order to make further progress the origins of HTS have to be understood. A speciality of SINQ is the further examination of materials which combine electrical and magnetic properties. This is usefully applied to the development of materials used in sensors, transducers and the performance of computer hard drives.

A third of the proton beam is used for producing the world's most intensive continuous muons, which are used as probes for structural research in materials sciences, solid-state physics and chemistry. Six instruments are currently available for this research. In 2005 they were used by 148 scientists in some 100 projects. The opening of the Low Energy Muon Facility (LEM) in 2005 opened up a completely new field of research, namely the depth dependent measurement of magnetic material properties in thin films, multi-layers and surfaces at nanometer scales.

Unique research offer

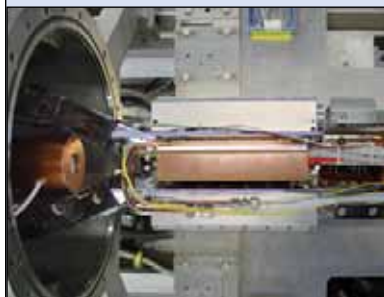
PSI's three major experimental research facilities, SLS, SINQ and S μ S, offer an internationally unique combination of complementary methods for structural research, spectroscopy and materials structuring. The EU's Large Scale Facility Access programme supports this provision with funding to PSI of around CHF 1 million per year, which is used for operating the beamlines, ongoing development of the equipment, and training and support of researchers from EU countries working on these major facilities.

As the demand for laboratory places and instruments is up to five times what PSI can supply, only top research projects can be allotted time on the beamlines. Allocation is based on research proposals assessed for merit by an international board of scientific experts.

Active in environmental research

Research into environmental situations and the development of environmentally friendly technologies frequently demands complex facilities and equipment. PSI operates and develops large scale facilities that are in continuous intensive use in these sectors. For example, two SLS beamlines will soon be used for studying the mechanisms of dispersion and intensification of environmental pollutants, as well as questions relating to the long-term disposal of nuclear waste. The proton accelerators enable production of short-lived radio-nuclides for use in atmospheric chemistry experiments.

The SINQ facility is used for neutron radiography investigating the distribution of liquids and gases in fuel cells in order to establish fundamental processes for efficient energy conversion. Processes for the production of solar hydrogen as an



Particle physics

Particle physics investigates the fundamental building blocks of matter and their interactions. Many experiments have confirmed the standard physical model with great exactitude, but one element of this theoretical structure – the Higgs boson – has not yet been found. Particle physics is currently engaged on a twofold quest, on the one hand for this heavy particle and on the other for a new super-symmetry that will link elementary particles and their interactive forces, including gravity.

ment of this theoretical structure – the Higgs boson – has not yet been found. Particle physics is currently engaged on a twofold quest, on the one hand for this heavy particle and on the other for a new super-symmetry that will link elementary particles and their interactive forces, including gravity.



The hot-lab

The PSI hot-lab is home to applied materials research on highly radioactive probes and radioactive waste disposal. The only facility of its type in Switzerland, it provides backup for Swiss nuclear power plants as well as for university and industrial research groups.

plants as well as for university and industrial research groups.

environmentally friendly alternative to fossil fuels are undergoing further development in PSI's solar furnace.

A new accelerator-based mass spectrometer that enables radio-carbon dating (using the C 14 method) of very small samples is being used in climate research for analyzing ice cores. And in the PSI smog chamber scientists are simulating the formation of aerosols in order to investigate the behaviour of these climatically relevant suspension particles in air.

Top quality for atomic particle physicists

PSI's proton beam also functions as an intensive secondary source of pions and muons, which are used for experiments in particle physics. Because of their exceptional quality – they are the world's best – they are highly sought after by American and Japanese as well as European scientists. Researchers are currently investigating the basic properties of pions and muons, looking in particular at subtle details that are crucially important for present-day particle physics.

Important news from particle physics at PSI is the development of extremely sensitive detectors, used for example in the CMS experiment at CERN, which should prove the existence of heavy particles; as predicted by the standard model of physics. Conversely, fundamental symmetries are being challenged by a group at PSI working with ultra-cold neutrons (UCN).

The proton beam is also used to generate radio isotopes for pharmaceutical research into new diagnostic and therapeutic methods. A small quantity of accelerated protons was still being used in 2005 for cancer therapy, but this will be the last time, as proton therapy will in future be based on the new COMET compact cyclotron developed specifically for medical applications.

Tissue-sparing cancer therapy

More than three hundred patients profited in 2005 from PSI's globally unique proton therapy. In co-operation with Zurich Children's Hospital 14 small children (under 4 years old) suffering from cancer were successfully treated under anaesthetic with proton radiation – a particularly tissue-sparing procedure used on a total of almost 50 children and adolescents up to the end of 2005. From late 2006 proton therapy will be offered year-round, which will enable treatment of 400-500 patients annually.

The PROSCAN project for extending proton therapy to deep-seated tumours has seen major progress in 2005. The new superconductive compact cyclotron came on stream in April and is expected to be available for patient therapy, after comprehensive testing and specialized application runs, from October 2006.

A bonus for Swiss industry

PSI has granted industrial licenses for its precision radio-therapy scanning technology. An initial privately financed commercial facility using the scanning process and compact cyclotron developed at PSI will soon commence operations in Munich. Further projects are planned. With contracts in the double figure range (CHF millions) for the delivery of components and systems; Swiss industry stands to gain from this unique PSI-developed technology.

Results from basic research become a product? Pictured here is the interferometer at the SLS.

(Photo: H. R. Bramaz)



The solar furnace

PSI's solar concentrator, an 8.5 m diameter concave mirror, bundles solar radiation to an intensity of 5000 suns. The high temperatures (up to 2000° C) created in a reactor aperture are used for re-

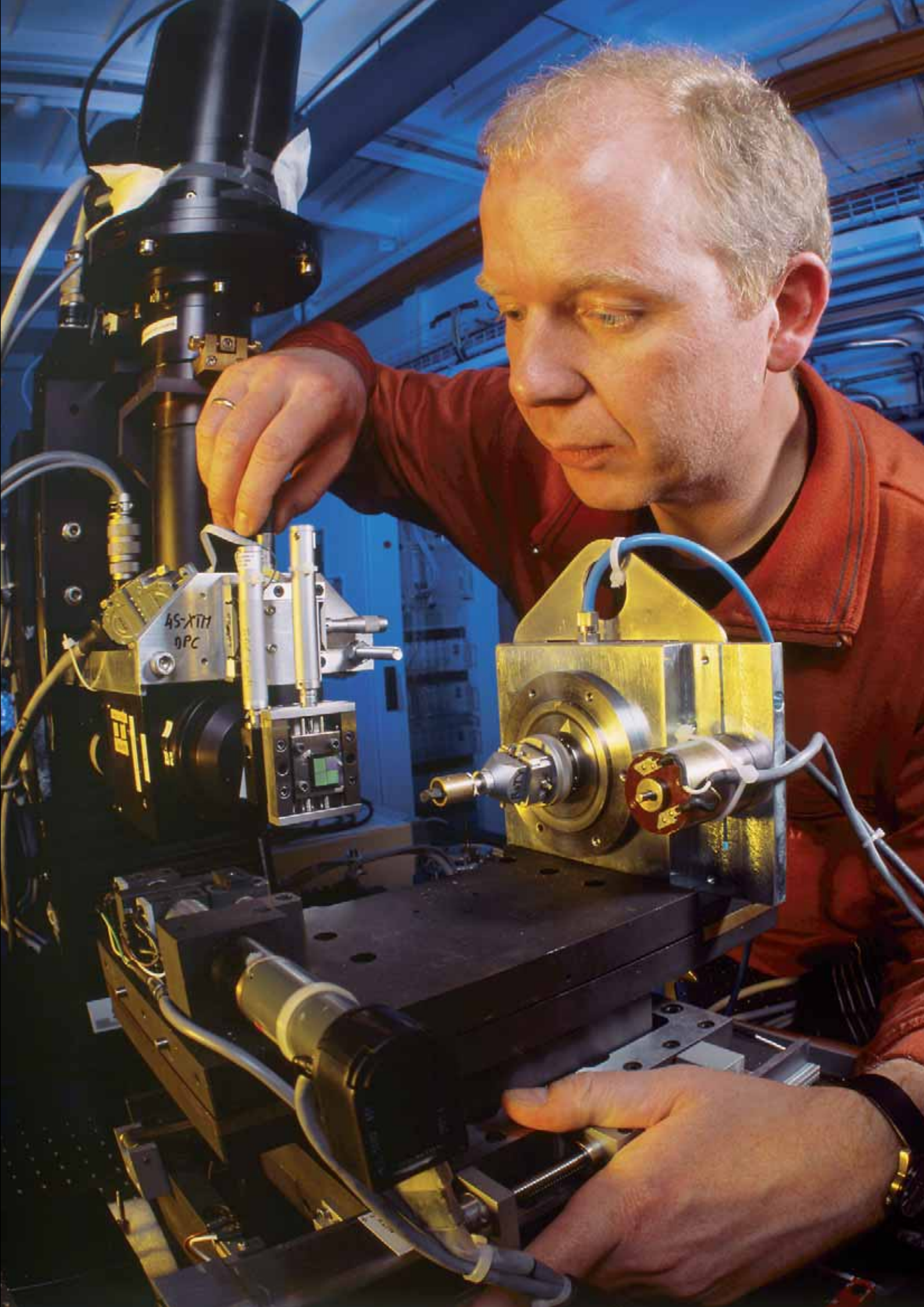
search into solar-chemical processes such as the efficient production of solar fuels and innovative materials. A high-flux solar simulator of double this power was recently installed for experiments into radiation under controlled conditions independent of the weather.



The smog chamber

The smog chamber simulates conditions for experiments in atmospheric chemistry. A 27 m³ Teflon sack can be filled, for example, with exhaust gases for exposure to artificial sunlight, and the ensu-

ing chemical reactions can be observed and measured. Results can be used for example, to determine how particulate matter transforms in the atmosphere.



Commission and committees

Research Commission

External Members

Prof. Dr. H.-R. Ott, President	Laboratory for Solid-State Physics, ETH Zurich, CH
Prof. Dr. U. Amaldi	University of Milano Bicocca, Mailand, IT
Prof. Dr. G. Aeppli	University College London, UK
Prof. Dr. W. Baumeister	Max Planck Institute for Biochemistry, Martinsried/Munich, DE
Prof. Dr. F. Carré	CEA, Gif-sur-Yvette, FR
Prof. Dr. Ø. Fischer	Department of Condensed Matter, University of Geneva, CH
Prof. Dr. B. Johansen	Research Center of Rossendorf, Dresden, DE
Prof. Dr. R. Klanner	Research Director, DESY, Hamburg, DE
Prof. Dr. D. E. Moncton	Nuclear Reactor Laboratory, MIT, USA
Prof. Dr. D. Richter	Institute for Neutron Scattering at the Institute of Solid-State Research, Forschungszentrum Jülich, DE
Prof. Dr. J.W. Tester	Laboratory for Energy and the -Environment, MIT, Cambridge, USA
Prof. Dr. Th. Sattelmayer	Chair of Thermodynamics, TU München, DE

Internal Members

Dr. M. Ammann	Particles and Matter (TEM)
Prof. Dr. K. Ballmer-Hofer	Life Sciences (BIO)
Dr. B. Delley	Condensed Matter Research with Neutrons and Muons (NUM)
Dr. R. Henneck	Particles and Matter (TEM)
Dr. I. Mantzaras	General Energy (ENE)
Dr. Joël Mesot	Condensed Matter Research with Neutrons and Muons (NUM)
Dr. W. Pfingsten	Nuclear Energy and Safety (NES)
Dr. G. Scherer	General Energy (ENE)
Dr. N. Schlumpf	Particles and Matter (TEM)
Dr. L. Simons	Particles and Matter (TEM)
Dr. U. Staub	Synchrotron Radiation and Nanotechnology (SYN)
Dr. W. Wagner	Condensed Matter Research with Neutrons and Muons (NUM)
Dr. P. Hasler, Secretary	Life Sciences (BIO)

Permanent Guest

Prof. Dr. A. Green	President of the ETH Zurich Research Commission; Institute of Geophysics, ETH Zurich, CH
--------------------	--

Research Committees

Synchrotron Radiation SYN*Scientific Advisory Committee (SAC)*

Prof. Dr. M. Altarelli, President
Sincrotrone Trieste, Trieste, IT

Prof. Dr. T. Baer
University of North Carolina, USA

Prof. Dr. P. Cramer
Ludwig-Maximilian University Munich, DE

Prof. Dr. W. Eberhardt
BESSY GmbH, Berlin, DE

Prof. Dr. R. Fourme
Synchrotron Soleil, Gif-sur-Yvette, FR

Prof. Dr. F. Farges
Université de Marne la Vallée, FR

Prof. Dr. J. Hastings
SSRL/SLAC, Stanford, USA

Prof. Dr. G. Margaritondo
EPFL, CH

Prof. Dr. G. Materlik
Diamond Project, Oxfordshire, UK

Prof. Dr. R. Prins
ETH Zurich, CH

Prof. Dr. T. Richmond
ETH Zurich, CH

Condensed Matter Research with Neutrons and Muons NUM*SINQ Scientific Committee*

Dr. A. Boothroyd, Chairman
Oxford University, UK

Dr. A. Arbe
University of San Sebastian, ES

Prof. Dr. C. Bernhard
University of Fribourg, CH

Prof. Dr. R. Caciuffo
Forschungszentrum Karlsruhe, DE

Dr. B. Fåk
CEA, Grenoble, FR

Prof. Dr. J. Löffler
ETH Zurich, CH

Prof. Dr. K. Mortensen
Danish Polymer Centre, Risø, DK

Dr. J. Rodriguez-Carvajal
Laboratoire Léon-Brillouin, Gif-sur-Yvette, FR

Dr. A. Wiedenmann
Hahn-Meitner-Institut, Berlin, DE

Dr. M. Würle
ETH Zurich, CH

Myon Spin Spectroscopy

Prof. Dr. H. Keller, President
University of Zurich, CH

Prof. Dr. A. Baldereschi
ITP, EPFL, CH

Prof. Dr. R. De Renzi
Università di Parma, IT

Prof. Dr. E. M. Forgan
University of Birmingham, UK

Prof. Dr. J. Gomez Sal
Universidad de Cantabria, Santander, ES

Prof. Dr. F. J. Litterst
IMNF, TU Braunschweig, DE

Prof. Dr. A. McFarlane
Univ. of British Columbia, Vancouver, CDN

Dr. F. Pratt
ISIS, RAL, Chilton, UK

Dr. B. Roessli
Paul Scherrer Institute/ETH Zurich, CH

Particles and Matter TEM*Experiments at the Ring Cyclotron*

Prof. Dr. C. Hoffman, President
LAMPF, Los Alamos, USA

Prof. Dr. A.B. Blondel
University of Geneva, CH

Dr. D. Bryman
TRIUMF, Vancouver, CDN

Dr. P. Cenci
I.N.F.N. sez. di Perugia, IT

Prof. Dr. S. Paul
Technical University of Munich, DE

Prof. Dr. M. Pendlebury
University of Sussex, UK

Prof. Dr. L. Tauscher
University of Basel, CH

Prof. Dr. D. Wyler
University of Zurich, CH

Life Sciences BIO

Prof. Dr. D. Neri, President
ETH Zurich, CH

Prof. Dr. Ch. Glanzmann
University Hospital Zurich, CH

Prof. Dr. M. Grütter
Biochemical Institute, Univ. of Zurich, CH

Prof. Dr. U. Haberkorn
Universitätsklinikum Heidelberg, DE

Prof. Dr. S. Werner
ETH Zurich, CH

Nuclear Energy and Safety NES

Dr. Ch. McCombie, President
Gipf-Oberfrick, CH

P. Hirt
Atel, Olten, CH

Prof. Dr. M. Giot
Université Catholique de Louvain, BE

Dr. P. Miazza
Nuclear Power Plant Mühleberg, CH

Dr. U. Schmockler
HSK, Würenlingen, CH

Dr. J.B. Thomas
CEA-Saclay, Gif-sur-Yvette, FR

Prof. Dr. K. Törrönen
Institute of Energy JRC Petten, NL

Dr. P. Zuidema
Nagra, Wettingen, CH

General Energy ENE

Prof. Dr. T. Peter, President
ETH Zurich, CH

Dr. T. Kaiser
Alstom Power Technology Center,
Baden-Dättwil, CH

Prof. Dr. A. Reller
University of Augsburg, DE

Dr. M. Schaub
CT Umwelttechnik AG, Winterthur, CH

H.U. Schärer
BFE, Berne, CH

Prof. Dr. L. Schlapbach
Empa, Dübendorf, CH

Prof. Dr. A. Voss
University of Stuttgart, DE



PAUL SCHERRER INSTITUT
PSI

Das Schweizer Institut
für Experimentelle und Angewandte
Physik und Chemie an der
ETH Zürich

PSI
ETH ZÜRICH

Lists and links to web

The publication lists for the PSI departments featured in this volume can be found on the accompanying CD and include the following:

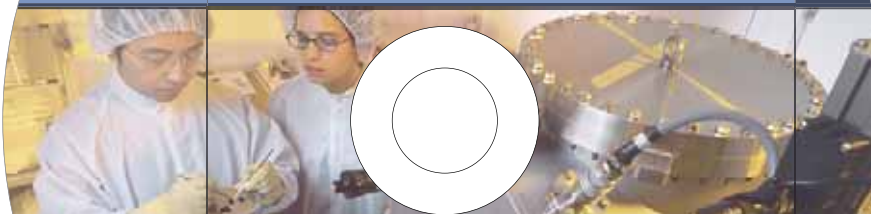
- Peer reviewed publications
- Invited talks
- Dissertations
- Conference proceedings
- Lectures

Electronic versions of all 3 volumes of the PSI Scientific Report 2005 and the Annual Report (Jahresbericht) in German are also included on the CD.

The Scientific Report 2005 Volumes 1, 2 and 3 are available at www.psi.ch (Media/Annual Reports).

Links to other research activities not highlighted in the PSI Scientific Report 2005 can be found at www.psi.ch (Research at PSI).

PAUL SCHERRER INSTITUT



PSI Scientific Report 2005

Volume 1 Condensed matter, photons, neutrons and charged particles (ISSN 1661-7002)

Volume 2 Life sciences and medicine (ISSN 1661-7010)

Volume 3 Energy and environment (ISSN 1661-7029)

PSI publication lists

PSI-Jahresbericht 2005 (German) (ISSN 1423-7261)

The PSI Scientific Report 2005 comprises:

- Volume 1** Condensed matter, photons, neutrons and charged particles
- Volume 2** Life sciences and medicine
- Volume 3** Energy and environment

PAUL SCHERRER INSTITUT



Paul Scherrer Institut, 5232 Villigen PSI, Switzerland
Tel. +41 (0)56 310 21 11, Fax +41 (0)56 310 21 99
www.psi.ch